An investigation into the deterioration of source detection due to positional uncertainty, and of how it might be remedied

Quartly, G. D.

Award date:
1989

Awarding institution:
University of Bath

AN INVESTIGATION INTO THE DETERIORATION OF SOURCE DETECTION DUE TO POSITIONAL UNCERTAINTY, AND OF HOW IT MIGHT BE REMEDIED

submitted by G.D.Quartly
for the degree of PhD
of the University of Bath
1989

COPYRIGHT

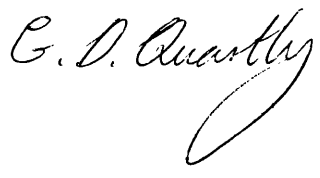

ProQuest LLC
789 East Eisenhower Parkway
P.O. Box 1346
Ann Arbor, MI 48106-1346

ABSTRACT

This thesis investigates a particular signal processing problem in the field of underwater acoustics, namely that of uncertainty in the shape of a hydrophone array, and of how this affects bearing determination. The problem is reduced by characterizing the array shape by a *limited* Fourier Series whose coefficients are to be determined. The processing applied to a particular shape estimate is Conventional Beamforming, because of its resilience to high noise levels and minor phase errors.

Degradation of the beam pattern is shown for errors in the various Fourier coefficients. The concept of a 'power function' is introduced — an empirical measure of the degree of focusing in an image. It is shown that in the absence of noise, such a figure is maximized for processing using the correct values for the coefficients. An investigation is undertaken into the accuracy in array shape and source bearing attainable by this process in the presence of various noise effects — additive noise, secondary sources and multiplicative noise (the latter representing inhomogeneities in the transmission medium).

This is followed by a wider investigation into the changes in value of a power function for errors in more than one Fourier term, to show the structure of the variations and to ascertain the viability of gradient methods for locating the peak value of this function of many unknowns.

ACKNOWLEDGEMENTS

This project was initially sponsored by CAP Scientific, for whose support I am most grateful. Further financial assistance was provided by the School of Physics. I am also especially indebted to my supervisor, Dr. N.G.Pace, for much discussion over the last few years and the gargantuan effort he made in proof reading this document so carefully.

I am very appreciative of the useful advice proffered by Prof. H.O.Berktay, Dr. W.G.Dawson, Dr. P.C.Hines and Wang L.S., and the great friendship and support of all in the department, especially during the agonies of writing up. Much too is owed to the friendly people in the computer unit, who proved to be much more reliable than the mainframes they ran.

Lastly, I am most grateful to the LORD for all that he has done for me, including arranging a total eclipse to enliven one of the otherwise interminable all-night sessions, and to my family and Annette for providing havens safe from all thoughts of the computer.

TABLE OF COMMONLY USED ABBREVIATIONS

AR	—	Autoregressive
CBF	—	Conventional Beamforming
CW	—	Continuous Wave (=pure sinusoid)
CZ	—	Convergence Zone
DFT	—	Discrete Fourier Transform
FFT	—	Fast Fourier Transform
FT	—	Fourier Transform
KT	—	Knox-Thompson
LP	—	Linear Predictor
lms	—	least mean square
MA	—	Moving Average
MATE	—	Mid-ocean Acoustic Transmission Experiment
ME , MEM	—	Maximum Entropy (Method)
ML , MLM	—	Maximum Likelihood (Method)
MUSIC	—	MUltiple Source Identification and Classification
NLM	—	Non-Linear Methods
pdf	—	probability distribution function
PHD	—	Pisarenko Harmonic Decomposition
PSD	—	Power Spectral Density
PSF	—	Point Spread Function
RI	—	Refractive Index
rms	—	root mean square
SI	—	Speckle Interferometry
SLL	—	Sidelobe Level
SNR	—	Signal to Noise Ratio
SPR	—	Successive Planewave Removal
ssp	—	sound speed profile
TDE	—	Time Delay Estimation
USC	—	Underwater Sound Channel

GLOSSARY

Below is a list of some of the variables used in this work, along with a description of what they represent. Some letters are used in more than one context; their main uses are given here.

a_i	AR coefficient	r_0	Scale length of fluctuations
a_i	Fourier coefficient	t	Time
A_i	Amplitude of source	v_i	Voltage at element
b_i	MA coefficient	V	Summed voltage
B	Change in Log-amplitude	w_i	Element weighting
c	Local sound speed	x_i, y_i	Element position
c_0	Reference sound speed	α	Inter-sensor correlation
d	Inter-element separation	β	Correlation across array
D	Length of array	γ_i	Log of multiplicative scalar
$e_i(\theta)$	Steering vector	Δu	Beamwidth
E[..]	Expectation operator	$\Delta\theta$	Separation/Error in bearing
f	Frequency (cycles/sec)	$\Delta\phi$	Phase difference
F_n	Array factor	ζ_i	Rms/Amplitude ratio
$f_i(x)$	Basis function	η_i	Multiplicative scalar
i, j	Summation indices	θ	Scan angle
I	Intensity (eqv. power)	θ_0	Specific angle e.g. source
j	Square root of -1	λ	Wavelength
k	Wavenumber ($=2\pi/\lambda$)	μ	Fractional change in RI
L	Length of array	μ	Correlation length / L
n	No. of elements	σ_A	Rms fluctuation in amplitude
n	Refractive index	σ_m	S.d. of multiplicative noise
N	No. of beams formed	σ_u	Rms error in angle
p_i	Power in direction θ_i	σ_x	Rms positional error
$P(\theta)$	Power in direction θ	σ_ϕ	Rms fluctuation in phase
r_i	Distance from origin	ω	Frequency (in rads/sec)

CONTENTS

SECTION ONE : GENERAL

SECTION TWO : LITERATURE SURVEY

SECTION THREE : PROJECT METHODS

SECTION FOUR : ACCURACY OF ESTIMATORS

SECTION FIVE : CONVERGENCE PROPERTIES

SECTION SIX : MISCELLANY

APPENDICES

Want alsο liefheeft God
de wereld gehad, dat Hij zijn
eniggeboren Zoon gegeven heeft,
opdat een ieder, die in Hem
gelooft, niet verloren ga, maar
eeuwig leven hebbe.

1. AIM OF PROJECT

When a towed array is used to detect sources in the underwater environment, one of the significant problems encountered is that the performance of the signal processing can be badly degraded by errors in the assumed positions of the sensors. The aim of this work is to investigate the deterioration in quality of a signal's beam pattern due to such errors, and also the resulting increased error in estimation of source direction, and thence to find an approach that will improve the detection and tracking capability of the system by determining the parameters that describe the configuration of the array.

2. INTRODUCTION TO THESIS

Passive sonar detection of distant submarines is often achieved by use of a towed array — a series of hydrophones along a cable towed some distance behind a ship. Many algorithms exist for locating sources when the sensor positions are well determined, especially when equally spaced along a straight line; however, for the case of interest the positions are neither accurately known nor constant in time. This has important effects on the processing that can be applied, and on the ability to locate sources.

The work contained herein relates to this signal processing problem, which is investigated by analytical and computational means. The first section of this thesis begins with some elementary aspects concerning sources of sound in the ocean, and an introduction to a simple beamforming technique for locating sources using a linear array of hydrophones. A brief explanation is then made of the causes of shape uncertainty and the problem this poses to the processing.

The second part is a literature survey, covering many of the aspects introduced in the first section, but concentrating more on the points of particular relevance to this work. The opening chapter relates the specific nature of this investigation to similar situations in many diverse areas of physics, showing how phenomena like positional uncertainty of detectors and variable transmission media are common to all. This indicates why some reference is made to work outside the confines of underwater acoustics. However, attention is also drawn to the real differences in scale and relative importance of the various phenomena, which prevent the automatic transfer of solutions from one field to another. There are chapters summarising the many high resolution algorithms for source estimation, the theoretical and observed structure of the refractive index in the ocean, and disturbances of the array. The last of these covers observed array configurations, their effect on processing, and various authors' efforts to overcome this problem, either by modelling the disturbance or by use of suitable averaging.

This project continues the line first advocated by Muller & Buffington[71], and then followed by Bucker[16], of characterizing the beam pattern for a particular shape estimate by a single value. This figure, here termed a 'power function' is devised to represent the sharpness or quality of the image, such that an iterative technique to maximize the value will lead to the correct array shape

being determined. The third section of this thesis details the particular means of this investigation, briefly explaining the hardware and software used, as well as the specific implementation used for certain subroutines. A list is given of various possible power functions, whose properties are to be compared over a variety of scenarios.

The next two sections contain the results discovered in this project. In the first one the emphasis is on array shapes close to true. The opening chapter details the degradation of the beam pattern caused by varying errors in the different Fourier coefficients that describe the shape. Note is also made of the pointing error associated with positional inaccuracy, and the limits on source visibility i.e. the magnitude of errors sufficient for the power lobe in the source direction to be superseded by its own sidelobes. Next follows an introductory chapter on power functions showing their applicability under perfect conditions (i.e. single source and no noise present), and an illustration of the effect of noise. The subsequent chapters are concerned with the best strategy for shape determination, contrasting the performance of the different power functions, and investigating their dependence on the processing conditions — angular sector of interest, beam sampling rate and system of sensor shading used. The remainder of this results section then explores how the shape accuracy attainable is independent of true array shape, but varies as a function of bearing, frequency and levels of additive and multiplicative noise (the latter being a means of modelling fluctuations in the refractive index along the transmission path). Where possible, comparison is made to the expected dependence upon such terms.

The second section of results relates to a different aspect of the problem. This looks at estimates of the array shape that are far from true, and explores the local variation in value of a power function. This is in order to determine whether an iterative technique, pursuing a route of increasing power function value, will converge to an array shape near the true one or to some other whose resultant beam pattern gives no assistance in localizing sources. Different processing approaches are again compared. In particular, are noted the constraints imposed on the initial estimate when high noise levels or secondary sources are liable to be present.

The final section of the main part of this thesis looks briefly at the particular problem of dealing with several unknowns at once. Firstly, note is taken of how an error in one Fourier coefficient affects the estimation of others, leading to the production of an orthogonal basis such that the errors in all the terms are independent of one another. The next chapter shows how a simple gradient routine may be created that effectively locates the maximum over several unknowns. This is followed by a short chapter comparing the various power functions tested, highlighting which are the

most suitable candidates for any continuation of this work. Then follows suggestions for further work along these lines and a summary bringing together all the findings from this research.

Appendices are provided at the end covering some of the more specialized (and mathematical) arguments — some of these are original, whilst others repeat less commonly found material.

3. GENERAL BACKGROUND

3.1 The 'Source'

This project is concerned with a passive sonar array i.e. one where the system purely listens for sound emitted by a submarine. [Active arrays, which emit a known signal and detect its echo off objects, are unsuitable for the long range detection and secretive monitoring that is the aim of this work.] There are many ways in which a vessel can emit sound. If it uses its own active sonar that emission may be detected and used to localize it, although it may not be aware of the silent observer's presence. However, even a silent vessel unwittingly produces noise. Some will be caused by turbulence as the vessel slips through water. More intense sound may be caused by cavitation noise around the propellor, which will be modulated by the blades to show a sharp frequency peak corresponding to the rotation rate of the propellor multiplied by the number of blades on it. Coupling of internal machinery noise through the hull may also lead to sharp well defined frequency emissions. It is on the assumption that these discrete frequencies are significant, that this project is simulated purely in terms of the signal at a few select frequencies rather than a series of time measurements at each sensor or else a large number of frequency components. In recent times, submarine builders have taken care not only to reduce the reflectivity of the vessels by use of anechoic tiles, but also to minimize the emission of sound[25].

Motion of a source or receiver will affect the received frequency via the Doppler Effect. Assuming that array motion transverse to its line is slow, the frequency shift experienced at all the sensors will be the same. This may vary with time depending upon changes in direction by the emitter or towing ship. Burlakova, Saichev & Slavinski[19] also refer to frequency wandering caused by inhomogeneities in the ocean. Such an effect would differ from sensor to sensor. If there are two or more frequencies present, then this effect can be distinguished from the Doppler shift as the two have different frequency dependence.

3.2 Structure of an Array

A device for converting an incoming underwater pressure waves into an electrical signal is known as a hydrophone. There are several different physical processes by which such a conversion may be achieved; those generally in use share the property of linearity i.e. the amplitude of the electrical signal produced is directly proportional to the amplitude of the pressure variations (i.e. the sound waves). Hydrophones can be made to have a response that varies according to the direction of the incident wave. However, for work with towed arrays, it is more common to use a type whose response is independent of angle — these are termed omni-directional. The reasons that these are used are that it is not possible to maintain a constant orientation for all hydrophones without rigid connections, and that it is often important to be able to search through all angles for sources of sound. Also, for the frequency range of interest in this work, directional hydrophones would be very large.

One hydrophone can merely detect the amplitude of a pressure wave; it cannot give any information as to its bearing. For this, two or more hydrophones are required — the direction of the source being obtained by comparing the phases of the signals received at each of the hydrophones. [In this context, any slight difference in amplitudes can not really aid in determination of the source direction.]

Any set of two or more hydrophones used for co-processing can be termed an array. Now, although just two such hydrophones could yield an accurate determination of bearing, it is usually necessary to use far more. The reasons for this being the need to detect more than one source and effects due to the presence of noise (caused by other sources, bottom reflections, receiver noise), which would seriously affect such a two element array.

Given many hydrophones, there are several different types of configuration that can be adopted:-

- Straight line
- Along the circumference of a circle or a set of concentric circles
- 2-D or 3-D grid
- Random

Each may have its merits, but the situation considered for this project is that of a towed array, which requires that the array lies along a line. This is achieved by placing the hydrophones in

a long flexible cable, which is let out of the back of the ship (or submarine). The actual active part of the array may be separated from the stern by hundreds of metres of towing cable. This enables the sensors to be reasonably distant from the ship (reducing the pick up of noise from it), and also allows the array to sink to a low depth. A combination of length of towing cable, its weight, and the towing speed determines at which depth the array lies. A device at the end of the array, called a drogue, provides the tension necessary to keep the array fairly straight. A taut cable is susceptible to resonances like a violin string — to prevent occurrence of such disturbing the array VIMs (Vibration Isolation Modules) are positioned either end of the active section in order to attenuate the oscillations.

However some freedom still exists in the positioning of the elements along that line:-

- Equally spaced
- All separations to be multiples of a standard length — a 'sparse' array
- Random

Many processing algorithms exist for the first case, relying on the symmetry of the arrangement, whereas little can be done for the other two cases. Bucker [14] has proposed an algorithm for the second case that can yield good resolution under suitable conditions. The first case is the one generally adopted because:-

- There exist many algorithms for that situation.
- Processing does not place undue emphasis on any particular elements (whereas the sparse array may), and is thus less affected by noise at that element or its failure.
- Sections of array can be replaced much easier if all are identical.
- It is more resilient against noise than the other methods.

A straight line array can only be used to determine the direction of a source relative to the line of the array. Thus the direction of a source can only be restricted to a cone centred on the line of the array. However, interest is generally only in distant sources, and as these must lie in roughly the same horizontal plane as the array, the indeterminacy is thus reduced to a question of which side of the array the source lies on. This is known as 'Left-Right Ambiguity'. When dealing with a perfectly straight array of constant orientation, this problem cannot be overcome by any processing. [Note that a horizontal planar array, either of grid or circular design would not be subject to such

difficulties.] If a line array is being used, it is necessary to pursue a route that will orientate the array in a different direction. A new determination of bearing will now remove this uncertainty in location [see Fig 3.1].

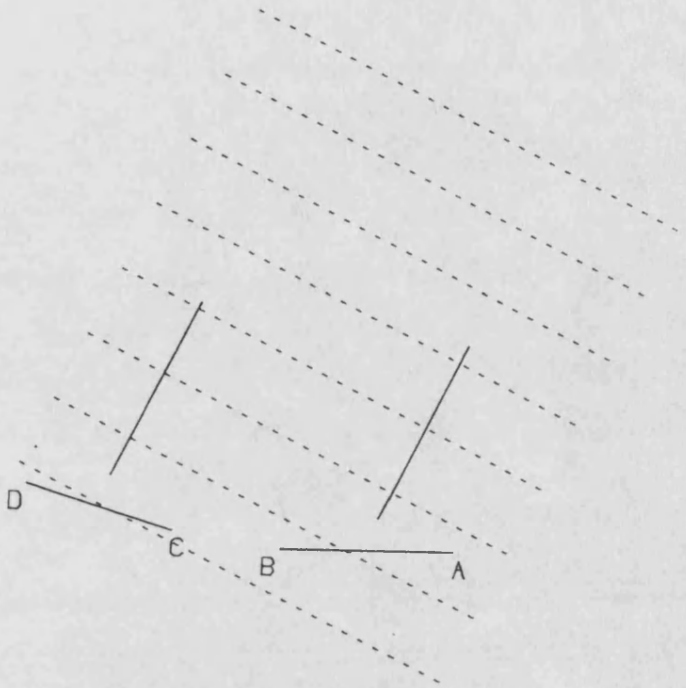

Fig 3.1 : Diagram to show how bearing determination using 2 non-parallel array lines removes the left-right ambiguity.

Note: if the array was not precisely straight, but rather curved in a *known* manner e.g. from A to D via B and C, then such an ambiguity would not exist. Rotating the line of the array also deals with the problem of poor resolution for an array towards 'endfire' i.e. along the line of the array.

3.3 Aliasing

The resolution capability of an array using Conventional Beamforming [see appendix 2] is given by:-

$$\Delta\theta \approx \frac{\lambda}{D} = \frac{\lambda}{nd} \qquad [3.1]$$

where n is the number of sensors and d their separation. Thus, to maximize the resolution, the sensors are placed as far apart as is permissible. There is, though, an upper limit on the separation, above which ambiguities in bearing again occur.

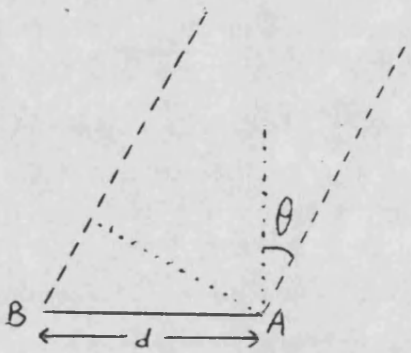

Fig 3.2 : Diagram to show how phase delays depend upon relative location of source and sensors.

Consider the situation illustrated for a 2 element array in Fig 3.2. The phase of the signals at elements A and B are determined as ϕ_A , ϕ_B respectively. This is due to the difference in travel time from the source to the two sensors. Assuming a far-field source and hence plane waves, the extra distance travelled to B is given by:-

$$\Delta S = d \sin\theta \qquad [3.2]$$

The difference in phase thus resulting is:-

$$\Delta\phi = 2\pi(d \sin\theta / \lambda) \qquad [3.3]$$

as phase changes by 2π over the distance of a wavelength. A source at a different angle, θ', may produce the same phase difference and hence be indistinguishable. For this to occur requires:-

$$2\pi(d\sin\theta/\lambda) = 2\pi(d\sin\theta'/\lambda)+2n\pi \qquad , n \in N$$

$$\rightarrow\ d = \frac{n\lambda}{\sin\theta - \sin\theta'} \qquad [3.4]$$

As $\sin\theta - \sin\theta'$ must be in the range 0 to 2, non-trivial solutions for the separation will only occur for $d \geq \lambda/2$.

If the separation is half a wavelength, sources at one endfire direction ($\theta = {}^1/_2\pi$) cannot be distinguished from those at the other ($\theta = -{}^1/_2\pi$). If such problems are to be avoided, it is necessary to insist that the separation of the elements is to be less than half a wavelength. This result is analogous to the Nyquist limit on frequency determination. Note, if interest is only in sources within $\pm\theta_0$ of broadside, then the limit upon element separation becomes:-

$$d \leq \frac{\lambda}{1 + \sin\theta_0} \qquad [3.5]$$

This situation, in which an uncertainty in source bearing occurs because of too large a separation of elements, is termed aliasing. This effect is independent of the nature of the signal processing used.

3.4 Various Causes of Noise

One of the major reasons for having many elements in an array is in order to be able to overcome the problems caused by noise. This noise may take various forms dependent upon origin; the relative importance of the different types will depend upon the frequency used for processing. This work is concerned with sharp frequency emissions in the range 150-400Hz, with most of the work being done at 250Hz. The arrays simulated generally have sensors at half-wavelength spacing i.e. 3m. Although many aspects of the problem scale with wavelength and array dimensions, the values are given here as the nature of various noise effects does change with frequency. Brief reference is given here to sources of noise over a wide range of frequencies, however only those in the aforementioned band are of concern here.

a) Other Sources

There may be many sources radiating at the selected frequency; some will be of interest, whilst others merely provide extraneous noise. Over large distances the oceans can be regarded as two dimensional — reflections of sound waves off the sea bottom and surface can be significant enough to cause the power of signals to fall off only as $1/r$ rather than $1/r^2$. Consequently, the effect of distant shipping can be noticeable. Apart from incidental discrete shipping, there are often situations where a strong source is deliberately activated to hide another. This is referred to as a 'jammer' or 'interference signal'. [In such cases, there is a need to be able to detect sources well below the level of the jammer. This may be achieved by standard processing using an algorithm with low sidelobes, or by implementing an algorithm that rejects such interference e.g. Adaptive Noise Cancelling (ANC) which directs a null of the array's directivity pattern towards the interference.] Another important source is the ship towing the array, which will of necessity be fairly close to the sensors. This problem is reduced by making sure that the active part of the array is far from the ship by using a long towing cable.

It is generally assumed that additive noise has Gaussian statistics; Bouvet & Schwartz[11] have shown this to be close to true for background noise and merchant shipping, however other sources such as snapping shrimp have a pdf (probability distribution function) that can not be modelled even in terms of a Gaussian-Gaussian mixture.

b) Reflections

There may be echoes of the desired signal from both sea surface and bottom. These will have taken a slightly different path through the ocean from source to sensor, and hence be of different (and varying) phase to the direct signal. Such echoes may appear to originate from slightly different bearings to the direct ray.

c) Local Noise

Underwater sound may also be generated by many other means — aquatic life, waves and rain upon the sea surface, cracking of overhead ice, or simply due to the wind blowing upon the top. This last effect is often characterized in terms of Sea States in a manner similar to the Beaufort Scale for winds. The power spectra of the various meteorological sources have been investigated by Scrimger et al[93], Ferguson & Wylie[35], Nystuen & Farmer[75] and Hamson[46] amongst others, and shown to be significant only at frequencies of the order of 1-20kHz. [Note, with a horizontal linear array these all-encompassing sources may appear to show directionality — this is due to focusing

towards broadside rendering the array sensitive to overhead sources too.]

d) Self-Noise

When an array is towed rapidly through water, noise is induced by the turbulent boundary layer surrounding the array; Owsley & Fay[76] have stated that the correlation length of such is only of the order of 0.1m.

e) Inhomogeneity

The sea is not homogeneous — there are both temporal and spatial variations in temperature, salinity and pressure, and hence in refractive index. Thus the phase delay at one element with respect to another is affected not only by the bearing of the source, but also by the difference in the nature of the medium through which the different rays have propagated. [This is dealt with in further detail in chapter 9.]

f) Electrical Noise

This is the term for effects due to non-linearity of the transducer response, thermal noise in amplification circuits and rounding error caused by digitising the analogue signal. Kazmirtsak & Tyutekin[54] have shown how the limited bit size of analogue-digital convertors (ADCs) affects the performance of bearing estimators.

There will also be effects caused by:-

g) Inexact balancing of propagation times for signals along wires in the array.

h) Uncertainty in location of elements of array relative to one another.

i) Relative motion of array and sources, which causes a Doppler shift of the signals to a frequency slightly different from the one used for processing.

j) A weakened response or failure in one or more channels.

Item h) is the main effect under investigation in this project, but several of the others will have to be modelled and taken into account during the processing.

4. CONVENTIONAL BEAMFORMING

4.1 Mathematical Formulation

A very simple method of processing such data is known as Delay-Sum & Square or Conventional Beamforming (CBF). In this method, searching is performed over all angles, θ, of interest by scanning over the corresponding values for the wavenumber vector, k.

For each sensor, the received signal, v_i $(=Ae^{jk.r})$ is multiplied by the complex number $e^{-jk'.r}$, the k' corresponding to the wave number in the chosen direction of the search. If this matches the true bearing of the source, the signals at all the sensors will be reduced to the same value A. The degree of correlation at these sensors (i.e. a measure of how 'correct' the choice of k' is) can be formed by adding all such processed values together, then taking the modulus squared, which represents the power in the signal. In mathematical notation this would be written:-

$$P(\theta') = V^2(\theta') = \left[\sum_{i=1}^{n} v_i e^{-jk'.r}\right]^2 \qquad [4.1]$$

where $k' = \left(\frac{2\pi}{\lambda}\sin\theta', \frac{2\pi}{\lambda}\cos\theta'\right)$. For a straight array of equally spaced elements, with no noise present, it can be shown [see appendix 2] that the power perceived in a direction θ', due solely to a source on a bearing of θ_0, can be expressed as:-

$$P(\theta) = [A]^2 \frac{\sin^2[\,{}^1/_2 kdn(\sin\theta - \sin\theta_0)\,]}{\sin^2[\,{}^1/_2 kd(\sin\theta - \sin\theta_0)\,]} \qquad [4.2]$$

This is shown in Fig 4.1a. The expression maximizes at $\theta = \theta_0$ i.e. for a beam formed along the direction of the true source, but it also renders finite values for the power in other directions, which could mask weaker sources. The subsidiary peaks, known as sidelobes, occur for:-

$$\sin\theta = \sin\theta_0 + \alpha\frac{\lambda}{nd} \qquad \alpha = \tfrac{3}{2}, \tfrac{5}{2}, \tfrac{7}{2}, \cdots \qquad [4.3]$$

with those further from the main one containing progressively less power. For lobes far from the main one, it can be shown that the level of the $2m$th is 6dB less than that of the mth. No power is perceived at angles midway between the sidelobes — these gaps are termed nulls. However,

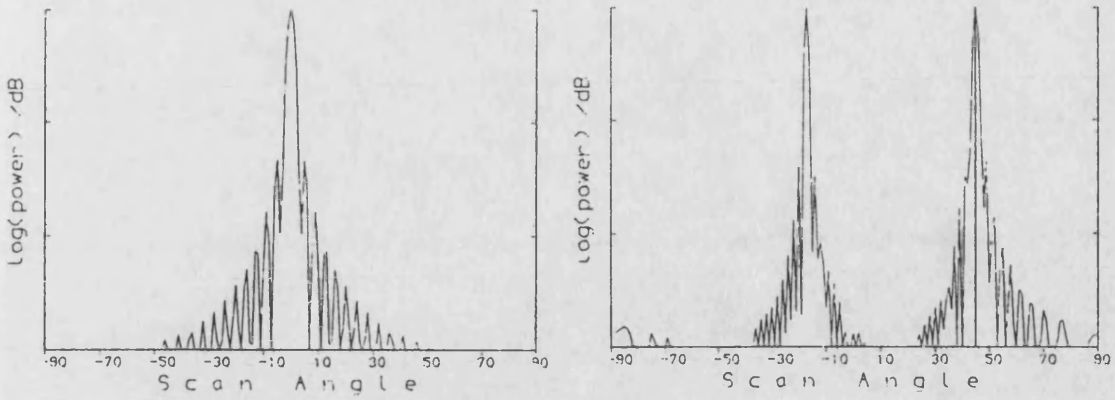

Fig 4.1 : a) Beam pattern for a source at broadside (0^o) with element spacing, $d = \lambda / 2$.
b) Beam pattern for a source at 45^o with element spacing, $d = \lambda$, showing that the true source is indistinguishable from its alias.

note that if the condition $d \leq \lambda/2$ is broken, there may occur other peaks at equal height to the main one satisfying:-

$$\sin\theta = \sin\theta_0 + \beta \frac{\lambda}{d} \qquad \beta = 1, 2, \cdots \qquad [4.4]$$

This is shown in Fig 4.1b, where $d = \lambda$. It is now not possible to distinguish which peak corresponds to the correct bearing. This effect, known as *aliasing* was referred to earlier [chapter 3.3].

4.2 Linearity

Consider the situation where an array is insonified by two sources at angles θ_1, θ_2 respectively. It can be shown that the beam pattern produced by CBF is exactly the sum of the beam patterns due to each source separately [see appendix 3]. This property is known as *linearity* and can be very useful in processing. It follows that the presence of an extra source in a pattern can not drastically alter the pattern due to the other sources, unless the others are at or below the level of the relevant side lobes. It also follows that the ratio of the heights of well separated main lobes will

represent the true ratio of the powers of the relevant sources.

There can be a problem when there is a great disparity in the power output of the 2 (or more) sources. The height of the first side lobe is -13.3dB (relative to the height of the main lobe), which represents only 4% of the power that is attributed to the true direction. However, if a much weaker source is located close to this bearing, its own main lobe may not appear to make a very significant difference to the whole beam pattern, especially when there is some noise present in the system. There are two approaches to dealing with this difficulty — weighting of the signals of the individual elements and post-processing of the image; these are discussed later in this chapter.

4.3 Statistics For Uniform Weighting

As has been shown earlier the beam pattern for the standard delay-sum-and-square technique is given by the discrete equivalent of a sinc^2 function:-

$$P(\theta) = \frac{\sin^2(\frac{1}{2}nkds)}{\sin^2(\frac{1}{2}kds)} \qquad [4.2']$$

where $s = \sin\theta - \sin\theta_0$, and the amplitude, A, set to 1 without loss of generality. The defining equation for this processor may be written as:-

$$V(\theta) = \sum_{i=1}^{n} w_i v_i e^{-jkid\sin\theta} \qquad [4.5]$$

where the weightings, w_i, are all taken to be equal, as the standard technique places equal emphasis on the values from all the sensors. Here, this uniform weighting will be represented by all w_i being unity; other authors prefer the definition $w_i = 1/n$, as this corresponds to unit magnitude for the response in the direction of the source.

Approximating the above expression by the form for a finite continuous receiver, $P(\theta) = \sin^2(\frac{1}{2}nkds) / (\frac{1}{2}nkds)^2$, and denoting the array length, $n\,d$ by D, the statistics given in Table 4.1 may easily be derived.

3-dB half-beamwidth	$4\lambda/9D$
Position of first null	λ/D
Position of first sidelobe peak	$3\lambda/2D$
Height of first sidelobe	-13.3dB
Fall off in sidelobe height	-6dB/octave
Peak sidelobe level	-13.3dB

Table 4.2 — Characterization of beam pattern for uniform weighting.

Many of these figures have great significance when a situation involving two or more sources is being considered. Linearity implies that if multiple sources insonify an array, the resultant beam pattern is the sum of those for the individual sources scaled according to their respective amplitudes. Two sources may only be resolved if their main lobes can be distinguished. For sources of equal amplitude, this corresponds, to a close approximation, to each source lying on the first null of the other or further away. The often quoted Rayleigh criterion for resolution is then λ/D. [The slightly different value for 2-D imaging is referred to later.] Note, all the angular sizes expressed in Table 4.1 are actually in terms of $\sin\theta$ — this simply reduces to changes in θ for a source near broadside; close to endfire the resolution is much poorer.

However, if one of the sources is considerably weaker (e.g. more distant or the stronger is a deliberate interference signal) then it may easily be overlooked even if at a very different bearing to the stronger one. This is where the values for the peak sidelobe level and fall off rate are significant as they indicate how far a weak source has to be from the main one in order that it might be discerned.

4.4 Different Weightings

Changing the relative values of the weights affects the shape of the beam pattern and thus all the characteristics listed in Table 4.1. Many different series of weights have been proposed; the relevant amplitude scalings for some are illustrated in Fig 4.2, along with the effect of each on the beam pattern. The characteristics of a selection of these are compared in Table 4.2 with those for the uniform weighting. The full statistics of considerably more shadings have been detailed by Harris[45].

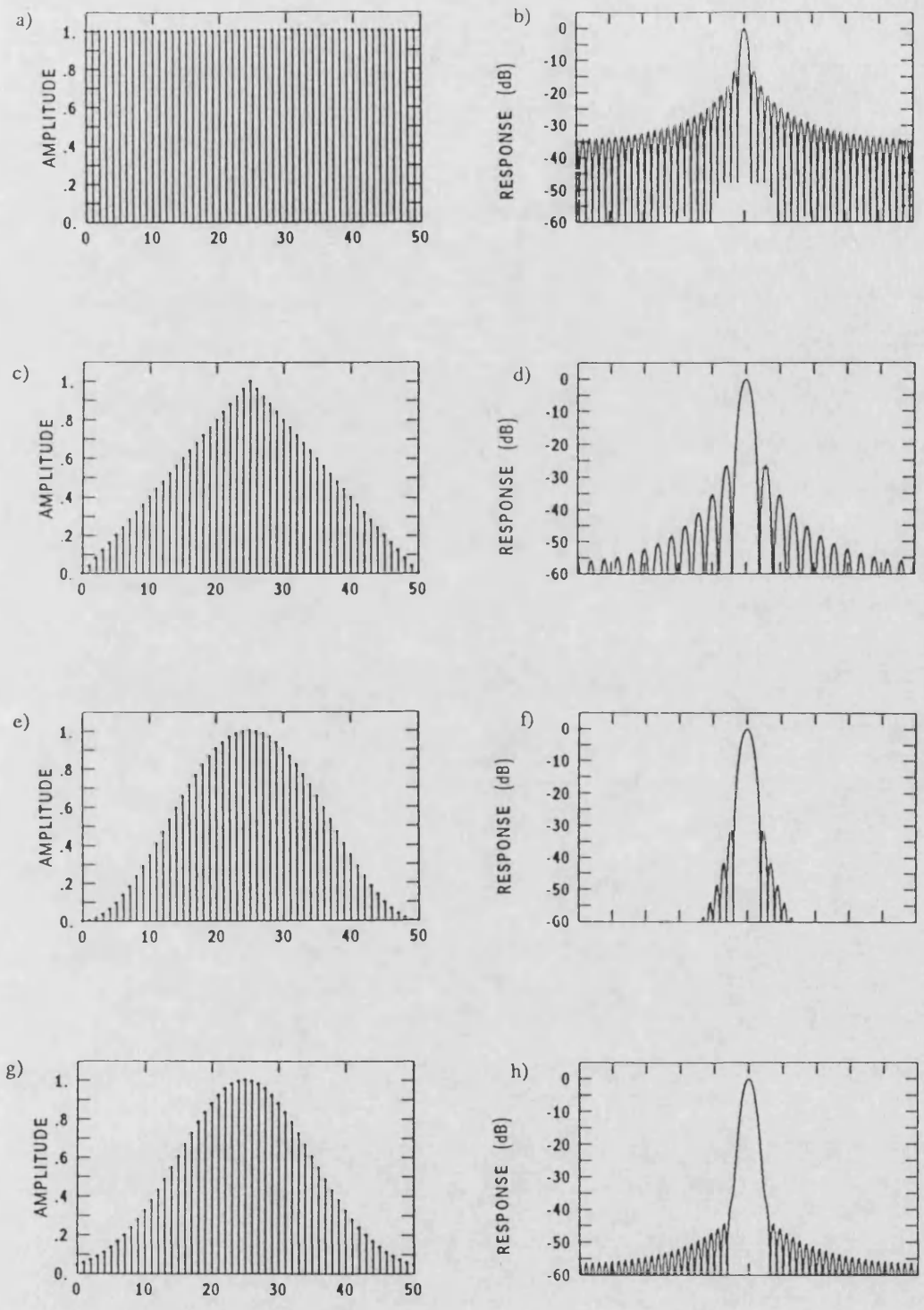

Fig 4.2 : Plots of amplitude scaling for different weighting systems, and the resultant beam patterns.

a), b) Uniform weighting and the image produced by it ; c), d) Bartlett weighting and image ;

e), f) Hann weighting and image ; g), h) Gaussian weighting and image.

[Taken from Marple[67]]

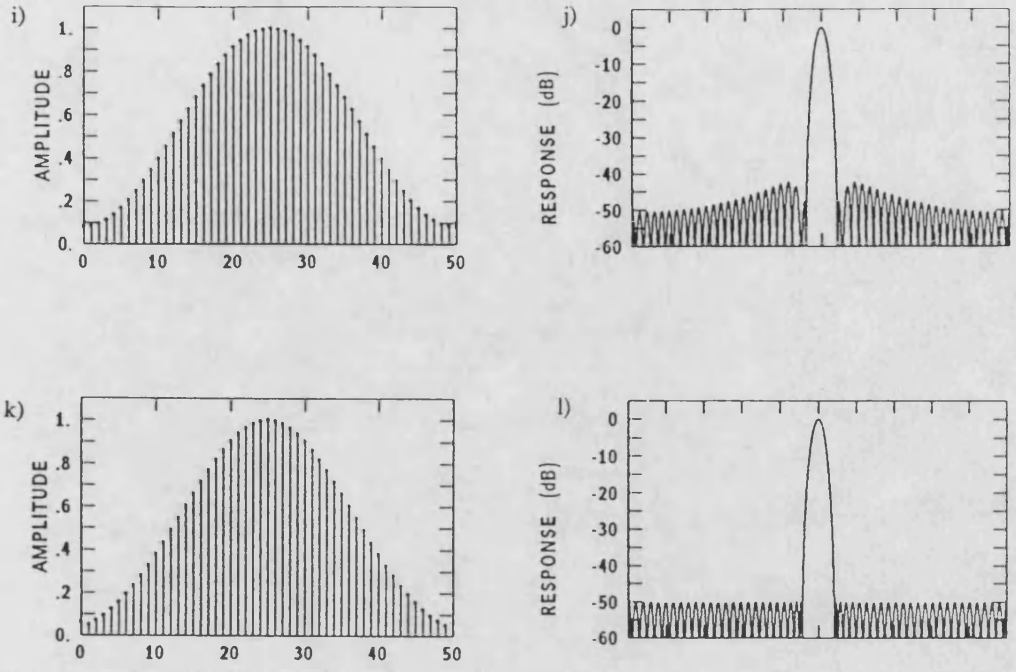

Fig 4.2 (cont.) : Plots of weighting systems and resultant beam patterns.

i), j) Hamming weighting and the image produced by it ; k), l) Dolph-Chebyshev weighting and image.

[Taken from Marple[67]]

For the 2-D situation alluded to earlier, the uniform weighting over a circular aperture may be viewed in one dimension as a weighting of $\sqrt{1-x^2/r^2}$, and thus the different beamwidth observed in this case may be understood. [Actually, a 2-D FFT of the uniform disc generates the first Bessel equation, which has its first null at $1.22\lambda/D$.]

It can be seen that many shadings cause a lower sidelobe level (SLL) than that for uniform weighting, but usually at the expense of increased width of the main lobe. Some of the simplest forms are those of Hann ('Cosine Squared' ; $w_i = {}^1/_2(1+\cos(\pi i/n))$, $i=-n, n$) and Bartlett ('triangular' ; $w_i = |n-i|/n$, $i=-n, n$). The latter may be viewed as a uniform weighting convolved with itself. A further self-convolution yields the Parzen set of weights. There is no single 'best' choice of weights, but rather a different 'optimum' for each specification.

That which produces no sidelobes at all may be thought best in a way, but the binomial weighting which achieves this, also causes a very wide main lobe. Butterworth weighting is one

Type of Window	Height of First Sidelobe	Width at -3dB level (Relative Values)
Uniform	- 13.3 dB	0.89
Bartlett	- 26.5 dB	1.28
Hann	- 31.5 dB	1.44
Gaussian	- 42. dB	1.33
Hamming	- 43. dB	1.30
50dB Dolph-Chebyshev	- 50. dB	1.33

Table 4.1 : Comparison of sidelobe levels and beamwidths for various shadings.

which produces a 'maximally flat' response i.e. it has the maximum number of main peak derivatives equal to zero. 'Dolph-Chebyshev' refers to a series of different shadings. For a chosen peak sidelobe level, a set of weights can be calculated that yield the minimum beamwidth consistent with this restriction. This is achieved by matching the conditions to a Chebyshev polynomial — a method first proposed by Dolph[30,84]. One important characteristic of this choice is that all the sidelobe are at the maximum height i.e. there is no fall off in level for lobes further from the main one. Wang[103] has worked on the implementation of an algorithm that minimizes the power spilt outside a certain desired sector. More recently, techniques have been developed which control the weights adaptively, depending upon the received signal. An example is the Maximum Likelihood Method (MLM) which is discussed in chapter 8.6.

Despite its high sidelobes, uniform weighting is a common choice as 'best'. Of those commonly encountered, it has the narrowest beamwidth [see Table 4.2], and the actual weights are the simplest to implement. Later, in discussions on the effects of element failure and phase and amplitude errors, the statistic $\sum w_i^2/(\sum w_i)^2$ is shown to be important. This is minimized, for a fixed number of elements, when all the w_i are equal.

4.5 Superdirectivity

All of the shadings so far shown have given a positive or zero weighting to each of the elements. Narrower beamwidths than those tabulated previously can be achieved by a method called superdirectivity. In this some of the elements are given negative weighting i.e. their values are subtracted from the total. If this is done then the desired narrow main lobe is achieved, but even larger lobes are present just outside the range of real angles. Although such superdirective arrays can sometimes be of use, they are found to be sensitive to random additive noise, as subtraction of signals from one another reduces the signal power, whereas noise powers always add as they are uncorrelated. Indeed, superdirective arrays will be sensitive to other errors in the system, such as misshapen arrays or imperfect coherence of the signal across the array. Recently Cox, Zeskind & Kooij[27] have proposed that the poor resolution of arrays towards endfire may be overcome to some extent by oversteering (i.e. directing the mainbeam beyond real angles, $|\sin\theta| > 1$, such that that part of the main lobe within real space is narrower). This is only possible if the elements are nearer than half wavelength separation. However, this too must involve some subtraction of signals in the desired look direction, and thus reduce its rejection of noise.

4.6 Post-Processing of CBF Image

If conventional beamforming has been applied to data containing signals from sources of very different amplitude, then it may be difficult to recognise the weaker ones, or else there might be great uncertainty in their bearings. This can be overcome, to some extent, by removing from the formed pattern the beam pattern expected for the strong source alone. The bearing of the strong source is taken to be that of the midpoint of the highest lobe in the pattern, and its amplitude to be the value of that peak or close to it. When this source and all its inherent sidelobes have been taken away, the pattern resulting should be that of the remaining sources. This follows from the principle of linearity [chapter 4.2]. This procedure can then be repeated in an iterative manner until the bearing and strength of all the sources have been determined; that left otherwise unaccounted for is categorised as 'noise'. The following points are of particular interest:-

1) The process as outlined can be applied to any arrangement of hydrophones, not just equi-spaced linear arrays. The only requirement is that the sensor positions are well determined in order that the expected beam pattern for a source on a certain bearing may be calculated accurately.

2) If the array contains n sensors, the maximum number of meaningful sources that can be retrieved is $n-1$. This provides a limit for the iteration.

3) More advanced techniques terminate the search when the resultant beam pattern has no really significant peaks, or else when the highest remaining peak is, say, below 1% of the strength of the primary source.

4) Continued subtraction of powers may lead to negative values for some parts of the pattern; these are without physical meaning, but should be expected due to the presence of additive noise and interference between sources.

5) Although this technique can enable detection of weak sources masked by the sidelobes of a strong one, it will have difficulty resolving two equi-amplitude sources within a beamwidth of one another, as it will err in finding the first bearing estimate.

6) As subtraction of signals is once again involved, estimates can be significantly in error when the signal to noise ratio is low.

Schwarz[91] has created a more advanced version of this algorithm known as CLEAN. This operates on the complex voltage perceived in each direction, rather than the power, thus the available phase information is not ignored. In this case, the pattern removed for each source is that corresponding to $g.V_i$, where V_i is the complex amplitude at the peak, and g is the loop gain. The gain must be within the range $0<g<2$ for convergence of the algorithm. In many cases unity gain is used, but Högbom[51] suggests values between 0.25 and 0.5. The iterative process is then run such that many 'sources' are detected, and then all those within a beamwidth are summed together, and the bearing estimate defined as the weighted mean of all those within that group.

An article by Schwarz[92] indicates that care must be taken in the use of the CLEAN algorithm, although splendid results are shown for some real astronomical data. He warns of its susceptibility to errors in the model.

A further refinement was produced by Hebbert & Barkakati[47]. Their Successive Planewave Removal (SPR) algorithm acts on the observed covariance matrix. With SPR the first source is estimated as previously and removed from the image. However, during the course of the pinpointing of subsequent sources, slight errors in the previous estimates are searched for in terms of second order effects. Thus the estimates of the strongest sources are successively updated to allow for the more minor sidelobes of the weak sources.

4.7 Summary

Conventional Beamforming is a simple process for detecting from which bearings energy is being received. The processor merely adds the voltages with suitable weighting; the beam being made to point in various directions by the use of appropriate delays. The resolution limit for CBF processing is given by λ/D, where λ is the wavelength of interest and D is the length of the array. Sources more closely separated than this can not be resolved by this means. High resolution beamforming methods exist [chapter 8] which can achieve this under certain noise conditions. The other difficulty with CBF processing is the detection of source(s) in the presence of much stronger ones.

The characteristics of the beam pattern may be altered by changing the weights, although a compromise has to be made, as no set will both lower SLL and reduce the width of the mainbeam. In many ways, Dolph-Chebyshev is seen as the ideal compromise. However for the purposes of this project, both additive and multiplicative noise levels are large, so there is no benefit in having the sidelobes for the perfect pattern at -50dB. Uniform weighting will generally be used here, partly for simplicity, but also as it has properties to recommend it. An alternative means of locating the weaker sources is to apply some form of post processing to the image in order to remove the effect of known (i.e. visible) sources.

If the number of sensors is limited, a non-uniform layout of them may be used in order to achieve resolution performance equivalent to that of a much larger array with all its sensor positions filled. The main requirement for a 'sparse array' like that is in radio astronomy, because of the vast cost of each receiver. Bucker[14] shows the implementation of the sparse array processing for an acoustic array. As the number of sensors is less than for a full array, the amount of wiring running inside the tow-cable can be reduced considerably. However, such are not widely used as they do not have the SNR gain of the full array.

5. EFFECT OF CHANNEL FAILURE

The processing discussed above uses the output from all the sensors. If one or more of these sensors should be faulty e.g. due to damaged wiring, the performance of the system will be degraded. Ramsdale & Howerton[82] have shown that if the output of sensor i, with weighting w_i (normalized so that $\sum w_i^2=1$), has been reduced to zero due to a failure in the channel, then:-

i) The whole pattern is scaled down by a factor of $1-w_i^2$

ii) There is an additive noise level across the spectrum of w_i^2

If more than one element has failed the effect is more complicated, the additive effect being modulated by the beam pattern of solely the faulty elements.

Fig 5.1 shows the result of various simulations by Ramsdale & Howerton. They have shown the effect of failure for a 32-element array with Hann weighting [see chapter 4.4]. The lines show the effect for loss of the 2nd, 4th, 8th and 16th elements in turn, and indicate the greater degradation for those elements with the larger weighting.

Below are listed six possible approaches to this effect:-

i) Ignore the problem — i.e. perform beamforming as though all channels performed perfectly, and accept the consequent degradation in performance.

ii) Only use the larger whole part of the array — if faulty element is near middle or there is more than one defective, the number of sensors being used may be reduced considerably. Consequently the resolution is reduced markedly as well as noise rejection capability.

iii) Perform separate processing for the two (or more) complete parts and then treat these sub-arrays as directional receivers for the purpose of further processing of their outputs — this technique may work quite well with the approach proposed by Hinich & Rule[49] for dealing with positional uncertainty [see chapter 10.3]; however its incorporation in the shape determining algorithm used later is more difficult.

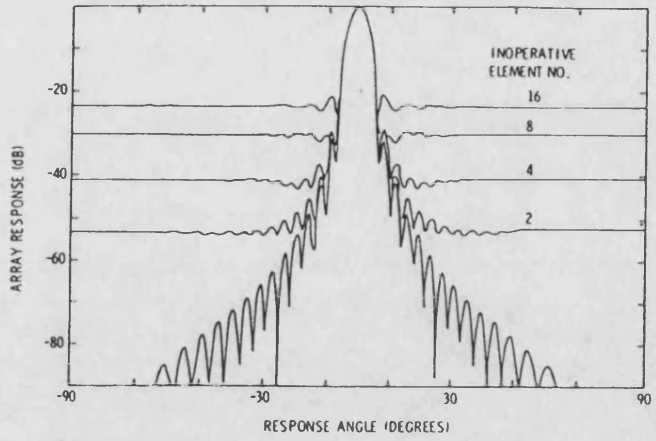

Fig 5.1 : Average beam patterns associated with failure of various elements in a Hann weighted array. [Taken from Ramsdale & Howerton[82].]

iv) Wang[103] has proposed a method for recalculating all the weights used, subject to a criterion of minimizing the power outside a certain angular region. This method requires no assumptions concerning the spacing of the elements.

v) The approach proposed by Bucker[14] for sparse arrays could be applied — i.e. form all the cross-products for certain element separations individually and combine them as needed for the desired element weighting.

vi) Estimate the voltage at the failed sensor by simple linear interpolation between its nearest neighbours — this will increase the effect of the noise from neighbouring elements.

vii) Estimation of voltage using 4 nearest neighbours.

As investigation of this noise effect is not the prime objective of this project, no attempt has been made to discern which of the above is the best approach to this difficulty. Operation i), by default, is thus the one implemented.

6. PROCESSING OF CURVED ARRAY

6.1 Causes of Positional Uncertainty

In all of the forgoing analysis, it has been assumed that the sensors lie equally spaced along a straight line. Whilst this assumption may be correct in many areas in which beamforming of arrays is performed, such is usually not the case when the elements are in a long flexible line towed through water. There are two main causes for this non-linearity of the array:-

i) Changes in direction of the towing vessel.

ii) Cross-currents in the ocean.

There are various reasons why a ship deploying an array has to veer from a straight course:-

a) To avoid ships or coast that lie ahead.

b) In order to return to the section of the coast that it has been patrolling.

c) In order to be able to investigate better those sectors that had been endfire to the array — areas in which array performance is poor.

If a ship towing a long array attempts a sharp turn, the tension along the array will be significantly reduced, causing the array to sink to a lower depth. Whilst such is going on, the array would not be useful for detection. Thus, although this work and others referenced may contain examples of arrays contorted into a semi-circular curve, such a condition is unlikely to be encountered in practice.

Some information concerning the present shape of the array can be inferred from a knowledge of the route followed by the ship. It can be assumed that the array follows itself to some extent, as the tension moving it will be approximately parallel to its axis. However, the second cause (ocean currents) prevents much useful information being derived from the ship's route.

However, once the array shape has been correctly determined for a certain instant, it will be valid for some time afterwards to assume that the array is following itself i.e. all sensors trace out roughly the same route in space as the ones immediately preceding it, but with an appropriate time delay. Although such is not exactly true, it can be used to produce a first estimate of the new array shape.

This project investigates processing problems when the array shape is unknown. The remainder of this chapter details beamforming using the correct array shape; processing with slightly erroneous shape estimates is covered in chapter 15.

6.2 Processing Using the True Array Shape

Beamforming relies upon the estimates of the sensor positions being sufficiently accurate that the compensating phase shift used is close to the correct one. If the component of the location error of a sensor is of the order of half a wavelength in the direction of the source, then the error in phase shift will cause the part of the signal due to the source to be subtracted from the sum, rather than added. Thus, if the position errors of several sensors are of the order of a quarter wavelength, then the beam pattern will be badly degraded.

However, if all the sensor positions are well determined, the beamforming exercise will usually produce a pattern akin to that for a straight array. Figs 6.1a,b,c show an array of 24 elements at $\lambda/2$ separation with the true positions being used in the beamforming. In Fig 6.1a, the sensors lie along a straight line, in Fig 6.1b, they lie along a shallow arc of radius 30λ (array length = $11^1/_2\lambda$); and in Fig 6.1c they lie along a semi-circle (radius = 3.7λ).

All the patterns have roughly the same form, but in the third case, the separation between the end sensors is significantly less than when the array is straight, and consequently the beamwidth of the mainlobe is increased. Also as the sensors appear concentrated towards the ends, the first sidelobes are not reduced as much as for a straight array; the effect is similar to an equi-spaced straight array, with greater sensor weighting towards the ends of the array.

The effect for a source near endfire is rather different as Figs 6.2a-c show. Again, when the array is only slightly curved, correct compensation yields a beam pattern close to that for the straight array. The semi-circular array, however, has an apparent width greater than for the straight array; its projection perpendicular to direction of source has an asymmetric distribution of sensors which cause the asymmetry of the resultant beam pattern.

To summarise, for array shapes close to a straight line, correct compensation will yield a beam pattern almost identical to that for a straight array. For more significantly curved arrays, the pattern is similar but with raised sidelobes. These can be reduced by use of elemental weighting to

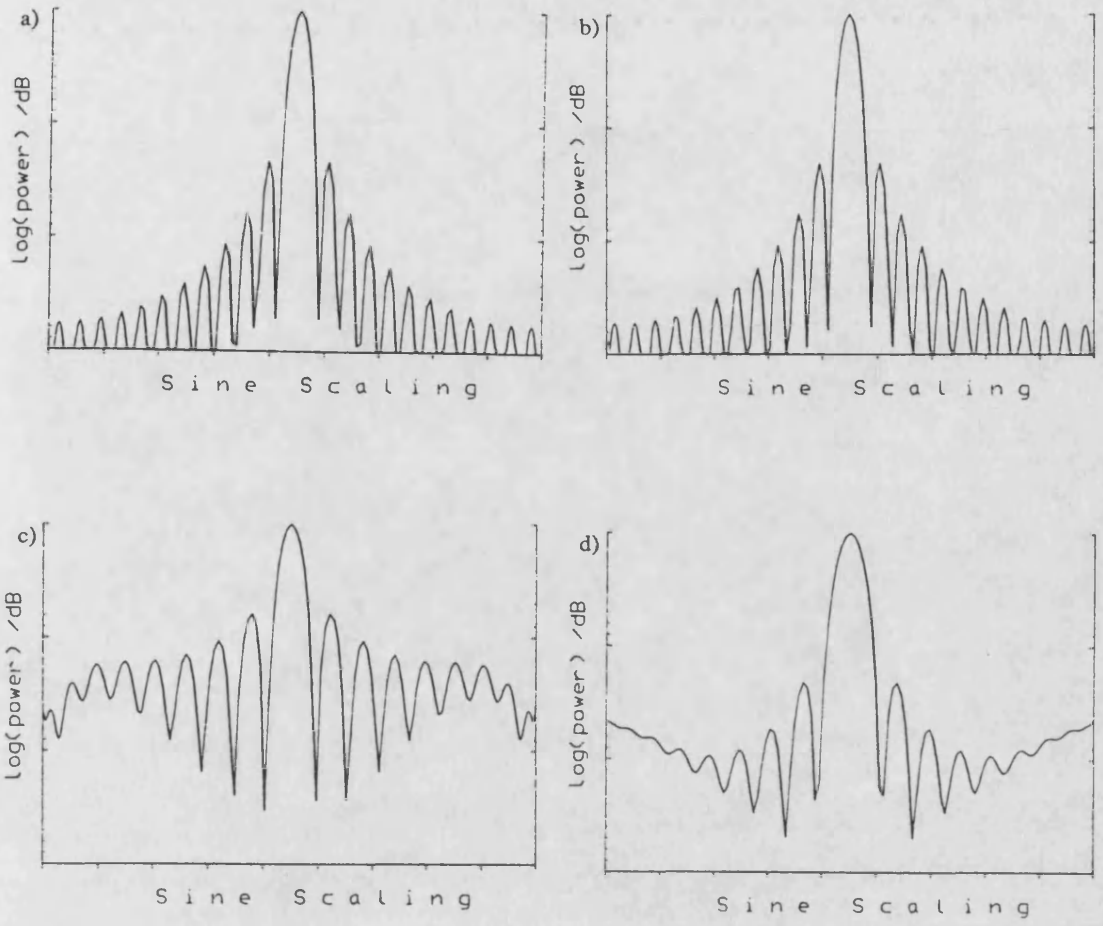

Fig 6.1 : Beam patterns as a function of curvature and weighting.

a), b), c) are for uniform weighting of elements on a straight line, shallow curve and semi-circle respectively. d) is for semi-circle, but with compensatory weighting.

compensate for the density tapering, i.e. the non-uniformity of elemental separation along the equivalent straight array. Fig 6.1d displays the result of processing the same data as for Fig 6.1c, except that now a weighting function $\cos(\pi m/n)$ is used, where $m = {}^1/_2 n - i$ corresponds to numbering the sensors from the centre of the array. This was adopted because the element density along the equivalent straight array is as $1/\cos(\pi x/L)$. The beam pattern in Fig 6.1d is not the same as for the original straight array [Fig 6.1a], as the latter has a larger effective length, and consequently a narrower mainlobe. Fig 6.1d most closely resembles the pattern for a 24 element straight array with only 2.375m separation of the sensors (i.e. $d = \lambda/\pi$), and hence of the same effective length [see Fig 6.2d].

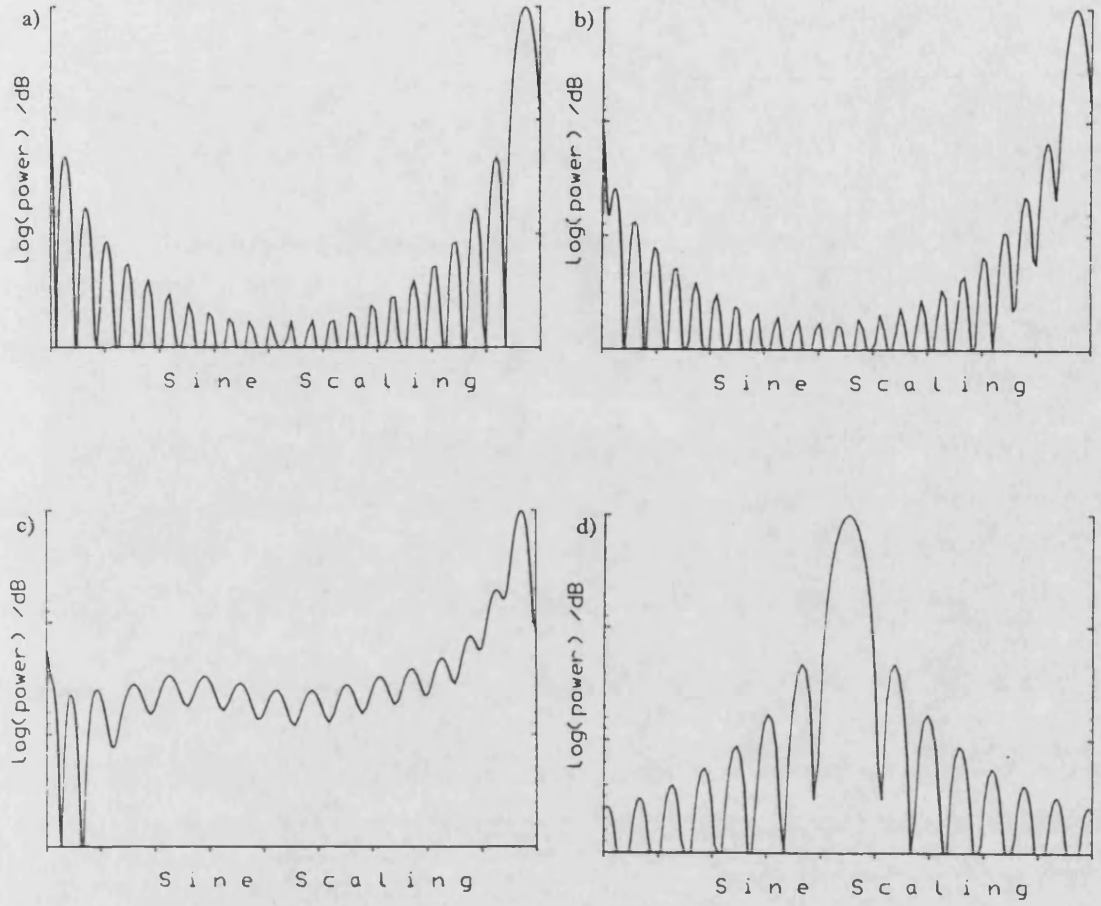

Fig 6.2 : Beam patterns as a function of curvature and weighting.

a), b), c) are for uniform weighting and a source at 70^o, with the array lying along a straight line, a shallow curve and a semi-circle respectively ; d) represents the beam pattern for a more closely spaced array, with uniform weighting and a source at 0^o.

7. MANY FIELDS OF PHYSICS

7.1 Analysing Wave Phenomena

The estimation of the parameters of a simple signal contaminated with noise occurs in many branches of physics.

A common example of such is frequency estimation from a sampled time record at a sensor. If a single known frequency is of interest (i.e. only its phase and amplitude is to be determined), this may be achieved by the use of a very narrow band-pass (notch) filter — in this work, the data supplied are the complex amplitudes produced by such filters on each of the elements. However, it is often necessary to sample the time record at a detector, and apply digital processing techniques to estimate the coefficients at previously undetermined frequencies. In this case, one may be looking for several sinusoids in a noisy data record.

A similar situation exists in the spatial processing of the complex amplitudes at a finite number of receivers in order to gain information concerning the angular distribution of the sources. This occurs not only in underwater acoustics, but also in radio astronomy, optical astronomy and other imaging systems with visible light, formation of microwave images and seismology: indeed, such processing is applicable in most situations involving multiple detection and comparison of wave functions.

Indeed, if the given data contained a single sinusoid and no noise whatsoever, the task of fixing the signal values could be performed accurately by many methods (with impunity). However, in all cases (apart from purely mathematical ones) there is some degree of noise present, whether it be due to lack of constancy in the emitted signal, fluctuations in the medium used for propagation, extraneous noise in the detectors or a combination of all three. It is also possible that one is not concerned with a single sinusoidal variation — there may be multiple emitters or a single one of finite (as opposed to infinitessimal) width.

These many areas of physics are listed to explain why some items of the literature survey are taken from works not associated with underwater sound transmission. However, it is also useful to compare and contrast the different areas to understand why articles covering one are not

necessarily of great use in another.

7.2 Active / Passive

First of all it must be emphasised that the present project is specifically concerned with passive sonar i.e. purely listening for signals emitted from the source(s), as opposed to active sonar, where a signal (a 'ping') is sent out, and its echo reflected from the target that is to be detected. Active sonar is not used for this particular case, as it alerts submersibles to the fact that they are being sounded, and also the energy of such a reflected signal falls as one over the fourth power of range, and is thus unsuitable for the very distant sources, which the array in question might be expected to detect. There are several important aspects of the processing of active arrays which need to be reconsidered for the passive case.

a) The 'ping' is close to an impulse, and as such will contain a wide variety of frequencies, whereas passive processing may be (although not necessarily) performed on the assumption of a CW signal. [Note, it is not possible for the emitted sound to be a CW, because of difficulty in achieving a high enough power level, and more importantly that such would provide a very large 'interference' signal effectively obliterating any of the desired echoes.]

b) Multipath phenomena may often be readily distinguishable, because of sufficient difference in transit times. With the CW signals of the passive case, additive interference is inevitable if more than one strong ray path exists.

c) Range may be estimated from delay times for echoes; whereas wavefront curvature must be used in the passive case. Also radial velocity can be deduced from the Doppler shift on reflected signals; such analysis is not possible for passive sonar, unless the true emitting frequency is known beforehand from previous observation of the same or identical objects.

It should be noted that most of the papers on microwave analysis are for a reflected signal, i.e. akin to an active array, whereas none of those dealing with astronomy are.

7.3 Sensor Layout

Another major difference between the above topics is the layout of the sensors. This is principally a question of 1-D or 2-D. The particular array of interest is a nominally straight one, consisting of a finite number of evenly spaced elements. Two and three dimensional arrays do occur in sonar use, but here we are confined to the 1-D case. A similar variety is encountered in astronomy — the 5km track at Cambridge is an example of a linear one, the VLA in New Mexico is a large regular 2-D array, and Merlin in the UK is an irregular, though well measured 2-D array. All the optical work is principally concerned with a regular 2-D matrix of receptors, although some works consider the image as a set of lines and apply 1-D strip-line processing to each direction in turn. In seismology, a complex 2-D structure may be employed, such as that of LASA in Montana, which is intended to detect and pinpoint seismic waves with a wide range of frequencies, arrival directions and even velocities (the various compressional and shear waves travel at different speeds).

Cost and ease of manufacture are also important factors in the layout of elements in the various cases. Production of hydrophone elements is fairly cheap — the number of receivers in a sonar array is limited rather by the time required for processing (proportional to number of elements to the second or third power), the number of wires to run along the array to retrieve the data, and the increase in hydrodynamical drag with the length of the array. In radio astronomy, the cost of a single large dish receiver is tremendous, thus the number of sensors is seriously constrained. Hence the great need in this field for 'sparse' arrays, which are ones which mimic well the performance of much larger 'filled' arrays of equally spaced detectors. Optical telescopes may also be thought of as consisting of many contiguous mini reflectors in a circular geometry; the advent of the Multiple Mirror Telescope should not change much the nature of such comments, so long as the mirrors are all correctly aligned.

7.4 Multipath

Multipath is the term used to describe the existence of more than one ray-path from source to receiver(s). In many situations one path may be dominant, but the contribution of others may increase considerably due to a change in the positions of the sources, or simply as a matter of conditions varying with time. In underwater sonar, extra paths may exist due to a varying sound speed with depth, or else reflection from sea bottom or surface. A similar situation is found for

'horizontal' radio paths — different ray paths being separated by the order of 0.2^{o}, and reflections occurring from the sea or land surface below the path or from various mounds. Interpretation of seismological records is highly concerned with different routes from source to array, but as the signal is usually a very short impulse (e.g. a detonation or a 'boomer'), the reflections from various interfaces can be resolved due to their different time lags.

7.5 Inhomogeneities

The medium between source and receiver cannot, however, be simply characterized by a slowly varying spatial function. There are also fluctuations in the refractive index (i.e. speed at certain instant in time and space, normalized with respect to the mean value) over all length and time scales. Variations in the sea can occur with a period of a day, due to heating by the sun, and tides induced by the moon, and also with a period of a year due to annual climatic changes. However, that of interest here is that which changes over the order of seconds or minutes, and often with a short correlation length. This can be due to temperature inhomogeneities, presence of biomass or advecting of water masses. Investigation has shown many of the spatial distributions of these variations to be lenticular in shape rather than spherical.

Microwave channels in the ionosphere suffer a similar problem, caused by variations in the electron density. These are found to be elongated along the direction of the Earth's magnetic field. Optical astronomy is limited by 'seeing', the term given to fluctuations in image (e.g. twinkling of stars) due to the refractive properties of the atmosphere changing with a correlation time of the order of 1/100 sec. The resolution capability of a telescope is limited by the transverse correlation of such fluctuations. The world's largest telescopes at present (such as the Hale telescope on Mt Palomar with a mirror 5m in diameter) are much wider than the typical correlation width. Thus resolution cannot be improved by making larger instruments, although such might be constructed for their increased light gathering power. In order to enable such massive 'scopes to function at their diffraction limited resolution, it is necessary to place them beyond the atmosphere (e.g. the proposed Hubble Space Telescope) or else apply some form of adaptive processing to correct for the fluctuations. Similarly, radio signals reaching the Earth after having passed close to the Sun deteriorate due to inhomogeneities propagating out in the solar wind.

7.6 Positional Errors

Clearly there will be uncertainties in the hydrophone locations if they lie along a flexible cable towed behind a ship. Such errors will be due to manoeuvres of the ship, cross-currents in the ocean and disturbances propagating along the array in the way that a flag flaps in a strong wind. Such problems would be considerably reduced by attaching the hydrophones to a rigid platform such as the hull of a ship. That is not possible in this case for several reasons:-

a) Arrays are often required to be longer than the ship.

b) It is commonly required to have the receivers at a depth of several hundred metres or more.

c) Most importantly, it is necessary that there are no sources very close to the array, such as the vessel itself, in order that distant faint signals will not be swamped by a strong nearby source.

The companion fields in which signal processing has been referred to, tend not to have such a flexible layout to their receivers; however, they can still have problems of positional uncertainty.

Sometimes, it is just a case of an unknown constant layout of receivers (such as random locations of microwave antennae on a hill slope), there being difficulty in directly measuring such a 3-D arrangement to the necessary precision. For a single rigid platform, or large receiver dish, there can be errors associated with their manufacture; and for space-borne antennae, varied thermal heating by the sun may cause some degree of warping. [Note the degree of accuracy required in these various fields may differ — in the underwater scenario, a rms error of 0.1λ may be tolerable, as it would generally still allow sources to be detected, whereas in other fields an error of 0.1λ would be unacceptable as it could cause significant degradation to a complicated image.]

7.7 Field of View

The intended function of these various detectors varies much. In the sonar case, a watch is being maintained over all angles of interest, typically either one side of the array (180^o sweep) or both sides (360^o). The aim is to detect a source in any direction and be able to fix its bearing. With a seismological array, interest is definitely only in the region below the array, and usually in angles fairly close to the array normal. Of necessity, the sonar receivers are omni-directional, in order that such a large sector may be surveyed. The opposite is the case in astronomy and radio-astronomy,

where the receiver itself has high directional properties, as interest at any one time is only in a very small sector of the sky. Here the aim is not merely detection, but observing details, for which algorithms that give a good resolution without bias are required.

7.8 Others

All the processing concerned with imaging of electromagnetic waves can also use any information available in the polarization of the signals; such is not possible for sonar, as the water waves are longitudinal only.

8. HIGH RESOLUTION METHODS

8.1 Introduction

Conventional Beamforming (CBF) provides a good general estimator of periodicity within signals, but there are methods which have been developed recently that achieve a much greater resolution with less overspill into directions with no source. These high resolution methods are particularly useful when the available data sequence is short and the SNR high.

The CBF method makes no assumption about autocorrelation lags outside those obtainable from the data, whereas some of the following methods implicitly select certain continuations using *a priori* knowledge of the expected form of the data sequence. Each of these methods, thus has a specific underlying model associated with it — first the correct model should be selected and then the necessary parameters are calculated from the available data using various estimators. It is to be observed that several methods are very efficient and precise when the true autocorrelation lags are used, but are significantly poorer in real implementation as only the estimates of the lags are available. These algorithms are often referred to as **Non-Linear Methods (NLM)** as the spectral estimates that each generates for a multi-source environment is not simply the same as the sum of the estimates for the individual sources.

Some of the more common high resolution methods are discussed below. More detailed explanations have been produced by Marple[67] and Kay & Marple[53]. Introductory papers to several of the methods have been written by Burg[18] (Maximum Entropy), Capon[22] (Maximum Likelihood), Pisarenko[79] (PHD) and Schmidt[88] (MUSIC).

8.2 Autoregressive Modelling

8.2.1 Introduction to AR Processes

An autoregressive (AR) model is one in which each value of a sequence can be expressed in terms of those preceding it, along with an error term i.e.

$$x_n = -\sum_{i=1}^{p} a_i x_{n-i} + n_n \qquad [8.1]$$

where p is the order of the filter, a_i are a series of fixed coefficients (to be determined) and n_n is the nth number of a sequence of uncorrelated random numbers. [Note, the minus sign has no specific meaning — it is merely an artefact of the re-arrangement of an earlier formulation.] When written as above, it can be seen that this is also the equation of a forward linear prediction (LP) filter, and in some literature it is referred to under that name.

Autocorrelation lags, expressing the observed relationship between successive items of data, may be calculated from the observed sequence by:-

$$c_k = \frac{1}{N-k} \sum_{i=1}^{N-k} x_i x_{i+k} \qquad [8.2]$$

The AR coefficients are related to the autocorrelation lags by the Yule-Walker equations. These produce a set of $p+1$ linear equations, often expressed in matrix form. Straight forward Gaussian elimination requires of the order of p^3 operations, however, an efficient method known as the Levinson-Durbin algorithm exists that only needs of the order of p^2 operations. Another particular advantage of this algorithm is that it successively calculates the coefficients of all the AR filters up to order p. This is particularly useful as the true order is often not known beforehand, so the order which best fits the data can be selected afterwards.

As the model order is increased, successive estimates of the variance, σ^2, of the random noise will be monotonically decreasing. If the generating model is actually an AR(p) process (i.e. of order p), then the variance estimate will remain constant for attempted orders greater than or equal to p, thus giving a clear indication of the true order. If the actual generating process was not a pure AR(p) one, then the estimates of σ^2 will always be decreasing, even though the higher orders may not be giving any extra information.

If the order selected is too low, the spectrum appears smoothed, lacking the sharp responses that pinpoint source completely; if the order is too high, spurious peaks are introduced.

8.2.2 Maximum Entropy Method

It is possible to propose a series of lags outside the observed range — this will create a larger data window and hence narrower resolution. There are an infinite number of possible continuations consistent with the given lags; Burg[18] proposed the selection of the one which corresponds to the time series with the maximum entropy, thus applying the fewest constraints on the unknown data. This corresponds to the Power Spectral Density (PSD) with the flattest (whitest) spectrum. This processing of AR data is called Maximum Entropy (ME) processing, but is also often known as the **Burg Algorithm** in his honour.

The Maximum Entropy spectral estimate is given by:-

$$P(\theta) = \frac{\sigma^2}{\left[1 + \sum_{i=1}^{p} a_i e_i(\theta)\right]^2} \qquad [8.3]$$

where a_i are the autoregression coefficients and $\{e_i(\theta)\}$ are the components of the steering vector i.e. the required phase delays for each element.

The actual power in a direction is proportional to the area under the peak rather than the peak height itself. ME is equivalent to AR PSD for Gaussian random processes, when the true autocorrelation lags are known for uniformly spaced samples. ME can be performed for unequally spaced autocorrelation lags. If this is the case, or if the lags are estimates then the ME and AR PSDs will differ.

When additive noise is present, the filter function is not now an AR process, but an ARMA one (see later). If the data is interpreted via an AR model, this may give rise to a double peak i.e. the PSD showing two nearby sharp peaks for just one source. This effect, usually referred to as spectral line splitting (SLS) from its occurrence in problems of frequency estimation, is particularly prevalent at high SNR, and can be shown to be dependent upon the initial phase of the signal. This is true for both real and complex data sets. Kesler, Boodaghians & Kesler[55] refer to the problems associated with the Burg Algorithm when the sources are correlated e.g. due to multipath. Their Generalized Burg Algorithm has less resolution than the original but shows less bias on those it can resolve. Further discussion of the effects of coherence can be found in a paper by Luthra & Steinberg[66].

Meredith & Ramsdale[70] have compared the performance of MEM and WBB (Wagstaff-Berrou Broadband — a variant of MEM) to CBF processing using real acoustic data. For a single high SNR source, the bearing estimation of all three were identical. MEM and WBB proved better at resolving two sources using only a few data samples; however, these methods produced greater variance in estimates of the power ratio than CBF did.

8.2.3 Covariance and Modified Covariance Methods

The Burg Algorithm corresponds to least mean squares (lms) minimization with respect to a single parameter (the reflection coefficient) whilst satisfying the Levinson recursive relationship; alternatively, lms minimization can be performed with respect to all linear prediction coefficients, removing the Levinson recursion constraint. This generates a version of the AR spectral estimator known as the covariance method. Rewriting the problem in terms of forward and backward linear predictors and minimizing the coefficients associated with both leads to the formulation of the modified covariance method. Although based on the AR model, this does not exhibit the spectral line splitting that can occur with the Burg Algorithm.

8.2.4 Selecting Model Order

All the AR methods require specification of the order of the process, p. In some cases the appropriate value may be known beforehand; in others, this value has to be selected, either by the operator judging the visual impact of the image, or by minimization of some measure. As mentioned earlier, the error variance associated with successive model orders will be monotonically decreasing (unless the process is a true AR one). Too high an order will lead to better fits to the noise corrupted data, adding false peaks. To overcome this many people have developed criteria that are intended to enable order selection. Many work well on data simulations of an AR process plus noise, but generally underestimate the necessary order for real data, where the model is not so close. It has been experimentally observed that choosing the order to be about a third of the number of lags available will generally produce the best results.

8.3 Moving Average (MA) and ARMA Models

A Moving Average (MA) model for the data assumes that the given series can be written as a scaled sum of a set of random numbers i.e.

$$x_n = \sum_{i=0}^{p} b_i n_{n-i} \qquad [8.4]$$

where p is the order of the filter and $\{n_i\}$ is a series of independent random numbers. Spectra associated with this model have broad smooth topped lobes and sharp nulls, as opposed to the sharp peaks and broad nulls of AR modelling, and hence are of little use in this context.

An ARMA model is a combination of the AR and MA models. The underlying model for an ARMA(p,q) process is given by:-

$$x_n = \sum_{j=0}^{q} b_j n_{n-j} - \sum_{i=1}^{p} a_i x_{n-i} \qquad [8.5]$$

[Alternatively, if expressed as a filter function in z-transform notation, it is given by $H(z)=B(z)/A(z)$, where $B(z), A(z)$ are the transfer functions of the MA and AR portions respectively.] The spectra produced by such a process have some of the attributes of both parents' spectra, being able to represent both sharp peaks and sharp nulls. However, estimating the various coefficients is difficult, as the equations relating them to the autocorrelation lags are non-linear. Sub-optimum methods exist which independently estimate the MA and AR parameters.

8.4 Pisarenko Harmonic Decomposition

Pisarenko[79] produced a model for analysing geophysical data which assumed that the signal was due to perfect sinusoids plus additive uncorrelated noise. To match a data set to the model requires the estimation of both frequency and amplitude for each spectral component, as opposed to the FFT formulation of CBF which simply estimates the power for certain pre-selected frequency intervals.

This method, known as Pisarenko Harmonic Decomposition (PHD), produces a line spectrum rather than a continuous one, and is thus poor at representing broad sources or dealing with

coloured noise. This is not surprising as the model assumes perfect sinusoid signals, and the decomposition relies heavily on this. The standard Toeplitz form generates biased estimates even when there is no noise. Barrett & McMahon[7] refer to a non-Toeplitz variant with similar structure to the Prony method (see below), and which produces similar results.

8.5 Prony Model

In 1795, Baron de Prony produced an algorithm for exactly fitting p exponentials to $2p$ data points, as he was interested in such a model for interpolation purposes. More recently, this was *extended* to use more than $2p$ items of data, and achieve a least-mean-square fit. Performing such requires solution of a difficult non-linear problem, which is usually achieved by an iterative technique. This can be re-formulated in ARMA form similar to PHD, only here the poles (representing frequencies) are not constrained to have unit modulus, and thus may be damped, broadening the peak. This model then has the ability to match sharp spectral lines and also broad sources.

A spectral line estimator has also been introduced based on Prony's model. This has several advantages over PHD — autocorrelation are lags not required, it is easier to determine model order, frequency and power estimates are less biased and it is computationally simpler.

Gitel'son, Glebova & Kuznetsov[41] have simulated the performance of the Prony algorithm with three correlated equi-strength sources. For various correlations from none to fully correlated, the algorithm managed to determine source directions accurately and the phase locks between them. However, the additive noise level used was 20dB below that of the signals. Bucker[15] has tested the Prony algorithm more thoroughly. He found that for reasonable SNR, it was better than CBF for sources towards endfire, but CBF (in its FFT implementation) was better when noise levels were high.

8.6 Maximum Likelihood Method

A Maximum Likelihood (ML) processor can be viewed as similar to CBF for the output can be expressed as the sum of phased records with appropriate weighting. However, here the weights are not constant, but dependent upon the received signal record. The ML method is defined such that the power in all directions other than that desired is minimized subject to the constraint of unity gain in the 'look' direction. Because of its defining conditions, this algorithm is often also called the **Minimum Variance (MV)** one. The weighting vector fulfilling this condition will vary with angle, and the power perceived from those various directions. It can be shown that the set of weights is given by:-

$$w_{ML} = \frac{R_{xx}^{-1}\, e(\theta)}{e^{H}(\theta)\, R_{xx}^{-1}\, e(\theta)} \qquad [8.6]$$

where R_{xx} is the autocorrelation matrix of the signals, $e(\theta)$ is the steering vector and $e^{H}(\theta)$ is its Hermitian counterpart (complex conjugate transpose). [Note, in practice the true autocorrelation matrix is not used, rather only an estimate of it.]

The PSD estimate of the ML processor can be expressed in terms of all the AR PSD estimates from order one to the order of the autocorrelation matrix. Thus, it is not surprising that the resolution of MLM is inferior to that of an AR method of the same order, although it is far superior to the simple CBF approach. However, ML estimates exhibit much less variance than those from AR methods.

Care must be taken in interpreting ML spectral plots — peak height does not indicate power, rather area under the peak is proportional to the square root of the power. [For AR PSD, area is proportional to power.]

Porter, Dicus & Fizell[80] have compared the performance of CBF and ML using simulations with a complicated sound speed profile. ML appeared to perform better, in that its sidelobes were lower; however, its localization of a source was no more accurate, and it could produce sharp false peaks in the display. Kirlin & Dewey[57] have calculated the Cramer-Rao Lower Bound (CRLB) (to which the ML estimator often approximates) for the problem of correlated noise. However, they principally detail the pointing accuracy for a single source case, without examining the possibility of secondary or false sources.

8.7 Eigenanalysis Methods including MUSIC

Another family of algorithms is based on examination of the structure of the autocorrelation matrix associated with the data. A NxN matrix will have N eigenvalues associated with it (not necessarily all distinct), and an eigenvector for each of these, thus spanning the whole space. In this case, all the eigenvalues will be real and positive, as they can be shown to represent power in the direction of the orthogonal bases of the matrix.

The p highest eigenvalues each correspond to the power of a signal plus a constant additive noise term; the remaining $N-p$ values correspond to noise alone, and will thus be expected to be equal. A biased autocorrelation estimate must be made to ensure that the matrix is positive definite. Determining the order, p, should be simply a matter of noting the number of distinct eigenvalues; however, with real data, all the noise-only eigenvalues will differ slightly, thus care is required in order estimation.

One of the first estimators to be based on this approach was PHD described earlier. Two other common PSD estimators based on the above eigenanalysis are the MUSIC (MUltiple Source Identification and Classification) and EV (Eigenvector) algorithms. These utilize the near orthogonality of signal subspace vectors to the estimated noise-only ones. MUSIC is the more widely used one, although it produces more spurious peaks than EV. The form for MUSIC is:-

$$P_{MUSIC}(\theta) = \frac{1}{e^H(\theta)\left(\sum_{i=p+1}^{N} v_i v_i^H\right)e(\theta)} \qquad [8.7]$$

where v_i is the eigenvector corresponding to the ith eigenvalue. Note, this does not generate a true *power* estimate.

The above methods achieve better performance at low SNR than Prony and AR-based processes. In his explanation of MUSIC, Schmidt[88] shows how it outperforms ML, ME and CBF in resolving two sources insonifying a 3-element array. However, it is to be noted that the present problem involves considerably more elements and much higher noise levels, so that the applicability of MUSIC in this project does not necessarily follow. Indeed, Schmidt showed how sensitive it could be to the slightest truncation of the data.

Farrier & Jeffries[34] state that eigenvector methods are very sensitive to phase and amplitude errors, and propose another algorithm based only on the signal subspace vectors. Paulraj & Kailath[77] refer to bias and resolution problems that occur when the sensor noise is coloured. Their

solution involves subtraction of successive estimates of the autocorrelation matrix, under the assumption that the statistical properties of the noise will not have changed. Such an approach is suspect with rather high noise levels. A later proposal by Paulraj & Kailath[78] involves rescaling of the autocorrelation matrix to allow for the known (i.e. expected) decorrelation. This enables criteria for order estimation to perform better. However, the rescaled matrix does not enhance source determination unless the SNR is very high. If the coherence function is unknown, it must be parametrized and a multi-dimensional search performed. Roy, Paulraj & Kailath[87] have created a further eigenvector based algorithm, ESPRIT. Like MUSIC, this is based on PHD, but able to use all the autocorrelation lags available. Its proponents claim that it has certain advantages over MUSIC.

8.8 Summary

As can be seen there are a multitude of methods, all providing better resolution than the conventional beamforming method. However, selection of a method is not merely a matter of picking that which claims the finest resolution. Many other factors need to be taken into consideration, such as behaviour in the presence of additive noise (possibly coloured). Also, in many cases a perfect plane wave source cannot be assumed — Paulraj & Kailath[78] state that a slight decorrelation across the array may give the effect of rays converging from a broad source. Alternatively, there may be correlation between two or more sources, possibly due to multipath. Byrne & Steele[21] have indicated that many NLMs are unstable when either multipath or correlated noise is present. Other factors to be taken into consideration are the computational complexity (and hence run-time of each) and as to whether they can be successfully applied to sensors that are not equally spaced on a straight line.

Each of the above algorithms may see use in the field of signal processing, as each in turn has a niche in which it is particularly applicable, often having been designed with that specific function in mind. The applicability generally depends upon the appropriateness of the underlying model and the assumptions that go with it.

Many papers have been written upon the deleterious effects of certain conditions upon specific algorithms, and often introduce variants that cope with the problem in question. Thus the number of different signal processing algorithms is large, but with mainly only those detailed above having been fully investigated. A more detailed description of their derivation and implementation

may be found in works by Kay & Marple[53] and Marple[67]. Both compare the performance of all the algorithms on specific data sets. Further comparisons, using either simulated or real acoustic data have been performed by Barrett & McMahon[7], Scholz & Kroll[89], Bucker[15], Porter, Dicus & Fizell[80], Fizell[37] and Meredith and Ramsdale[70]. The relative performance of various Time Delay Estimators (TDEs) is detailed by Fertner & Sjölund[36] and Nikias & Pan[74].

For the particular case of this project, where noise levels may be high, the signal partially decorrelated across the array and great uncertainty exists in the location of the sensors, then the CBF approach is the one selected. This is because the other algorithms tend to perform poorly when the true situation is far from that which the model assumes, whereas CBF is fairly robust. Given reasonable length arrays, and the narrowness of the frequency band being processed, it is unlikely that there will be two closely spaced sources, so the shortcomings of CBF in this respect may be overlooked. Also, note that CBF is computationally simpler than most of the high resolution methods, even though the FFT implementation will not be able to be invoked when the array is contorted.

9. PHASE FLUCTUATIONS ALONG THE TRANSMISSION PATH

9.1 Various Causes of Phase Error

In the ideal case, it would be expected that for a linear array insonified by a source oblique to it, the phase of the received signal at each sensor would show an exact linear trend across the array. However, in any particular realization it will not do so, for the following reasons:-

1) Addition of random additive noise will disturb the organized distribution across the array.

2) The signal may pass through slightly different patches of the sea on its way to the various receivers — spatial variations in the refractive index will cause propagation times to be different from that predicted simply in terms of geometrical distances; this is modelled by correlated multiplicative noise.

3) Non-linearity of the array — those sensors nearer the source receiving the signal earlier than expected, those further away later. This effect is greatest for a source at broadside.

4) Mismatch of the time delays in the cables returning the signals from the elements to the processor.

5) Errors in the phase shifters used for beamforming.

Although all of the above can cause phase errors, their results may be different both spatially and temporally. First of all the phase shifter errors may be discounted, as they are likely to be very small, effectively uncorrelated between sensors and completely different between consecutive realistic realizations. In a similar way, random additive noise should not make that significant a contribution to phase error, unless the noise is fairly correlated across the whole array, e.g. when multipath interference occurs between the direct ray and that reflected off the sea bottom. Considerable investigation of the effect of uncorrelated additive noise is referred to in this thesis, especially in the presence of pure phase errors, such as caused by misshapen arrays.

Inhomogeneities in the medium are quite likely to lead to phase errors that are correlated across the length of the array. The fluctuations for different sources will be different, although not in

any predictable way, simply that they will have similar correlation widths. There will be some variation with the bearing of the source if the transverse and longitudinal correlation lengths are different; the latter being the speed of sound times the correlation time.

Phase differences due to non-linearity of the array geometry can certainly be significant in long arrays. Given the phase errors associated with the array shape for a source at one angle, an approximation to the true shape might be deduced and hence the errors for a source at a different angle may be computed. The precise mapping between different phase errors here contrasts with the virtual independence of those due to phase fluctuations. [Signal degradation due to non-linearity (transverse displacements) should not be observable towards endfire, whereas that caused by the changing refractive index will be as present there as elsewhere.] It is to be expected that array shape fluctuations will have a characteristic time different to the typical duration of the inhomogeneities, and thus that the two effects will be able to be distinguished on a temporal basis too.

The existence of errors in the compensation time along the cables is a constant malfunction of the array. This might possibly be detected in the long term, when it is seen that certain elements seem to have a bias in their error location when examined over many hours of data in vastly different situations. It is unlikely that such errors would be large, and thus that the time and trouble would be taken to measure them.

This project is principally concerned with the errors resulting from array shape deformations. The following pages first discuss the variations in phase (and amplitude) associated with inhomogeneities in the ocean, as they are expected to be significant, and a necessary part of any realistic simulation. Their magnitude is noted, as is their correlation length and correlation time. After that, investigation is commenced into the various causes of locational uncertainty for the elements and then of how this affects the processing of the received data. Finally, there are a few pages indicating how various authors have approached the task of overcoming phase disturbances in the many fields in which it has manifested itself.

9.2 Sound Speed Dependence

The speed of a sound wave in the open sea is a function of temperature, salinity and pressure (and hence depth). It also varies with frequency, so dispersion of a pulse will occur i.e. its various spectral components will travel at different rates, causing the shape of the pulse to evolve with time. The refractive index (RI) of a medium, represented by n, is given by:-

$$n = c_0 / c \qquad [9.1a]$$

$$\mu = n - 1 \approx -\Delta c / c_0 \qquad [9.1b]$$

where c_0 is the standard speed, defined for specific conditions, and μ is the fractional change, which is very small compared to unity.

If the sound speed is greater over one route than another, then the signal will travel quicker over the former. Application of Fermat's theorem implies that sound will tend to travel over a route that is locally shortest in time. Consequently, the principal ray between two well separated points is a curve that spends a considerable proportion of its route in the deep, as that is generally where the speed is greatest. For a typical sound speed profile, many of the rays emitted by a source near the surface will take a broad range of routes through the deep ocean, reaching the surface close to one another. The resultant Convergence Zone (CZ) occurs at about 55-65km from the source.

Heating of the surface by the sun, increases the sound speed at the top. Consequently, there is usually a region some way below the surface where the sound speed is a minimum. This is typically at a depth of a few hundred metres, although the sound speed profile (ssp) will vary both diurnally and with the seasons, as is shown, for instance, by Flatté & Stoughton[38].

This section of minimum speed acts as a duct for the sound rays; those descending from it being refracted up, whilst those rising being bent down. Such an occurrence is often referred to as an Underwater Sound Channel (USC). Artel'nyi, Didenkulov & Raevskii[5] show that sound trapped in a USC should theoretically lead to an intensity distribution with a minimum at the centre, the point of minimum sound speed. However, intensity is often observed to be a maximum there; this is attributed to internal waves, which are mentioned later. For a source located on the axis of the duct, it is to be expected that all the rays emerging within a certain sector near the horizontal will travel along the channel without escaping. Observation of the angular intensity distribution on the channel's axis, caused by a multitude of incoherent sources, will show most of the energy to be received from such a sector. In measurements by Artel'nyi et al. this corresponds to $|\theta| < 16^o$,

where θ is the angle from the horizontal. They state that theory predicts that little energy should be transported by near horizontal rays, but that for frequencies below 100Hz the angular distribution is roughly uniform across the sector. However, for higher frequencies, both they and Aredov, Okhrimenko & Furduev[4] observe a broad drop in intensity for the near horizontal rays.

9.3 Lateral Differences

Many workers model the ocean as layered i.e. with all physical values (and hence RI) constant for a fixed depth. This is usually adequate for investigations of transmission loss, and other work where a simple source-receiver situation with time averaging is envisaged. However, the real sea departs from such a simplified view — the refractive index varies in a way that cannot be properly predicted, although its statistics may be understood. The refractive index is a function of 3-D space (not just depth) and time. In a paper concerning propagation models, Jensen[52] illustrates the temperature variations to be observed in various 2-D vertical sections of the sea. Although effectively random in nature, these variations are smooth, such that a correlation will exist between the RI fluctuations at one location and those at close neighbours in space and/or time. The correlation length (time) is a single figure indicating the region (interval) over which such variations are similar. The values for these parameters will depend significantly upon the frequency considered, and also on the conditions in the water mass.

9.4 Causes of Fluctuation

Fluctuations in RI occur on all scales from metres to thousands of kilometres, and from milliseconds to a year. Ali, Ferla & Akal[3] tabulate such information in terms of the underlying causes for each interval of the spectrum, ranging from microstructure to circulation of the ocean due to the annual variation in its heating by the sun. The tidal effects are only particularly relevant in shallow water. One of the causes of disturbance is thermal microstructure, which is the presence of minuscule fluctuations in temperature; Whitmarsh, Skudrzyk & Urick[105] describe the statistics of this. The horizontal scale length associated with such is in the region of metres to hundreds of metres, but the correlation time of such variations is around a few milliseconds. Thus scattering is

only effective for frequencies greater than a kilohertz. As the frequencies considered in this project are significantly below this, finestructure can be ignored. Medwin[68] mentions the effect of entrained bubbles near the surface being greater than scattering by microstructure.

Internal waves are the movement of large masses of water, and have correlation lengths of the order of 100m to several kilometres, whilst their correlation times cover the range from 10 minutes to 24 hours. A display of the intensity of RI fluctuations versus spatial wavenumber is called the Kolmogorov spectrum. Gregg[44] refers to a distinct change in the slope at 0.1 cycles/metre; this is sometimes taken as the dividing point between microstructure and internal waves.

9.5 Expected Level of Fluctuations

Various models have been devised to predict the expected degree of fluctuation in phase and amplitude. Wilson & Tappert[106] state that the Parabolic Equation method works well for low frequencies, but for those of 1kHz or more the method is impractical; they propose use of the radiation transport equation to cover such a range. Chotiros & Culbertson[24] favour formatting the fluctuation spectrum in terms of Gaussians, as the scatter of such a disturbance is well known. They reckon this approach simpler than using that involving wavenumber spectra and structure functions.

Komissarov[62] has performed careful mathematical analysis of the expected effect of random anisotropic inhomogeneities on phase and amplitude fluctuations. Defining B to be the logarithmic change in amplitude i.e. $B = \ln [A(x,y,z)/A_0] \approx \Delta A / A_0$ and ϕ to be the phase fluctuation, the expected variation in each is given by:-

$$\langle B^2 \rangle = \langle \phi^2 \rangle = {}^1/_2 \sqrt{\pi}\, \langle \mu^2 \rangle\, k_0^2\, L\, a_x \qquad [9.2]$$

where μ is the refractive index change as defined earlier, a_x the correlation length of such along the ray path, k_0 the wavenumber of the signal and L the distance travelled. Not surprisingly, the rms variation in ϕ is found to be inversely proportional to the wavelength, λ. The mutual correlation of the amplitude and phase fluctuations, $R_{B\phi} = \langle B\phi \rangle / \sqrt{\langle B^2 \rangle \langle \phi^2 \rangle}$ is finite for short ray paths, but tends to zero for large distances. The transverse correlation coefficients for sensors far from the source are predicted to fit the distribution below:-

$$R_B = \langle B_1 B_2 \rangle / \langle B^2 \rangle = \exp(-l^2/a_x^2) \quad [9.3a]$$

$$R_\phi = \langle \phi_1 \phi_2 \rangle / \langle \phi^2 \rangle = \exp(-l^2/a_x^2) \quad [9.3b]$$

where l is the lateral separation of the sensors.

Yang & McDaniel[107] predict the expected level of fluctuations of a 3kHz signal due separately to finestructure and internal waves. For the former a horizontal correlation length of 74m is used, whilst the value is only 2m for the vertical direction. Internal waves were shown to lead to much greater changes in RI, and consequently decoherence due to them dominates over the effect for finestructure.

9.6 Observed Spectrum of Fluctuations

Many experiments have been done to measure the amplitude and phase fluctuations over totally refracted paths (i.e. ones where there is a single path from source to receiver, and it involves no reflections off the sea surface or bottom). Some of the most thorough ones were those at the Cobb Seamount[31,32] and the one called MINIMATE[33] which was performed at Quilcene Bay. [The second experiment at the the Cobb Seamount site was given the acronym MATE — Mid-ocean Acoustic Transmission Experiment.] All three involved measurement of the physical properties of the water e.g. temperature profiles, whilst the correlation measurements were being taken. The first Cobb Seamount experiment used pulses of 4kHz and 8kHz sound over a 17.2km path to sensors up to 15m apart. For both frequencies the phase difference at the two sensors was found to be normally distributed. Both Cobb experiments showed that the intensity of the phase fluctuations followed a ω^{-3} dependence as expected, where ω is the frequency of the fluctuations, rather than of the sound used. However, the amplitude variations obeyed a ω^{-1} law instead, whereas the expectation from the theory of internal waves was that it too would be proportional to ω^{-3}. Desaubies[29] quotes the amplitude fluctuations as having a variance of about 5.0 $(dB)^2$ at 4kHz. He suggested the spectral discrepancy might be explained in terms of finestructure being passively advected by the internal waves. Ewart[32] has extended this line of thought to show good agreement with the data, although he does not claim that the model is necessarily true. The Cobb experiments showed that the phase difference between the signals at two sensors were proportional to $\omega^{-1/2}$.

MINIMATE looked at 4 frequencies (all in the kilohertz) range, but only over a path length of 1.1km. It was observed that the travel time variations were approximately the same for different frequencies whereas the amplitude fluctuations were uncorrelated across frequency. Little correlation was observed in the changes in travel time at two sensors 3m apart.

This project is primarily concerned with CW signals in the frequency band 100-400Hz, for which measurements can be found dispersed throughout the literature. In a summary table of others' results, Urick[101] gives a figure of 400m for the correlation width of a 400Hz signal, travelling over 430km; Flatté & Stoughton[38] quote a figure of 1km for a 178Hz signal over a 135km route.

The above discussion has been for totally refracted paths; however, if the dominant path involves reflection off the sea surface, then the correlation length is reduced considerably — Urick[101] states this may be by as much as a factor of 6. Akulicheva & Frolov[2] have studied the characteristics of two singly reflected rays over a distance of 65km. The different degree of fluctuations associated with the two could be attributed to the different sea surface conditions at the relevant reflection areas — changes in angle of surface being the primary contributor rather than the varying height of the water mass. Surface reflections lead to small variations with a period of around a second. Galkin & Frolov[39] attribute significant variations of the vertical arrival angle to variations of the surface slope, because the angle of arrival (AoA) only changes by 0.2^{o} for purely water-borne rays. Urick[100,102] has shown that in a multipath environment, there is a 1 in 10 chance that the signal level may drop by as much as 10dB; but if a single dominant path exists then there is only a 20% chance that level will fall by more than 2dB.

Beran & Whitman[9] explain how velocity inhomogeneities in the water mass itself affect the passage of sound waves in a similar way to RI variations. However, they conclude that such an effect only becomes at all significant for frequencies greater than 20kHz.

Urick[101] states that for significant fluctuation levels, there is no benefit to be obtained from using an array any longer than twice the correlation length of the fluctuations.

9.7 Simulated Fluctuations

Despite Komissarov's derivation of the Gaussian form for cross-sensor correlation, and the results of Ewart[31] and others to support such, many authors involved in simulation work e.g. Paulraj & Kailath[78], Butler[20] and Kirlin & Dewey[57] invoke the simple exponential decay law for the correlations i.e.

$$\langle B_i B_j \rangle = \exp[-\alpha \mid i-j \mid] \qquad [9.4]$$

as this is a very simple correlation to simulate. Given a set of uncorrelated random numbers, $\{n_i\}$, one way of producing a set with the desired properties, is to set:-

$$a_1 = n_1 \qquad [9.5a]$$

$$a_i = \alpha a_{i-1} + \sqrt{1-\alpha^2}\, n_i \qquad [9.5b]$$

A series of random numbers whose correlation is described by a Gaussian can be obtained by taking a set of independent random numbers and convolving them with a Gaussian, a process most efficiently implemented in the inverse Fourier domain. Any other desired distribution, such as the sinc function can be achieved by this method. Buckley[17] details the simulation and use of such random numbers to provide a 'phase-changing screen'. Tough[98] has looked at methods of generating distributions such that their development in time may be as required too.

9.8 Summary

As can be observed from the above, many people have spent a lot of time attempting to determine the nature of the variations due to the medium. The experimental results for specific processing parameters tend to show great variability, depending upon the oceanic conditions present. Komissarov has produced a clear prediction of the expected degree of fluctuations, assuming rays involve no reflections. Although such an assumption may not be too representative of the true situation to be encountered, his results may prove a useful guide to the size of the correlation length.

Workers who have had need to perform simulation of correlated noise, have often modelled the correlation as either Gaussian or exponential decay. Their investigation has generally been over a large range of values for the correlation length, the span often having been chosen in terms of the

degree of coherency at neighbouring hydrophones or over the whole length of the array. This was in order to show the varied behaviour of their processors, rather than through reference to any pertinent figures in the literature. This, consequently, is the approach adopted here — use of a breadth of correlations varying from totally uncorrelated to fully correlated. Naturally computation time restricts the number of intermediate degrees of correlation which can be investigated.

10. MISSHAPEN NATURE OF ARRAY

10.1 Physical Causes

This project is particularly concerned with the effect of misshapen arrays upon signal processing techniques. There are many reasons why an array will not correspond to the ideal equi-spaced line array assumed by many algorithms. Manufacturing errors may cause the element separation to be non-uniform, but errors of the order of a few percent are unlikely to be significant here. Rapid towing of the array through the water, with resistance provided by the drogue will cause variable stretching of the array along its line. However, much more important are the effects that cause the elements to lie off the 'line of the array' by possibly several wavelengths. Two major causes for this exist.

Firstly, there is the presence of cross-currents in the ocean. A steady uniform cross-current will principally only cause the line of the array to rotate such that its direction is now no longer parallel to that in which the ship is pointing. However, large eddies and other major disturbances will produce variable forces on the array and cause it to adopt some other configuration. Note the resultant shape is likely to be analytically smooth, as the cross-forces, although fluctuating, will show some correlation across the array.

The other common cause of contorted arrays is that the towing ship is undergoing (or has just completed) some manoeuvre changing the route that it is pursuing. It may be required to do this for a number of reasons — avoiding islands or other ships, turning back to continue patrol of a certain patch of the ocean, or in order to produce a different direction of the array such that the range of a far off source may be determined by triangulation.

The above two processes are complicated to model fully, as not only do the forces vary in space, but also in time, and the array is being towed through the spatial distribution too. Some papers have assumed that an array towed around a curve will pursue a circular arc. Such is certainly easy to model, but it is not totally representative of the evolution of the array shape. Brandenburg[12] has investigated the changing shape of an array, utilizing such a model in which the array follows itself. With this model of array movement, he continues on to propose a specific trajectory for the turning vessel in order to minimize the amount of time required for the array to straighten again. Other

authors have concluded that an array will 'cut the corner' i.e. take the shortest route, if the turning circle is sufficiently sharp. Indeed in some cases, cornering may reduce the tension at the end of the array, thus leading to a sag.

Bedendender[8] has explored the various models detailing the curve adopted by a cable subject to tension and hydrodynamical loads. Unfortunately, the cases considered are complicated 3-D ones rather than just planar, so little insight is gained, although the models could be constrained to deal with variations in a specific horizontal plane, or else the planar projection of the 3-D result for a nominally level array could be used. Also, the models predict a steady-state shape, giving no indication of the curves likely to be encountered when the forces are fluctuating. Cartwright & Mayers[23] have applied kinematic equations to the case where the towing ship is not adopting a perfectly straight course. The resultant form for the evolution of the array shape was solved by two mathematical methods, whose results were consistent; however no comparison was made to *in situ* measurements on an array.

Ketchman[56] has calculated the vibrations in array shape likely to be caused by vortex shedding (i.e. eddies) as the array moves through the water. He was principally concerned with the existence of high frequency vibrations (around 50Hz), and concluded that the associated correlation length is 1-3.5 cable diameters, and that pitch (up-down) variations dominate over yaw (left-right) ones. These rapid vibrations are of tiny amplitude — extension of these findings to slower large amplitude oscillations seems uncertain.

10.2 Effect on Processing

Some of the causes of phase error mentioned previously have had their specific effect on processing investigated e.g. Godara[42] has made predictions of the effects of limited phase shifters, and Gray[43] has shown how 'quantization lobes' can arise because of the need for interpolation when examining a sampled time record. Many more authors have simply investigated the effect of independent errors. The source of such errors could be most of those listed previously, although usually the resulting variances in amplitude, σ_A^2, and in phase, σ_ϕ^2, will be small i.e. $\ll 1$. [Errors caused by misplaced sensors are unlikely to be independent i.e. totally uncorrelated, unless their separation is far greater than the wavelength of the disturbances travelling along the array, or else they are all independently held in position e.g. attached to separately moored buoys.]

Ramsdale & Howerton[82] have examined the probable height of error related sidelobes for a given level of distortion. They rigorously derived an expression for the effect of independent errors in amplitude and phase, not only finding the mean error-induced sidelobe level (SLL), but also the probable height of the peak sidelobe — for 30-50 elements, this is about 7dB above the mean value. The full derivation for the height of the error lobes contains an expression of the form $\sum w_i^2 / (\sum w_i)^2$, where $\{w_i\}$ is the set of weights used for the n elements. This is minimized ($\rightarrow 1/n$) for the selection of uniform weighting. Other weighting schemes thus induce higher SLLs, although, for most commonly used scalings, the difference from that for uniform weighting amounts to no more than a few decibels. An exception is superdirective arrays, which show great sensitivity to such errors.

Quazi[81] has shown that where the error induced level dominates over the true beam pattern i.e. the true sidelobes are negligible to the levels simply due to noise, the probability on a chosen bearing of observing a certain power level, x, is given by the pdf $pr(x) = (1/\mu^2)\exp(-x/\mu^2)$, where μ^2 is the mean level added to the beam pattern due to the errors. Quazi also detailed the effect of amplitude and phase errors upon the pointing accuracy of the beamformer. The rms error, σ_u, is given by:-

$$\frac{\sigma_u}{\Delta u} = \left(\frac{3}{n\pi^2}\right)^{1/2} \frac{\sqrt{1+\sigma_A^2}\ \sigma_\phi}{\sqrt{1-p_r(e)}} \qquad [10.1]$$

where Δu is the beamwidth, and $p_r(e)$ is the probability of element failure. Note that element failure alone cannot cause pointing error.

Ling, Lo & Rahmat-Samii[65] have modelled a similar problem for microwave dishes, noting the effect on mean and peak SLLs. Tsao & Steinberg[99] have simulated the effect of such errors upon a microwave antenna array that was implementing the CLEAN algorithm. Positional errors of the order of 0.2λ or more, led to false targets of significant amplitude; however Tsao & Steinberg's 'absolute threshold' seemed to be able to discriminate sufficiently well to prevent acceptance of such peaks as real sources. Kleinberg[58] has simulated the loss in array gain due separately to amplitude and phase errors, later expressing this in terms of a combined measure for the errors.

Cox, Zeskind & Owen[28] have compared the performance of a linear predictor algorithm (similar to MEM), ML processor and CBF under the effect of such independent errors. They found that the phase errors caused the same shift of peak for all three, although in the case of LP it corresponded to more than one beamwidth. Amplitude errors were found not to cause the LP peak to wander, but rather to lead to splitting of the peak. Mumford & Lawton's[72] investigation for ML

processors stated that the amplitude and phase errors were equally important, the effects being dependent on the total variance of the errors. Smallish independent errors still enable the processor to resolve sources, but the ability to compare magnitudes is severely degraded.

Schultheiss & Ianniello[90] have detailed the effect of independent small errors on estimation of both bearing and range. They also consider correlation in sensor displacements of the form $E\{x_i x_j\} = \rho^{|i-j|}$, and show that for 5 or more sensors the errors in range and bearing are uncorrelated and almost constant over the interval $-0.5 < \rho < 0.5$. Schultheiss & Ianniello had specifically studied an ML estimator; however, they state that at high SNR, CBF is only slightly more erroneous. Ginzkey[40] has compared the effect of positional errors on several different processors — CBF, MLM, MEM and EDM (Eigenvector Decomposition Method). The maximum errors investigated corresponded to only about a tenth of a wavelength. The output SNR of CBF remained relatively unchanged, whilst that of the others decreased markedly — MLM and EDM showing no better gain than CBF for $\lambda/10$ errors.

Their emphasis had been predominantly on small arrays with a short correlation length for the sensor disturbances; Hodgkiss[50], on the other hand, has looked at the degradation of large arrays following a perfect circular arc, in which case the correlation is significant across the whole array. Nakatsuka[73], too, has examined the effect of 'wavy phase errors' - in this case the field of application was space-borne microwave arrays. Steinberg & Yadin[97], in turn, give the equation for the reduction in gain of a 'radio camera' (high resolution microwave antenna) resulting from random phase errors:-

$$\Delta G = 4.3\,\sigma_\phi^2 \ \text{dB} \qquad [10.2]$$

Their analysis was continued for partially correlated phase errors; however, interest was principally only in very small scan angles and phase errors due to multipath interference.

Knapp[59] has looked at the influence of significant phase errors on the detection probability of large arrays, rather than upon the bearing accuracy. He states that when the rms error is 0.1λ the effect of the deformity is noticeable, the success rate for detection being reduced to only 75%. He proposes the form for a processor with optimum detection capability. For small position errors, less than 0.1λ, the standard CBF processor yields equivalent performance, but for very large errors the detection rate of the standard is reduced to that of one sensor alone, whereas that of the 'optimum processor' is $\sqrt{n}$ better. However, even for his processor with no additive noise, errors greater than half a wavelength cut the detection rate to less than 20%. It is pointed out that processors which use *a priori* knowledge of the fluctuation statistics may be prone to great discrepancies if that knowledge

is inaccurate. Specifically, ANC (Adaptive Noise Cancelling) can be very suspect to disturbances, as mismatch errors in cancelling will add to the problems due to imperfect addition in the look direction; Reed[83] covers the details for one specific processor.

10.3 Restoring Image Quality

Hinich & Rule[49] have approached the problem of a misformed array by considering it as a collection of successive mini arrays. Specifically, they looked at division of a 50 element contorted array into 4 and 8 element sub-arrays. Beamforming of these independent systems creates a distribution of estimates, whose average is close to the true bearing of the source. For a perfectly straight array, CBF processing of the whole array is preferable to use of sub-arrays. However, when the array is contorted, sub-array processing improves the estimation of source bearing — 4 element sub-arrays being best for a source near broadside, and 8 element ones for angles close to endfire. Use of median rather than mean, or 'closing aperture' sub-arrays (i.e. pairs from each end successively inwards) were found not to improve performance. As an extension, Hinich[48] also suggested division of time record into short segments with averaging over time estimates too. Such an approach seems rather suspect for the noise levels envisaged in this project, and detection of a second source is unlikely. A possible adaptation would be to reconstruct the believed array shape using the various sub-array estimates, and then perform CBF with these element locations to see whether weaker sources exist.

Brown & Ghiglia[13] have looked at a variant of this. In their discussion of the map-drift technique, they divided the sensors up into n sub-arrays, and performed beamforming for each to yield bearing estimates, and then used these values to fit an nth order polynomial curve to the whole array, rather than simply producing a 'curve' of n straight lines. They also investigated a cubic spline fitting method. Butler[20], too, has looked at this in attempting to use information from a few position calibrators on the array in order to infer locations for them all. Cubic splines were shown to give a good fit to the array shape (which was modelled by a sinusoidal curve) and thus the sidelobes could be kept down.

A similar approach has been adopted by Bouvet[10], except that he interests himself in locating each sensor individually using a 'co-operative source' (i.e. one whose bearing and range is approximately known beforehand).

The general self-survey equations linking sensor and source positions have been developed by Lee & Dorny[64] for a 3-D microwave array. As no restrictions exist on the relative positions of the detectors (such as a linking cable), three distinguishable sources are required. If a certain three are used for localization of elements, then no information on their position can be obtained. With 4 sources, each in turn may be located. Lee & Dorny have looked at the stability and complexity of the solutions of the resulting equations. They conclude that localization calculations will be well behaved if the individual sources are at least 28 beamwidths apart. The distinguishable sources may either operate at different frequencies, or else be scheduled to emit at different times. Only three sources are required for the two dimensional problem. Rockah & Schultheiss[85] have investigated the theoretical limit on such determination, by calculating the Cramer-Rao Lower Bound (CRLB) for the estimation. For a set of sensors independently disturbed from their nominal positions, the resultant variance in bearing estimate is given by:-

$$\sigma_{\phi}^2 = \frac{2n\sigma_x^2}{\sum_{i=1}^{n}\sum_{j=1}^{n} r_{ij}^2} \qquad [10.3]$$

where σ_x^2 is the total variance in the individual position estimates (i.e. of both x and y co-ordinates), and r_{ij} is the distance between the ith and jth sensors. [Note, this value was derived assuming a 2-D array of arbitrary design.] The individual fixing of each element's position as detailed above will tend to be rather erroneous when the signal level of the source is low. In Bouvet's simulation, the array estimate differed markedly from true when the SNR was 5dB. In the particular situation envisaged for this project, strong calibratory sources will not be available; instead only the vessel(s) to be located will be present, and they will be weak emitters. Such a procedure of shape determination is also unlikely to cope with multiple sources broadcasting over the same frequency band.

An entirely different approach involves examination of the structure of the beam pattern resulting from a particular guess. This technique was applied to the problem of misshapen acoustic arrays by Bucker[16], but originated in a proposal by Muller & Buffington[71]. They were looking at a scheme of adaptive correction for an optical telescope, in order to overcome signal decorrelation due to the variability of the atmosphere through which all the rays were passing.

The fundamental limit of the resolution of a telescope due to diffraction is approximated by λ/D, where D is the width of the main mirror (or lens). However, the atmosphere in a column above the mirror is not uniform. If the variations in refractive index (RI) are equal across any horizontal

section of the medium, then the signal would still be perfectly correlated. However, the horizontal scale length, r_0, of the isoplanatic patches (that part of the atmosphere over which RI fluctuations are correlated) is only of the order of 10cm. Thus the turbulence related resolution of a telescope, given by λ/r_0, is in the region of a few seconds of arc, which is much wider than the equipment's theoretical limit. Thus it should be noted that large Earth-based telescopes are not designed to improve the resolution attainable, but to have greater light gathering power.

Muller & Buffington calculated various statistics of the image intensity pattern, $I(x,y)$, amongst which were the intensity at the central point, $I(x_0,y_0)$ and the summed square intensity, $\int I^2(x,y)\,dx\,dy$. Maximization of any of these criteria should correspond to correct retrieval of the phase information and production of a diffraction limited image. Some of the measures were shown to converge analytically, whilst others were found to do so experimentally. Sica[94] indicates a simple proof for $\int I^2(x,y)\,dx\,dy$ using Parseval's relation, but continues on to show that such analysis cannot be applied when the effective point spread function (PSF) varies with spatial co-ordinates.

To cope with such a space-variant situation, he compares long-term exposures (blurred images) with a specially blurred version of a 'snapshot'. A snapshot (short-term exposure) of a small sector of the sky will contain diffraction-limited information, as long as the exposure is no longer than the correlation time of the atmospheric inhomogeneities, which is approximately 10ms. This method requires knowledge of the expected blurring due to long time exposures, however, more recently, Sica[95] has shown that just the shape of the transfer function is required, as the appropriate width can be determined. Ward & Saleh[104] have applied a blurring filter that simply corresponds to addition of a small number of images, shifted by predetermined amounts. Their method is driven by the maximization of a function of both the beamwidth of the overall system and the noise variance.

Rosenfeld & Kak[86] provide a good summary and mathematical derivation of many of the processes that may be applied to blurred images. They comment that use of the Laplacian operator to sharpen images is physically justifiable, as it emphasises the high wavenumber components that have been most affected by blurring. However, they add that such a procedure is only suitable in the absence of any knowledge concerning the blurring mechanism; if such information is available, restoration techniques such as inverse filtering are generally superior.

In astronomy, observers are generally interested in a very small field of view, such that the object in which detail is to be sought is smaller than the isoplanatic patch size. By 1970 it had been realised that very short exposures (of the order of 10ms) could yield diffraction- rather than

turbulence-limited images. However, in such short exposures the photon flux is low, and consequently the quality restricted by photon probability statistics. Straight forward averaging (long-time exposure) removes this problem at the expense of the superposition of many slightly shifted images creating a blurred view. Labeyie[63] showed that useful information for averaging could be obtained from each short exposure image by taking the modulus squared of its Fourier transform. This technique, called Speckle Interferometry (SI), is equivalent to forming the autocorrelation of the image, which loses all the phase information.

SI performs reasonably for binaries or simple symmetrical objects. Knox & Thompson[60,61] produced an improvement which utilizes the phase information. Their method was devised to cope with resolving more complicated images, such as planetary moons. The KT (Knox-Thompson) method requires the presence of a reference point-source star; but this does not have to be in the same isoplanatic patch (area suffering identical degradation effects), but must be close enough to have the same mean square fluctuation characteristics as the complicated image to be restored. This averaging approach can work with low levels of random additive or multiplicative noise. Ayers, Northcott & Dainty[6] have looked at an extended version of the KT method, which is based on a higher order statistic, that is an average of the correlation value for two intervals. This is compared with the Triple Correlation method, which uses higher order statistics too. Little real difference was found between the performance of the two.

As for high resolution beamformers [chapter 8], further algorithms exist that are slight variants of others, but with some particular defect removed. For example, Aitken & Johnson[1] cite certain advantages of the Phase-Gradient method over KT. Cowie & Songaila[26] discuss application of another algorithm on real astronomical data recorded at Mauna Kea. They claim to be able to achieve diffraction-limited images using a reference star up to 5 patches away. With the good 'seeing' associated with that site, the process can be applied to objects of interest within 30 arc seconds of a bright point source.

10.4 Summary

Little information seems to be readily available on the configurations adopted by large towed arrays, although significant deviations from a straight line are known to exist. To a good approximation, hydrophone elements are believed to follow the route of preceding ones, thus enabling good estimates to be made of the positions a short interval after they have been determined. However, such cannot be simply extended to infer array shape from the route of the towing vessel, as cross currents and eddies provide significant changes along the length of the towing cable. Some work has been done using a limited number of directional sensors along the array — if these were accurate enough for sonar work, then this problem of positional uncertainty would not exist.

Many authors have investigated the effect of minor phase and amplitude errors on the bearing estimate and sidelobe level — a rms positional error of 0.1λ being the tolerance limit for most forms of processing. At this level of errors, high resolution beamformers showed no gain over the conventional 'delay sum and square' technique.

Many different approaches to the problem of shape uncertainty have been proposed, coming from various different environments. The practical applicability of each individually depends upon how well the specified scenario matches that envisaged in this project. Here we are concerned with scanning over all angles with considerable noise present. Thus those methods which rely on an 'almost empty' object field will not be applicable here. The various speckle imaging techniques require the presence of a neighbouring strong point-like source. No strong sources are likely to be present in the acoustical case, except for the towing ship, which always being close to endfire can be of little help for element location. Oceanic fluctuations would shift the pattern for an otherwise well-focused image. In which case independent realizations might be profitably averaged by some implementation of the KT algorithm. However, such tends to be used to bring out detail in an already located source; use of such averaging to detect the source is suspect for if an individual processed 'snapshot' can not be made to yield the source location(s) itself, then it is unlikely that the image restoration will be any good.

Several more of the above methods required the existence of strong co-operative sources — an invalid assumption for the present case. The phase correcting approach of Muller & Buffington seems the most applicable. Although convergence using some 'power functions' is proved in their appendix, it must be borne in mind that they were working on a single source situated in the centre of their narrow field of view, and that no additive noise was assumed. Bucker has indicated that the process can be applied to a multi-source environment with significant noise. There seems to have

been little follow up of this, so this work is primarily concerned with determining the performance limits of such a method, and of investigating which power functions converge quickest, and which are most stable.

11. COMPUTER IMPLEMENTATION

11.1 Hardware and Incorporated Software

This entire project was a computational investigation of the problem in question, namely determination of the effect of array positional uncertainty on source detection and bearing estimation, and testing of a means of overcoming it. The approach used involved maximization of a measure termed a power function (pf), which was calculated from the power variations within the beam pattern; various pfs are defined in chapter 12.

Original work was done on a Honeywell 68 DPS level 2, running *Multics* operating system. All programming was done in Fortran 77, with use of NAG for random number generators and GINO-GRAF for graphical output. This machine had to be replaced due to aging — subsequent work was done on a Gould NP1 running *Unix*. Due to considerable changes and improvements required, the work on the Gould was done with a completely rewritten program, although many of the subroutines were very similar to the versions used on the first machine.

Fortran 77 was used once again, as was NAG for random number generation. However, this time GINO-GRAF was unavailable, so the inferior NAG Graphical Supplement (NGS) was incorporated instead. The relevant coding amounted to approximately 2400 lines, and was stored in 4 files.

Word processing and laser writing had originally been performed by a GEC 63/40 using *troff* — its departure, and the eventual availability of appropriate software (*SoftQuad*) on the Gould, meant that this machine was in the end used both to produce results and to present them in this thesis.

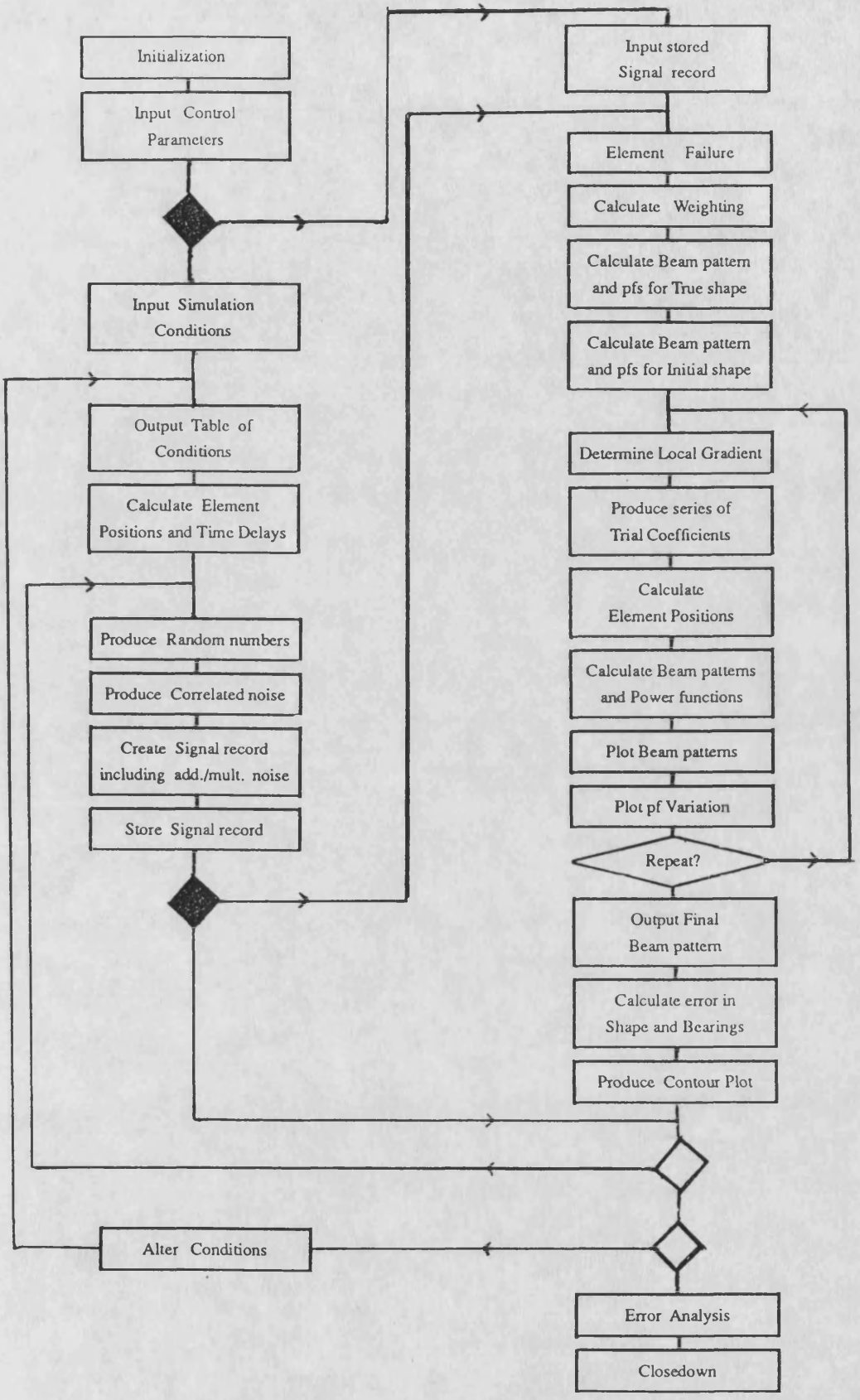

Fig 11.1 : Flowchart of program performing the investigations detailed in this project.

11.2 Organization of Program

The flowchart in Fig 11.1 describes the action of the program, and the sequence of subroutine calls. However, usually some of the routines were bypassed for any particular run; for example, when hundreds of simulations were needed for averaging, then graphical output such as beam patterns and contour plots were not called. Also, although the local gradient might often be calculated, the search direction used was often set to a predetermined one e.g. a single member of the Fourier basis.

The routines on the left-hand side of the diagram were concerned with simulation of the signal, whilst those on the right related to the processing — beamforming, calculating power functions and relevant graphical output. The coloured in decision boxes enable selection of one of three possible tasks for the program:-

i) Creation of signal record only (and storage)

ii) Processing of stored signal record.

iii) Production of new signal record, storage of its values, and processing of it.

The two decision boxes at the bottom gave the program the ability to repeat all its work either for exactly the same conditions (inner loop) or for slightly modified ones (outer loop). Many repeats of identical conditions being necessary to produce sufficient results that statistical analysis could be applied meaningfully; repeated sequences of runs for modified conditions enabled many similar scenarios to be processed successively, rather than using repeated calls of the main program, with different values read in from the input files.

If the program was truly divided into simulation and processing parts, then the element failure routine should belong to the former. However, it was felt advantageous to store the full element record, and incorporate the failure in the processing side, so that the effect could be applied to stored simulations, enabling more precise comparisons with processing of unadulterated signals.

Beam patterns, on output, could either be independently scaled, such that their maximum corresponded to the full scale of the graph, or else drawn on axes calibrated such that full scale corresponded to the peak response for processing using the true shape.

11.3 Input / Control

The program was required to investigate a large variety of conditions, and to use different processing, depending on which aspects of the problem were being investigated. To cope with the large range of scenarios, the input conditions were read from 3 different files. One characterized the sources present — no. of sources, frequencies emitted, and for each source the bearing and range, as well as the phase and amplitude at each of its frequencies. Another file dealt with the noise — levels (standard deviations) and correlations of both additive and multiplicative. The third file described the array — no. of hydrophones, their spacing and the true array configuration in terms of its Fourier components.

These 3 files contained all the information necessary to simulate the signal record. Any such record produced was automatically stored; an option within the program permitted retrieval of previously produced data to enable different processing approaches to be used on not just the same situations, but on exactly the same data. In such cases, the previous 3 input files were superfluous.

A fourth file contained all the conditions pertinent to the processing of the signal record. Some values in this file were parameters describing the initial shape estimate, search range to be tried, beam sampling rate and sector to be scanned etc., whilst others were 'flags' i.e. simple integer values destined to switch on or off various pathways in the program, such as plotting of beam patterns or contours, accurate bearing estimation or use of gradient search methods.

11.4 Parametrization of Array Shape

For this work, the array shape is characterized by a limited Fourier series. This is specified by the Fourier coefficients, a_j, $j = 1, 8$, such that the sensor locations are given by:-

$$x_i = \left(\frac{n+1}{2} - i \right) d \qquad [11.1a]$$

$$y_i = \sum_{j=1}^{8} a_j \sin\left(\pi j \, (i-1)/(n-1) \right) \qquad [11.1b]$$

where array length, $L = n-1\, d \simeq n\, d$, n is the number of elements and d their separation. Alternatively, the variety of possible array shapes may be regarded as a domain spanned by the basis functions, f_j, where f_j are given by:-

$$f_j(x) = \sin\left(j\,\pi(\frac{L}{2} - x)/L \right) \qquad [11.1c]$$

Note, that:-

i) The array is actually numbered here from right to left (i.e. x decreases as i increases).

ii) The array is centred about the origin.

iii) The nodes of the Fourier series are located at $i=1$ and $i=n-1$ (i.e. on the end elements).

This type of characterization was chosen because it generates a smooth form for the cable, as would be expected, without needing many numbers to be specified. This particular parametrization also seemed a wise choice for a basis, as components of a Fourier series are mutually orthogonal. The application of orthogonality concepts to estimation of several independent coefficients is discussed in chapter 30.

The first 3 of these Fourier terms are illustrated in Fig 11.2. It can be seen that the shape of II is such that the line of the array i.e. the straight line which best fits the points is no longer parallel to the original straight form. Indeed, this conceptual 'line of the array' will shift linearly with the amplitude of the 2nd Fourier coefficient.

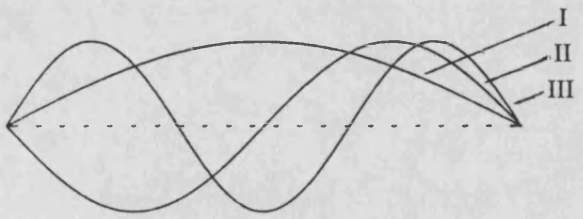

Fig 11.2 : Illustration of first 3 Fourier terms in simple basis

As there is generally no fixed reference point in open sea operation, source bearings can only be determined relative to the array. If data for a certain signal record are processed using an inappropriately rotated array (possibly due to an erroneous value for a_2) then the estimates of the source bearing will be out by the same amount. To overcome such a simple estimation error for the wrong a_2 value, it is convenient to alter the 2nd basis function to its Fourier equivalent rotated through the correct compensatory angle. As deviations perpendicular to the array are small relative

to the array length, it is sufficient merely to subtract out the equation of the best fit line to this curve. The equation for this line and for the equivalent higher order even terms is calculated in appendix 7. Thus the basis functions generally used in this work have the y-values computed according to:-

$$y_i = \sum_{j=1}^{8} a_j \sin(\pi j\,(i-1)/(n-1)) + \sum_{j=1}^{4} a_{2j}\,(12x_i / 2j\,\pi L) \qquad [11.2]$$

The difference in bearing estimation between these two characterizations ([11.1b], [11.2]) is shown in chapter 15.4.

11.5 Noise Generation

It was required to be able to generate complex Gaussian noise of standard deviation, σ_n, and inter-sensor correlation, $E[n_i n_j^*] = \sigma_n^2 e^{\alpha|i-j|}$. [Note, as correlated noise is only a small aspect of this investigation, a fully realistic modelling of the correlation of ocean noise is not needed, rather what is required is a simple form characterized by one or two parameters that enables correlation length to be changed easily. This particular form for the correlation was chosen for its simplicity both in implementation and interpretation. All other correlation forms, including Gaussian (the other commonly used one) could be produced by a filtering technique; however, the exponential form can be created more simply.]

The NAG routine used was G05DDF(M,S) which generates a number randomly from a Gaussian distribution of mean, M, and s.d., S. This was called twice with mean zero and s.d.=$1/\sqrt{2}$, which were then equated to the real and imaginary parts of the complex noise, viz:-

```
S = SQRT(0.5)  ;  XN = G05DDF(0.,S)  ;  YN = G05DDF(0.,S)
CN(J) = CMPLX(XN,YN)
```

The complex noise, CN(J) (J = 1, NEL — no. of elements), generated by this method has a mean of (0., 0.) and a s.d. of 1. Rescaling of the magnitude of the noise (i.e. the s.d. → SD) and production of the desired correlation, using ALPHA = α, is achieved by:-

```
      BETA = SQRT(1 - ALPHA*ALPHA)  ;  CN2(1) = CN(1) * SD
      DO 10 J = 2, NEL
10    CN2(J) = CN2(J-1) * ALPHA  +  CN(J) * SD * BETA
```

Thus the array CN2(J) contains random values with a Gaussian distribution of zero mean and a standard deviation of value SD, and having an exponential form for the correlation as required.

11.6 Element Weightings

The reasons for attributing greater importance to the signals from some elements than from others is discussed in chapter 4.4. This paragraph merely states which ones have been used in this project, and their actual coding, especially as to the locations of zero weighting for the Hann and Bartlett schemes (compare to chapter 4.4). The five used were:-

UNIFORM	:	$w_i = 1$
HALF - COSINE	:	$w_i = \cos\left(\frac{\pi}{2} \cdot \frac{i-n'}{n'}\right)$
HANN	:	$w_i = 0.5 + 0.5\cos\left(\pi \cdot \frac{i-n'}{n'}\right)$
HAMMING	:	$w_i = 0.54 + 0.46\cos\left(\pi \cdot \frac{i-n'}{n'}\right)$
BARTLETT	:	$w_i = \frac{n' - \lvert i-n' \rvert}{n'}$

where w_i is the weighting of the ith element, and n' is the midpoint of the array of n elements i.e. $n' = {}^1\!/_2 (n+1)$.

11.7 Measuring Estimation Accuracy

To investigate the accuracy of the estimates it is necessary to evaluate power functions (pfs) for various shape estimates close to true. Generally, the trial shapes are described by:-

$$\zeta_i = \zeta_0 + i\,\Delta\zeta \qquad , \; i = -n, -n+1, \cdots, n \qquad [11.3]$$

where ζ_i is the vector representation $(a_1, a_2, a_3, \cdots)$ of the series of Fourier coefficients describing the trial shape, ζ_0 is that for the true, and $\Delta\zeta$ the incremental step. Often $\Delta\zeta$ has zero values for all terms except one i.e. it corresponds to a search over just one of the unknown coefficients, with the rest already determined. In chapter 30, work is also done for cases where the central guess, labelled ζ_0, does not correspond to the correct set of values, and neither does any of the others — this is to test whether the power function algorithm selects the shape nearest to true when the true shape is not one of those tested.

The number of combinations tried, N, equals $2n+1$. Now, although it is expected that on average the power function will peak for $\zeta_i = \zeta_0$, the effects of noise will lead to the maximum lying at some other shape nearby. Care must be taken in the search procedure to ensure that the range of values investigated contains all the likely locations of the peak i.e. the range must be such that the peak rarely occurs at $i = -n$ or $i = n$, as this would be indicative of the true maximum being much further away. However, it is also useful to have $|\Delta\zeta|$ small as this is the resolution capability of the shape determination. A small value for this improves the accuracy of the measurement error and allows more precise comparison of different situations. These two variables are linked by N, the number of beam patterns to be calculated and stored. In this program, N was constrained to have a maximum value of 50.

11.8 Repeated Searches and Convergence

It is not practical to extend the linear search method highlighted above to a higher dimension i.e. to calculate pf values for all possible combinations of all possible values for the coefficients. Instead, 2 main approaches are possible:-

i) Repeated linear searches — independent evaluation of each of the coefficients via the linear search method.

ii) Method of steepest ascent — investigation of changes in pf for small increments of the various a_i leads to a direction vector for the steepest rate of change; a linear search can then be used in this direction.

There are also further algorithms appropriate for gradient climbing that involve alterations to the up-slope vector, using extra knowledge about the structure of the n-dimensional surface close to the power function peak. However, much of this project is about whether the pf peak (and thus

hopefully the true source shape) will be reached, rather than how efficiently the program converges to that point.

11.9 Increased Resolution

Much of this work was done with beamforming using an angular separation of 2^o between beams. In cases where higher precision was required, the angular sector local to the peak was scanned again at, say 0.01^o resolution.

A routine had been written which took the highest peak and the points either side and fitted a quadratic curve to them. The implementation of this is discussed in appendix 9. Although the application of this in the determination of the peak position led to a reasonable gain in accuracy, it was not generally used in this situation — the increased resolution beamforming being implemented because of the certainty of its results. [Alternatively, methods such as Fourier interpolation or fitting of a cubic spline could be used, but each makes assumptions about the shape of the lobe.]

In the attempts to converge towards the true shape, power functions were calculated for a number of shapes differing by constant increments in one or more parameters; the peak pf value indicating the shape closest to true. Here the method of fitting a quadratic was beneficial, as it reduced the number of trial shapes to be tested, and hence the computation time.

11.10 Timing

This project has not been particularly concerned with the amount of computation time required, save when it was large enough to severely delay the gathering of results. However, in any eventual implementation, this is an important item. In such a case, it would be desirable to have real-time processing, i.e. analysis of data in less time than taken to acquire a new set of voltages.

Most of the computing time is taken up with beamforming operations. The time required for this is proportional to the number of hydrophones, the number of shapes tested and the number of beams formed for each. One commonly timed situation involved formation of 56 beams at 2^o

separation using 16 elements; 49 shapes could be tested and compared in 6.0 seconds (to within 0.1 secs).

Note, some knowledge of the location of the source(s) could reduce the size of the angular sector scanned; coupled with a decrease in initial resolution to, say 3^o, this would reduce the number of beams needed (and thus the processing time) by half. More efficient coding and implementation of the vector preprocessor could lower the time taken for 49 shapes to 1.0 secs.

A more complicated question is the number of trial shapes really needed. Although as many as 4 Fourier terms might need to be evaluated, updating of array shape from that of a few seconds past should keep the total number of trial shapes down, probably to well below 40. Thus a calculation time of 1.0s may well be viable for the situation described above. However, note that a doubling of the number of elements effectively quadruples the processing time, as the limiting resolution would have to be halved. As an example, some work was done on an array of 128 elements — beamforming for one shape estimate took about 5 seconds; that to do 50 shapes (i.e. typical of a search routine) was 4 minutes.

12. LIST OF POWER FUNCTIONS TESTED

The quality of a particular beam pattern is to be characterized by a single figure, the maximization of which is hoped to correspond to retrieval of the correct array shape. Bucker[16] in his work used only $\int p^2 \cos\theta \, d\theta$, whilst Muller & Buffington[71] had investigated a variety of measures. Some of theirs were rather specific to their situation, assuming a circular aperture and the source to be at the centre. This project investigated a number of different estimators, here termed 'power functions', as they are generally summations of functions of the power over different directions. All the ones tested are listed below, although some were only briefly investigated, or intended as part of the definition of others.

$$\text{pf1} = \sum_{i=1}^{N} p_i \qquad \text{pf13} = \sum_{i=2}^{N} p_i p_{i-1}$$

$$\text{pf2} = \sum_{i=1}^{N} p_i \cos\theta_i \qquad \text{pf14} = \sum_{i=2}^{N} p_i p_{i-1} \cos\theta_i$$

$$\text{pf3} = \sum_{i=1}^{N} p_i^2 \qquad \text{pf15} = \sum_{i=2}^{N} p_i^2 p_{i-1}$$

$$\text{pf4} = \sum_{i=1}^{N} p_i^2 \cos\theta_i \qquad \text{pf16} = \sum_{i=2}^{N} p_i^2 p_{i-1} \cos\theta_i$$

$$\text{pf5} = \sum_{i=1}^{N} p_i^3 \qquad \text{pf17} = 2\ \text{pf3} + 1\ \text{pf13}$$

$$\text{pf6} = \sum_{i=1}^{N} p_i^3 \cos\theta_i \qquad \text{pf18} = 2\ \text{pf4} + 1\ \text{pf14}$$

$$\text{pf7} = \sum_{i=6}^{N-5} p_i (p_{i-5} + p_{i+5}) \qquad \text{pf19} = 1\ \text{pf5} + 1\ \text{pf15}$$

$$\text{pf8} = \text{Max}\{p_i\} \qquad \text{pf20} = 1\ \text{pf6} + 1\ \text{pf16}$$

$$\text{pf9} = \text{pf5} / \text{pf3} \qquad \text{pf21} = \sum_{i=4}^{N} p_i p_{i-3} \cos\theta_i$$

$$\text{pf10} = \text{pf6} / \text{pf4} \qquad \text{pf22} = 2\ \text{pf4} + 1\ \text{pf21}$$

$$\text{pf11} = \text{pf3} / \text{pf1} \qquad \text{pf23} = \text{pf14} / \text{pf2}$$

$$\text{pf12} = \text{pf4} / \text{pf2} \qquad \text{pf24} = \text{pf22} / \text{pf2}$$

where N is the number of beams formed, and p_i is the power perceived in direction θ_i.

Note, this is a full list of all those available for investigation. Usually, only a small number of these would be looked at — the most frequently adopted ones being nos. 4, 5, 6, and 8. Some parts of the work also concentrated on 12, 14, 15 & 16; and others compared different versions of the pf4 estimator, viz: 4, 12, 14, 18, 21, 22, 23 & 24.

Those which involve the product of the power at two different angles are referred to as 'correlation pfs'; numbers 17-20 are 'interpolation pfs' in that they are devised to approximate the behaviour of nos. 3-6 at higher angular resolution [see appendix 11].

13. INTERPOLATION OF DATA IN 2-D

13.1 Requirement when Plotting Contours

Facilities exist within the NAG Graphical Supplement and other libraries for the production of contour plots representing the variations of a function of two parameters; the data being supplied as the values of the function at the intersection points of a rectangular 2-D grid. The NAG routine used here, determines where a specific contour would cut this imagined 2-D mesh, by using simple linear interpolation between the known values at the intersections. The contour is then drawn by connecting these points with straight lines. This will work well for gently undulating surfaces if a large number of points is supplied e.g. 100 x 100, but here it is proposed to make do with far fewer points because of the computational time involved in the calculation of each value. [In the present context, the surface represents one of the 'power functions' under investigation — this corresponds to a weighted sum over all look directions, where the power response in each direction in turn involves the sum of the weighted phased (delayed) signals from each of the sensors.] It is hoped that an 11 x 11 array will contain sufficient information to display the behaviour of the power functions.

However, straightforward use of the aforementioned NAG routine would lead to very angular contours [see Fig 13.1], which would detract from the smooth variations expected for the surface. To overcome this, it is beneficial to increase the size of the grid artificially, by adding in interpolated values between those actually calculated.

The power function surface is expected to be smoothly varying, so as long as the original grid points are not too widely spaced, no extrema should be overlooked. [This can also be confirmed by displaying separately single sections of the surface with the extra points actually calculated.]

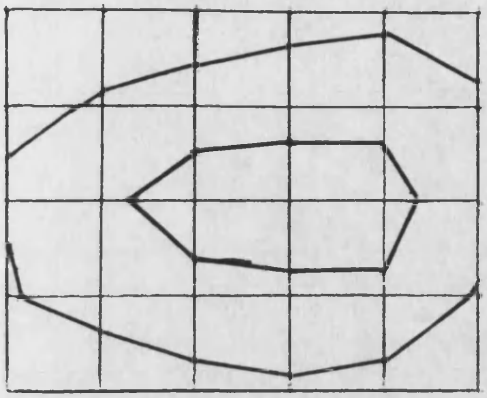

Fig 13.1

Angular Contour

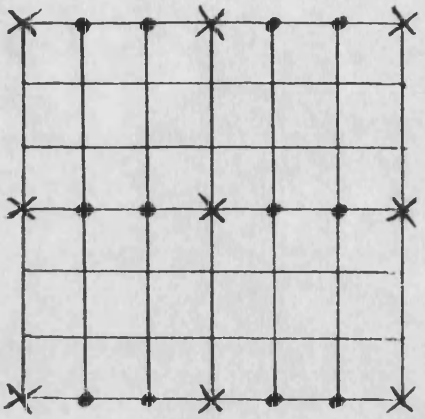

Fig 13.2

Interpolation Points

13.2 Interpolation Methods

There are three simple interpolation methods which can be easily invoked; these are briefly explained below:-

i) Linear Interpolation

Consider the surface to be represented by $f(i,j)$, where only the values for integral i,j are known. These points are symbolised by the crosses in Fig 13.2. Values at the extra points along the horizontal lines (represented by circles) may be derived from:-

$$f(i+\tfrac{1}{3},j) = f(i,j) + \tfrac{1}{3}[f(i+1,j)-f(i,j)]$$

$$= \tfrac{2}{3}f(i,j) + \tfrac{1}{3}f(i+1,j) \qquad \text{etc.} \qquad [13.1]$$

The procedure may then be repeated over the other index, j, to yield values for all the required points.

ii) Quadratic Interpolation

Using the three nearest known points, a quadratic curve may be fitted, and the value corresponding to the required point calculated. With the nomenclature introduced previously, this can be written as:-

$$f(i-\tfrac{1}{3},j) = \left[2f(i-1,j) + 8f(i,j) - f(i+1,j)\right] / 9 \qquad [13.2a]$$

$$f(i+\tfrac{1}{3},j) = \left[-f(i-1,j) + 8f(i,j) + 2f(i+1,j)\right] / 9 \qquad [13.2b]$$

A similar process is then applied to obtain values for non-integral j. Note, some other method such as linear interpolation may be needed for points just within the limits of the grid, or else the formula for points two thirds of a step from the central datum will have to be used.

iii) FFT Interpolation

There is a well-known method of fitting a smooth curve to a set of points that merely involves Fourier Transforming the data (actually with a Discrete Fourier Transform (DFT)), padding out extra high frequency terms with zeros and inverting the transform. This is easily extended to a grid of points on a surface — a 2-D FFT is performed, zeros added in the locations shown in Fig 13.3, and then an inverse 2-D FFT used to produce the desired smooth surface fitting the given points.

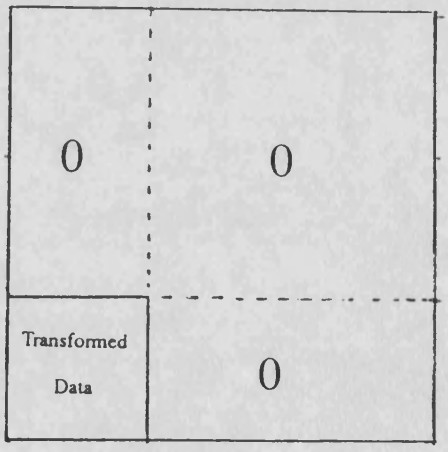

Fig 13.3 : Location of zero-padding in frequency domain

13.3 Comparison of Methods

All 3 methods involve simple extensions of procedures for 1-D interpolation — methods i) and ii) simply correspond to interpolation in one direction followed by interpolation in the other. It is to be noted that the values obtained are independent of which direction is first processed.

With the availability of ready-written Fourier routines, method iii) is actually the easiest to implement, although the computational complexity within the FFT calls is greater than in the other methods. The FFT method needs equi-spaced data points, although not necessarily a square grid of them. Such is not the case for the others; however, this does not confer an advantage, as the data will be supplied as a regular grid of values anyway.

The quadratic method has the disadvantage that extra care is needed for points near the edge of the grid. There is also a slight problem concerning the matching of interpolation intervals which may give neighbouring values the incorrect ascendancy over one another. The quadratic method is also more difficult to extend to 4-fold or 5-fold increase in the number of points.

Earlier investigations using the FFT method for the simple 1-D case have shown that problems arise if there is a mismatch in the values at each end of the supplied data set, as the actual DFT implementation assumes that the data interval corresponds to the repeating period of the function (like for a Fourier Series). In reacting to a large jump in value where the ends join up, oscillations may occur in the fitted curve, leading to spurious peaks.

Finally, if the true surface contains a high peak that sharply falls away to undulations just above zero, then the quadratic and FFT methods may possibly yield some points with negative values. This is not desirable here, as the power functions, due to their definition, are always positive. Linear fitting can not cause this problem. For this reason, and also to prevent unwarranted oscillations or mismatches, the linear method is the one chosen, although it does yield a more jagged match to the surface than the others.

[Note, negatives may be prevented from occurring in methods ii) and iii) by taking the logarithms of the data prior to the interpolation, as all resulting values in that domain will correspond to positive ones in the original. Addition of such a scheme, not only complicates the comprehension of the routine, but also affects the performance of the methods previously detailed e.g. linear fitting would now correspond to fitting exponential curves to the data.]

14. COMPARISON OF THE PERFORMANCE OF VARIOUS POWER FUNCTIONS OVER 2-D

The contour plots produced for each of the power functions indicates how each of these measures changes with various guesses at the array shape. In a more limited way, linear sections show similar behaviour, although, of course, only for variations in one unknown. The 1-D sections are often individually scaled so that the lowest and highest recorded delineate the extremes of the ordinate. Thus it should not be thought that the power function values shown actually descend to zero. Variations in value greater than a factor of 10 may occur for some measures over a suitably wide variety of shape estimates; however, in several cases fine details of the variation will be being examined, such that the range of estimates causes the measure to change by only a few percent.

Similar caution must be applied when analysing the contour plots. The plots have equi-spaced contours at 10, 15 or more levels (generally 15), exactly covering the full range of the supplied data. It may then be thought simple to compare power functions merely in terms of numbers of contours e.g. height of main peak relative to mean level or to other peaks, or steepness of slope in terms of how closely packed contours are. [Note, in this context steep slopes are not desired, rather a peak with broad slopes is preferred as this indicates its presence over a greater region of the plot, thus enabling gradient ascent methods to converge quickly from distant i.e. highly erroneous initial estimates.]

The inappropriateness of merely counting contours to register a power function's performance is easily seen by comparing a typical power function such as $\sum p_i^2$ [as defined in chapter 12], with its logarithm, $\ln | \sum p_i^2 |$. Naturally, they are equally suitable for use as a measure of shape fitting; however their apparent characteristics in terms of equi-spaced contours will be very different. This situation is analogous in many ways to the problem of characterizing the 'best' frequency/bearing estimator [chapter 8.8].

The more useful measures of a power functions performance can be seen to be:-

a) The mean error in peak position (i.e. any bias).

b) The rms error in peak position (i.e. standard deviation of estimate).

c) The percentage of occasions in which the highest peak is approximately correctly placed — high levels of noise may occasionally cause a subsidiary peak to exceed the 'main' one.

d) The distance in the vector space to the nearest saddle point of the surface — this is an indication of the limit of the region in which a gradient climbing routine would perform perfectly i.e. without any chance of ascending a subsidiary peak.

Note, in an analogous manner to beam patterns, there will be fixed subsidiary peaks (sidelobes) indicative of a repeating distance, and also some random ones, due to that particular realization of the noise field (both additive and multiplicative). The statistics of a power function surface, as detailed above, will vary with level of noise.

15. VARIATION OF DIRECTION OF MAXIMUM SIGNAL

15.1 Introduction

The beam pattern produced by the delay-sum-and-square method has a main lobe in the direction of the source, and subsidiary sidelobes of gradually diminishing level. The overall shape, and its dependence upon the shading of the elements, has been discussed more thoroughly earlier [chapter 4]. This chapter introduces the effect of hydrophone positional errors, showing how these affect the beamforming, and consequently the estimation of the location of the source. The array shape is described by a limited Fourier series [chapter 11.4] — here are described the effects of errors in each individual term.

15.2 Variations in First Coefficient

For a given true array shape, and consequent signal record, beamforming was performed for a multitude of other shapes, differing in the first term from the original by as much as 7.2m. [The wavelength used here is 6m, with the 16 sensors at half-wavelength separation.] The resultant beam patterns for some of the situations are given in Fig 15.1. Note, all the illustrations of beam patterns in the results sections of this report, are for angles between -90° and 90°, with the power axis covering a range of 30dB.

It can be seen that for small errors ($< \lambda/2$), the source direction corresponds to the highest lobe, but that for errors greater than this the adjoining sidelobes assume a larger value than the main one. As the beam pattern has remained symmetrical despite the large errors, the bearing of the source could still be deduced from the centre of symmetry of the pattern. However, if there were other sources present, or significant background noise, then the deformed response for the source would not be manifest, and thus the source 'lost'.

Table 15.1 details the approximate bearings of the 5 highest lobes for various trial shapes, along with a more accurate determination for the highest one.

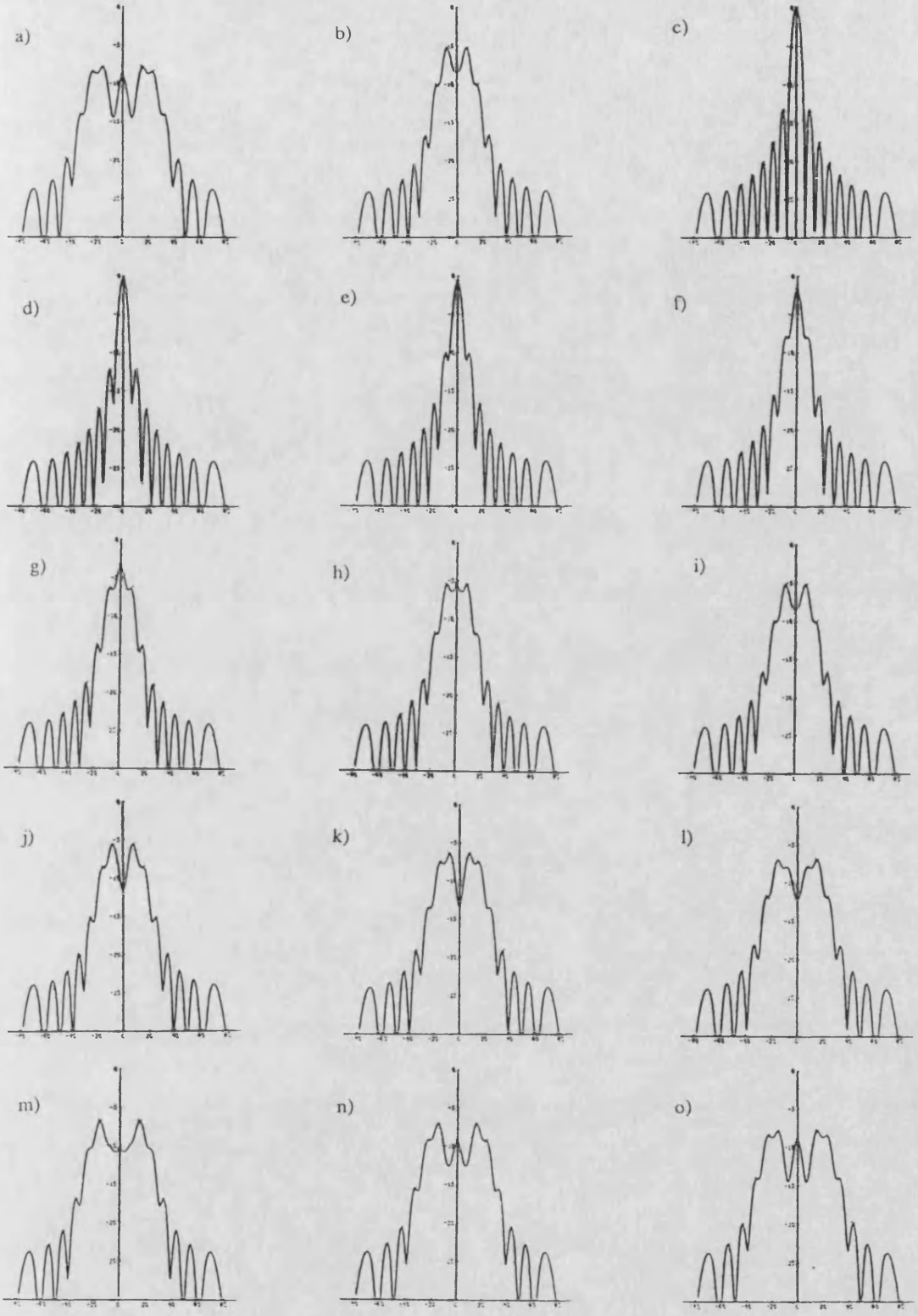

Fig 15.1 : Beam patterns for various erroneous estimates of the array shape.

From left → right and top → bottom, Δa_1 = -7.2m, -3.6m, 0.0m, 0.6m, 1.2m, 1.8m, 2.4m, 3.0m, 3.6m, 4.2m, 4.8m, 5.4m, 6.0m, 6.6m & 7.2m. [16 elements; source at broadside (0^o) and no noise]

Δa_1 / m	$\Delta a_1/\lambda$	Position of 5 highest peaks / degs					1st peak (to 0.001°)
-5.2	- 0.87	-15.0	15.0	-7.9	7.9	23.6	-15.059
-4.8	- 0.80	-7.7	7.7	-15.0	15.0	-24.1	-7.727
- 3.2	- 0.53	-7.7	7.7	0.0	16.2	-16.2	-7.673
- 2.8	- 0.47	0.0	-7.7	7.7	16.7	-16.7	-0.001
- 1.6	- 0.27	0.0	-8.7	8.7	17.7	-17.7	0.003
0.0	0.00	0.0	10.3	-10.3	-17.9	17.9	0.001
1.6	0.27	0.0	8.7	-8.7	17.7	-17.7	0.001
2.8	0.47	0.0	7.7	-7.7	16.7	-16.7	-0.001
3.2	0.53	7.7	-7.7	0.0	16.2	-16.2	7.672
4.8	0.80	7.7	-7.7	15.0	-15.0	24.1	7.726
5.2	0.87	15.0	-15.0	-7.9	7.9	23.6	15.023

Table 15.1 : Location of power lobes caused by beamforming with erroneous shape estimates.
[16 elements insonified by a broadside source (noise at -80dB) : beamforming over -90°, 90°.]

15.3 Second Coefficient

Here the second coefficient is characterized simply as the second Fourier term, $\sin 2\pi x/L$ [see chapter 11.4, equation 11.1] i.e. without removal of the straight line that fits the shape closest. The effect of changes in this coefficient are shown in Fig 15.2.

It will be noted that the beam pattern corresponding to an erroneous shape is no longer symmetrical about the true source direction. The direction of the highest peak shifts noticeably for small errors; this can be alleviated considerably by defining the basis function for the second coefficient to incorporate the removal of the 'best-fit' line, described in chapter 11.4 and calculated in appendix 7.

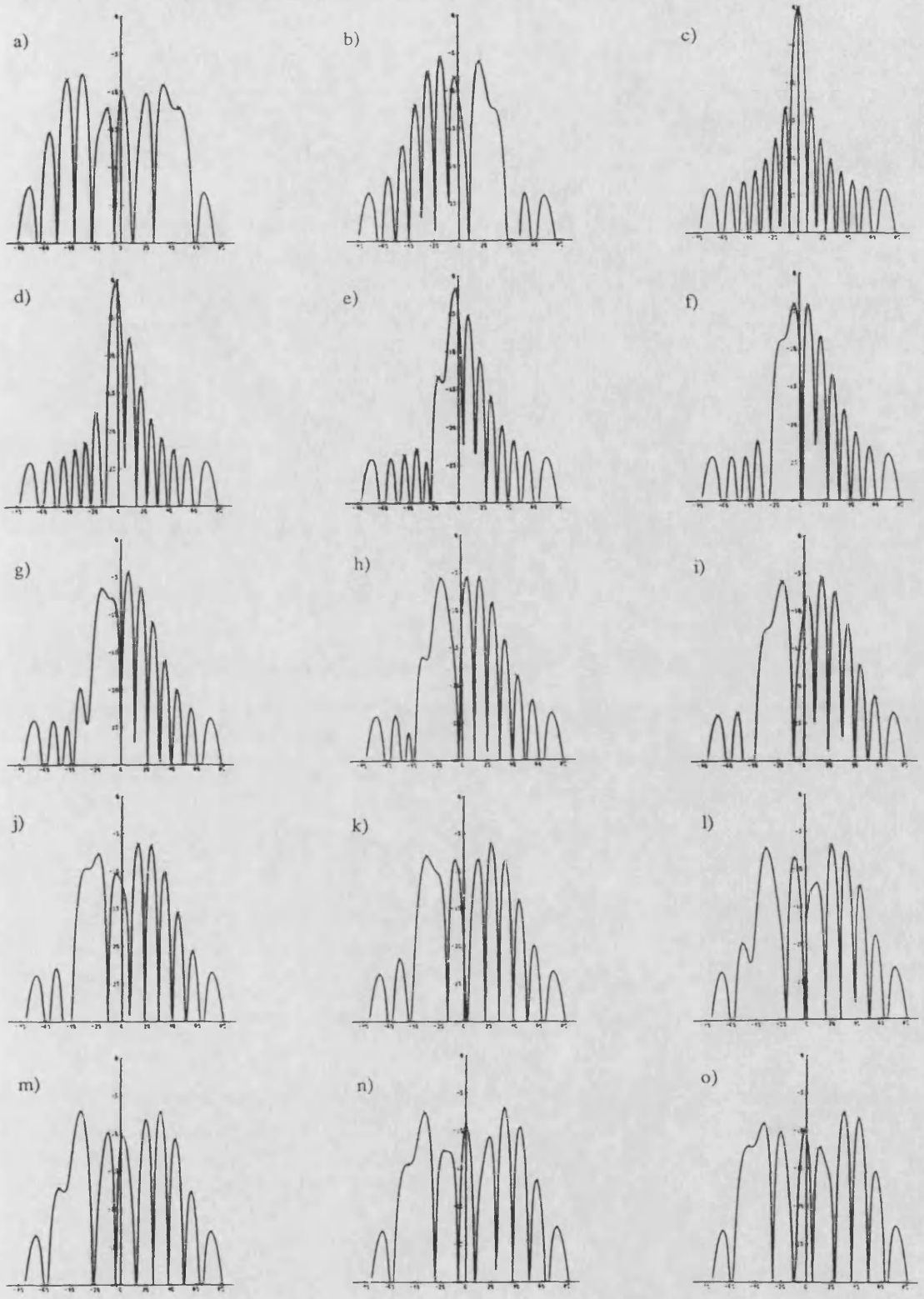

Fig 15.2 : Beam patterns for various erroneous estimates of the array shape.

From left → right and top → bottom, Δa_2 = -7.2m, -3.6m, 0.0m, 0.6m, 1.2m, 1.8m, 2.4m, 3.0m, 3.6m, 4.2m, 4.8m, 5.4m, 6.0m, 6.6m & 7.2m. [16 elements; source at broadside (0^o) and no noise]

15.4 Higher Coefficients

The manner in which the beam pattern alters for errors in the higher order terms is briefly illustrated in Figs 15.3, 15.4.

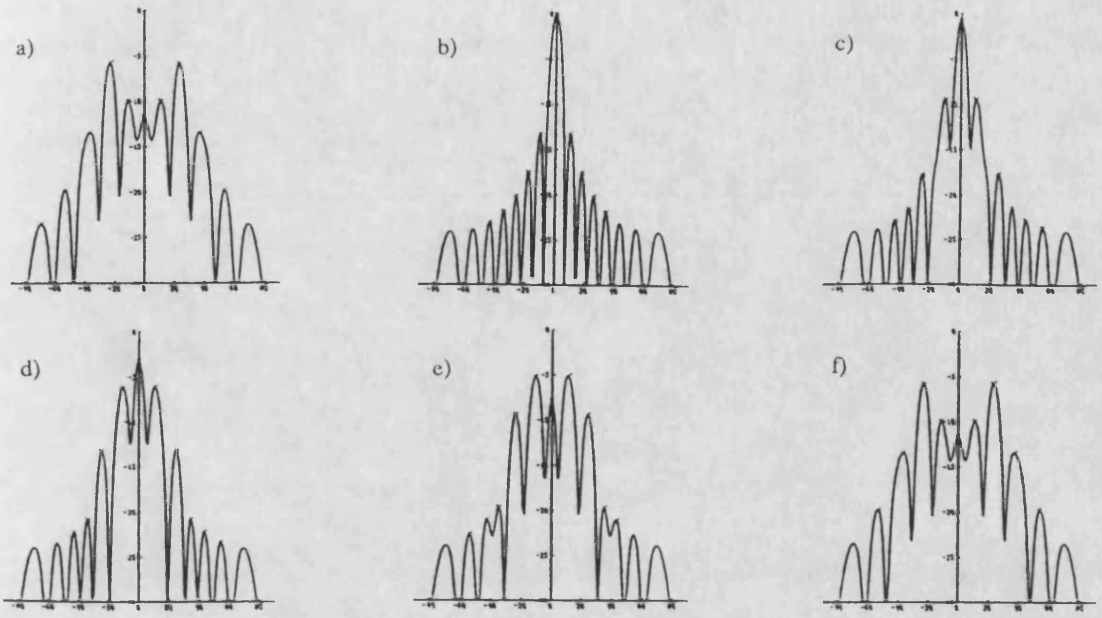

Fig 15.3 : Beam patterns for various erroneous estimates of the array shape.
From left → right and top → bottom, Δa_3 = -3.0m, 0.0m, 0.6m, 1.2m, 1.8m & 3.0m,
[16 elements; source at broadside (0^o) and no noise]

From the beam patterns already shown, it can be concluded that:-

i) Errors in odd Fourier terms still lead to symmetric displays, whilst those in even terms do not. This is explained in appendix 4 part I.

ii) An error of $-\Delta a_i$ will lead to the same degraded pattern as an error of Δa_i, but with reflection about the source direction. This is demonstrated mathematically in part II of appendix 4.

iii) Errors in the even terms lead to incorrect peak directions approximately consistent with the concept of the best fit straight line.

iv) For all Fourier terms, other than the first, the necessary error for the source to be lost is below 2.4m.

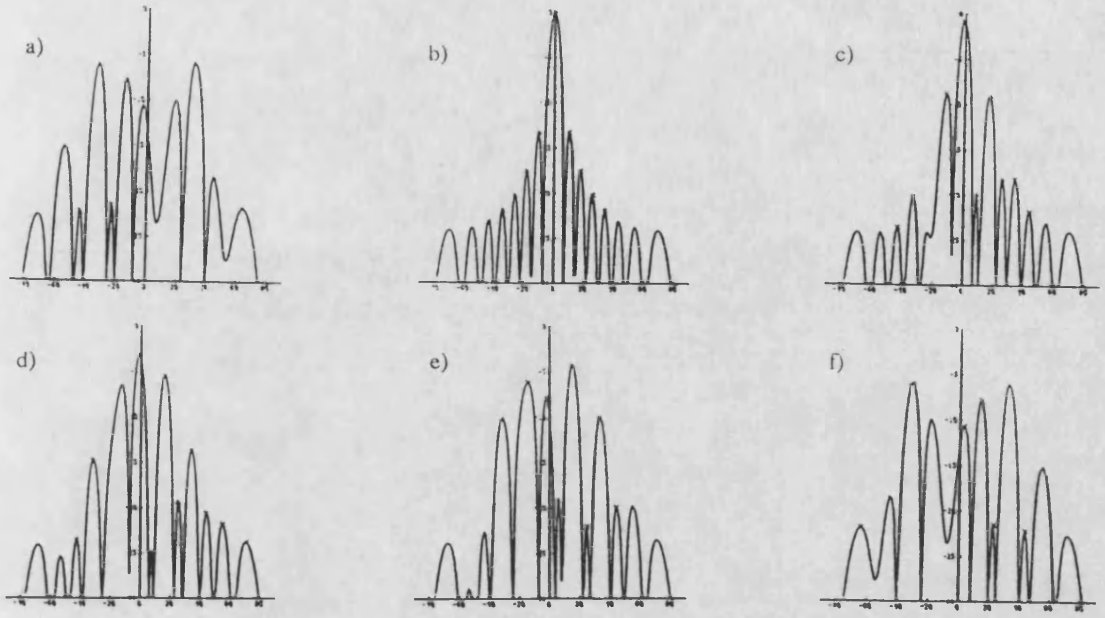

Fig 15.4 : Beam patterns for various erroneous estimates of the array shape.
From left → right and top → bottom, Δa_4 = -3.0m, 0.0m, 0.6m, 1.2m, 1.8m & 3.0m,
[16 elements; source at broadside (0^o) and no noise]

A more thorough investigation is summarised in Table 15.2 which gives the error in the main beam direction for various magnitudes of error, thus indicating how the pattern evolves with the misshapen nature of the array. In the table, 2^* and 4^* indicate searches using the 2nd and 4th Fourier terms respectively, but with the 'best line' removed.

15.5 Arrays of Different Size

The results already given are caused by the sensor location errors perpendicular to the array. Placing twice as many hydrophones along the same length of array, leads to minimal change in the values observed. Using twice as many hydrophones, but at the same spacing, thus doubling the array length, does cause some changes, but these are solely due to the increased array length. The effects are:-

Error in Shape		Fourier Coefficient						
Δa_i / m	$\Delta a_i / \lambda$	1	2	2*	3	4	4*	5
-1.0	-0.17	0	2021	- 262	- 1	989	- 149	- 1
:	:	:	:	:	:	:	:	:
0.0	0.00	0	2	0	0	0	0	1
0.2	0.03	1	- 400	61	1	- 190	40	1
0.4	0.07	- 2	- 793	117	- 1	- 380	75	- 2
0.6	0.10	1	- 1200	170	0	- 578	109	- 1
0.8	0.13	- 1	- 1607	219	- 1	- 779	132	2
1.0	0.17	2	- 2018	263	1	- 989	154	3
1.2	0.20	2	- 2450	290	1	- 1212	165	- 2
1.4	0.23	2	- 2892	306	0	- 1448	153	- 1
1.6	0.27	- 1	- 3368	290	11 degs	15 degs	17 degs	19 degs
1.8	0.30	- 2	- 3886	240	11 degs	15 degs	17 degs	19 degs
2.0	0.33	1	7 degs	12 degs	11 degs	15 degs	17 degs	19 degs

Table 15.2 : Error in primary lobe peak / 10^{-3} degs

[Figures for 16 element array at $\lambda / 2$ spacing.]

i) Sidelobes are located much nearer to main lobe; so, when the source is 'lost', the maximum peak becomes 6^o rather than 12^o, for example.

ii) The wandering of the main lobe for small errors in the even terms is only half that observed previously, simply because the deviation of the line of the array is halved.

Thus, it follows that the results given here for a 16 element array at half wavelength spacing may be applied to many other arrays; the important parameter being the ratio of the errors perpendicular to the array to the wavelength of the radiation.

15.6 Further Analysis of Maximum Tolerated Error

The first Fourier term, $\sin \pi x/L \quad [0 \le x \le L]$, represents a deviation from straight, with all the sensors shifted to one side of the local zero; thus the amplitude (i.e. the maximal disturbance) is a poor measure of the change for a general element. If the corresponding coefficient is a_1, the straight line that best fits the points (in a least mean square sense) is given by $y = 2a_1/\pi$. Denoting the rms deviation from this closest linear approximation by υ_1, it can be shown that:-

$$\upsilon_1 = \sqrt{1/2 - 4/\pi^2} \cdot a_1 \qquad [15.1]$$

The mean value for the third Fourier term is given by $\bar{y} = 2a_3/3\pi$, which is sufficiently small compared to a_3 that it may be approximated by zero. The rms deviation of a sinusoid from zero is given by the familiar $a_i/\sqrt{2}$, thus for all the coefficients of order greater than or equal to 3, the rms error is given by:-

$$\upsilon_i \approx \sqrt{1/2} \cdot a_i \qquad [15.2]$$

However, this can not be used as the value for the 2nd coefficient as $a_2 \sin 2\pi x/L$ is best approximated by a line of significant slope, $y = -a_2 (6/\pi L)(x - L/2)$, where L is the length of the array. The modified basis function generally invoked here involves the removal of that term i.e.

$$y = a_2 \left[\sin 2\pi x/L + (6/\pi L)(x - L/2) \right] \qquad [15.3]$$

A little calculus shows that the rms value of y for x in the interval [0, L] is given by:-

$$\upsilon_2 = \sqrt{1/2 - 3/\pi^2} \cdot a_2 \qquad [15.4]$$

Several simulations using 32 elements were done in order to be able to measure accurately the tolerance error for each basis function i.e. the maximum error in each term for which the mainlobe is just greater than all of the sidelobes. This is tabulated for the first 5 functions in Table 15.3, along with the relevant conversion figure, $\zeta_i \; (= \upsilon_i / a_i)$, and the corresponding rms error — the latter being expressed both in metres and wavelengths.

It can be seen that the maximum rms error tolerated, before the mainlobe is superseded by its subsidiaries is a sixth of a wavelength. This agrees with the comments by Steinberg[96] and others who state that the loss in array gain of *randomly* disturbed arrays becomes significant when the rms error exceeds $\lambda/10$.

Basis Function	Conversion Value, ζ_i	Amplitude Tolerance, Δa_i/m	Rms Error υ_i / m	Rms Error υ_i / λ
1	0.308	3.15	0.97	0.162
2	0.443	1.98	0.87	0.146
3	0.707	1.46	1.03	0.172
4	0.707	1.48	1.05	0.174
5	0.707	1.43	1.01	0.169

Table 15.3 : Comparison of the maximum tolerated errors for each of the basis functions.
[Answers derived from simulations using 32 elements, with λ = 6m.]

15.7 Dependence of Tolerance upon Weighting and Bearing

15.7.1 Effect of applying weighting to the elements

Searches over the first 4 Fourier coefficients were repeated using Hann weighting. As this shading scheme takes relatively less notice of the end elements than uniform does, it is found that errors for the first 2 Fourier terms of as much as 10m still leave the central peak as the highest. [Note, that if the few elements at either end are totally ignored (i.e. given zero weighting), this corresponds to a shorter array, with a smaller amplitude disturbance, so the 'improved' performance for Hann is not surprising.] Higher order coefficients correspond to basis functions which contain significant variation within the central portion, thus a weighting scheme that emphasises that area, loses the source for errors of similar magnitude to that for uniform weighting. For errors in a_1, when the sidelobes finally exceed the mainlobe level, the location of the false peak is only of the order of 5^o away from the source, rather than 8^o away, as occurred for uniform weighting under the same circumstances.

It should be noted that the modified basis functions labelled 2^* and 4^* no longer correctly compensate for the line of the array. The best fit line would have to be recalculated, by minimizing the mean square error as before, but this time with application of Hann weighting to emphasise some

of the points.

15.7.2 Dependence upon source bearing

As the conjugate variable to y_i in the Fourier notation is $k\cos\theta$, it may be expected that the errors in $k\,y_i\cos\theta$ term will be constant. Thus, for a fixed wavenumber, the tolerance to errors in y_i should be inversely proportional to $\cos\theta$ i.e. for sources at 0^o, 45^o and 60^o the errors should be in the ratio $1 : \sqrt{2} : 2$. This is approximately borne out in simulations — the necessary errors in Δa_i for the source to be just lost, had the relationship $1 : 1.5 : 2.2$; however, errors for the 60^o source were hard to determine, involving vastly misshapen arrays.

15.8 Effect of Added Noise upon Bearing Error

A few simulations were done with noise of the same level as the signal. The required errors in shape, Δa_i, to cause the source to be lost were noted. Often the value was far less for a positive(/negative) error than for the other, so both values were recorded. Note was also taken, of the location of the corresponding 'false' sources i.e. high sidelobes. Finally, the bearing of the peak of the beam pattern for processing with the true shape, and the maximum bearing error for true source location, were noted. [The former differed from 0^o due to the added noise; the latter due to noise and erroneous shape estimate.] A total of 20 simulations were done; half were tested over the first Fourier term and half over the second. The relevant averages are given in Table 15.4. It can be seen that noise only alters the main bearing slightly; its major effect being to cause the source to be lost within the sidelobes for a less misshapen array.

15.9 Summary

The results of this chapter have shown that for no added noise, reasonable errors in the sensor positions can be absorbed without causing erroneous bearing estimates, provided that the best-fit line of the true array and the estimate are parallel. With suitably chosen basis functions, errors in the even order terms need not cause bearing error either, although the choice for the basis function

Basis function label	1	2*
$\lvert \Delta a_i \rvert_{min}$ for loss / m	2.1	1.2
$\lvert \Delta a_i \rvert_{max}$ for loss / m	3.2	2.2
Bearing error for true shape / degs	0.5	1.0
Maximum bearing error in convergence area / degs	2.4	2.1
Location of false peak / degs	7.9	11.0

Table 15.4 : Statistics for a few realizations with added noise at 0dB SNR.
Function labels 1 and 2^* refer to first and modified second Fourier terms respectively; $\lvert \Delta a_i \rvert_{min}$ is the minimum deviation from true which may lose source, $\lvert \Delta a_i \rvert_{max}$ is the limit beyond which it is probably lost.

depends upon the weighting scheme used.

However, once the errors exceed a certain value (rms error $> \lambda/6$), sidelobes prove to be more significant than the main one. As the displacement in the direction of the source is the crucial indicator, measures of deviations perpendicular to the array indicate a limit proportional to $1/\cos\theta$. Again, results for different weightings appear more tolerant of shape errors; but, if expressed more appropriately as weighted rms errors, the results are the same.

Presence of additive noise of comparable level to the signal leads to bearing estimate errors of approximately 1^o for beamforming using the true shape. Beamforming using incorrect shapes can lead to errors of twice this magnitude. However, the most significant effect of the noise is to reduce the range of shapes for which the mainlobe level exceeds the sidelobe level. A more detailed investigation of the effect of added noise is given in chapter 20.

16. DEMONSTRATION OF APPLICATION OF POWER FUNCTIONS

16.1 Variation of pf4 over Bases

It has been simply stated that power functions were defined as a measure of the sharpness or quality of the beam pattern. Here it is shown that, in the absence of noise, most of the definitions of chapter 12 are maximized for the correct shape i.e. that the *ideal* beam pattern, corresponding to processing with the true array configuration, exhibits a greater spread of power values, than any beam pattern formed using erroneous position estimates.

Figs 16.1a-d show the value ascribed to pf4 (the 4th power function from the list in chapter 12) for the beam patterns illustrated in Figs 15.1-4.

16.2 Other Power Functions

The displays in Fig 16.1 are for pf4, but most of the other pfs (power functions) behave similarly. A comparison of several differently defined pfs is shown in Fig 16.2. [Note, for the first diagram, the true array shape is a straight line, characterized by all coefficients being zero; in the second case, a more complicated contortion is used, having non-zero values for the first 4 coefficients, the true value for a_1 being 5.

The majority are seen to behave like pf4; pf6, and others with cubic terms, show a faster fall-off rate than pf4, but still have only one peak and smooth changes in value. That which measures peak height alone, pf8, follows the same general form as pf4, but has many subsidiary peaks and sharp changes in its first derivative. The relevance of this is brought out in the chapters on convergence regions [chapters 27-29]. A few of the pfs are of no use alone — pf1 and pf2 produce little variation over the range of errors, with the peak generally not near the correct parameter value (Fig 16.2a is an exception, as the true shape is a straight array). Similarly pf21 can not be applied by

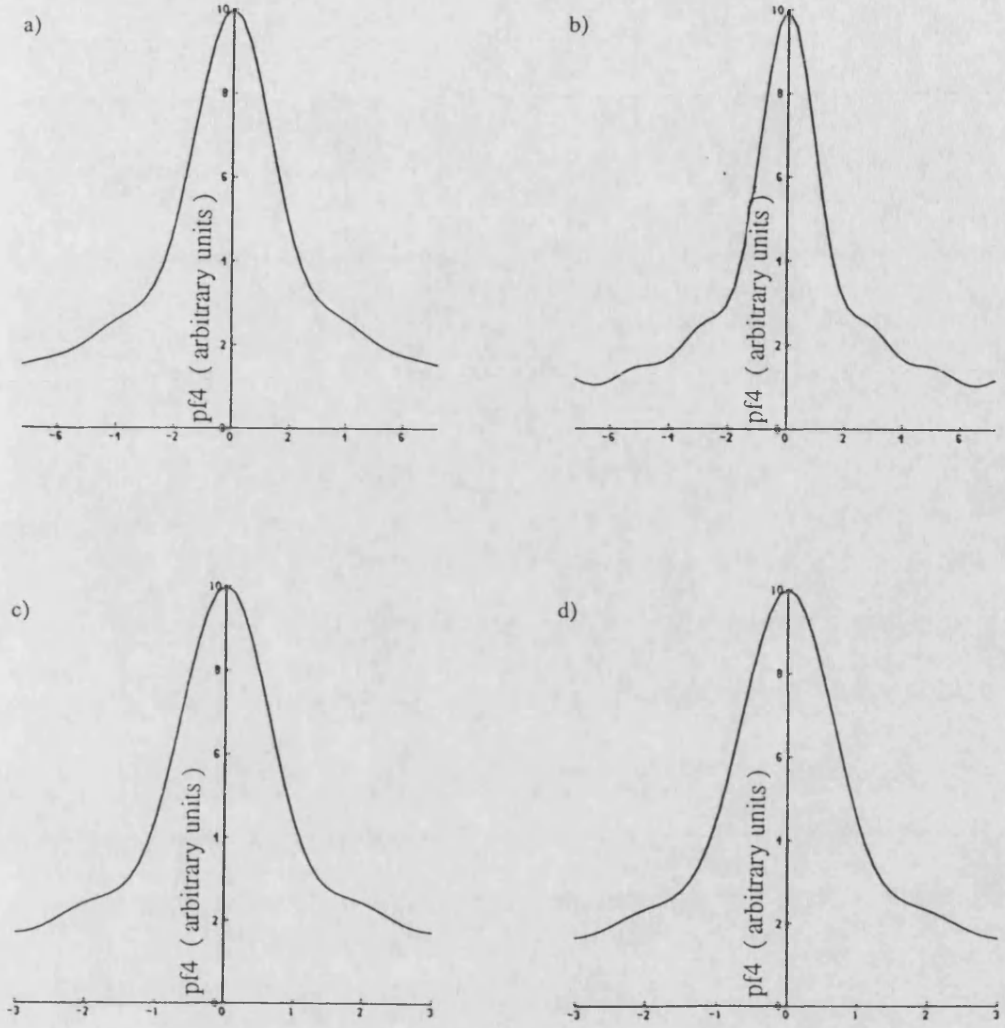

Fig 16.1 : Diagram to show variation of the sharpness measure, pf4,
for errors in the various Fourier coefficients. Error ranges correspond to those in Figs 15.1-4.
a) Error in first term : $-7.2\text{m} \leq \Delta a_1 \leq 7.2\text{m}$; b) Error in first term : $-7.2\text{m} \leq \Delta a_2 \leq 7.2\text{m}$;
c) Error in first term : $-3.0\text{m} \leq \Delta a_3 \leq 3.0\text{m}$; d) Error in first term : $-3.0\text{m} \leq \Delta a_4 \leq 3.0\text{m}$.

itself, as it has a definite local minimum at zero error. However the latter, in combination with pf4, produces pf22 [see chapter 12], which has a correctly placed peak with a slower fall-off than most others.

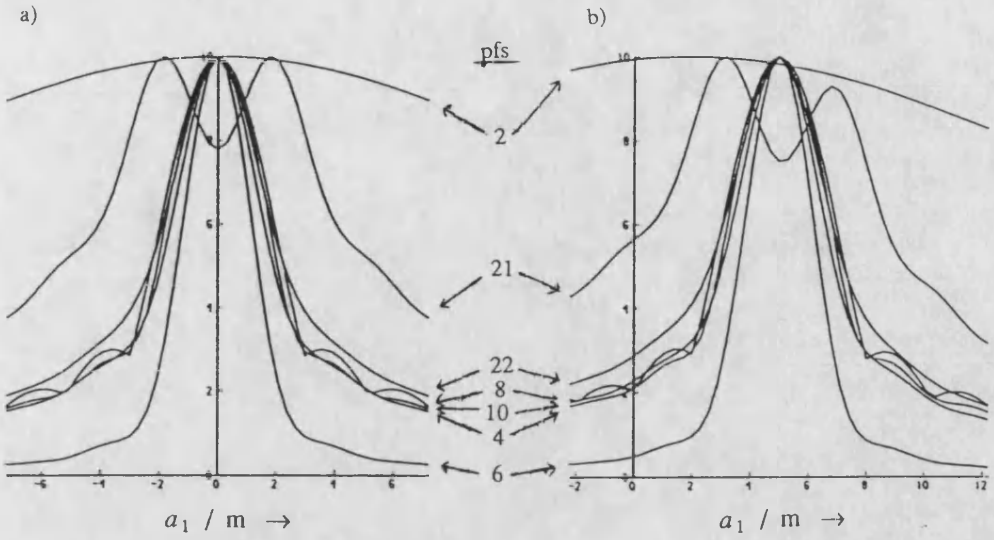

Fig 16.2 : Comparison of the variations in value of power functions over $-7.2\text{m} \leq \Delta a_1 \leq 7.2\text{m}$.

a) True value for a_1 is 0.0m ; b) True value for a_1 is 5.0m.

16.3 Effects of Noise

The preceding paragraphs have shown that in the ideal case, i.e. with no noise effects present, the true array shape is characterized by the maximum value of pf4. When additive noise is part of the simulation, the situation is somewhat different as shown in Fig 16.3.

The noise can be seen to have disrupted the position of the pf4 maximum, although only by a metre or so. In all cases, the pf value for large errors is much greater than occurs for no noise — in all of the realizations subsidiary peaks occur for errors of the order of 6m. In terms of assessing the accuracy with which power functions can aid shape restoration, it is the displacements of the main peak that matter, rather than the fall-off rate or the propinquity of subsidiary peaks. The remainder of this section of results [chapters 17-26] is thus concerned with the wandering of the pf maximum.

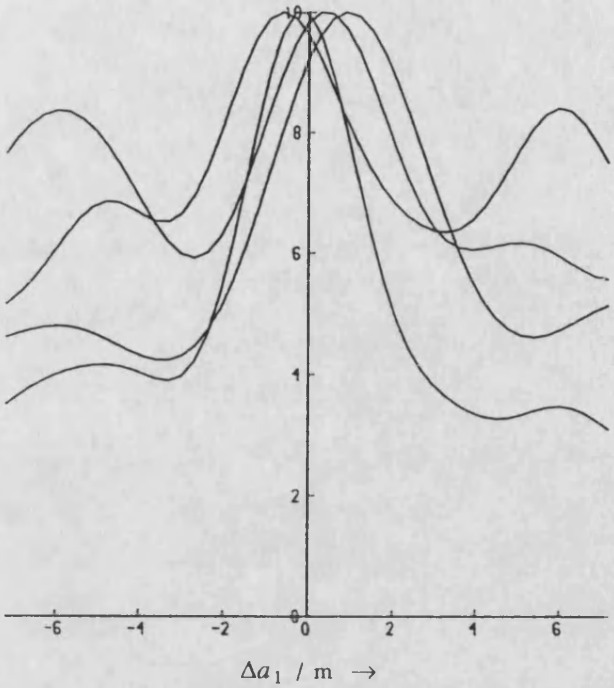

Fig 16.3 : Variations of pf4 with error in a_1, when high levels of noise are present.

[16 element array, with uncorrelated noise at 0dB per element.]

17. OBTAINING STATISTICS FOR COMPARISON OF POWER FUNCTIONS

17.1 Introduction

This project is concerned with the use of power functions to lead to approximately correct estimations of the array shape. The investigation of such can be divided into principally two different areas. One aspect is that of convergence from shapes far from true; this is dealt with later [chapter 27 and onwards]. The other important area of investigation is that concerned with small scale effects i.e. looking only at array shapes close to true, and examining the error associated with each of the power functions for the various different situations. The procedure for measuring these effects is detailed in chapter 11.7.

17.2 Distribution of Peaks

It is expected that the location of the power function peak will be approximately normally distributed about the true shape. To test this 1500 simulations were performed and the specific peak locations recorded. [The actual scenario used 16 elements at half-wavelength spacing, a single source at 10^o, and uncorrelated additive noise 20dB below that; searching was only over the first Fourier coefficient.] Results were logged for 4 different pfs (power functions) — these are tabulated below, along with their calculated means and standard deviations. Fig 17.1 compares each result graphically with a normal distribution with the same parameters.

Trial Shape No.	Frequency of Selection			
	pf4	pf5	pf6	pf8
-15	0	0	0	2
-14	0	3	2	3
-13	3	1	2	7
-12	2	11	11	12
-11	10	8	8	9
-10	6	10	10	9
-9	16	14	14	15
-8	17	20	20	25
-7	24	35	34	31
-6	54	38	40	46
-5	38	46	45	47
-4	63	60	60	62
-3	82	76	76	83
-2	106	109	109	84
-1	113	104	104	113
0	97	113	113	106
1	117	96	95	74
2	119	84	86	83
3	103	107	106	92
4	91	92	93	111
5	109	107	107	76
6	72	82	81	91
7	80	72	73	69
8	51	53	52	60
9	47	47	47	52
10	31	43	44	38
11	15	26	25	42
12	11	12	12	18
13	4	9	9	16
14	7	7	7	3
15	12	15	15	21
Mean	1.54	1.65	1.65	1.73
S.D.	5.05	5.40	5.39	5.76

Table 17.1 : Table to show the relative occurrence of various shape estimates and their means and standard deviations.

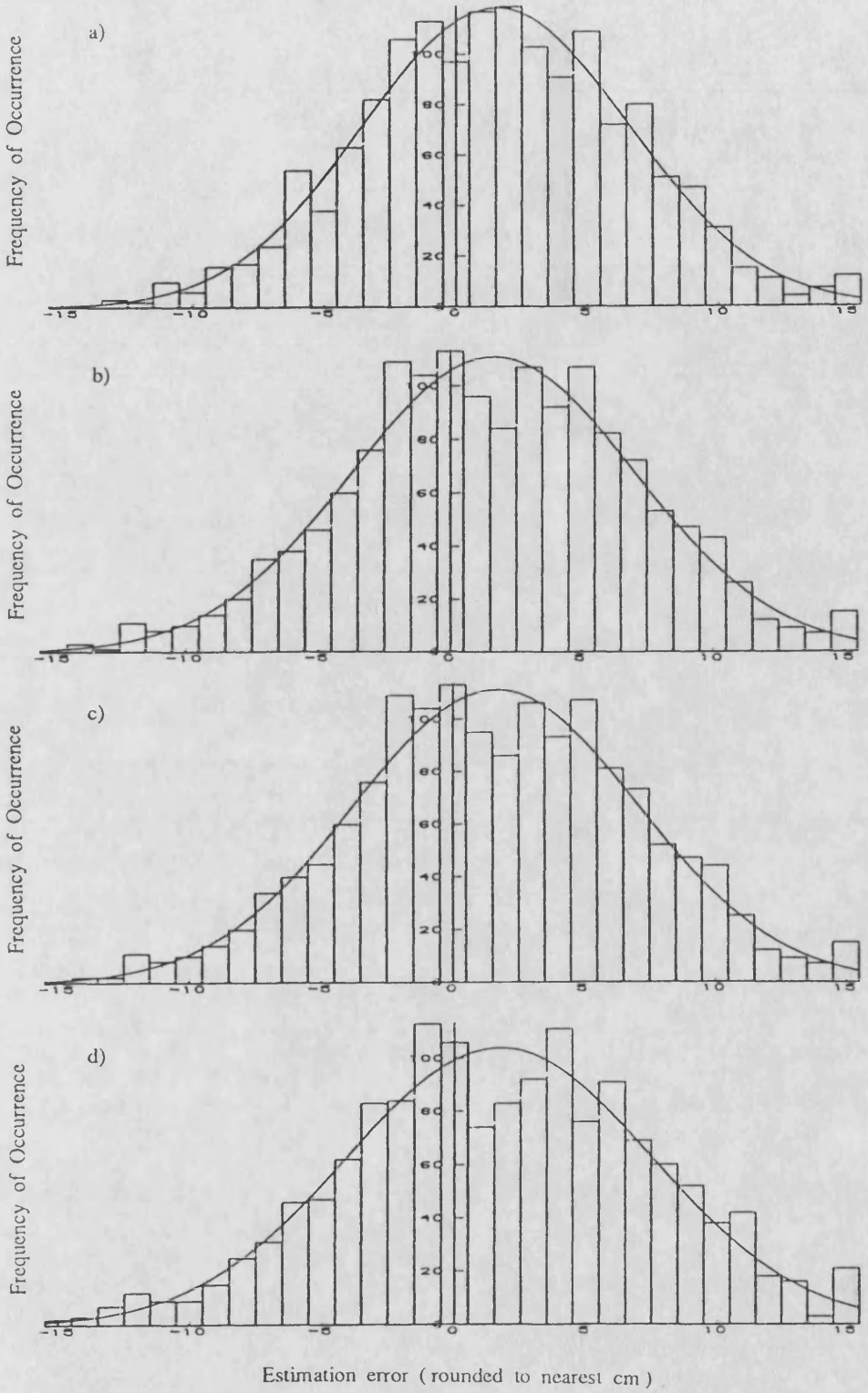

Fig 17.1 : Comparison of distribution of shape estimates with suitably scaled Gaussians. Results relate to 1500 simulations of a low noise scenario, and graphs are for power functions 4, 5, 6 & 8 respectively.

17.3 Statistical Significance

The results in Table 17.1 are not displayed in terms of actual physical dimensions because such is not relevant here. The accompanying graphs [Fig 17.1] shows how the scatter of measurements approximately fits a normal distribution. In all cases, the deviation of the mean from true (zero) is only a fraction of the standard deviation (s.d.) of the scatter, but it does show that the estimator is statistically biased, as can be seen from looking at the data for pf4. If the mean of the samples was zero, then the s.d. would be equal to the rms (root-mean-square) value of the data set, which is 5.28. The expected s.d. of the mean would then be $5.28 / \sqrt{1500} = 0.136$; the observed mean is thus 11.3 standard deviations away from zero, making the original assumption of a zero mean highly improbable.

It may thus be concluded that the estimator is biased in this particular situation; some measurements for different conditions repeat this observation, but usually the mean of the data is around a seventh to a twentieth of the s.d., rather than a quarter as here. A more thorough analysis of the statistics of samples from a normal distribution is given in appendix 13.

18. EFFECT OF PROCESSING CHOICE

18.1 Introduction

From the preceding chapter it can be seen that for a single scenario (set of parameters describing the simulation conditions) and a set shape estimation strategy (set of search values, weightings and power functions used to determine shape) there will be a range of estimates of the array shape. This has been shown to be approximately normally distributed, with a mean close to the true shape, although the difference may be significant on a statistical level. It is thus generally convenient to characterise the set of results for a specific scenario and strategy by the rms error associated with the estimates. In cases where the mean is of a similar order to the rms error, significant bias may be understood to exist and this will be noted.

In order to appreciate fully how the estimation error varies with different aspects of the scenario, it is instructive to determine first how much such a measure depends upon the type of processing applied. One of the most obvious variables in the processing is the selection of which power function [see chapter 12 for list] should be heeded. Examination of the spread of results in the simulation of the previous chapter shows that there is only a small difference between those illustrated. It is found that generally there is little to discriminate between the 'successful' ones. Measures such as $\int p \, d\theta$ and $\int p \cos\theta \, d\theta$ are 'unsuccessful' in that they fail to estimate the shape with anything like the accuracy of the others. This is not surprising, as both are measures of the integrated power over all angles i.e. the total power received, and thus would be expected to be constant. Estimators such as $-\int \ln | p | \, d\theta$ are of intermediate performance i.e. poor compared to those illustrated previously. A more detailed comparison of the 'successful' ones is given later [chapter 32].

For the majority of the ensuing chapters, a specific set of the power functions (nos. 4, 5, 6 & 8) will be investigated — in cases where only one is used this is likely to be the first of these. Thus the phrase *the power function* without a qualifying number will either refer to power functions in general or that of prime interest for now viz. pf4. This one is selected as 'the standard' on account of its simplicity in construction and generally agreeable behaviour.

18.2 Dependence Upon Processing Angles

It must be borne in mind that the power functions are not actually implemented as integrals, but as a finite sum of samples from θ_1 to θ_2 in steps of $\delta\theta$. It is useful to note whether the rms error depends much on the choices for these values.

Two specific situations are examined. Both have a single source plus uncorrelated additive noise 20dB below that and have the same true shape, characterized by the first 2 Fourier terms being 2.7 and -1.83, with the rest zero. This shape is illustrated in Fig 18.1 below. In the first case, the source is at 10.0°; in the second at 34.5°. One hundred realizations are made of each (differing due to the random noise) and recorded. These two sets are then processed for many choices of θ_1, θ_2 and $\delta\theta$, so that the differences appearing are due solely to the selection of processing parameters and not to different individual realizations. The results are presented in Tables 18.1 and 18.2.

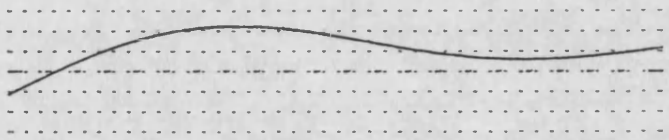

Fig 18.1 : Diagram of true array shape ($a_1 = 2.7$, $a_2 = -1.83$, other $a_i = 0.$)

[Dotted lines represent wavefronts at $\lambda/4$ separation.]

The first table [Table 18.1] shows a selection of different angular ranges, all with $\delta\theta \simeq 2°$, and the estimation error pertaining to each. In the second table [Table 18.2], a 180° sector [-90° to 90°], corresponding to one side of the array, is investigated at resolutions varying from 6° to 0.5°. Results are normalized w.r.t. (with respect to) those for 2° sampling over [-90°, 90°] to enable easy comparison of values. [The actual error variations for 'standard' processing are included at the bottom of Table 18.1; it can be seen that there are greater variations in the estimates of a_1 than a_2, and that a source oblique to the array, makes the processing slightly less sensitive to positional errors.]

Sector scanned		First Coefficient, a_1		Second Coefficient, a_2	
θ_1/degs	θ_2/degs	10° Source	34.5° Source	10° Source	34.5° Source
-180	180	1.017	1.485*	2.027*	1.261*
-120	120	1.008	1.002	1.000	1.060*
-90	90	1.000	1.000	1.000	1.000
-60	60	1.000	1.006	1.000	0.987
-45	45	1.000	1.025	0.996	1.199*
-30	30	1.000	##*	1.000	##*
-15	15	0.999	##*	1.112*	##*
0	180	1.042*	1.298*	1.868*	1.667*
0	90	1.006	1.003	0.994	0.994
0	60	1.006	1.006	0.996	0.990
0	45	1.006	1.022	0.996	1.197*
0	30	1.002	##*	0.997	##*
Absolute values for standard / cm		5.11	5.39	3.80	4.02

Table 18.1 : Table to show how rms error of the pf4 estimator depends upon search sector. For all cases $\delta\theta \approx 2°$, and scan is over first coefficient only. Results are normalized w.r.t. values for the *standard* [-90°, 90°]. * Indicates bias present ; ## Indicates errors greater than search range (±16cm) , so comparison not possible.

It should be borne in mind that there is a resolution limit to the experiment. For each of the 100 signal records, standard processing (-90° to 90°, in steps of 2°) selects one of the 41 closely similar shapes as its idea of the true one. For several of the changes in the angular sector searched and in the angular resolution, the power function selects exactly the same shapes for all 100 cases, hence a value of 1.000 for the relative merit. This does not mean that performance is exactly identical, but that the difference is at least very small. Sometimes a change in the angular parameters

Angular Resolution $\delta\theta$	First Coefficient, a_1		Second Coefficient, a_2	
	10^o Source	34.5^o Source	10^o Source	34.5^o Source
6^o	1.130	1.197*	2.514*	2.549*
4^o	1.004	0.999	1.001	0.995
3^o	1.000	1.000	0.997	1.002
2^o	1.000	1.000	1.000	1.000
1^o	1.005	0.998	0.996	1.002
0.5^o	1.007	1.001	0.996	1.001

Table 18.2 : Table to show how rms error of pf4 estimator depends upon resolution. For all cases search is over -90^o to 90^o, with scan over first coefficient only. Results are normalized w.r.t. values for $\delta\theta = 2^o$. * Indicates bias present

affects the shape chosen in 1-10 cases. Typically this results in a figure of relative merit ranging from 0.97 to 1.03 i.e. differing only by a few percent. Those figures differing by more than 3% may well show a real change in performance. This was observed to occur for angular sampling at 6^o (the beamwidth here for 16 elements is approximately 8^o) and also for searching over 0^o to 180^o and -180^o to 180^o.

For all the tables, an asterisk indicates situations where the mean was observed to be significantly biased i.e. its magnitude was greater than a third of the rms error. Biasing and/or increased rms error tended to occur when one of the edges of the interval was close to the source direction. This was observed for processing of the 10^o source using $[-15^o, 15^o]$ and for the 34.5^o source with $[0^o, 36^o]$ (data not shown). Note, further runs investigating other pfs than pf4 showed reasonable agreement with the above statements. However, it was found that pf8 was usually more sensitive to sources near the end of the search interval. The other major cases of biasing, involving searches over both sides of the array, were found to be much less for pf5, pf6 and pf8 than for pf4. Consequently, the rms error for pfs 5, 6 & 8 in these cases was significantly less than for pf4. With the pf8 estimator (i.e peak height of beam pattern), there was increased error and bias at 4^o resolution for the 34.5^o source, and at 3^o for both sources. This was due to none of the pre-selected beams

being sufficiently close to the true source direction for pf4 to be fully sensitive to the power from that direction.

18.3 Power Functions with Interpolation

With 6^o beam sampling, the accuracy associated with power functions decreases from what was attainable for 2^o — this is because the samples no longer adequately represent the detail of the beam patterns. To overcome this, an approximation to the beam patterns may be constructed by linear interpolation between the sampled points. Power functions such as $\int p^2 d\theta$ can then be calculated over a continuous range of θ. Appendix 11 shows how a pf may be created that achieves this quickly without explicit interpolation for all the intermediate points. The interpolation variants of pf3, pf4, pf5 and pf6 were implemented as pf17, pf18, pf19 and pf20 respectively [see chapter 12]. Testing on the output of the 6^o processor showed pf4 to exhibit slightly increased variance for a_1 estimation, and considerably greater for a_2. However, the interpolation power function pf18, was found to overcome this problem, having minimal change in estimation error, and no biasing. The pfs containing the correlation terms alone showed variations similar to pf4.

It is unlikely, however, that any approach akin to power functions will work well for sampling less frequently than 6^o, as the beamwidth ($\approx 8^o$ here) provides a real physical limit.

18.4 Shape Inversion

It can be seen that the signal record received for one situation is exactly identical to that which would be received for the mirror image case i.e. with both the shape inverted and the source(s) on the opposite side of the array. Naturally, if power functions are evaluated over a full 360^o, the values for the two situations will be identical. This may affect certain shape estimation techniques, if the true shape is close to a straight line, with a wide range search for coefficient to be estimated. For example, consider an array shape specified by a_1=3. with the other terms zero, and with scanning for the first coefficient over ±6m. An algorithm utilizing beamforming over all angles will show the power function to have two distinct peaks at ±3m [see Fig 18.2a], one corresponding to the true shape

and one to its inverse (and consequently with the perceived source on the wrong side of the array). However, if beamforming is constrained to one side of the array (i.e. [-90°, 90°], the false peak is not encountered [Fig 18.2b].

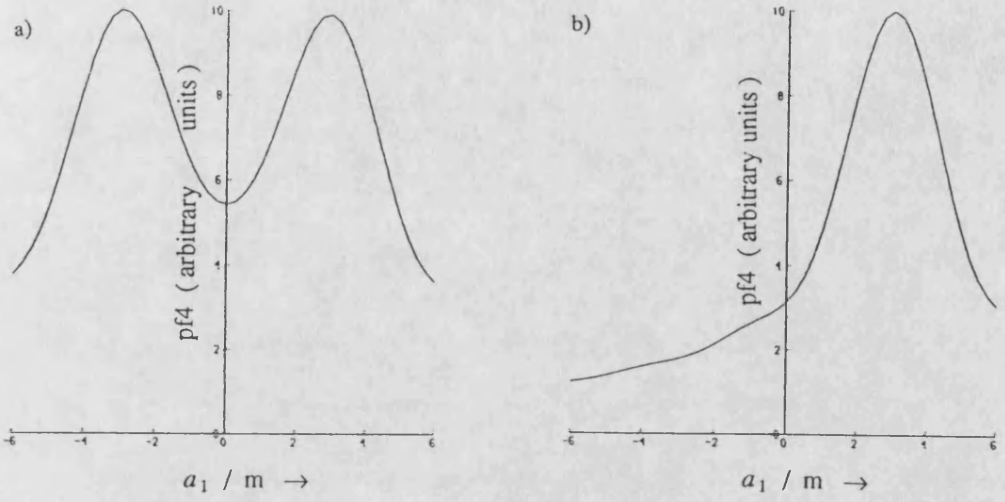

Fig 18.2 : Plots of power function variations as a function of estimated coefficient, a_1.
Search range for a_1 is -6m to 6m with the true value being 3.0m — correct values (all zero) used for other coefficients. Both graphs are for pf4 with processing for a) over [-180°, 180°] and for b) over [-90°, 90°]

In the situation described two exactly opposite situations were covered in the search; however, if one of the other terms has been determined as a non-zero value, and is kept constant during the search, then the reflected shape will not be investigated. Such a situation is shown in Figs 18.3a, where the true value of a_3 is now 0.8m, and has been correctly determined prior to the search over a_1.

Note, for the 360° processing, the value of the power function for a_1=-3 (an error Δa_1 of-6m) is the same as would be calculated for the inverse shape with $(a_1, a_3) = (+3., -0.8)$ (i.e. an error Δa_3 of -1.6m). Thus the estimator continues to show a peak for a_1=-3 (albeit weaker than for a_1=3) as it is close to a 'version' of the true shape.

Fig 18.3b once again shows that knowledge of which side of the array the source is on, not only reduces processing time by a half, but also prevents power functions converging to a subsidiary peak, not close to the true one.

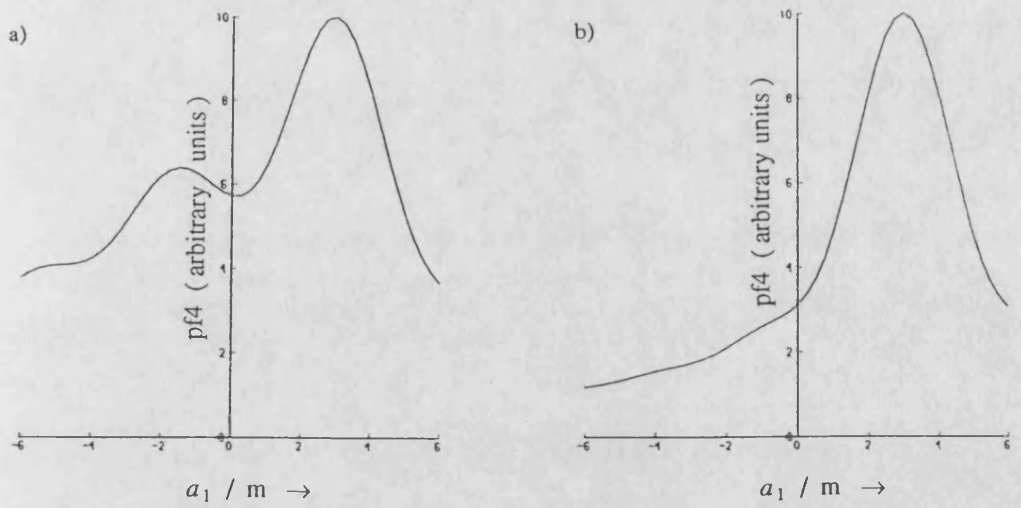

Fig 18.3 : Plots of power function variations as a function of estimated coefficient, a_1.
Search range for a_1 is -6m to 6m with the true value being 3.0m — correct values (all zero, except a_3=0.8) used for other coefficients. Both graphs are for pf4 with processing for a) over [-180°, 180°] and for b) over [-90°, 90°]

18.5 Relative Source/Beam Alignment

A more detailed investigation was completed for the choice of 6° resolution to show how the performance of the estimators varies with the position of the source relative to the beams. An initial test was done with scanning over [-42°, 42°] for sources at 0°, 1°, 2°, ... However, the estimates showed considerable variation simply due to the random nature of each 100 or so realizations, as explained in appendix 13. This cause was clearly demonstrated by the difference between estimates for sources at 0° and 6°. In order to remove this difficulty, a single set of realizations was recorded and the directions of the beams altered slightly between passes to produce the required variation in alignment of the source. The ith sequence of beamforming ($i = 0$ to 12) was performed over $[-42° + \delta\theta, 42° + \delta\theta]$ in steps of 6°, where $\delta\theta$ was chosen to be $0.6i°$. Only one specific set of noise realizations was used, and thus the 1st and 11th rms estimates (a shift difference of 6°) should be almost the same.

A source of SNR=10dB was simulated at 0° i.e. directly broadside, and a total of 300 realizations produced. Scanning was performed independently over the first and second Fourier

coefficients and the statistics for pf4 and pf8 monitored. These two were chosen as the former has an integral form, whilst the latter reflects the power level in the peak and thus may be expected to behave differently. The results observed are given in Table 18.3.

Beam Shift,	1st Fourier term		2nd Fourier term	
$\delta\theta$ / degs	pf4	pf8	pf4	pf8
0.	1.000	1.000	1.000	1.000
0.6	1.014	1.016	1.802*	1.653*
1.2	1.053	1.069	2.855*	2.704*
1.8	1.074	1.173	3.43*	3.64*
2.4	1.055	1.377	2.79*	4.19*
3.0	1.021	1.683	1.134	4.25
3.6	1.054	1.359	2.66*	4.25*
4.2	1.062	1.165	3.28*	3.65*
4.8	1.037	1.062	2.67*	2.69*
5.4	1.008	1.015	1.61*	1.63*
6.0	1.001	1.001	1.002	1.004
6.6	1.017	1.015	1.803*	1.652*
7.2	1.054	1.068	2.858*	2.702*

Table 18.3 Comparison of the rms errors for different source/beam alignments.
Single source at 0^o with SNR=10dB. Scanning over $[-42^o + \delta\theta, 42^o + \delta\theta]$ in steps of 6^o with various values for the shift, $\delta\theta$. Note $\delta\theta = 0^o$ directs a beam at the source; all figures are relative to this one. 300 simulations used. * Indicates bias has occurred.

18.6 Observations on the Effects of Misalignment

As a shift of the 6° beam fan by 6.0° would leave it unaltered (except for loss of -42° beam and appearance of 48° one), the performance of the shape estimators should remain unchanged too. This is clearly shown in the results — the very slight differences being due to the very occasional effect of the extra beam at 48° instead of -42°, and to the limited accuracy of numbers in the computer, causing the beams to be shifted by 6.000001°. From the symmetrical nature of the situation, it would be anticipated that errors for main beam, say 1.8°, to the right of source should be the same as for the main beam 1.8° to the left. This too is represented in the results — the greater differences here being due to this only being true for the *expected* level of error, not for each individual realization (as was the case for the 6.0° shift).

For estimates of the first Fourier term, pf4 (and indeed other integral pfs) showed little change in performance as the fan was gradually moved. However, pf8, which solely records the peak value, became significantly less accurate as the beams moved away from the peak of the mainlobe.

Investigation of the second Fourier term showed all power functions being dependent upon the alignment of the beams relative to the source. In this case, the degradation was more severe, pf8 still being the most susceptible. It is interesting to note that pf4 showed near-optimum performance for the source dead between beams (3° shift), whereas this marked the poorest performance for pf8. Also, the estimators usually showed extreme bias in their shape determination; for shifts $0.6° - 2.4°$, the array was estimated to be straighter than it really was, whilst for $3.6° - 5.4°$ the bias was the other way. This held for all the estimators.

A further pair of runs was performed on the stored 300 realizations. Both used the angular scan range [-40°, 44°] with a step of 6°, and both were investigations of the the second Fourier term. The difference between them was that one used the 2nd basis function as generally invoked in this project i.e. with the best fit line to the sinusoid subtracted out to leave a shape variation that maintains a constant direction for the mainbeam [see Table 15.2], whilst the other was just the simple Fourier term. The inconstancy of the mainbeam direction in the latter case, meant that various erroneous shapes might line the source direction up with a fan beam far better than the true shape would, and consequently an estimator using that characterization of the array shape had far greater errors in its estimates. For the case referred to, the rms error was nearly 5 times the magnitude of that achieved using the modified basis function.

It can be seen that although a simple investigation showed only slightly increased errors for a resolution of 6^o, there are many cases in which the processing is sensitive to the relative direction of the source with respect to the beams. Of course, the bearing of the source is not generally known beforehand.

18.7 Summary

No noticeable benefit in performance can be gained by changing the search range or resolution from that selected as 'standard' for an array of length 8λ, i.e. $[-90^o, 90^o]$ in steps of 2^o ; however, decreasing the resolution (i.e. increasing the value for $\delta\theta$) may lead to significant loss in performance once $\delta\theta$ is of the order of half a beamwidth or more. Results tend to show that much processing time would be saved without performance degradation if beamforming could be restricted to within 20^o of the source direction, using 2^o or 3^o resolution. Note, such may not necessarily be the case for shapes far from true when the bearing of the primary source is undetermined or when several similar strength sources are present. Clearly, it is to be expected that the source direction need be in the search sector; this is a fact generally borne out by the cases where the 34.5^o source was outside the scan, resulting in errors a magnitude greater at least.

19. EFFECT OF CHOICE OF WEIGHTING FUNCTION

19.1 Introduction

Different shadings of the array are sometimes used in order to accentuate various facets of the beam pattern. Dolph-Chebyshev is often used when low sidelobes are required; uniform weighting is generally more appropriate when high levels of noise are present. [These and other observations are made in greater detail in chapter 4.4.] It might, in some cases, be worthwhile to perform all the beamforming for shape estimation with one weighting, whilst applying another to extract details for the array configuration finally selected. Below is introduced the concept of an 'array factor' — a single figure which is often useful as a characteristic of the effect of a specific set of weights. This is then followed by results derived from many simulations, using different shading patterns for the array elements.

19.2 The Array Factor

A useful characteristic figure for a set of weights is provided by the array factor which is defined as follows:-

$$F_n = n \cdot \sum w_i^2 \; / \; \left(\sum w_i\right)^2 \qquad [19.1]$$

This definition is similar to that occurring in rigorous calculations of the effects of amplitude and phase errors, and also of element failure (see Ramsdale & Howerton[82] and Quazi[81] respectively). Note, from the above definition it follows that:-

i) F_n depends only on the values of w_i used, not on their order of occurrence — thus an array with its largest weightings at the periphery may have the same array factor as one shaded more conventionally, with the emphasis on the central elements.

ii) For a given number of elements, the factor is minimized for uniform weighting; other generally used weightings produce a value only 20-50% greater.

iii) *Ideally*, any chosen weighting scheme will produce the same factor, independent of n.

The above factor has been introduced as it is believed likely that the positional errors associated with the power function estimates may show a similar dependence on the choice of weighting to that found for phase and amplitude errors. Five different sets of shading have been used; these are detailed in chapter 11.6. Table 19.1 lists the array factors for each. The first figure given, F_{∞}, corresponds to that calculated by representing the weights by a continuous filter and performing integrations where necessary; this would be the value achieved in the limit for a very large array. As the specific implementation used in this program may differ slightly from the standard for a finite set (e.g. zero-points for Bartlett weighting are at $i=0$ and $i=n+1$ here), the array factor is explicitly evaluated for 16 and 256 elements, producing the statistics F_{16} and F_{256}.

Weighting	F_{∞}	F_{16}	F_{256}
Uniform	1.000	1.000	1.000
Half-Cosine	1.234	1.168	1.229
Hann	1.500	1.412	1.494
Hamming	1.363	1.427	1.367
Bartlett	1.333	1.259	1.328

Table 19.1 Array factor calculated for different weightings

19.3 Results of Simulation

Two sets of 100 realizations were performed for a 16 element array, using the sources, background noise and array shape referred to in chapter 18.2. Independent searches were performed over the first two Fourier components for each weighting in turn. The standard deviations of the estimates are summarised in Tables 19.2 and 19.3 below.

Weighting System	Source at 10.0°		Source at 34.5°	
	1st term	2nd term	1st term	2nd term
Uniform	1.000	1.000	1.000	1.000
Half-Cosine	1.158	1.077	1.113	1.283*
Hann	1.543	1.535*	1.432	2.748*
Hamming	1.446	1.393*	1.336	2.403*
Bartlett	1.245	1.139*	1.181	1.504*

Table 19.2 Shape estimation error by pf4 for different weightings

[Averaged over 100 realizations, and normalized with respect to that for uniform weighting.]

* Indicates bias has occurred

19.4 Summary of Effects of Weighting

As can be seen from the above, uniform weighting leads to the least error, although the difference is often not very large. The rms estimation error is greatest for those weightings with the largest array factor. Bartlett and Half-Cosine perform well, producing errors only about 10% greater than those for uniform. However, the relative errors for Hann and Hamming weightings are not in the order predicted by their F_{16} array factors. The results asterisked correspond to situations where the magnitude of the mean was more than a quarter of the rms value — in some cases it was as much as 80%. It will be noted that severe bias does not occur for searches over the first Fourier coefficient, and that they are less common for uniform and Half-Cosine weighting than for the others.

Weighting System	Source at 10.0°		Source at 34.5°	
	1st term	2nd term	1st term	2nd term
Uniform	1.000	1.000	1.000	1.000*
Half-Cosine	1.082	1.100	1.042	1.760*
Hann	1.352	1.217	1.271	2.415*
Hamming	1.205	1.154	1.169	2.182*
Bartlett	1.115	1.111	1.075	1.908*

Table 19.3 Shape estimation error by pf8 for different weightings

[Averaged over 100 realizations, and normalized with respect to that for uniform weighting.]

* Indicates bias has occurred

19.5 Element Failure

A similar effect should be observed due to element failure. If there are 16 elements equally weighted, but one has failed, providing no signal, then it is just as though its weighting was set to zero. Consequently, the effective array factor would be 16/15 = 1.067.

A routine can be invoked in the program to simulate random element failure. It may be set to attribute a possibility of 1/16 for the failure of each individual element. [This is slightly different to an expected single failure on an element chosen at random, but should be approximately the same.] The two sets of 100 realizations were processed to yield records with an element failure probability of 1/16, and then the shape determined as before. This was then repeated for probabilities of 2/16, 3/16 and 4/16 — the results are summarised below in Table 19.4.

The results in the table show fairly reasonable agreement with expectations — however, in one case, element failure seems to improve the accuracy of the estimator! The results given are for pf4, but similar behaviour was observed for other power functions; however, for many pfs, one of the scenarios led to smaller errors with 3 failures (on average) than for 2. Possibly, slightly more consistent results might have been produced by constraining the failure routine to produce exactly one dud element instead of an average of one etc.

Probability of Failure	Effective Array Factor	10° Source		34.5° Source	
		1st term	2nd term	1st term	2nd term
0/16	1.000	1.000	1.000	1.000	1.000
1/16	1.067	1.052	1.020	1.092	1.034
2/16	1.143	1.076	0.934	1.125	1.132
3/16	1.231	1.129	1.101	1.128	1.306
4/16	1.333	1.201	1.556	1.316	1.415

Table 19.4 : Further investigation of array factor.
A comparison of the shape estimation errors occurring due to element failure; each independently normalized with respect to the value for the failure-free result for that case.

19.6 Summary

Note, in this chapter it is not implied that the figure for relative performance is expected to be identical to the array factor, merely that the values should be in the same order — there may be a square root or logarithmic relation. The results for various weightings fit fairly well with expectations, although those for Hann and Hamming are not in the order predicted by their F_{16} values. For the case of element failures, an expected order of merit is much more obvious. Although, the figures in the table reflect the correct order for most cases, the actual range of values for a particular failure rate is large considering that 100 realizations were averaged. Consequently, it is difficult to fully compare shadings and element failure via their effective array factors. Clearly, averaging over a greater number of realizations could improve matters, although considerable computation time would then be incurred. It had been hoped that using a single set of signal data would reduce the effect of random fluctuations, making it possible to discern accurately small performance differences with only, say 100, different realizations.

20. LEVELS OF ADDITIVE NOISE

20.1 Introduction

All the above discussion has been concerned with testing the stability of the power function estimates to various changes in the processing parameters. The signal was of amplitude 100., and the noise of rms value 10. — an amplitude ratio of 10., corresponding to a signal to noise ratio (SNR) on input of 20dB. With perfect processing using 16 elements, a gain of $10\log_{10}16 = 12$dB is achieved, yielding an output SNR of 32dB. The SNR for various other amplitude ratios is given in Table 20.1. The value of 20dB referred to earlier is of intermediate value — it is far less than that required by some of the specialist high resolution signal processing techniques discussed in the literature survey, but is also considerably greater than that realistically likely to be encountered in the situations for which this work is intended. Typical input SNR values for sources (other than 'co-operative' ones i.e. calibratory beacons) are 0dB or less; this is because they may be quite distant, and are endeavouring to travel as quietly as possible.

Below is an investigation of how the rms error in shape estimate depends upon the level of the additive noise.

20.2 Observed Dependence upon Noise Level

The set of results given here relate to one of the standard scenarios specified earlier [chapter 18.2] — the only change being the level of additive noise used. [The search range must be simultaneously updated to prevent the actual peaks of the power functions from straying outside of the range of shapes investigated.] The results tabulated below are now absolute, rather than relative as before; it is helpful to bear in mind that the array length is 48m and that the wavelength of the radiation is 6m.

All four sets of results are broadly similar. Note, the number of digits given in the columns does not reflect the true accuracy of the situation. Each is merely the result of 100 independent

Amplitude Ratio (S/N)	Input SNR /dB	Output SNR /dB	
		16 elements	64 elements
1000.	60.0	72.0	78.1
300.	49.5	61.6	67.6
100.	40.0	52.0	58.1
30.	29.5	41.6	47.6
10.	20.0	32.0	38.1
5.	14.0	26.0	32.0
3.	9.5	21.6	27.6
2.	6.0	18.1	24.0
1.5	3.5	15.6	21.6
1.	0.0	12.0	18.1
0.8	-1.9	10.1	16.1
0.6	-4.4	7.6	13.6
0.4	-8.0	4.1	10.1
0.3	-10.5	1.6	7.6
0.2	-14.0	-1.9	4.1
0.15	-16.5	-4.4	1.6
0.1	-20.0	-8.0	-1.9

Table 20.1 : Conversion table between amplitude ratios and decibels

computer simulations, and so a value from such realizations may be calculated accurately; however, this is only within 10-20% of the 'true' value, due to the limited number of trials. A few other observations may be made:-

i) The accuracy in estimating the second Fourier term is noticeably better than for first for an SNR in the range 10-25dB. However, note should be taken of the observations in 15.6 that the rms error is a more representative measure than amplitude, and that the conversion value between the two

Noise Amplitude	Input SNR / dB	1st Fourier term		2nd Fourier term	
		pf4	pf8	pf4	pf8
0.1	60.0	0.86	3.04*	2.70*	##
0.2	54.0	1.44	3.24*	2.71*	##
0.4	48.0	2.08	3.65*	3.05*	##
0.8	41.9	4.08	4.74*	3.75*	##
1.6	35.9	7.24	8.11*	6.69*	##
3.2	29.9	15.3	16.1	12.3	48.2*
6.4	23.9	33.7	34.7	19.8	48.8*
12.8	17.9	80.4	80.3	44.3	64.5*
20.0	14.0	95.	100.	70.	91.
30.0	10.5	155.	156.	108.	112.
45.0	6.9	199.	207.	164.	170.
67.5	3.4	329.	331.	265.	266.
101.3	-0.1	625.	605.	406.	354.
151.9	-3.6	1794.	1628.	1673.	1538.
227.8	-7.2	4628.	4546.	4803.	4442.

Table 20.2 : Variation of estimator error (in mm) for various noise levels

Single source, of amplitude 100. is located at 10^{o}, noise is uncorrelated. * Indicates bias has occurred.

Indicates where error in pf8 is more than 5 times that of pf4, and hence outside search range.

[The number of elements and the wavelength of radiation used were 16 and 6m respectively.]

is markedly different for the first and second coefficients.

ii) The pf4 estimator showed significant bias in estimating the 2nd Fourier coefficient in all the cases of high SNR. [Note, further work using a SNR of 80dB, and much finer resolution, seems to indicate that 2.6mm is the limiting error in estimation of a_2 by pf4. However, under the same conditions, those power functions involving a p^3 term (nos.5, 6, 19 & 20) could reduce the size of the

estimation error to about 0.5mm; pf19 being the most precise of them.]

iii) Although an SNR of 60dB is not realistic here, such a situation was modelled to show more fully the variations with noise level. However, as all cases gave biased estimators, and those for pf4 on the 2nd term are unexpectedly large, it may be that problems are being encountered due to the limited precision of data handling.

iv) The likely shape error for an input SNR of -4.5dB or lower, is sufficient that the source be masked by its own sidelobes [see Table 15.3] as well as the noise induced ones. Thus estimation errors for noisier scenarios are meaningless, unless some weighting is applied.

v) In chapter 26.2 the equivalence is shown between low levels of uncorrelated additive and multiplicative noise, and the variance of the shape errors predicted for the latter. The implication is, that for situations with a SNR of greater than about 10dB, the estimation accuracy of each coefficient should be proportional to the amplitude ratio of noise to signal, and also that the variances for the first two coefficients be in the ratio 1.44 to one. These predictions are for the defined 'optimum estimator' — clearly pf4 does not quite fulfil such a description.

For easier interpretation, the two sets of rms errors for pf4 (one for each of the Fourier terms) are plotted against noise level in Fig 20.1. Note, the performance curves of the 'optimum estimator' discussed in chapter 26.4, when plotted on the same axes as Fig 20.1, would be straight lines of slope -1.

20.3 Variation with Number of Sensors

As it is possible that the behaviour of the estimators depends primarily upon the effective output SNR, a collection of realizations was performed over a small range of input SNR, using varying numbers of hydrophones so that many situations had the same ideal output SNR. For beamforming using the correct element locations, the output power ratio is n times the input power ratio, where n is the number of hydrophones. Expressed as SNRs in decibels, this becomes:-

$$(\mathrm{SNR})_o = (\mathrm{SNR})_i + 10\log_{10} n \qquad [20.1]$$

Thus a doubling of the number of hydrophones, improves the output SNR by 3dB if nothing else is changed. Note, this analysis does assume that the sensor positions used for the beamforming are close to the true ones. The results displayed in Table 20.3 are for estimates of the

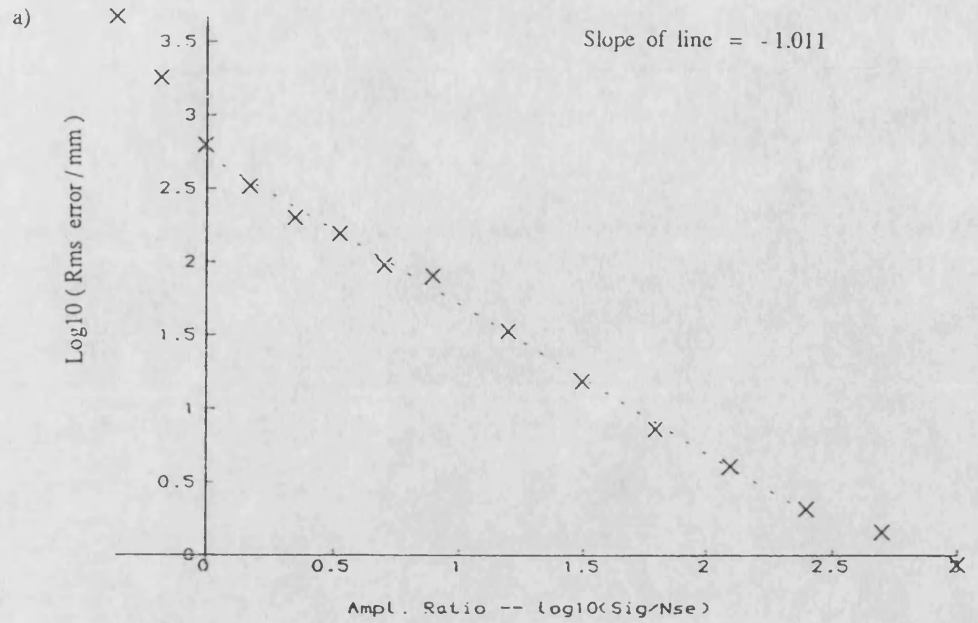

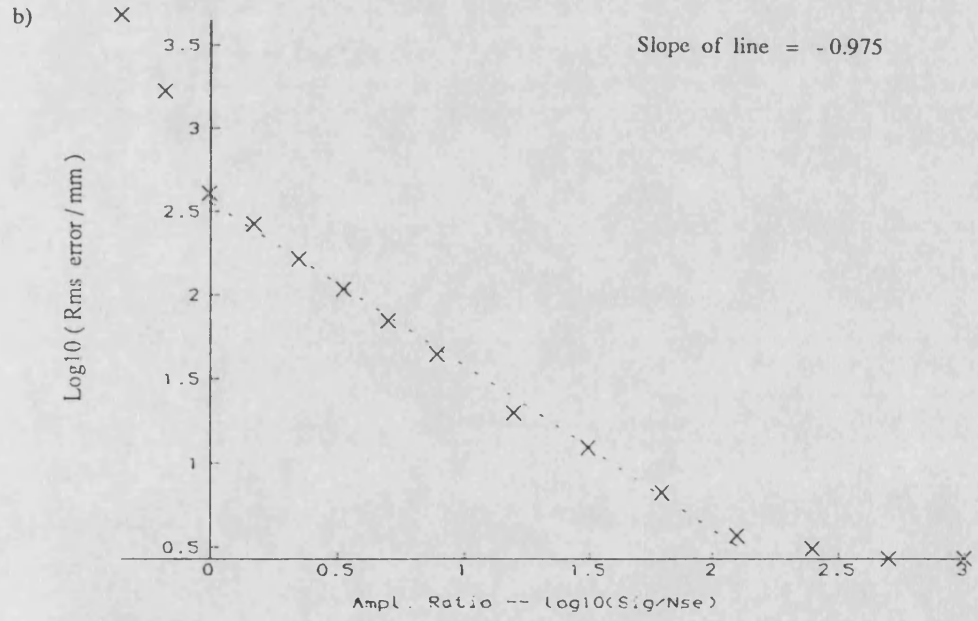

Fig 20.1 : Plot of pf4's shape estimation error for various noise levels.

a) Estimation error of first coefficient, a_1 ; b) Estimation error of second coefficient, a_2 .

Each point is the result of 100 simulations for a 16 element array, with a single source at broadside and beamforming over [-90°, 90°] in steps of 2°.

second Fourier coefficient using a source at 4.7°, and beams formed at intervals of 2°. In all cases, the effective array length, $L = n\,d$, was maintained at 48m, by altering the element separation, d, as well as n. [Note, other simulations using a constant separation of 3m (and hence variable values for L) gave similar results.]

No. of elements n	Input SNR / dB			
	14.0	11.0	8.0	4.9
8	9.0	13.7	18.3	28.8
11	8.7	13.0	15.3	24.9
16	6.6	10.5	14.5	19.9
22	6.7	8.0	11.8	16.5
32	4.9	7.4	10.7	14.5

Table 20.3 : Comparison of the rms errors (in cm) for the estimation of a_2 by pf4, using different noise levels and no. of elements. In all cases, array length = 48m, and processing was over [-40°, 40°] in steps of 2°. Results are from 200 simulations, with the source at 4.7°.

The data in the table show that the rms shape error decreases as number of elements and SNR increase, as would be clearly expected. To draw conclusions on a possible dependence on the overall output SNR, requires that similar values be obtained for situations where one has double the number of elements of the other, but an input SNR 3dB lower. Appendix 13 indicates that caution should be observed when comparing measures obtained from a finite number of samples; nonetheless, the data recorded may be understood to show good agreement with expectation. Taking logs of the number of elements, and also of the rms errors (because of their general exponential increase) enables a plane to be fitted to the points by a least-mean-square process [see appendix 8]. The resultant plane has the form:-

$$\log_{10}(\sigma(a_2)) = -0.4555 \cdot \log_{10}(n) - 0.5034 \cdot \log_{10}(p_s/p_n) - 0.679 \qquad [20.2]$$

where $\sigma(a_2)$ is in terms of the wavelength (6m), and p_s / p_n is the ratio of signal power to noise on input. Thus, the expected rms error in the estimate may be expressed in terms of a single measure via:-

$$E[\sigma(a_2)] \approx 0.21 f(n^{\alpha} \cdot p_s / p_n) \qquad [20.3]$$

where $\alpha = 1.105$, and $f(x) = 1/\sqrt{x}$. Note, $\alpha = 1$ corresponds to dependence solely on the total output power; the value observed differs only slightly from this. The results achieved *may* only be relevant for SNRs in the above range; certainly, $f(x) \neq 1/\sqrt{x}$ for all SNRs, as could be seen from Table 20.2 and Fig 20.1.

21. ERRORS INDEPENDENT OF TRUE SHAPE

Much of the simulation work has been done using one particular array shape as the true one. This one had the first 2 Fourier coefficients taking the values 2.7 and -1.83 respectively, with the rest zero. Work was generally done on only the one shape, because it was believed that the results were dependent only on the scenario and the *error* in any estimate of the array shape. However, it was felt necessary to show that this assumption was correct. In order to demonstrate this 300 simulations were done for 4 different array shapes — the shapes used all had $a_i = 0$ for $i \geq 3$, with the first two coefficients taking on the values (2.7, -1.83), (3.2, 2.5), (-0.7, 1.1) and (-7.2, -0.4) respectively.

These shapes were chosen as they were representative of many cases, from nearly straight to a bow of 1.2λ, and contain all possible combinations of signs for the first 2 coefficients. The simulated source was at 15^o to broadside, with additive noise 10dB below the signal level. Beamforming was done over $[-20^o\ 90^o]$ in steps of 2^o, and the searching was done over the 2nd coefficient. The source was deliberately selected to be off from broadside, and the angular scan range not to be symmetric with respect to array normal or source, in order to provide a general case. Table 21.1 contains the rms errors for 4 different power functions produced from the 300 simulations for each array shape.

The generally close agreement shows that the pfs are sensitive to errors in the deviation, but not the actual misshapen nature itself. Therefore measurements for one particular array shape can be taken to be typical of a multitude of configurations, thus preventing the need for repetition of all measurements for many different array shapes, and subsequent averaging. It is to be noted that although a range of rms values was observed, all the larger ones were for pf8, indicating that it is in general a much poorer estimator than the others for the conditions used. None of the estimators showed any significant bias.

Array Shape No.	Rms errors of estimators			
	pf4	pf5	pf6	pf8
1	1.000	1.000	1.000	1.000
2	1.003	1.007	1.006	1.188
3	0.919	0.927	0.928	1.104
4	1.015	1.031	1.032	1.046
Absolute error for no.1 / mm	37.2	36.9	36.9	74.9

Table 21.1 : Comparison of rms errors of various pfs for different array shapes.

Values are normalized with respect to those for array 1; the absolute values for that shape are included too.

[Statistics from 300 simulations of a source at 15° with noise at -10dB.]

22. EFFECT OF RANGE UPON ESTIMATION

For situations where passive sonar is used, the source is generally at a considerable distance (of the order of a 100km or more), such that the ratio of array length to source range is far less than one. Consequently, it is appropriate to model the scenario by a far-field source i.e. one which yields plane-waves at the array. The basic shape estimation algorithms make this fundamental assumption. Appendix 5 gives a more complete form for the distance (or time) from a source to each individual element. When the second order terms cause a variation of $\lambda/2$ (i.e. 180° phase shift) from that expected for a source at infinite distance, then the emitter is generally perceived to be in the 'near-field'. This occurs at a distance, $z = L^2/4\lambda$, where L is the full length of the array. [Note, the rms variation in the spatial delays, relative to the plane-wave case, is approximately a factor of 0.3 times smaller [see chapter 15.6] i.e. $\approx \lambda/6$; this agrees well with the figures observed in Table 15.3, for the limits on shape error that permit clear visibility of the source.]

As the principal effect of the source being close is to add a quadratic term to the delays of the wavefronts, this will be closely matched by the phase compensations for a distant source insonifying an array with an increased value for the a_1 component (a gentle bow). The proof of this is given in appendix 6. Denoting the range of the source by r, the form for the modified coefficient becomes:-

$$a_1' \approx a_1 + \frac{L^2 \cos\theta}{8r} \qquad [22.1]$$

A simulation to test this is recounted below.

An array of 32 elements was insonified by a source at a range of 1000m emitting at a frequency of 250Hz ($\lambda = 6$m). The array elements were at half wavelength spacing (hence $L = 96$m) and the first 4 shape coefficients were (2.7, -1.83, 0., 0.). No additive noise was used. Beamforming was performed over [-90°, 90°] in steps of 2°, with higher resolution then used to pin-point the source. Four different bearings were used in order to assess the accuracy of [22.1]. Table 22.1 contains the results.

Source Bearing	Expected value for Δa_1 / m	Observed Increment / m				Bearing error $\Delta\theta_1$ / degs	Highest sidelobe /dB
		a_1	a_2	a_3	a_4		
0°	1.15	1.10	0.001	0.035	0	0.00	-15.5
30°	1.00	0.90	0.020	0.015	0	-0.03	-12.0
45°	0.82	0.70	0.029	0.002	0	-0.04	-10.9
60°	0.58	0.46	0.012	-0.008	-0.007	-0.05	- 9.2

Table 22.1 : Measurements of apparent shape distortion due to proximity of source. Array used had 32 elements at half wavelength (3m) separation; source was at 1000m from array centre and there was no additive noise.

It can be seen that there is generally good agreement between the predicted values and those observed. When the source is at 0°, the change in a_3 is approximately 1/31 of that for a_1 — close to the value of 1/27 expected. As the source moves from broadside, the increment in a_1 changes as predicted, however its ratio to a_3 does not remain constant. This is because the effect is so small, so that it is soon swamped by low order terms ignored in the theory. Similarly, the values for a_2 and a_4 are finite, showing the importance of the '$y_i \sin\theta$' terms neglected in appendix 6.

Note, here it was necessary to have a very close source in order to make a distinct change in the shape parameters. The new value should not so much be regarded as a 'wrong' estimate, but as a modified one, appropriate for the situation, as it is that which best helps the array to give a focused image. However, if two sources exist, one in the near-field, and one in the far, then they will be trying to drive the shape estimation algorithms towards different points — consequently, at least one will be poorly focused. If the two are widely separated in angle, judicious use of windowing on the beamforming operations will enable each to be focused in turn, using the array configuration relevant for each case.

23. DEPENDENCE UPON BEARING AND FREQUENCY

23.1 Introduction — Expected Behaviour

This chapter investigates the dependence of the rms shape error upon the bearing of the source. It is clearly to be expected that the power functions will be less able to determine sensor positions perpendicular to the line of the array as the source bearing moves from broadside. As the particular characterization of array shape used here represents the y-components of the positions in terms of a limited Fourier series, leaving the x-values fixed, it follows that the rms error will depend only on the wavenumber perpendicular to the array, given by $k_y = (2\pi/\lambda)\cos\theta$. Although the mean value of the additive noise is zero, and also its expected correlation, any particular realization will yield finite values. Similarly, the changes in phase of the complex phasors due to the added noise will have non-zero mean and correlation for each individual simulation — it is this variation in phase that the power function attempts to counter, a positional 'error' of Δy_i for the ith element leading to a compensating phase change of $\Delta\phi_i = k_y \Delta y_i$. The noise-induced phase changes have statistics for rms error and rms correlation value that relate solely to the level of the noise (i.e. the SNR), not the bearing of the source. Thus the statistics of the required phase compensation are independent of bearing. Consequently, the statistics relating to the deviation in the shape estimation will vary with θ, as k_y is a function of such. In short, for a fixed SNR, it is expected that:

$$k_y \cdot (\Delta y_i)_{rms} = \text{constant} \qquad [23.1]$$

As error in a Fourier term is proportional to rms error in y-values, it follows that the rms error in a Fourier coefficient, such as a_1 will depend upon bearing.

$$\rightarrow (\Delta a_1)_{rms} = A_1 (\lambda/\lambda_0) \sec\theta \qquad [23.2]$$

where the resulting constant of proportionality, A_1, includes the relationship between Δy_i and Δa_1 and also the factor of 2π. A_1 is thus the rms error in estimate of the a_1 coefficient for the standard wavelength ($\lambda = \lambda_0$) and for a broadside source ($\theta = \theta_0$). To test these predictions, a series of many simulations was performed, the results of which are given in the following pages.

23.2 Observed Dependence Upon Bearing

Separate simulations were performed for sources at each of 0°, 15°, 30°, 40°, 50°, 60°, 65°, 70° and 75°, with an additive noise level 20dB below the signal strength. Independent estimates were made of the rms errors for the first two Fourier terms — these are summarised in Table 23.1. Results for pf8 are included as well as those for pf4, as for large angles, those of the latter were atypical of the performance of the other power functions.

For most of the cases, beamforming was reduced to the angular sector -20° to 90°, as this required only 56 beams at 2° separation, instead of 91, and thus saved on computation time. Elsewhere in this thesis [Table 18.1] it is shown that similar alterations have negligible effect for sources at 10° and 34.5°. A further check on the validity of this is included here — the signal records for the source at 70° were processed with beams formed over the sectors [-20°, 90°], [-90°, 90°] and [-180°, 180°] in turn.

An SNR of 20dB was used for the simulations, as this had been a 'standard' test in much of the earlier work. It is of an intermediate level, suffering neither from the problems of too high a ratio (limited precision of data handling), nor too low a value (source indiscernible from noise-related sidelobes). However, as many of the 'in the field' measurements will have signal and noise of comparable strength, a repeat of all the investigations was performed for an input SNR of 0dB. These are presented in Table 23.2.

23.3 Discussion of Results

The following points may be concluded from the tables:-

i) Rms error increases with bearing (apart from slight discrepancies for 0°/15°).

ii) For the 70° source, processing over [-20°, 90°] does not give noticeably different results to that which would be achieved for [-90°, 90°]. However, a full search over [-180°, 180°] leads to significantly greater errors, probably due to the large width mainlobe near endfire, which spills over into angles greater than 90°.

iii) Although usually of comparable performance, the rms error for pf4 is much larger than that for pf8 when both are estimating the 2nd Fourier term using a source at 70 °. [The figures for the other two pfs monitored (nos. 5 & 6) agree well with those for pf8.]

Source Direction		1st Fourier term		2nd Fourier term	
θ	sec θ	pf4	pf8	pf4	pf8
0	1.000	1.000	1.000	1.000	1.000
15	1.035	0.932	0.986	1.044	1.910
30	1.155	1.221	1.220	1.266	1.264
40	1.305	1.241	1.233	1.195	1.221
50	1.556	1.754	1.785	1.966	1.470
60	2.000	2.018*	1.886	5.8*	1.923
65	2.366	3.77	3.74	9.5*	2.182
70	2.923	3.63	2.946	17.9*	2.639
70	(a)	3.71	2.946	18.7*	2.639
70	(b)	5.77	2.944	26.*	2.639
75	3.863	4.979	4.949	28.*	3.919
Absolute values for source at 0° / mm		47.2	47.5	35.8	35.5

Table 23.1 : Variation of rms errors with bearing of source

Each figure results from 100 independent simulations of a source of SNR=20dB, and with beamforming over -20° to 90° step 2°. All figures in main table are *relative* to that for a broadside source. * Indicates bias has occurred. (a) Search range modified to [-90°, 90°] ; (b) Changed to [-180°, 180°]

iv) The tables for the two widely separated noise levels are in good agreement with one another; not just in the manner predicted, but also in the conditions that cause the pf4 estimator (and others) to be biased.

Source Direction		1st Fourier term		2nd Fourier term	
θ	sec θ	pf4	pf8	pf4	pf8
0	1.000	1.000	1.000	1.000	1.000
15	1.035	0.992	1.121	0.965	1.018
30	1.155	1.047	1.098	1.229	1.215
40	1.305	1.301	1.359	1.408	1.395
50	1.556	1.778	1.744	1.887*	1.477
60	2.000	2.124	2.044	3.1*	2.159
65	2.366	3.15	2.25	3.6*	2.257
70	2.923	4.14	3.23	4.2*	2.585
70	(a)	4.33*	3.23	4.9*	2.597
70	(b)	4.29*	3.38	6.6*	3.395
75	3.863	5.75	4.09	5.5*	3.98
Absolute values for source at 0° / mm		559.	532.	403.	378.

Table 23.2 : Variation of rms errors with bearing of source

Each figure results from 100 independent simulations of a source of SNR=0dB, and with beamforming over -20° to 90° step 2°. All figures in main table are *relative* to that for a broadside source. * Indicates bias has occurred. (a) Search range modified to [-90°, 90°] ; (b) Changed to [-180°, 180°]

23.4 Experimental Variation with Frequency

In furtherance to the investigation of the dependence of the errors upon bearing, it was seemly to assess the importance of frequency, as the earlier analysis [23.2] had yielded a prediction that the rms shape errors would be proportional to the wavelength of radiation used. As this was felt to be an important area to explore, a large series of simulations was run — 300 realizations for each of 7 frequencies, and all at 2 different noise levels too.

As the elements were spaced at half-wavelength separation for the standard wavelength ($\lambda_0 = 6$m), beamforming for the higher frequency runs could have led to problems due to aliasing. In order to prevent such difficulties, the scan for all cases was over $[-30^o, 30^o]$ in steps of 2^o. The source simulated was at 4.7^o, a value near broadside, but differing a little to avoid any extreme effects that might exist for that direction. The findings are given in Table 23.3.

Simulated Signal		Relative Estimator Error	
Frequency / Hz	λ / λ_0	SNR=10dB	SNR=0dB
128	1.953	2.211	1.950
160	1.563	1.810	1.739
200	1.250	1.352	1.282
250	1.000	1.000	1.000
312.5	0.800	0.860	0.834
390.6	0.640	0.629	0.646
488.3	0.512	0.648*	0.535

Table 23.3 : Comparison of the rms errors at different frequencies ($\lambda_0 = 6$m).
Results are for estimation of 2nd Fourier term, using a single source at 4.7^o and processing over $[-30^o, 30^o]$ in steps of 2^o. 300 realizations used for each; columns independently normalized w.r.t. value for 250Hz.
* Indicates bias has occurred i.e. mean not close to zero error.

The results show reasonable agreement with that expected from [23.2], although the figure for the 10dB source at 488Hz appears a little inconsistent. Broadly similar observations were found for other pfs; some actually gave a greater error at the 10dB level for 488Hz than for 312Hz.

24. EFFECT OF CORRELATED NOISE

24.1 Introduction

All the results given so far have been for uncorrelated additive noise i.e. that for which the expected value for the correlation between 2 different sensors, $E[n_i n_j^*]$, is zero, although on any single realization this will have a finite value. This is not always the case in the real environment. This chapter concerns investigation using a simple exponential model for the autocorrelation of the noise viz. $E[n_i n_j^*] = \alpha^{-|i-j|}$, $|\alpha| \leq 1$.

Note, if a signal record consisting solely of uncorrelated noise (i.e. no signal) is processed via conventional beamforming techniques, the resulting beam pattern for any individual realization will still show a lobed structure [Fig 24.1a], with some lobes of greater height than others. This image is not 'real' i.e. representative of the experimental conditions, array configuration or processing parameters. [The *expected* form, which is that achieved by ensemble averaging, corresponds to a power display that is constant over angle.] However, the shape estimation algorithm discussed will still strive to focus the beam pattern, selecting an array shape that causes the greatest variation in the level of the lobes [Fig 24.1b]. Ideally, the algorithm should make some estimate of the power of any possible signal, and terminate the shape estimation if this value lies below a certain threshold level.

24.2 Processing with no Signal

24.2.1 Fully Correlated Noise

If the correlation coefficient, α, is unity, then all the values for the sensor. are fully correlated i.e. identical. This is exactly equivalent to the signal received by a straight array from a perfectly coherent source perpendicular to the array. Thus, application of shape estimation algorithms to perfectly correlated noise causes convergence towards a straight array with a pseudo-source at broadside, independent of the true shape. Note, if the correlation had been given by

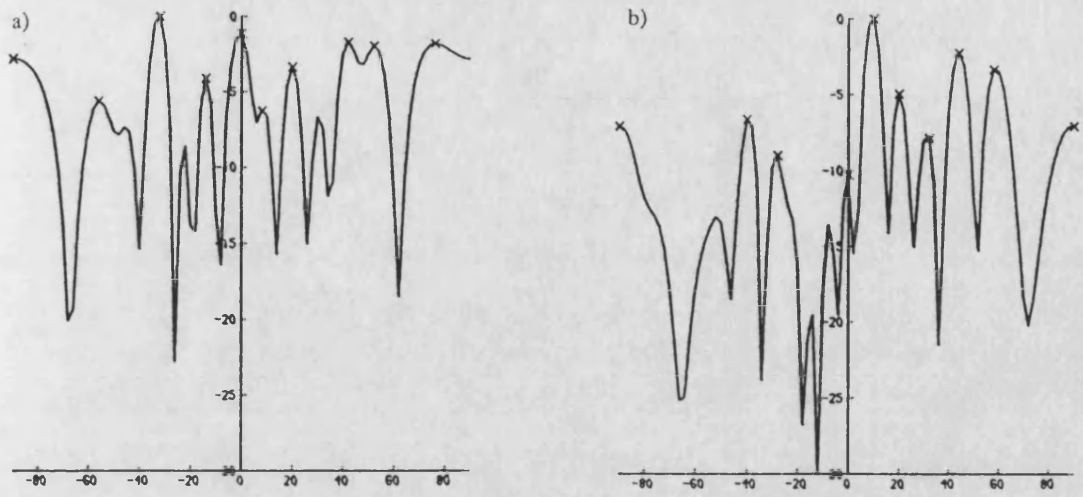

Fig 24.1 : Plots of beam patterns due solely to noise

(a) is the typical result for a pre-selected array shape; (b) is the result of an attempt by power functions to focus pattern. The number of 'error lobes' is limited by the number of elements, here 16.

$E[n_i n_j^*] = z^{i-j}$, with $z = e^{j\phi}$, then the effect would be of a source at θ insonifying a straight array, where $kd \sin\theta = -\phi$.

24.2.2 Partially Correlated Noise

If α is now reduced to a value just below unity, say 0.95, the noise values at neighbouring sensors will still be closely correlated, but over the length of the array, the correlation will be small. This will produce a 'fuzzy' or diffuse image, as shown in Fig 24.2 — the effect of the slight incoherence being to broaden the width of the mainbeam, to weaken it, thus making the sidelobes relatively higher than normal, and to reduce the depth of the nulls.

Again, as the expected correlation between sensors is real and positive, shape estimators will on average tend towards a straight line, with a source at broadside. However, any particular realization of the noise may be more adequately represented by a gentle bow in the array shape. The rms value of this bow, $(a_1)_{rms}$, will increase with the degree of incoherency i.e. as the signal becomes less correlated.

Although the variable specified in the simulation conditions is the correlation between adjacent elements, α, a figure more representative of the variation across the array would be useful.

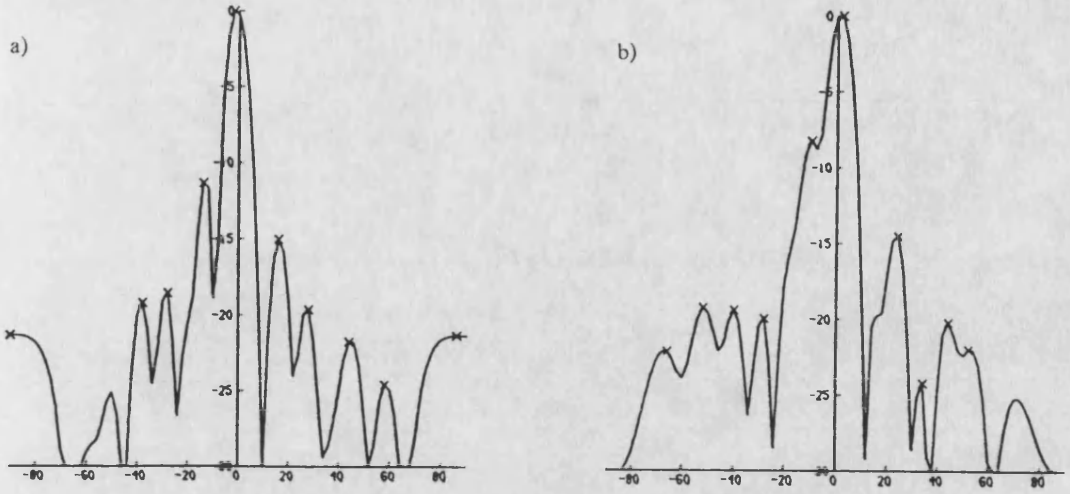

Fig 24.2 : Plots of beam patterns for different correlation coefficients

No signal present; 16-element array, solely insonified by correlated noise. a) $\alpha = 0.95$; b) $\alpha = 0.90$

In both cases, array shape used was a straight line.

There are 3 suitable candidates — β, the correlation between the two end sensors; $\bar{\alpha}$, the mean correlation between any two elements; and μ, the ratio of array length (L) to the decay length of the correlation (L^*). These three are given by:-

$$\beta = \alpha^{n-1} \approx \alpha^n \qquad [24.1]$$

$$\ln \bar{\alpha} = \frac{1}{n^2} \sum_{i=1}^{n} \sum_{j=1}^{n} \ln \alpha(i,j) \approx \frac{1}{n^2} \sum_{k=0}^{n-1} (n-k) \ln \alpha^k = \frac{1}{n^2} \sum (n-k)\, k \ln \alpha = \tfrac{1}{6}\, n \ln \alpha$$

$$\rightarrow \quad \bar{\alpha} = \alpha^{n/6} \qquad [24.2]$$

$$\mu = (nd) / (-d / \ln \alpha) = -n \ln \alpha = n \ln (1/\alpha) \qquad [24.3]$$

[The measure, $\bar{\alpha}$ was written in terms of logs simply because the normal evaluation of the mean led to a cumbersome expression.] A series of simulations was performed to give an indication of the rms shape error for various degrees of correlation; these are summarised in Table 24.1.

These results show that the rms error associated with correlated additive noise is a function of both the number of elements and of the correlation coefficient. The table indicates that β is a useful indicator of the coherence of the signal across the whole array; however, it is not fully clear

n	α	β	$(a_1)_{rms} / \lambda$
16	1.000	1.000	0.000
16	0.975	0.667	0.100
8	0.903	0.440	0.123
16	0.950	0.440	0.125
32	0.975	0.440	0.139
16	0.925	0.287	0.141
16	0.900	0.185	0.166
8	0.563	0.010	0.239
16	0.750	0.010	0.242
32	0.866	0.010	0.235

Table 24.1 : Variation of the parameter a_1 with the correlation of the noise.
Each figure is the result of 200 simulations of the correlated noise with no signal present i.e. effectively a semi-coherent or 'fuzzy' source. Hydrophone separation = 0.26λ (λ =11.7m).

whether the shape error is a function of β alone, of if there is some residual dependence upon the number of elements in the array.

One set of realizations was done with the same element separation, but using a wavelength of 3m. The value of $(a_1)_{rms} / \lambda$ recorded then was consistent with the relevant entry in the table. This shows that results for correlated noise scale with wavelength in a similar manner to those for uncorrelated [see chapter 23.4].

24.3 Single Source plus Correlated Noise

In the previous section it was shown that correlated noise causes shape estimation algorithms to converge towards a straight line, the effect being strongest (and thus having less variance) for the most correlated cases. Thus when a curved array is insonified by a strong source and correlated noise of a similar level, there is a choice of two different configurations towards which shape estimation algorithms may tend, depending upon the relative power levels and distributions of the two 'sources'. Table 24.2 gives the results for a series of simulations investigating this.

True array shape	$\alpha = 0.3$		$\alpha = 0.5$		$\alpha = 0.7$		$\alpha = 0.85$		$\alpha = 0.95$	
	Δa_1	$\Delta\theta$	Δa_1	$\Delta\theta$	Δa_1	$\Delta\theta$	Δa_1	$\Delta\theta$	Δa_1	$\Delta\theta$
No. 1	1.54	4.0	1.73	5.0	1.84	6.5	1.98	5.1	2.62	6.2
No. 2	1.48	4.6	2.04	5.4	2.32	5.6	2.97	7.1	3.15	7.3
No. 3	1.01	2.3	1.26	3.5	1.35	4.9	1.39	5.4	1.52	5.1

Table 24.2 : Comparison of the rms errors due to correlated noise for differently shaped arrays. Shape no. 1 was characterized by Fourier coefficients a_1, a_2, a_3, = (4.0, 0.0, 0.0) ; shape no. 2 by (-6.0, 0.0, 0.0) ; and no. 3 by (3.7, -1.83, 1.2) . Investigation was only of first coefficient and source bearing, the units being metres and degrees respectively. 100 simulations were performed for a 16 element array with a source at 9.4°. The additive noise was at 0dB relative to the source.

The results for the 3 different shapes show the same overall trends, although the magnitudes differ, as the shapes are varying amounts from a straight line. In all case the estimates of a_1 showed a bias towards zero, indicative of the effect expected due to correlated noise. The magnitude of the bias was observed to be approximately 1m less than the rms variation.

Sometimes the maximization of the power function (pf4) led to a beam pattern where the highest lobe was due to noise rather than the signal. Note was taken of how often the highest lobe was within 3.5° of the true source bearing. [A value of 3.5° was selected as it is just under half the beamwidth — any peaks within 3.5° of true must lie on the correct power lobe, albeit displaced

somewhat; peaks displaced further probably lie on different lobes of the beam pattern.] For most of the cases in Table 24.2, the success rate for source location was around 90%; however, noise correlations of 0.7 or greater reduced the success rates for shapes 1 and 2 to 60-75%.

In order to examine the dependence upon the level of the noise, one shape (no. 2) was selected for further trials. This one was chosen as it differed more from a straight line than the others, and consequently the effects should be more pronounced. The variations with both noise level and correlation are displayed in Table 24.3.

SNR	$\alpha = 0.3$		$\alpha = 0.5$		$\alpha = 0.7$		$\alpha = 0.85$		$\alpha = 0.95$	
/dB	Δa_1	- % -	Δa_1	- % -	Δa_1	- % -	Δa_1	- % -	Δa_1	- % -
-1.9	1.08	96	0.81	99	1.36	90	1.95	83	2.27	76
0.0	1.48	91	2.04	84	2.32	76	2.97	57	3.15	60
1.9	2.39	74	3.02	61	3.38	48	3.29	54	3.64	51
3.8	3.04	62	3.91	43	3.81	48	4.10	36	4.61	22

Table 24.3 : Comparison of the effects of noise of varying levels and degrees of correlation. 100 simulations were performed for a 16 element array with a source at 9.4^o. Shape search was only over 1st coefficient, for which Δa_1 is given in metres; the '%' refers to the number of occasions upon which the highest peak of the beam pattern occurred within 3.5^o of source bearing.

24.4 Summary

Correlated noise has been shown to mimic the effects of a 'fuzzy' or indistinct source. On account of the way that such noise is generated in the program, its effect here is of a broadside source insonifying a straight array. When a true source is present, the effect on source detection and shape estimation depends upon the relative strengths of source and noise, and on the correlation of the

latter. The more correlated the noise is, the more it resembles the output of a source, and consequently, the greater its effect on shape estimation algorithms. With signal and noise of equal strength (on input), the detection rate is good if the noise is poorly correlated ($\alpha \leq 0.5$).

Estimation of a_1, the lowest order coefficient, shows that the frequency distribution of the selections is no longer centred on zero error; instead a bias is found, generally corresponding to a magnitude of 1m ($\lambda/6$) less than the rms error. A further series of realizations with a source at 42.8°, rather than 9.4° led to increases in bias and rms error of 20-50%. This is in rough agreement with expectations as secθ has increased by a factor of 1.34. The percentage detection rate for the more oblique source does not appear to be significantly different from that for the one near broadside.

When the correlation is large, such that the noise resembles a source at a different focal distance, the distribution of selected shapes is bimodal, with peaks near $a_1 = -6$m (the true characterization of the array shape) and $a_1 = 0$m (the straight array favoured by the 'noise-source').

25. PRESENCE OF A SECONDARY SOURCE

25.1 Dependence upon Phase

It is found that a single realization of a particular 2 source scenario, with only one frequency and no additive noise, will not enable beamforming or shape estimation to yield the exact values for the various parameters. This is not due to random noise, as none is present, but rather the interaction of the 2 sources. Any single realization of a pair of sources at a single frequency will be equivalent to a phase lock between the two signals. The biases observed are dependent on the relative phase of the two signals. A series of simulations with gradual increase in the relative phase shows the full relationship between the biases and the phase — these are shown in Table 25.1.

25.2 Measurements of Sinusoidal Variations

Table 25.1 shows that the fluctuations seem to follow a sinusoidal variation, depending upon the phase difference and having negligible bias of the mean. Appendix 3 shows that such a relationship is clearly expected for the power pattern. Whereas this is not clearly demonstrated for the other measures, the results seem to fit such a pattern well. Appendix 12 shows that 3 realizations with 120^o phase shift between them should be sufficient to estimate the mean and variance accurately. In Table 25.2 the mean and s.d. for the conditions of Table 25.1 are compared with the results obtained i) using 12 realizations with random phase, and ii) using 3 realizations with phase separation of 120^o. [Note, the data for 30^o phase shifts is slightly different to the previous table, as a different search range was employed here.]

Note, the results for random phase are not necessarily worse than for stepped phase — different series of 12 realizations yield slightly different figures, sometimes greater than the stepped results, sometimes less. This variation shows that a dozen random runs does not give as consistent results as 3 at fixed phase increments.

Phase diff. $\phi_1 - \phi_2$ /degs	Shape estimate error / cm				Bearing error $\Delta\theta_1$ / degs	Bearing error $\Delta\theta_2$ / degs	Power ratio P_2 / P_1
	pf4	pf5	pf6	pf8			
0	0	0	0	0	0.13	-0.98	0.136
30	3	4	4	4	0.12	-0.94	0.132
60	6	8	8	8	0.08	-0.78	0.119
90	8	9	9	10	0.01	-0.24	0.101
120	7	8	8	10	-0.06	0.98	0.091
150	5	5	5	6	-0.12	2.03	0.092
180	0	1	1	1	-0.15	2.26	0.094
210	-4	-4	-4	-5	-0.13	2.03	0.091
240	-7	-8	-8	-9	-0.07	1.09	0.089
270	-8	-9	-9	-10	0.01	-0.11	0.098
300	-7	-8	-8	-9	0.08	-0.68	0.116
330	-4	-5	-5	-5	0.12	-0.90	0.130
Mean	-0.08	0.08	0.08	0.08	0.0017	0.32	0.107
Rms error	5.6	6.5	6.5	7.2	0.100	1.27	0.019

Table 25.1 : Variation of various estimates with relative phase of signals.
Results are for 2 sources — one at 5.0^o, the other (-10dB) at -25.4^o — insonifying a 16 element array.
Shape estimates are for coefficient a_1.

In a genuine acoustic situation, there would be no dependence between the phases of the 2 sources (unless one was an echo of the other off a nearby object), and so all realizations would be independent and correspond to totally random values for the phase. It can be seen here, that a dozen or so measurements would be needed to accurately assess the mean and standard deviation of the estimates. However, as a simulation exercise, only 3 samples are required to make an unbiased and accurate estimate of each. [Of course, in this particular case the errors in shape and source direction are minuscule; the estimates of the second source do show more noticeable variation.]

No. of samples and phase increment	Calculated Statistic	Estimation Error / cm				Bearing errors		Power Ratio
		pf4	pf5	pf6	pf8	$\Delta\theta_1$	$\Delta\theta_2$	P_2/P_1
12 at 30°	Mean	-0.08	0.08	0.08	0.08	0.0017	0.32	0.107
	S.D.	5.61	6.46	6.46	8.43	0.100	1.27	0.019
12 random	Mean	-1.42	-2.00	-2.00	-2.25	0.043	-0.18	0.115
	S.D.	6.00	6.76	6.76	8.67	0.099	1.09	0.023
3 at 120°	Mean	0.00	0.00	0.00	2.00	0.0033	0.29	0.107
	S.D.	5.66	6.38	6.38	9.49	0.098	1.29	0.018

Table 25.2 : Comparison of sampling methods.

[Results refer to estimates of a_1 for a 16 element array insonified by one source at 5.0°, and a weaker one (-10dB) at -25.4°. There was no additive noise present — variations are due to varying interaction.]

A wider investigation of the problem shows that a s.d. of 5.6cm for pf4 is not typical of all similar scenarios. Variation of the secondary source direction by 0.5° changes this value to 6.4cm. Gradual movement of the secondary source shows that the variance fluctuates in a manner akin to a sinusoid, having a period of about 8.5°; i.e. standard deviation of error variations peaks for certain secondary angles approximately 8.5° apart. The size of the error in a_1 varies from a minimum of zero (i.e. all estimates for that direction are correct) to a maximum of 8.3cm (corresponding to a phase dependence with amplitude 11.7cm).

Further simulations were performed, using the same primary source at 5°, and secondary at angles between 25° and 35°. These runs used different power levels for the second source — -6dB, -3dB and -0.9dB (relative to the first source). Examination of the rms errors for estimates of a_1, P_2/P_1, θ_1 and θ_2 continue to show fluctuations with a period of 8.5°. The maximum values for each measure are presented in Table 25.3.

Power Ratio, P_2/P_1		Rms Errors for poorest case			
Magnitude	/dB	a_1 / cm	P_2/P_1	θ_1 / degs	θ_2 / degs
0.10	-10.0	8.3	0.018	0.11	1.29
0.25	-6.0	10.7	0.015	0.18	0.83
0.50	-3.0	10.5	0.040	0.25	0.60
0.81	-0.9	6.2	0.023	0.31	0.48

Table 25.3 : Variation of errors with level of secondary source.
[Results show worst level of errors encountered for 2nd source in the interval [-35.4°, -25.4°] ; values at each angle estimated using 3 realizations for each situation with 120° phase increment.]

It is to be noted that the maximum rms errors in the estimated power ratio and source directions occur when the source is at the bearing which causes the *minimum* error variation in a_1. This bearing was the same for all power levels.

25.3 Two Adjacent Sources

In cases where the second source is close to the first, the behaviour differs a little from that detailed earlier. Maintaining the primary source at 5.0°, a second source (3dB weaker) was simulated at angles of -7.4°, -5.4° and -3.4° in turn. [Note, the beamwidth for the 16 element array is roughly 8°.] The statistics of 12 phase-stepped simulations for each situation are given in Table 25.4.

As expected, the closer proximity of the sources caused greater interaction of the signals as evidenced by the larger shape and bearing errors. However, the variation with phase difference $\phi_2 - \phi_1$ no longer shows a sinusoidal relationship. For example, the shape errors, Δa_1, produced by different phases for the -5.4° source are given by

Bearing of 2nd source,	θ_2	- 7.4°	- 5.4°	- 3.4°
Source separation,	$\Delta\theta_{12}$	12.4°	10.4°	8.4°
Error in 1st coefficient,	Δa_1 / cm	22.5	75.5	85.0
Bearing error	$\Delta\theta_1$ / degs	0.51	0.43	0.89
	$\Delta\theta_2$ / degs	1.06	1.29	12.2*
Rms power ratio,	P_2/P_1	0.51	0.38	0.24

Table 25.4 : Variations in estimates of shape and source parameters, when 2 sources are close.
[Results obtained by use of 12 stepped phase changes with an increment of 30°. Array has 16 elements at 3m separation, with $\lambda = 6$m. The true power ratio is 0.50 and no noise is present.]
* Large error due to 2nd source being lost.

$$\Delta a_1(\Delta\phi_i) = 0, -12, -17, -14, -8, -3, 0, 3, 8, 14, 16, 13$$

where $\Delta\phi_i = 2\pi(i-1)/12$, and the quantization unit for the shape selection was 7.5cm. The variation is still of mean zero, and has symmetry about the zero-crossings; but the maximum errors no longer occur at $\Delta\phi_i = \pm 90°$. With the second source at -3.4°, the interaction is so strong, that the reduction of the 2nd mainlobe for 5 successive simulations out of the 12, causes it to be exceeded by the sidelobe on the other side of the primary. This results in the large error in $\Delta\theta_2$ highlighted by the asterisk.

All results in the table relate to beamforming using the shape selected by pf4; using the correct shape improves a few of the bearing estimates. However, it does not alter the depression of the 2nd mainlobe for the 3rd run, and so consequently loses the weaker source for 5 occasions out of 12.

25.4 Summary

For situations concerning two sources and no additive noise, there is an estimation error in all the parameters due to the phase relationship between the two sources. These biases show a variation with phase possessing zero mean and approximately sinusoidal behaviour. Therefore sufficient averaging over different phases will result in no residual bias. The degree of variation also depends upon the specifics of the scenario e.g. angular separation of sources and relevant power levels, but in all cases the errors are small — $|\Delta a_1| \ll \lambda/10$, $\Delta\theta_1 \ll 1^o$. When the second source is 10dB weaker than the first, the estimation of its bearing may be out by more than 1 degree; however, a signal that weak would be obliterated anyhow by any reasonable level of additive noise.

However, the above is not necessarily correct when the two sources are about a beamwidth apart. Then the interaction will make a significant change to the estimation of the second source, even if it is of comparable strength to the first. Note, in such cases even information as to the true element positions can not make a great difference.

26. EFFECT OF MULTIPLICATIVE NOISE

26.1 Introduction

The causes of multiplicative noise have been referred to earlier [chapter 9], along with the simple model used here to provide such an effect in the simulations. To summarise, the transmission path between a source and sensor has a complex number η associated with it — the effective voltage perceived at an element i due to a source, being η_i times the value expected for a perfectly homogeneous ocean. Thus η models both amplitude and phase fluctuations. The value $\gamma = \ln \eta$ (also complex) has mean zero, and a correlation between 2 sensors i , j given by:-

$$E[\gamma_i \gamma_j^*] = \sigma_m^2 \, \alpha^{|i-j|} \qquad [26.1]$$

where σ_m is the standard deviation of the Gaussian from which γ_i is drawn (and hence the rms value of γ_i) , and α is the correlation coefficient between neighbouring sensors.

26.2 Simple Cases

26.2.1 Fully Correlated

A considerable simplification of the problem is made when $\alpha = 1$. Then the multiplicative terms are fully correlated, causing all the signal voltages to be premultiplied by the same quantity, and thus the beamforming, source detection and shape estimation are totally unaffected. This corresponds to a change in the refractive index of a large mass of water between the source and the array, whose correlation width is far greater than the length of the array. The unchanged performance is easily confirmed by simulations. A slight reduction in α to, say 0.95, corresponds to closely correlated fluctuations across the length of the array. Once more, the statistics for correlation over the whole array [see chapter 24.2] enable easier comprehension. [Using a value of α of 0.95 for a 16 element array corresponds to β (correlation between end sensors) being 0.4. The comparable value for μ is 0.82, indicating that the transverse correlation length is roughly the size of the array.] So for

an array of 16 sensors, effects of the incoherence are expected to be manifest for values of α of 0.95 or less.

26.2.2 Totally Uncorrelated

The other easy reduction of the situation occurs when the noise is totally uncorrelated between sensors. Multiplicative noise can be expressed as additive noise associated with a specific source in the manner below:-

$$v_i' = \eta_i v_i = v_i + n_i \qquad [26.2a]$$

where:-

$$n_i / v_i = \eta_i - 1 = \exp(\gamma_i) - 1 \simeq \gamma_i \qquad (\text{for } |\gamma| \ll 1) \qquad [26.2b]$$

Thus a value of n_i for the additive noise at a single sensor is equivalent to a multiplicative coefficient of η_i (or γ_i) as given above. Evaluation of mean and correlation over all elements gives:-

$$\overline{\gamma_i} = \overline{n_i} \; / \; \overline{v_i} \qquad [26.3a]$$

$$E[\gamma_i \gamma_j^*] = E[n_i n_j^*] \; / \; E[v_i v_j^*] \qquad [26.3b]$$

[Note, this 2nd expression does not simplify further, as $E[v_i v_j^*]$ is not, in general, constant. For the specific case of a broadside source and a straight array, $E[v_i v_j^*] = |v|^2 =$ constant, and thus the two sources of errors are exactly equivalent then.] However, the situation of uncorrelated multiplicative noise, $E[\gamma_i \gamma_j^*] = 0$, for $i \neq j$, corresponds perfectly with uncorrelated additive noise, whatever the phase relationship of $\{v_i\}$. Statistical results for uncorrelated multiplicative noise of magnitude σ_m should be the same as that occurring for uncorrelated additive noise, when the amplitude ratio of noise to signal is σ_m.

26.3 Observed Effect of Correlated Noise

A varied series of simulations was performed to examine how different values for the magnitude (standard deviation) and correlation of the multiplicative noise affect both shape estimation and source characterization. These are given in Tables 26.1 - 3.

Noise S.D.	$\alpha = 0.0$			$\alpha = 0.5$			$\alpha = 0.85$			$\alpha = 0.95$		
σ_m	a_1	a_2	a_3	a_1	a_2	a_3	a_1	a_2	a_3	a_1	a_2	a_3
0.1	4.5	3.3	2.1	6.4	4.0	2.6	6.0	3.4	1.6	4.0	2.1	1.0
0.2	10.7	7.0	4.1	12.9	8.3	5.0	11.9	7.2	3.4	7.7	4.3	1.8
0.3	16.0	10.9	6.3	18.2	13.4	7.2	17.9	10.0	5.3	10.4	6.1	2.7
0.4	18.8	13.3	9.0	27.7	16.3	10.2	25.6	14.1	6.8	16.4	7.9	3.8
0.5	26.9	17.5	12.1	34.2	23.0	13.4	31.3	16.2	9.0	19.2	11.4	5.2
0.6	32.	28.	13.	47.	28.	17.	40.	20.	11.	25.	13.	6.2
0.7	42.	26.	17.	51.	32.	22.	47.	23.	13.	27.	15.	6.6
0.8	52.	30.	21.	69.	38.	24.	49.	31.	14.	36.	18.	7.1
0.9	122.	192.	184.	83.	56.	104.	74.	29.	7.	35.	0.	0.
1.0	614.	993.	885.	226.	594.	627.	65.	17.	203.	20.	0.	0.

Table 26.1 : Shape estimate errors (in cm) for different levels of multiplicative noise.
All results are from 150 simulations using 16 element array, with $d / \lambda = 0.5$.

All the entries in the tables refer to the pf4 estimator, using 150 simulations of a scenario with a single source at 9.4° from broadside insonifying the array at 250Hz ($\rightarrow \lambda = 6$m). The spacing of the hydrophones was 3m, and there was no additive noise present. It should be noted that a value of σ_m of 0.0 or a value of α of 1.0 results in an error free pattern, for which the errors in a_1, a_2, a_3 and θ_1 are zero, and the height of the highest sidelobe is -13.3dB. [Note, as the power level near a lobe peak varies slightly for a change of 1°, the actual relative sidelobe level observed will depend slightly upon the orientation of the chosen beams; thus a sidelobe level lower than -13.3 might be recorded.] Fig 26.1 shows some examples of the effect upon beam patterns of various levels of multiplicative noise.

S.D. of Noise σ_m	Highest sidelobe level / dB			
	$\alpha = 0.0$	$\alpha = 0.5$	$\alpha = 0.85$	$\alpha = 0.95$
0.1	- 12.3	- 12.1	- 12.3	- 12.2
0.2	- 12.1	- 12.1	- 12.1	- 12.2
0.3	- 12.0	- 11.8	- 12.1	- 12.0
0.4	- 11.4	- 11.4	- 11.8	- 12.1
0.5	- 10.5	- 10.4	- 11.4	- 11.9
0.6	- 9.4	- 9.6	- 11.0	- 12.0
0.7	- 8.2	- 9.0	- 10.3	- 11.3
0.8	- 7.4	- 7.6	- 9.3	- 10.7
0.9	- 5.3	- 6.2	- 8.5	- 10.1
1.0	- 1.9	- 3.3	- 7.1	- 9.7

Table 26.2 : Average peak sidelobe level for different levels of multiplicative noise.
All results are from 150 simulations using 16 element array, with $d / \lambda = 0.5$.

26.4 Expected Magnitude of Shape Errors

As shown in [26.2], the effects on a single element of multiplicative noise and additive noise are equivalent. Ignoring the change in amplitude, which only has a minor effect upon the processing, the change in the signal is consistent with the phase error due to an erroneous element location; therefore a certain value for the noise at an element, will be equivalent to the sensor displacement that causes the same phase error. If the cause of the multiplicative noise yields values which are totally uncorrelated between sensors, then the resultant deviations of their positions will show no correlation either. Fourier analysis of a set of totally random mislocations is equivalent to examination of the frequency spectrum of white noise — i.e. all the terms have zero mean, and a constant standard deviation.

S.D. of Noise σ_m	Error in Bearing Estimate / degs			
	$\alpha = 0.0$	$\alpha = 0.5$	$\alpha = 0.85$	$\alpha = 0.95$
0.1	0.08	0.11	0.14	0.10
0.2	0.14	0.23	0.25	0.22
0.3	0.21	0.28	0.41	0.31
0.4	0.31	0.45	0.53	0.40
0.5	0.35	0.56	0.71	0.48
0.6	0.48	0.73	0.76	0.65
0.7	0.53	0.78	1.08	0.71
0.8	0.62	1.02	1.13	0.79
0.9	9.6	4.8	1.24	0.82
1.0	26.6	15.6	4.3	1.02

Table 26.3 : Average bearing error for different levels of multiplicative noise.
All results are from 150 simulations using 16 element array, with $d / \lambda = 0.5$.

Thus uncorrelated noise should cause shape estimates to converge on configurations for which the expected value for each coefficient is zero, and its expected magnitude is a constant, independent of the order of the term. In the particular application used here, it is the rms error associated with each basis function that should maintain a constant value. The conversion factor, ζ_i, employed in 15.6, related the amplitude coefficients of the basis functions to their respective rms deviations. Applying the values 0.31, 0.44 and 0.71 obtained for the first three terms, to the 'error' values associated with $\alpha = 0$ [first results column of Table 26.1], shows the rms deviations of all three to be approximately equal. This is only true for uncorrelated noise of magnitude $\sigma_m \leq 0.8$. Above this level, the formulation is unable to deal with the large shape variation required, and thus no relationship is apparent between the magnitudes of the various Δa_i rms values produced.

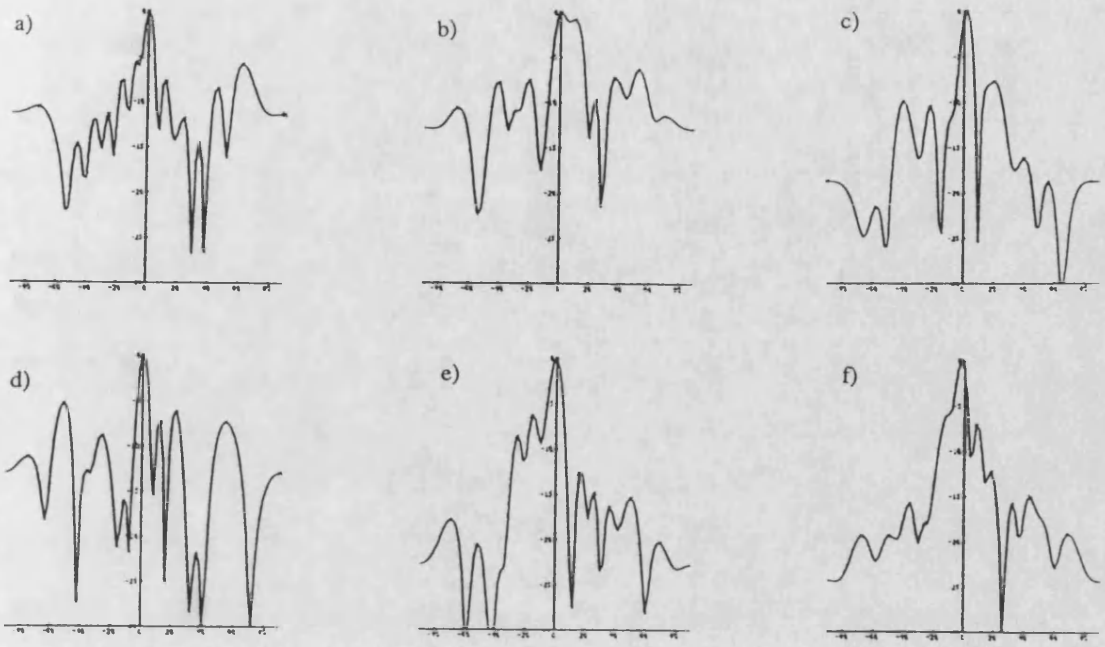

Fig 26.1 : Plots of beam patterns for different values for the standard deviation (σ_m) and correlation (α) of multiplicative noise. a-c) $\sigma_m = 1.0$, $\alpha = 0.5$; d) $\sigma_m = 1.0$, $\alpha = 0.0$; e) $\sigma_m = 0.8$, $\alpha = 0.5$; f) $\sigma_m = 1.0$, $\alpha = 0.85$

The phase change due to a multiplicative value of η_i is given by:-

$$\Delta\phi_i = \arg(\eta_i) = \arg(e^{\gamma}) \simeq \gamma_2 \qquad [26.4]$$

where $\gamma = \gamma_1 + j\,\gamma_2$ and $|\gamma| \ll 1$. As the multiplicative noise was created with mean zero and s.d. σ_m, the phase change, $\Delta\phi_i$, will have zero mean and a rms value of $\sigma_m/\sqrt{2}$. Therefore:-

$$\mathrm{var}(\Delta\phi_i) = \sigma_m^2 / 2 \qquad [26.5]$$

For an error in a single basis coefficient, Δa_i, the rms position error of the hydrophones is $\zeta_i\,\Delta a_i$. Consequently, errors in all the coefficients cause a total rms phase error, $\Delta\Phi$, given by:-

$$(\Delta\Phi)^2 = k^2 \sum_{i=1}^{n-2} \zeta_i^2\,(\Delta a_i)^2 \qquad [26.6]$$

where n is the number of sensors, and k is the wavenumber. Applying the expectation operator, and noting as before that $E[\zeta_i^2 (\Delta a_i)^2]$ is a constant over all i, reduces the expression to:-

$$E[(\Delta\Phi)^2] = k^2 \cdot n\text{–}2 \cdot E[\zeta_i^2 (\Delta a_i)^2] \qquad [26.7a]$$

$$\rightarrow \quad \text{var}(\Delta\Phi) \approx k^2 n \zeta_1^2 \ \text{var}(\Delta a_1) \qquad [26.7b]$$

Now, the cause of the phase fluctuations here was not the misshapen array, rather it was the response to match the phase changes arising from the multiplicative noise. Substituting the statistics for such phase changes [26.5] into [26.7b] yields the expected dependence of shape mismatching upon multiplicative noise, namely:-

$$(\Delta a_1)_{rms} \approx \frac{\sigma_m}{\sqrt{2n}\, k\, \zeta_1} \qquad [26.8]$$

The figures in the first results column of Table 26.1 show reasonable agreement with this prediction. [Note, the derivation assumed that $\sigma_m \ll 1$ and that the noise was uncorrelated — consequently the above treatment applies to additive noise as well.]

27. REGION OF CONVERGENCE TO TRUE SHAPE

27.1 Introduction

The preceding chapters (nos. 18-26) show how precisely power functions may be able to estimate array shape and source bearing(s) in the presence of various noise levels, correlations, secondary sources, different weighting schemes etc. Chapter 30 indicates how a suitably constructed basis removes any bias in the estimation of one Fourier term, despite errors in the others; whilst chapter 31 relates how a gradient search routine may be used to locate the peak promptly. In these it is demonstrated that the shape parameters can be determined quickly and accurately using power functions from errors of over 2m (one third of a wavelength).

This and the ensuing chapters (28, 29) are concerned with the size of the 'convergence region' i.e. that part of the vector space spanned by the coefficients from which use of power functions can enable the correct shape specification to be approached.

Fig 27.1a shows how one of the power functions (pf4) varies for various errors in the first coefficient, a_1. The pf is 'well behaved' over the range of values shown in that there is only one maximum and the pf does not achieve a constant level. Therefore processing of two trial shapes, differing slightly in their value for a_1, will always yield pf values ordered such that that for the shape nearest to true is the greater. In such a case, an algorithm can correctly infer the direction in which a_1 needs to be altered.

Fig 27.1b shows the same scenario examined over a greater range of a_1. For values of a_1 less than -17m or greater than 17m, comparison of neighbouring trial shapes may fail to infer the correct direction for approach to the global maximum; thus the algorithm will then converge to one of the local subsidiary maxima at $a_1 = -32$m or $a_1 = 32$m.

Note, as the beam patterns *gradually* evolve with changes in the estimated parameters it follows that power functions will change smoothly too i.e. there will be no discontinuities in the variation of a pf with shape. Also, for the pfs of integral form, their derivative with respect to the shape parameters will be continuous too. The spiky nature of some of the diagrams contained in this thesis is simply due to insufficient sampling in terms of values of a_i — this is due to processing time

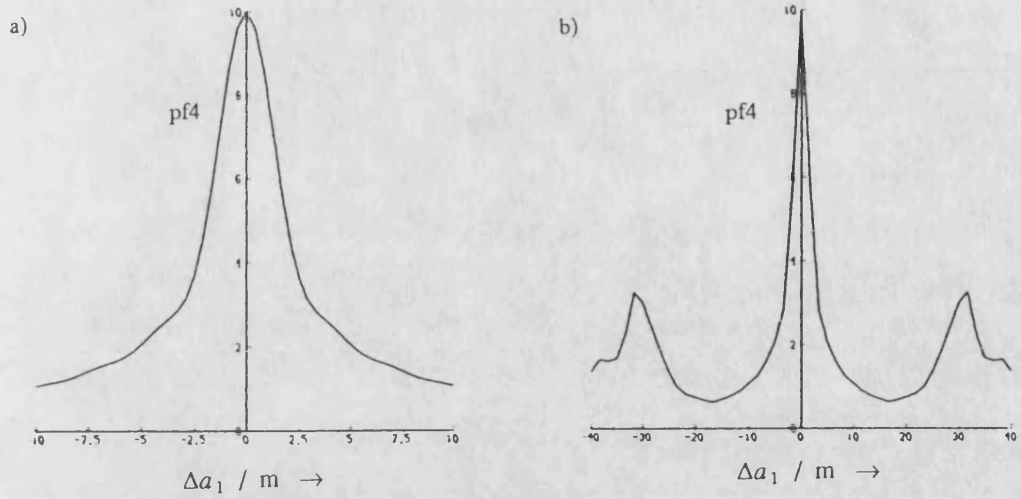

Fig 27.1 : Variation of a power function with the error in estimation of the first coefficient.
Plots for a 16 element array, with λ/2 spacing (λ = 6m). a) $-10.0\text{m} \leq \Delta a_1 \leq 10.0\text{m}$; b) $-40.0\text{m} \leq \Delta a_1 \leq 40.0\text{m}$.

and storage limiting the number of trial shapes that could be tested.

It should be observed that the deviations referred to here (> 10m) are unrealistic for a 16 element array of length 48m. Not only is an array that short unlikely to contain such variations, but also the characterization of the array shape [Eqs. 11.1, 2] is no longer valid, as the elements will no longer have equally spaced x-values. Consequently, most of this section is only pertinent to larger arrays, of at least 16λ in length (32 elements at λ/2). However, as computation time increases approximately as the square of the number of elements (due to the required reduction in separation of the beams), most simulations are done for arrays of 16 or 32 elements.

27.2 Location of Minima

From parameter searches, such as illustrated in Fig 27.1b, the important measure as regards the size of the convergence region is not the locations of the subsidiary maxima, but rather the positions of the minima nearest to the parameter value for the correct shape, as it is these which delimit the range of a_i for which convergence to true is certain. [Note, these local peaks observed in

section may not necessarily have zero gradient w.r.t all parameters — thus it is possible that search routines may uncover a continuously uphill route from a subsidiary 'maximum' to the true one, that makes an excursion in one or more of the other dimensions. Such will greatly increase convergence time, and is not easy to demonstrate. An artificial surface is shown in Fig 27.2a for which this is true.]

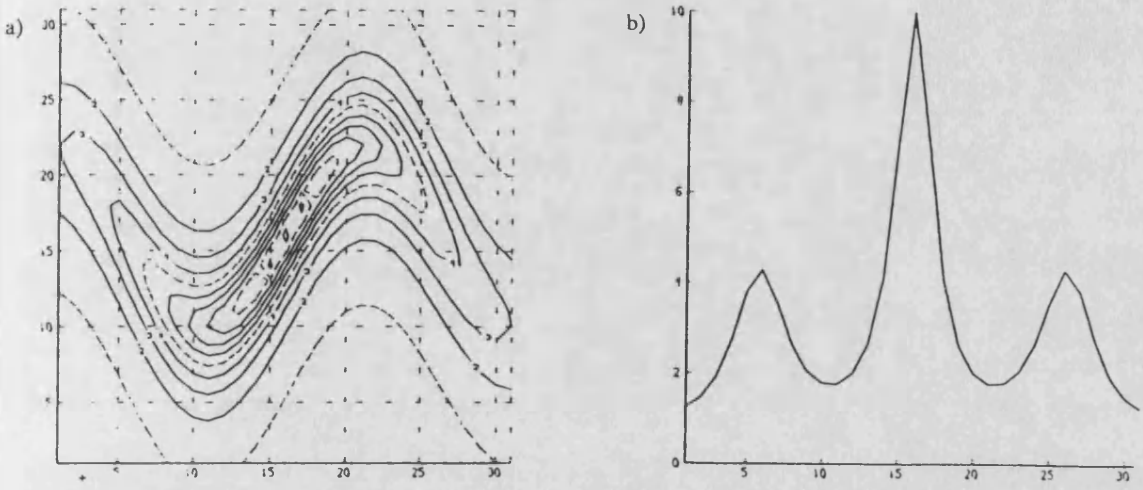

Fig 27.2 : a) Contour plot of a surface with only one maximum.

b) Cross section of a) showing 3 apparent maxima. [All units arbitrary.]

It would be expected that the locations of the minima be specific to a particular scenario and type of processing. As the pf display (as in Fig 27.1b) has stretches of nearly constant level, slight fluctuations in the power function may easily give rise to extra peaks and consequently nearer minima; thus the positions of the minima can be surprisingly sensitive to details of the scenario. As an example, Table 27.1 gives the approximate positions of the nearest minima for a series of scenarios with identical array shape and processing, but different bearings for the only source.

Although it may be expected that the minima should be approximately symmetrically placed about the true value (or rather about the particular peak for that realization), this is clearly not always the case. For most of the entries in Table 27.1, the values for lower and upper minima are the same or differ by only 1m. In some cases, the difference amounts to 2 or 3m. [Note, here the resolution limit, i.e. the separation in a_1 of different trial shapes, is 1.0m.]

Source Bearing / degs	-40.	-36.	-32.	-28.	-24.	-20.	-16.	-12.
Δa_1 / m for lower minimum	-13.	-13.	-14.	-14.	-15.	-14.	-17.	-16.
Δa_1 / m for upper minimum	12.	13.	14.	13.	15.	16.	15.	19.

-8.	-4.	0.	4.	8.	12.	16.	20.	24.	28.	32.	36.
-16.	-20.	-17.	-17.	-16.	-16.	-15.	-14.	-14.	-13.	-13.	-12.
17.	17.	15.	18.	17.	16.	15.	15.	14.	14.	14.	12.

Table 27.1 : Variation of minima locations with source bearing.

[Results relate to estimation of a_1 for a 16 element array, with λ=6m, and beamforming every 2^o.]

The variations for other power functions mirror approximately those given in the table for pf4, showing a maximum size of the convergence region for the source near broadside, with a gradual reduction towards $\pm 40^o$; however, each shows different variations about the general trend indicating a fine sensitivity to bearing angle. Similarly, a source at a fixed bearing insonifying various differently shaped arrays gives a range of convergence limits. Variations of a few metres depending upon the fine scale of the scenario make comparisons more difficult; however, generally a processing approach that improves convergence range for one particular array shape and source scenario will do so for others, even though the results for the two situations may differ by as much as 20%. [An exception is pf8, whose behaviour for the range of conditions in Table 27.1 showed fluctuations about a curve with a minimum for a source at broadside. Its behaviour is not always anomalous in this manner.]

27.3 Minima for Higher Order Terms

In a similar manner, the minima for the 2nd, 3rd and 4th coefficients may be determined for a range of source bearings. The results given in Table 27.2 relate to 20 different bearings from -40.7° to 25.8° in steps of 3.5°. The locations are given for the average positions of the lower and upper minima for pf4. Also included are the equivalent results achieved with a small but significant noise level (-20dB relative to the source). Using the results for the no noise case, a mean absolute position of the minima may be calculated, $\overline{\Delta a_i}$, — the final column expresses this value in terms of wavelengths.

Fourier Index i	Resolution limit da_i / m	Mean Δa_i / m for no noise		Mean Δa_i / m for -20dB noise		Mean Abs. Position $\overline{\Delta a_i} / \lambda$
		Lower min.	Upper min.	Lower min.	Upper min.	
1	1.00	15.40	15.20	14.43	14.33	2.55
2	0.40	6.56	6.28	6.41	7.37	1.07
3	0.33	4.63	4.33	4.42	4.60	0.75
4	0.33	3.92	4.07	3.82	3.98	0.67

Table 27.2 : Location of minima of pf4 for an array of 16 elements at $\lambda / 2$ spacing (λ = 6m). Minima averaged from 20 source position over -40.7° to 25.8°, using beamforming over [-60°, 60°]. Resolution, as given in column 2, is coarse, but due to averaging results should be fairly accurate.

It can be seen that the mean positions of the upper and lower minima are symmetrically placed about true. Also, noise at the -20dB level (or lower) has minimal effect on these positions.

Note, when the description of the convergence range is altered from amplitudes of Fourier coefficients to their rms displacements (via the conversion factor, ζ_i, introduced in chapter 15.6) the estimator still shows more resilience to errors in the first function than to those in the lower order terms, $(\Delta a_1)_{rms} / \lambda$ being 0.79, whilst for the others $(\Delta a_i)_{rms} / \lambda$ is around 0.55.

27.4 Different Choices of Average

In the above work, the 'average' location of the minima, $\overline{\Delta a_i}$, was calculated as the mean of the absolute values of the whole ensemble. In many statistical applications an rms value is deemed appropriate — this always being larger than the aforementioned one, as it takes greater note of the large values. In a lot of simulations it is right to highlight the extremely large values, however here it is the smallest values which should be thought of as critical. Occasional occurrences of very close minima are causes of grave concern, and special note should be taken of them. Consequently, more suitable definitions of 'average' for this situation are:-

$$a_i^{\dagger} \qquad \text{where} \qquad N \,/\, a_i^{\dagger} \;=\; \sum_{i=1}^{N} \left(1 \,/\, |\, \Delta a_i \,| \right) \qquad [27.1a]$$

$$a_i^{\dagger\dagger} \qquad \text{where} \qquad N \,/\, \left(a_i^{\dagger\dagger} \right)^2 \;=\; \sum_{i=1}^{N} \left(1 \,/\, \Delta a_i \right)^2 \qquad [27.1b]$$

Of these two, [27.1b] is probably the more appropriate, simply because it corresponds to an rms error in wavenumber space, and thus may be more open to mathematical manipulation than the definition containing the modulus function. As all results in this section bear some degree of uncertainty, because of values' fluctuation with fine scale, and the poor resolution obtainable (e.g. in Table 27.2, the individual Δa_1 measurements were only available to the nearest metre), it is not too important which definition is used, as long as comparisons are always made between situations with similar processing and averaging. Consequently, the mean absolute value, $\overline{\Delta a_i}$, as used earlier, is retained throughout.

There is one case of particular note. If the true array shape is a straight line, i.e. all the a_i are zero, then the lower and upper minima occur at exactly symmetrical locations, and these values are symmetrical w.r.t bearing too. A simple smooth variation is observed over θ — the minima locations becoming closer as the source moves towards endfire at a rate intermediate between $\cos\theta$ and $\cos^2\theta$. As the minima points seem so well behaved for the straight line array with broadside source, such is often adopted as the standard situation to avoid the complications of the averaging required to remove fine scale effects.

27.5 Accuracy in the Determination of the Minima Points

As the pfs are only calculated at a finite number of values of a_i, the observed minima points will be displaced from the true values (which could be found by more frequent sampling). The storage constraint on this computer program limits the number of a_i values that can be used in one search. The resulting sampling error over a_i, means that any particular result may err from true by 10-15%.

If no noise is present in the simulation, repeated realizations will yield the same values, and so averaging will not yield a more accurate figure. Many realizations of a noisy scenario *will* produce a useful and meaningful average, as will slightly different source directions or true array shapes for the no noise case.

Much of the zero noise investigation can be done adequately from individual realizations, as high accuracy is not required. It is to be noted that with such an approach occasional results may be anomalous i.e. a quirk of the particular combination of scenario and processing, and not reflect the general behaviour. Care has been taken to minimize such incidents.

27.6 Different Numbers of Hydrophones

An increase in the number of hydrophones usually corresponds to an increased array size, and consequently the magnitude of the array deviations is likely to change. However, this does not reduce to the original situation rescaled by a factor throughout, as the beam pattern has changed (become finer) due to the increased resolution of the larger array. Also, a bow error (incorrect value of a_1) of $\lambda/2$ [see Table 15.3] is sufficient to obscure a source no matter how high the SNR or long the array.

Therefore, it is not necessarily simple to extrapolate the minima locations from a 16 or 32 element array as used in these simulations to ones of 64 or more elements that may be used in practice. Consequently some work was done on large arrays; Table 27.3 compares the results of such with the shorter ones that have been more thoroughly studied.

The results show an increase in convergence region with number of elements, n, as would be expected. The size of the region appears to be approximately proportional to n; albeit that the

No. of elements n	Average location of pf4 minima / m			
	$\overline{\Delta a_1}$	$\overline{\Delta a_2}$	$\overline{\Delta a_3}$	$\overline{\Delta a_4}$
16	18.0	8.0	6.0	4.7
24	28.5	15.3	7.3	6.0
32	38.0	21.0	7.3	7.3
48	63.0	33.0	12.0	7.3
64	90.0	42.0	19.0	19.0

Table 27.3 : Increase of convergence region with number of receivers.
All arrays had sensors at half wavelength separation (λ = 6m). [Results are for a source at broadside and a straight array, using beamforming over [-60°, 60°] in steps of 0.75° ; no noise present.]

results are rough owing to the coarseness of the measurements. The actual values given in the table show a slightly greater rate of growth for the a_1 and a_2 spans than for the lower terms; however the figures given are not sufficient to indicate whether such occurs in general i.e. for all shapes, and repeatedly larger arrays.

27.7 Different Power Functions

Although the majority of the useful power functions can be seen to have very similar properties as regards estimation accuracy [see chapters 17, 20], it is important to examine whether such is the case for the size of the convergence region. The results of an investigation into this are shown below in Table 27.4.

It is apparent that for the cases shown (zero noise) there is negligible difference between most of the pfs. An exception is pf8, that which is solely a measure of the peak height. Although the primary source ceases to be prominent for errors in excess of 3m, it is clear that for, say a 32 element

No. of elements n	Average location of minima, $\overline{\Delta a_1}$ / m				
	pf4	pf5	pf8	pf14	pf16
16	18.	14.	3.0	18.	18.
24	28.5	22.5	7.5	28.5	27.
32	38.	32.	20.	38.	32.
48	63.	63.	39.	63.	63.
64	90.	90.	48.	90.	90.

Table 27.4 : The variation of minima locations with choice of power function.
Results are for a source at broadside, with a straight array using beamforming over [-60°, 60°] in steps of 0.75°, and different numbers of elements. [Wavelength, $\lambda = 6$m ; no noise present.]

array, *all* the lobes are decreasing in size as $\Delta a_1 \rightarrow 20$m, albeit that the one in the direction of the source diminishs quickest. [This is only true on a coarse scale — examination at more finely spaced values of a_1 [see Fig 16.2] shows several small lobes in the variation of pf8.]

For a great many situations, pf4 continues to provide a performance that equals or surpasses others. In certain of the simulations involving noise, a difference can be discerned: this is mentioned where appropriate.

27.8 Effect of Different Weighting Schemes

Although all of the weighting schemes investigated had the effect of reducing the sidelobe levels for processing using the true shape, this did not in itself make the source peak visible for any greater range of a_i. A heavily shaded array is in many ways similar to consideration of only the central part of the original. Consequently, an error of a certain size in the a_1 term corresponds to a much smaller bow in the central 'effective' array. For this smaller error, the source might still be

visible whereas the larger error in the whole array would have obscured it. Thus weighting can increase the magnitude of the bow error that still leads to a primary peak in the source direction. A similar argument holds for errors in a_2. Of the five systems of weighting investigated [see chapter 11.6], Hamming led to the largest convergence region — for a_1 and a_2 it was about 25% bigger than for uniform. For higher order coefficients, the convergence regions are approximately equal for all weightings, as then consideration of predominantly the central portion can not improve the performance. This is because the relative deviations within the central section are the same as those for the array viewed as a whole.

The majority of the estimators behave as the one detailed above (pf4), the exception being pf8 (the peak height measure). On account of the reduced sidelobe level and increased source visibility associated with Hamming weights, the improvement in performance of pf8 is even more marked than for pf4, such that over a_1 and a_2 its limiting range is the same as for the others, rather than only 50% of their value as occurred for uniform weighting.

28. CHANGE IN CONVERGENCE REGION DUE TO A SECOND SOURCE

28.1 Effect on Estimation of a Single Term

Chapter 25 shows that the presence of another source does not improve the accuracy of the shape estimate; rather the interaction between the signals of the two sources causes a bias in the determination of the coefficients, and that bias is dependent upon the relative phase of the two emissions. Consequently, care was taken in the measurement of the convergence range for two source scenarios to allow for similar behaviour. Table 28.1 indicates how the minima for a specific two source situation vary with changes in the relative phase.

The presence of the extra source has vastly reduced the convergence region for both a_1 and a_2. In the case of a_1 there is a shallow minimum near ±3.5m that varies little with the relative phase of the two sources. However, the minima points for a_2 are strongly dependent on the phase difference — the positions of the nearest minima varying from ±1.8m to ±6.4m.

The pf display for a_2 (i.e. plot of values of pf4 versus errors in a_2) shows sizable secondary peaks for $\Delta\phi \approx 0^o$. These peaks rapidly fade to nothing as the phase changes by 180^o, so the larger minima locations for $\Delta\phi \approx 180^o$ are not due to the minima moving, but rather to them disappearing to reveal the distant ones.

Examination of the behaviour for different power functions shows that they all exhibit similar behaviour — though most produce minima slightly nearer to true than pf4 does. The minima for a_3 show wide variation like those for a_2.

Relative Phase $\phi_1 - \phi_2$	Position of minima of pf4 / m				
	Lower Δa_1	Upper Δa_1	Mean $\overline{\Delta a_1}$	Lower Δa_2	Upper Δa_2
0°	- 3.60	3.65	3.63	- 1.9	1.8
30°	- 3.60	3.45	3.53	- 2.0	1.8
60°	- 3.55	3.30	3.43	- 2.1	2.0
90°	- 3.55	3.30	3.43	- 2.5	6.4
120°	- 3.55	3.30	3.43	- 6.3	6.2
150°	- 3.65	3.40	3.53	- 6.0	6.1
180°	- 3.60	3.60	3.60	- 5.9	6.1
210°	- 3.40	3.65	3.53	- 6.0	6.1
240°	- 3.30	3.55	3.43	- 6.3	6.2
270°	- 3.30	3.55	3.43	- 2.5	6.4
300°	- 3.30	3.55	3.43	- 2.1	2.0
330°	- 3.45	3.60	3.53	- 2.0	1.8
Average	- 3.49	3.49	3.49	- 3.8	4.4

Table 28.1 : Variation of minima locations with relative phase of sources.
[16 element array at $\lambda/2$ spacing (λ = 6m); primary source at 4.7° and secondary (3dB weaker) at -25.4°. No noise present. Uniform weighting applied at beamforming stage.]

28.2 Two-Dimensional Searches

The minima in a_1 and its associated subsidiary maxima are very shallow, so it is possible that search routines will not be distracted from the true peak by those minor ones. Also, several independent signal records will contain different values for the relative phase of the sources; consequently the variable peaks for a_2 will not always be present to deflect search routines from the true shape, although they may succeed for 5 occasions out of 12 [see Table 28.1].

However, convergence to the true shape parameters from a significantly erroneous one is not a simple matter, as typically neither of the initial values for a_1 or a_2 is correct. The importance of this statement is shown by the contour plots in Fig 28.1.

The plots are for 4 of the situations referred to in Table 28.1 — phase differences of 0^o, 90^o, 180^o and 270^o. The weak minima for errors in a_1 alone are not discernible; the strong subsidiary peak for an error in a_2 can only be seen clearly for a relative phase of 0^o. However, a common property for all the diagrams is a significant peak in the region of $(a_1, a_2) = (3.5, 1.5)$ and its reflection points in a_1 and a_2. Coupled with the two variable ones on the a_2 axis, they provide a 'protective shield' around the true peak, rendering it unlikely that simple gradient search routines will converge to the correct shape.

This is thus a definite limitation to the power function approach. It is to be noted that an error in a_1 of only 3.0m is sufficient to mask the main source for 9 out of the 12 occasions [cf Table 15.3]. However, the combination of errors in a_1 and a_2 at the subsidiary peak define an array shape for beamforming that enables the primary to be found for 6 of the simulations, and the secondary too for 4 of those — albeit that the bearing estimates for both showed a bias of about -5^o.

28.3 'Fixed' False Peaks and 'Jumps' to True

Although the maxima near $(a_1, a_2) = (0., \pm 3.0)$ are transient in that their presence depends on the phase of the signals, that near (3.5, 1.5) appears more permanent. Not only does it occur for all phase differences for the scenario investigated above, but it and/or its mirror image at $(3.5, -1.5)$ is present for different power ratios of the sources and for different separations.

Increasing the power of the second source such that it is equal to the first makes little change to contour plots of pf4. Reducing the power ratio to -6dB causes the extra maxima to diminish, although their approximate positions are maintained. Further reduction to -12dB removes the maxima completely, producing a pf variation akin to that for a single source scenario. Clearly such a weak second source can only be discernible with significant element weighting and/or low noise levels. However, the increased probability of locating the primary, when the power ratio is reduced to -12dB, is important.

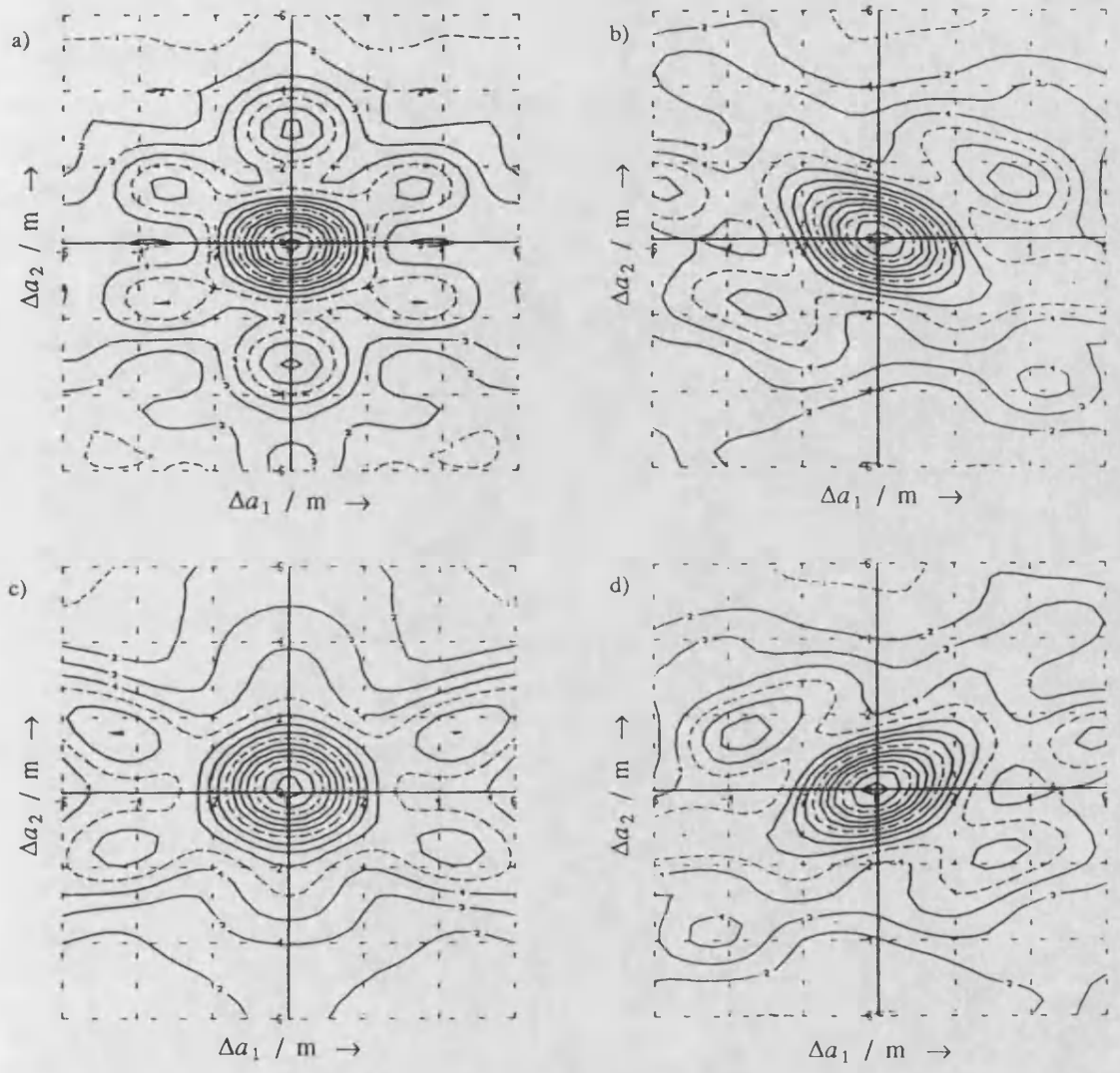

Fig 28.1 : Four contour plots to show variation of pf4 over a_1 and a_2.

All diagrams are for a 2 source scenario — primary at 4.7°, secondary (3dB weaker) at -25.4°.

Diagrams show the differences for $\phi_1 - \phi_2$ equal to 0°, 90°, 180° and 270° respectively.

[$\lambda = 6m$; $-6m \leq \Delta a_1 \leq 6m$; $-6m \leq \Delta a_2 \leq 6m$]

Altering the angular separation of the sources does affect the position of the maxima. When the sources are nearer than 15°, the subsidiary peaks disappear, leaving a convergence region of ±8m for both a_1 and a_2 — thus covering all realistic array contortions. [Note, this is for a 16 element array of beamwidth ≈8°.] A greater separation causes the maxima to be further away, although still in approximately the same vector directions as before.

These vectors, $(\Delta a_1, \Delta a_2) = (0.0, \pm 3.0)$ and $(\pm 4.0, \pm 1.5)$ are clearly important in that they are characteristic of maxima positions for this particular array design and processing. [The values given are averages, typical of the nearest peaks for a variety of source scenarios.] If the pf algorithm has converged to a shape specified by (a_1', a_2'), but in spite of locating a local maximum is unsatisfied by the focusing achieved, then a different strategy may be adopted. Previous convergence work relied on the smoothness of the pf variations and the uniqueness of the maximum; in cases where this second assumption is false, it can be beneficial to investigate the pf values at the points $(a_1', a_2' \pm 3.0)$ and $(a_1' \pm 4.0, a_2' \pm 1.5)$. If any of these yields a higher value than that at the top of the present peak, then that point must lie on a greater peak, probably the true one. Note, this will not lead to a 'jump' from the true peak to a false one, as the latter would be smaller.

This is in many ways an empirical approach, not in keeping with the concept of gradual convergence via a gradient method. However, its aim is the same — a strategy for reaching the point of highest pf value without explicitly beamforming and calculating the power function for all points on a grid of 2 (or more) dimensions. The key to this approach is the well defined locations of the subsidiaries relative to the true maxima, necessitating that only 6 points be tested prior to a 'jump' in the vector space.

[This is a slightly idealised view, as the relative positions do show some variation, thus an initial jump attempt may fail. As an example, for widely separated sources, the subsidiary may be at (6.5, 2.5), thus a leap of (–4.0, –1.5) will not reach the main peak. To cope with such situations, a secondary leap attempt might be required using vectors approximately 70% bigger than before, although this would increase the complexity of the process, and also the number of trial shapes tested. Note, in many cases for such distant maxima, the initial shape estimate is likely to be inside the 'defensive wall' and hence not led astray by the false peaks.]

28.4 Effect of Weighting the Elements

As mentioned at other stages, shading the elements places more emphasis on the signals from the central portion of the array, within which the deviations (and estimated errors therein) are smaller than for the array as a whole. Application of Hamming weights to the processing of the two source scenario detailed above leads to a great simplification of the problem, as the subsidiary maxima are absent from many of the contour plots. Where they remain, they are located about 30% further along the vectors specified before, but showing greater variation in position.

For simulations involving sources 17^o apart, Hamming weights lead to far fewer peaks than uniform, as the former causes much wider mainlobes in the beam pattern, such that they are almost like one source, for which convergence is simple. However, in the majority of such cases, the highest point on the contour plot corresponds to a shape erring by a metre or so in a_1 or a_2. Such is not the case for uniform weighting, which always gives a peak very close to the true specification of the array shape.

28.5 Increased Number of Hydrophones

Some investigations were done for a 64 element array with half wavelength spacing (hence 4 times as long as the previous 16 element one). They showed the maxima to be considerably more distant; rough measurements indicated the peaks to be about 3 times as distant as for 16 elements, rather than the 4 times expected for linearity. Certainly part of the reason for the improvement is that the beamwidth is considerably less, such that sources, say 30^o apart, have reduced interaction.

A short series of investigations over 3 unknowns indicated that a prominent peak is present at around $(a_1, a_2, a_3) = (11.0, 2.5, 1.6)$. There may be many extra peaks at this distance when all mirror images and other points are included. Thus the 'jump' approach may be of little benefit, if a large number of extra shapes needs to be tested. However, it was interesting to note that at this highly inaccurate shape estimate, a degree of focusing had been achieved which enabled both sources to be pinpointed to within a few degrees on 75% of occasions!

An important observation from this is that a clear convergence region of $\pm$12m (i.e. 2λ) in a_1 and a_2 might be expected for arrays in excess of 100 elements, whilst it is possible that the shape fluctuations for such a 300m array will not exceed that.

28.6 Summary

The presence of a secondary source, of significant amplitude compared to the first, has been shown to have grave consequences for shape estimation via the pf method. For a single source with no added noise the pf surface plotted over a_1 and a_2 exhibits a unique maximum, the pf falling off monotonically from it. However, the structure is not that of a simple hillock — ridges run off along the vector directions ($\pm 4.0, \pm 1.5$) as is shown by Fig 28.2. When the second source is within 6dB of the primary, the interaction between them causes subsidiary maxima to occur along some of these ridges. Also, a peak may occur on the a_2 axis (at $a_2 = \pm 3.0$ for a 16 element array) — though this depends very much on the relative phase of the sources.

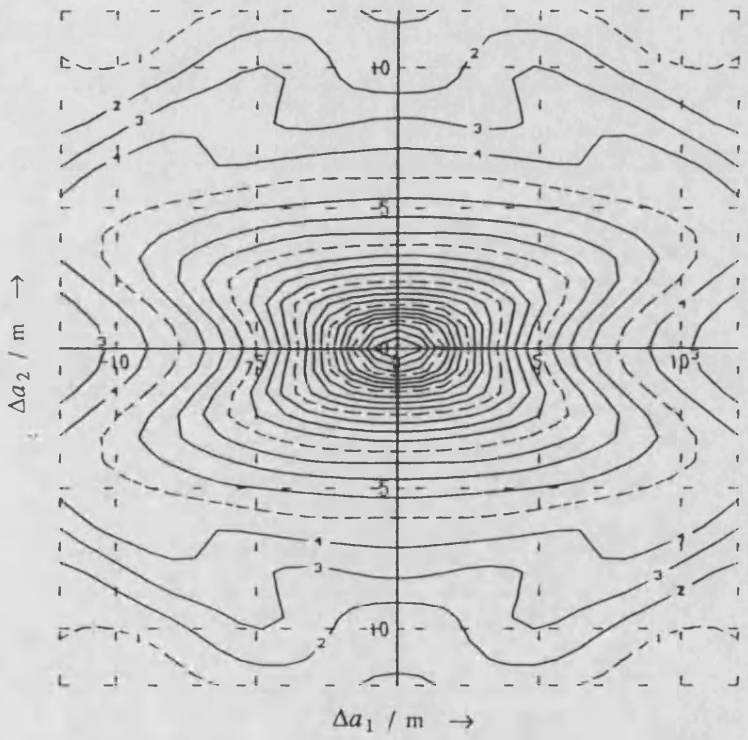

Fig 28.2 : Contour plot to show variation of pf4 for various values of a_1 and a_2.

[Array has 16 elements at $\lambda / 2$, ($\lambda = 6$m). Single source; no noise.]

The maxima are fairly constant in position, being constrained by the positions of the ridges. Altering the relative phase of the sources or changing the pf examined makes little difference. The relative power P_2 / P_1 mainly affects the intensity of the maxima, not their positions. A wider

angular separation of the sources causes the maxima to lie at a further distance along the ridges. Increasing the number of elements (for constant element spacing) also increases their distance.

Subsidiary maxima also occur in displays of the $a_1 - a_3$ and $a_2 - a_3$ planes. There is also evidence of significant peaks occurring for non-zero values of all of a_1, a_2 and a_3 — these are not easy to investigate, and hard to illustrate.

For many of the low noise cases investigated, use of significant element weighting removes any near subsidiaries, making convergence simpler. However, weighting schemes such as Hamming tend to show poor accuracy in locating the precise array characterization, thus it is prudent to use Hamming or others for convergence from afar, and then revert to uniform weights in order to pinpoint the true shape accurately.

Note, if the two sources emit at similar but distinguishable frequencies, then the problem will not arise — shape estimation could be performed independently (and accurately) using the two separate sources; comparison of the estimates will then confirm the validity of the approach. If the two sources are at indistinguishable frequencies (i.e. one characteristic sharp resonance for both sources, and no Doppler shift for either), then the situation is more complicated. However, varying refractive index in the ocean along the two different ray paths will remove any phase lock, such that successive measurements will yield situations with different structure for the subsidiary peaks. Some degree of averaging will remove several false peaks, but it is likely that some will remain along the ridges proving a hindrance to basic convergence routines.

One approach for overcoming the obstructions that these maxima provide to search routines is to employ the concept of a 'jump' in values. This involves calculation of pf values for a few trial shapes corresponding to particular step sizes along possible ridges. If a higher pf value is found than that at the current summit, then the tested place must lie on a larger peak, probably the true one.

Lastly, it is to be borne in mind that several of these 'false' peaks, corresponding to highly inaccurate shape estimates, can actually enable the sources to be located accurately, with a probability of success often exceeding 50%. [This observation, like the rest of this chapter, was based on simulation work with no additive noise, because the presence of such, would have made it harder to view the structure present. A few simulations of the two source scenario with noise have shown a marked degradation in the clarity of the beam pattern at a false peak, indicative of the importance of achieving the true pf peak.]

29. EFFECT OF NOISE ON CONVERGENCE REGION

29.1 Introduction

For a single source, without noise, the convergence region is large — this is illustrated in Fig 29.1a for a 16 element array. The pf variation over a_1 shows only one peak over the interval $-18\text{m} \leq \Delta a_1 \leq 18\text{m}$, and the limits for a_2 are $-8\text{m} \leq \Delta a_2 \leq 8\text{m}$. Addition of significant noise (-3dB per element) has a marked effect on the appearance of the contour plot, as evidenced by Fig 29.1b — the when $\Delta a_2 = 0$ and $-4.0\text{m} \leq \Delta a_2 \leq 2.2\text{m}$ where $\Delta a_1 = 0$ for this specific realization. For other combinations of Δa_1 and Δa_2 the region of convergence is significantly less due to the introduction of new secondary peaks.

The contour plot gives a good idea of the convergence region for uncertainties in both a_1 and a_2 ; however, an adequate representation for comparison purposes can be achieved by noting the mean absolute positions of the minima — $\overline{\Delta a_1}$ being 8.3m and $\overline{\Delta a_2}$ 3.1m for the case illustrated. Clearly, a meaningful value, representative of the given noise level can only be achieved by sufficient averaging.

29.2 Effect of Processing Choice

As this part of the work is concerned with how large a shape error lies within a convergence region, it was necessary to fix on a particular set of processing parameters as standard, such that different scenarios might be effectively compared. First of all, tests were done to register the relative merits of different power functions, beam sampling rates, angular scans and weighting systems. The findings are briefly summarised in Table 29.1.

The actual simulation conditions used for the comparison were carefully selected — a significant noise level (-3dB per element), as that was of concern here, and a 64 element array, as much of the work in this chapter is particularly relevant to lengthy arrays. [The large computational load for big arrays necessitates that only a small number of signal records be investigated.] For comparison with the tests of accuracy dependence upon different processing methods

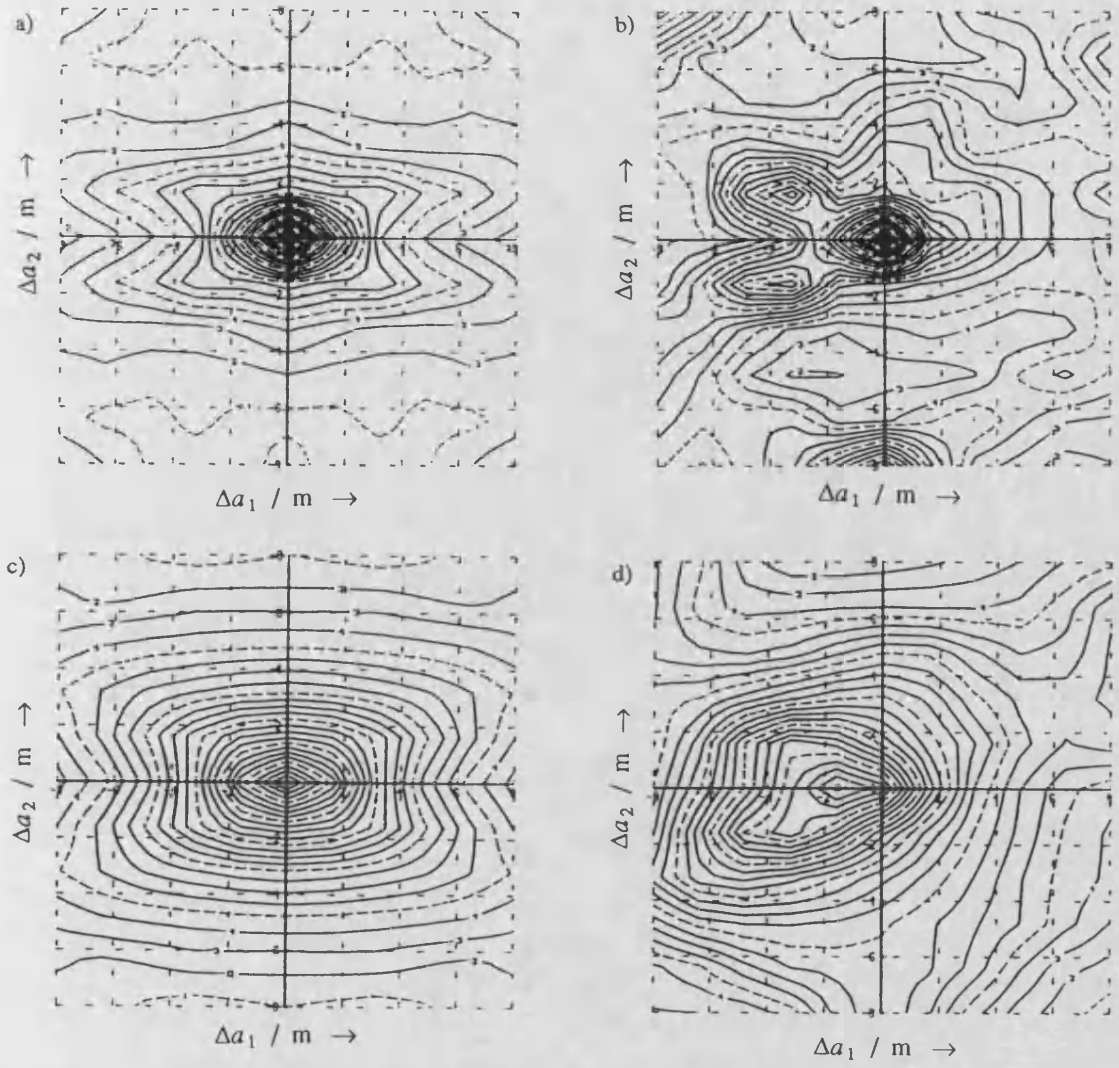

Fig 29.1 : Contour plots for 16 element array, showing variation of pf4 with a_1 and a_2.

a) Uniform weighting at the beamformer, with no added noise ; b) Uniform weighting with -3dB noise ;

c) Hamming weighting with no noise ; d) Hamming weighting for same signal record as for b).

[$\lambda = 6$m ; $-8\text{m} \le \Delta a_1 \le 8$m ; $-8\text{m} \le \Delta a_2 \le 8$m]

[see chapter 18], it should be noted that 0.5^o sampling for a 64 element array is equivalent to 2^o sampling for 16 elements, whilst 1.5^o is equivalent to the sparse 6^o sampling.

For a correctly focused 64 element array, the power perceived from angles more than 30^o from the source is minuscule and can be easily discounted without affecting the accuracy of the shape estimates; however, when ascertaining convergence regions, the power spread into such sectors

Angular Sector Scanned	Angular Resolution	Weighting System	Average Minima Locations $\overline{\Delta a_1}$ / m					
			pf4	pf6	pf8	pf12	pf14	pf16
± 90°	0.5°	Uniform	28.6	25.4	13.8	27.3	33.6	27.2
± 90°	1.5°	Uniform	36.3	26.5	13.8	29.3	38.8	29.3
± 30°	0.5°	Uniform	30.6	20.9	10.6	24.3	0.0	11.3
± 30°	0.5°	Hamming	49.1	38.4	16.6	43.6	54.8	39.8

Angular Sector Scanned	Angular Resolution	Weighting System	Average Minima Locations $\overline{\Delta a_2}$ / m					
			pf4	pf6	pf8	pf12	pf14	pf16
± 90°	0.5°	Uniform	15.3	13.2	7.5	14.3	15.1	12.3
± 90°	1.5°	Uniform	16.5	14.5	7.5	15.0	15.9	13.3
± 30°	0.5°	Uniform	11.3	9.4	6.5	10.8	0.4	3.5
± 30°	0.5°	Hamming	28.7	18.4	10.3	23.8	28.8	19.0

Table 29.1 : Investigation of how the size of the convergence region depends upon processing choice. Particular data in table relate to 7 simulations of a 64 element array of $\lambda / 2$ spacing ($\lambda = 6$m), with a source at broadside, and additive noise of level -3dB on input.

does appear to be important to the accounting — here neglect of such reduces the convergence region by about 30%. It appears that reduction of the angular resolution to nearly the order of the beamwidth improves the convergence properties; this too is totally in contrast to observations concerning the accuracy of parameter estimation [chapter 18.2]. This is looked at more carefully on the following page.

In chapter 27.8, it was explained that element weighting could be beneficial for the estimation of the 1st and 2nd Fourier terms, due to its concentrated emphasis on the central, less

distorted, section of the array. However, it is a little surprising that it still provides such a clear advantage when noise is of a significant noise level, as uniform weighting generally offers the best noise rejection properties.

Note, a second series of 7 simulations for a differently shaped 64 element array, with additive noise at +3dB, confirmed several of the above findings. A reduction in resolution once more increased the convergence region; however, this was not so for the correlation pfs (14, 15 & 16), their performance being reduced by 50-80%. The increase in size of the region was mainly in the a_2 direction. However, with Hamming weights applied (and consequently a larger mainlobe), a reduction in resolution led to the correlation pfs showing a significantly increased convergence region, whilst the others were relatively unaffected. A decrease in the angular sector processed led to no change for processing with uniform weights, whilst if Hamming weights were adopted, then the reduced search sector appeared to increase the convergence region, though only by about 5-10%. More thorough experimentation suggests that a cut in resolution will usually reduce the region slightly.

Over a wide range of situations, pf4 has again consistently proved to be one of the best. Generally, in work with large arrays, pf14 showed a slight advantage over it, but here the reduction in search sector has badly affected all the correlation pfs [see chapter 12] — in the case of pf14, a significant minimum occurred at the parameter value corresponding to the correct array shape. The estimator noting solely the peak height in any pattern, pf8, shows a convergence region much greater than that over which the source is visible, but not on par with the others. It shows little dependence on the beam sampling strategy.

Subsequent investigations in this chapter were generally done using beamforming over [-90°, 90°] and Hamming weights, with reference typically to the pf4 estimator. Although, the results in Table 29.1 had shown that sampling need not be too frequent, a policy was adopted of using 2° samples for a 16 element array, and finer sampling in proportion to beamwidth for larger arrays, i.e. 1° for 32 elements and 0.5° for 64 elements. This reflected the uncertainty in the applicability of the results for 'poor' sampling rates. For some work, the computational load necessitated that the angular scan be reduced to, say $\pm 30°$, and the consequent reduction in performance accepted.

29.3 Dependence Upon Noise Level and Number of Elements

Investigations using 20 realizations at a variety of noise levels produced the results given in Table 29.2, which show how the convergence region reduces as the noise becomes more significant.

Noise Ratio		Mean absolute locations of minima		
Amplitude	/dB	$\overline{\Delta a_1}$ /m	$\overline{\Delta a_2}$ /m	$\overline{\Delta a_3}$ /m
0.001	- 60.	24.	10.4	4.8
0.316	-10.	24.	10.4	4.6
0.500	- 6.	20.4	9.9	3.2
0.707	- 3.	17.4	9.3	2.6
0.900	- 0.9	10.7	7.4	2.4
1.000	0.	9.0	6.8	2.1

Table 29.2 : An indication of how the convergence region changes with increasing noise level.
[Single source at broadside ; 16 element Hamming weighted array with $\lambda = 6$m.]

Increasing the number of elements reduces the array's sensitivity to random noise. An array of 96 elements (total length 288m) has a convergence interval over a_1 that still amounts to ±90m when the noise level is -6dB. As values this large are hard to determine with any precision, it is difficult to compare arrays with the same input SNR but different numbers of elements. Thus it is advantageous to compare cases of similar output SNR; this is done in Table 29.3.

Examination of a few contour plots of pf4 for a 64 element array, show that the measures $\overline{\Delta a_1}$ and $\overline{\Delta a_2}$ are still fairly representative of the size of the convergence region. Thus it can be seen that for large arrays convergence is fairly certain, even for errors in the Fourier terms of up to 20m. The results in Table 29.3 show that, to a good approximation, the size of the convergence region is determined by the output SNR level. However, for a fixed number of elements, there does not seem to be a linear increase in the intervals with increasing SNR.

No. of Hydrophones	SNR / dB		Minima locations for pf4	
	Input	Output	$\overline{\Delta a_1}$ / m	$\overline{\Delta a_2}$ / m
16	10	22	24.0	10.4
	6	18	20.4	9.9
	3	15	17.4	9.3
	0	12	9.0	6.8
32	6	21	42.3	19.9
	3	18	29.4	16.3
	0	15	15.1	8.7
	-3	12	8.8	5.6
64	3	21	46.8	20.1
	0	18	26.2	13.1
	-3	15	14.7	8.6
	-6	12	9.7	4.8
128	0	21	38.6	21.1
	-3	18	23.7	13.6
	-6	15	13.3	7.7
	-9	12	9.0	5.3

Table 29.3 : A comparison of the convergence intervals for a_1 and a_2 for different noise levels. Results are for pf4 being evaluated over [-90°, 90°] except for 128 elements which used [-30°, 30°] ; Hamming weights were applied at the beamforming stage. [$\lambda = 6$m]

Using Hamming weighting on large arrays with very high noise levels, some differences can be discerned between the various pfs. Firstly, pf14 (one of the correlation pfs) showed a slight superiority to pf4 — the difference is noteworthy in that pf14 equalled or surpassed pf4 for all cases in Table 29.3, albeit that the differences were sometimes only 1 or 2%. The interpolation power

function pf18, formed from them both [see chapter 12], usually proved better still. Overall, the best performance in this regime was achieved by pf21, which looked at the correlation between powers at 3 times the beam separation (0.5° for 64 element array). With fine resolution, its convergence interval was up to 20% larger than that for pf4; if the resolution was reduced by a factor of 3, then this estimator was no good, and one that looked at power correlation between successive beams was best. Clearly, the angular separation for the desired autocorrelation corresponds to a certain fraction of the beamwidth, rather than a certain number of beams.

Further work using the 64 element array with noise at 0dB on input revealed that a source at 50° caused a larger convergence region than occurred for a broadside source. The increase in both of the dimensions analysed was about 1.3. No difference was observed between those pfs having a $\cos\theta$ term in their definition and those without.

It may be thought that further increase in the noise level will continue the shrinkage of the convergence regions; however, such is not the case. The convergence regions associated with a large peak in the pf surface have a minimum size dependent upon theprocessing; increased noise simply reduces the probability that the said peak lies anywhere near the point representing the true array shape.

In chapter 24.1 it is shown that a beam pattern can be produced from a totally noisy signal record, and that it will still show lobes of the characteristic width (λ / D), albeit that the heights will be random. In a similar manner, a contour plot can be produced from a record of pure noise — peaks, troughs and ridges will still be present in the pf surface, their dimensions being characteristic of the array (no. of elements and spacing) and also of the power function and weighting scheme employed. Fig 29.2 shows plots for several surfaces produced from the *same* record of pure noise.

All the diagrams show peaks in approximately the same locations — comparison of b) with a) and d) with c) shows that pf8 exhibits a more rapid descent from the peak, and more extraneous lobes than pf4 does. Use of Hamming weights, in both cases, leads to a significantly larger scale for the peak structure. These diagrams indicate the minimum possible size of convergence regions for each of the processing choices.

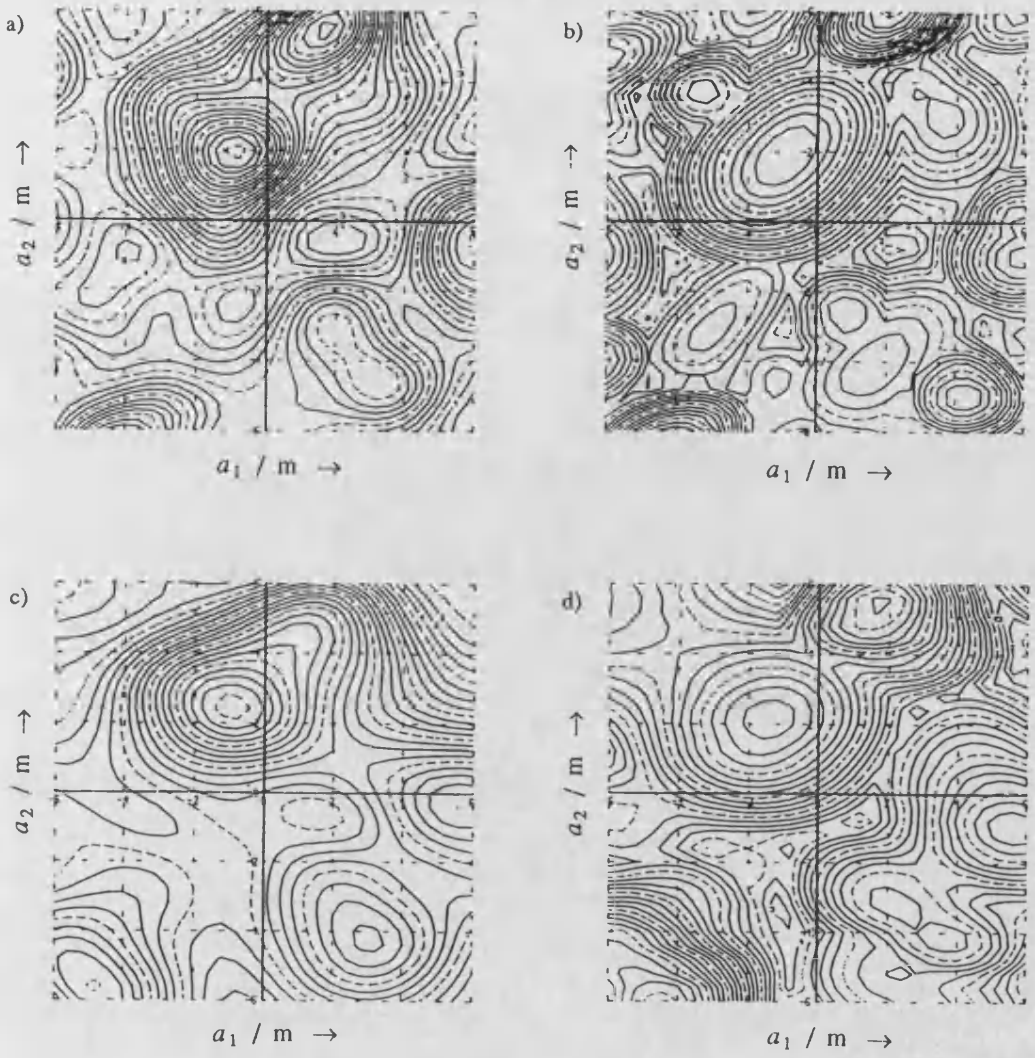

Fig 29.2 : Various contour plots of the same signal record of pure noise.

a) pf4 with uniform weights ; b) pf8 with uniform weights ; c) pf4 with Hamming weights ; d) pf8 with Hamming weights. Processing was for 64 element array at 3m spacing, with processed wavelength = 6m.

[$-6\text{m} \leq \Delta a_1 \leq 6\text{m}$; $-6\text{m} \leq \Delta a_2 \leq 6\text{m}$]

29.4 Effect of Multiplicative Noise

As discussed in chapter 26.2.2, uncorrelated multiplicative noise is similar in effect to uncorrelated additive noise, hence the discussion here of multiplicative noise is for the correlated form only. Such a type of noise has an effect upon the pf values, although usually the effect causes few subsidiary peaks in the vicinity of the true one. Instead it produces minor ripples in the surface,

which should not disrupt iterative techniques attempting to ascend to the peak. Typical examples are shown in Fig 29.3.

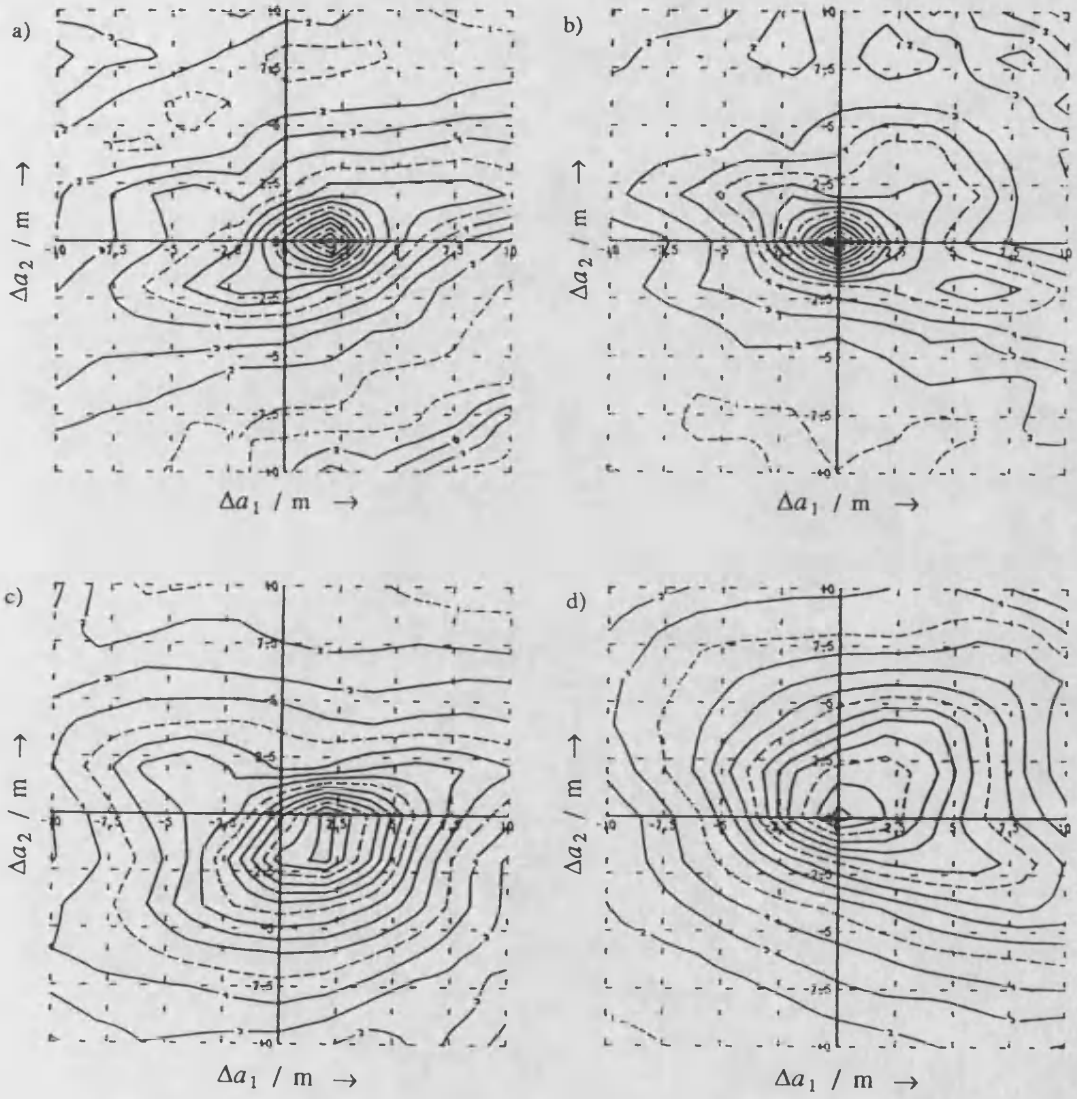

Fig 29.3 : Example contour plots to show effect of multiplicative noise on surface of pf4.

Plots relate to a single source and a 16 element array, and multiplicative noise characterized by $\sigma_m = 1.0$;

$\alpha = 0.85$ ($\beta = \alpha^n = 0.07$). a) and b) show processing of 2 realizations using uniform weighting ;

c) and d) are for the same data with Hamming weights. [cf additive noise case of Fig 29.1]

[$\lambda = 6$m ; $-10\text{m} \le \Delta a_1 \le 10\text{m}$; $-10\text{m} \le \Delta a_2 \le 10\text{m}$]

The presence of multiplicative noise in a two source scenario actually seems to simplify the situation, as it removes the problem of phase lock. Thus the local minima produced by the interaction of the sources disappear or are reduced in intensity. Some examples of this are shown in Fig 29.4.

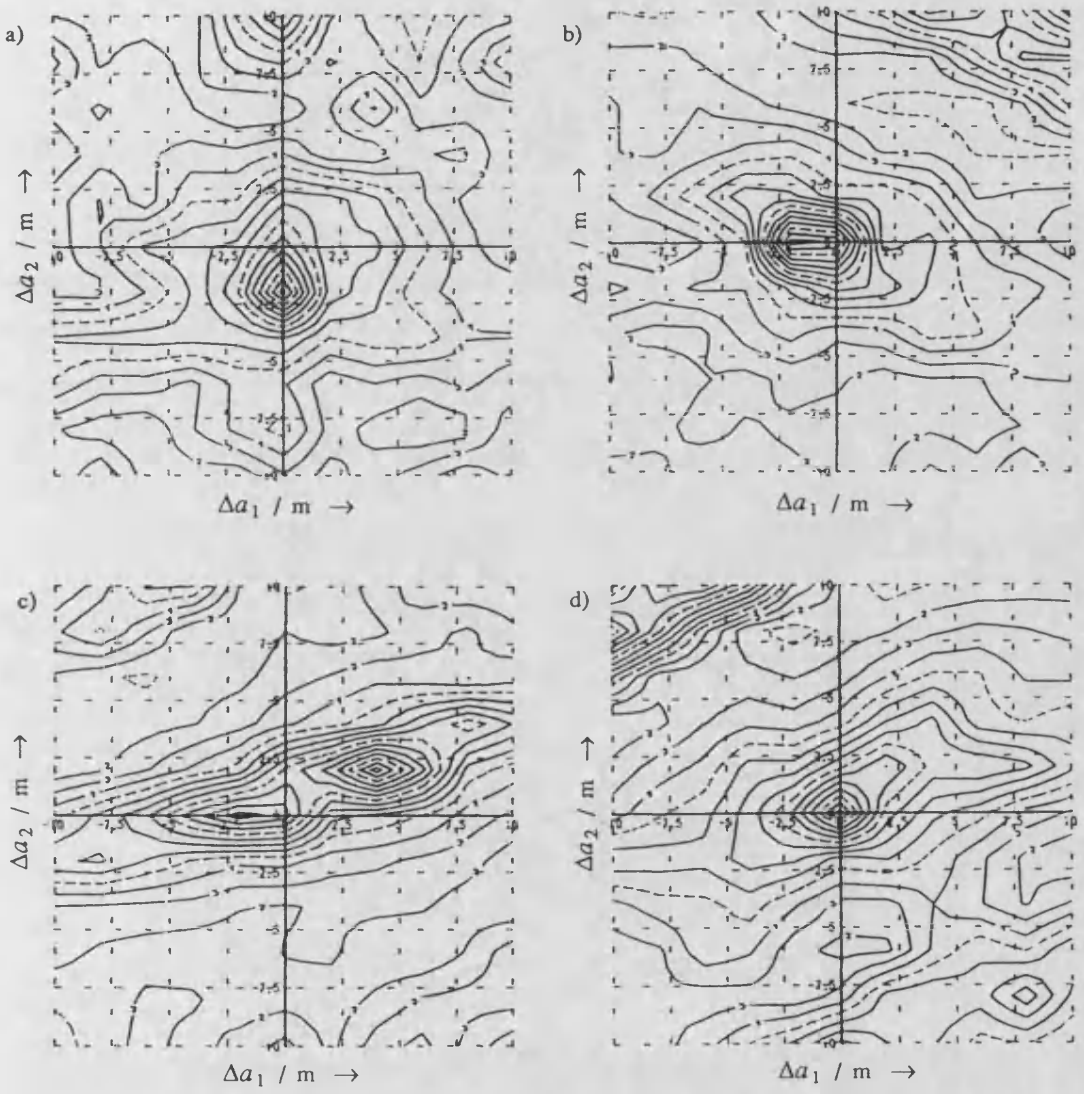

Fig 29.4 : Example contour plots to show effect of multiplicative noise on two source scenario.
Plots relate to a 16 element array, and multiplicative noise characterized by $\sigma_m = 1.0$; $\alpha = 0.85$ ($\beta = \alpha^n = 0.07$).
The second source is 3dB weaker than the primary and separated from it by about 30^o. a), b), c) and d) correspond to phase differences between the signals of 0^o, 90^o, 180^o and 270^o. [cf Fig 28.1]

[$\lambda = 6$m ; $-10\text{m} \le \Delta a_1 \le 10\text{m}$; $-10\text{m} \le \Delta a_2 \le 10\text{m}$]

It is to be noted that where the subsidiaries still occur, their locations remain in the directions ($\pm 4, \pm 1.5$), so the 'jump' method will continue to be applicable. Use of Hamming weights on signals corrupted by multiplicative noise again reduces the occurrence of subsidiaries; however, the improvement is not so marked as for the no noise case [cf chapter 28.4].

29.5 Summary

It has been shown that additive noise reduces the convergence region over a_1 and a_2, i.e. the errors in these values from which power functions are likely to be able to recover the true shape. When noise levels are high, the limits of the intervals for individual realizations may differ by a factor of 5 or more. Taking the mean absolute deviation of these minima, $\overline{\Delta a_i}$, as representative of a particular situation enabled simple comparisons to be made of the typical size of the convergence region for different scenarios and means of processing.

Some dependence on angular sampling rate and search sector was observed, but the effect is generally small, and varies between cases. More importantly, Hamming weights applied at the beamforming stage lead to a considerable increase in the convergence range. Comparison of contour plots for uniform and Hamming weights applied to the same data show the latter to be even more beneficial — the extra weighting leads to many of the subsidiary peaks being smoothed over. The only disadvantage of this weighting is that it produces a greater error in the location of the pf maximum.

Investigation at different levels of additive noise resulted in the observation that the convergence intervals are dependent mainly on the output SNR. Values for the ideal output level less than about 12dB correspond to conditions for which the rms error in parameter estimation is several metres (thus blurring the source); convergence intervals for such situations therefore have little meaning, as the shape achieved at the pf peak is too inaccurate for source detection.

The results in Table 27.3 for no noise (and uniform weights) infer that the convergence intervals for a_1 and a_2 expand at least as rapidly as the number of elements. However, a similar perusal of Table 29.3, say for an input level of 0dB, indicates that the range no longer increases approximately linearly with hydrophone number.

Investigation of correlated multiplicative noise was likewise confined to conditions for which a pf peak would exist close to the true values for the shape parameters. Examination of relevant contour plots showed only minor disturbances to the pf surfaces, guaranteeing fairly trouble free convergence.

The best approach for finding an unknown shape in a noise field of unknown properties would seem to be initial use of Hamming weights and pf23 estimator with reasonably fine angular sampling, but reverting to uniform weights and, say pf4, after a few iterations to ensure the best possible accuracy in the final estimate. In order to improve the speed of the process, the intermediate section may be done with Hamming weights and coarse angular sampling. The previous chapter demonstrated that if the noise field is complicated by other coherent sources, then convergence to the true parameter values is not guaranteed; a 'jump' in the vector space being necessary to overcome that. Note, when the shape determination routine is applied to signal records corresponding to successive positions of an array, then the first estimate for each situation is unlikely to be out by more than a few metres in any term, and hence problems of distant convergence and subsidiary maxima can largely be ignored.

30. INTER-DEPENDENCE OF BASIS FUNCTIONS

30.1 Independence of odd and even functions

The chapters on estimation accuracy (nos. 18-26) cover performance of the power functions for shape estimates close to true, using the correct values for all the coefficients, other than the one under investigation. This chapter deals with another facet of the problem, relating to the rate of convergence towards the correct set of parameters. Here, the rms error and mean estimate of the *i*th coefficient are determined, whilst maintaining a constant 'error' or offset in one or more of the other coefficients, in order to determine how accurately one may be found in spite of any errors in the others.

To achieve this, an error, Δa_j, was set up in the value for the *j*th coefficient, and then a series of estimates of the *i*th one performed. The mean and variance were calculated, and noted as a function of the various values of Δa_j. The actual conditions of this experiment involved a source at 4.7^o to a 16 element array of half wavelength spacing, with a low level (-26dB) of uncorrelated additive noise. Beamforming was over $[-50^o, 50^o]$ in steps of 2^o. The offset, Δa_j, was varied from 0.0m to about 2.0m (a third of a wavelength), and the statistics calculated from runs of 20 realizations each.

For a fixed deviation in an odd function, the estimates of the coefficient of an even basis function are found to be unbiased. The rms error increases with the magnitude of the error term, from figures of around 3–4.5cm for the true shape to 6–9cm for a biasing 'error' of around 1.4m. Similarly, a set shift in the value of an even coefficient causes little change in the estimation of odd coefficients. Thus the various odd and even functions affect the power function values in an independent manner.

An error of magnitude greater than about 1.5m affects the estimation of other coefficients more seriously, with greatly increased values for the rms errors. In some cases, the coupling of a sizable error in one term with a search over another, leads to selection of a shape, whose beam pattern peak is no longer in the direction of the source. In other cases, large offset terms may bias the estimate of another, whilst still retaining the peak lobe in the true source direction. In many of these cases, a further estimation of the coefficient for the offset term will improve matters, removing the

bias from subsequent estimations.

30.2 Dependence between Odd/Odd and Even/Even

The results summarised above indicate that the estimation of, say a_2, remains unbiased in the presence of errors in a_1 and a_3. However, it is found that if the value of a_4 used is incorrect, then the peak of the power function is shifted, hence resembling a biased estimator. In the same way, estimation of a_1 is affected by an erroneous choice for a_3. The statistics of the estimators, as a function of the magnitude of the 'error' term are given in Table 30.1.

Error in Δa_j / m	$m_1 \mid \Delta a_3$	$m_2 \mid \Delta a_4$	$m_3 \mid \Delta a_1$	$m_1 \mid \Delta a_3^*$
0.2	0.22	0.12	0.056	- 0.002
0.4	0.46	0.22	0.110	0.008
0.6	0.70	0.34	0.159	0.010
0.8	0.92	0.44	0.210	0.038
1.0	1.16	0.55	0.259	0.039
1.2	1.43	0.64	0.311	0.058
1.4	- 1.19	- 1.14†	0.375	0.082
1.6	- 1.42	- 0.23†	0.422	- 0.006
1.8	- 1.07†	- 0.45†	0.971	- 0.188†

Table 30.1 : Biasing of estimates of one coefficient, due to an error in another.

$m_i \mid \Delta a_j$ represents the bias in estimate of the ith term in metres due to an error in the jth coefficient. Results are for pf4 using 20 realizations with an SNR of 26dB. Estimates usually show little variation; † indicates cases where variance is large. a_3^* is the coefficient of the modified third basis function, described in the text.

It can be seen that the estimation of a_1 is seriously affected by an error in the value of a_3. The biasing is most significant for this pairing as larger values of a_1 are needed to alter the beam pattern [see chapter 15.6]. Notable shifts of mean are also observed for estimation of a_2 and a_3 in the presence of errors in a_4 and a_1 respectively. In all cases, the biasing is approximately proportional to the offset term.

These results suggest that it is likely that a slight alteration to the basis functions will render them independent. Using the notation of Eqn 11.1c,the third function may be redefined as:-

$$f_3'(x) = \sin(3\pi x/l) + \alpha \sin(\pi x/L) \qquad [30.1]$$

and noting the bias in a_1 estimation caused by different values for this function, leads to an optimum value for α close to 1.12. The final column in Table 30.1 gives the mean error in estimation of a_1 for various offsets in the coefficient a_3^* for this modified function.

Fig 30.1 shows contour plots of pf4 covering various values for the first and third coefficients. An off-centre section parallel to the x-axis corresponds to the pf variation over a_1 for a fixed error in a_3. Thus, the position of the peak of the a_1 section can be seen to depend upon the value of a_3 selected and vice versa.

The value of 1.12 was arrived at empirically. Similar investigations show that a suitably modified set of basis functions, $f_i'(x)$, may be defined in terms of the previous Fourier components, $f_i(x)$, by:-

$$\begin{pmatrix} f_1'(x) \\ f_2'(x) \\ f_3'(x) \\ f_4'(x) \end{pmatrix} = \begin{pmatrix} 1 & 0 & 0 & 0 \\ 0 & 1 & 0 & 0 \\ \alpha_{31} & 0 & 1 & 0 \\ 0 & \alpha_{42} & 0 & 1 \end{pmatrix} \begin{pmatrix} f_1(x) \\ f_2(x) \\ f_3(x) \\ f_4(x) \end{pmatrix} \qquad [30.2]$$

where $\alpha_{31} \approx 1.12$ and $\alpha_{42} \approx 0.56$. Using such a modified set of functions as the basis for characterizing the array shape, makes the estimation of one coefficient independent of the errors in the others, provided that none of the errors is more than a metre. Note, not only is estimation of a_1 independent of errors in a_3^*, but also the a_3^* peak is not affected by deviations in a_1. As $f_3'(x)$ is a combination of odd functions, estimation of its coefficient remains independent of the values of a_2 and a_4. This independence appears to be true for different noise levels, and for any original array shape and any bearing for the source (except close to endfire, which always hinders shape determination). This implies that if a trial shape is close enough to true, that the source is clearly visible, then convergence to the 'best solution' shape will be quick, as each of the coefficients is

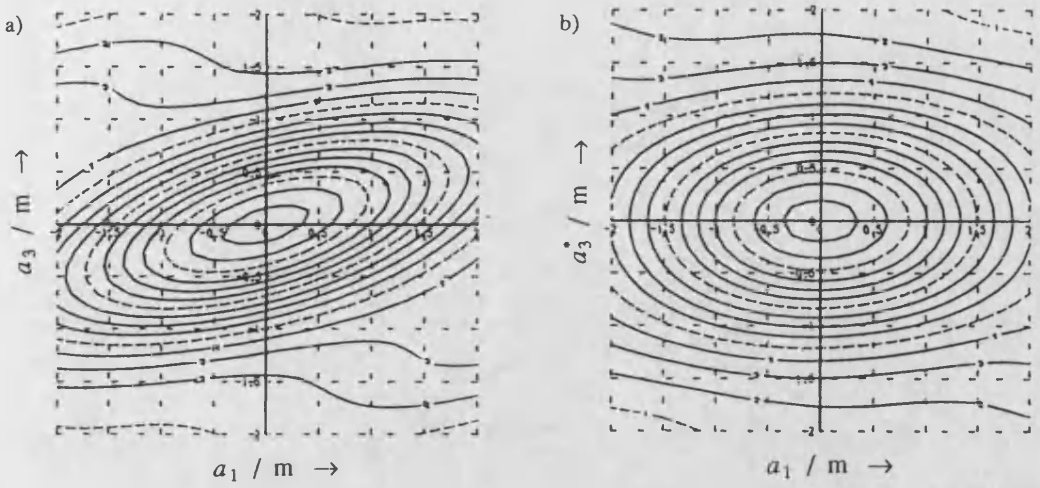

Fig 30.1 : Contour plots to show variation of pf4 in terms of 2 coefficients

a) Horizontal and vertical axes are a_1 and a_3 respectively ; b) Axes are for a_1 and a_3^*.

Both graphs encompass a span of ±2m for each coefficient, and minimal noise. [$\lambda = 6$m]

easily determined. With weak secondary sources present, this improvement from mislocations of the order of a metre to close to true, may be sufficient to render hitherto unobserved sources detectable [see Figs 30.2a,b]. The presence of the extra source does not affect the basis orthogonality in any noticeable way; convergence to within a few decimetres of true occurred for the case in Fig 30.2 after just 4 linear searches over the modified basis.

A simple physical justification for the actual values of α_{31} and α_{42} seems unlikely, as the various pfs yield different values, usually similar in magnitude, but noticeably different. The results here are for pf4. The numerical values for α were obtained empirically through repeated simulations. Surprisingly, it is found that not only do these values vary with array length, but also with the number of sensors within that length. Table 30.2 contains the experimentally determined values for α_{31} and α_{42} for various different arrays.

For any particular array design, the biasing effects (and consequent compensating terms, α) are independent of the frequency used; provided that the frequency is not too high, causing problems with aliasing and undersampling of beam pattern. This is extremely important, as it means that the same basis can be used for many frequencies at once, or even for work in the time domain.

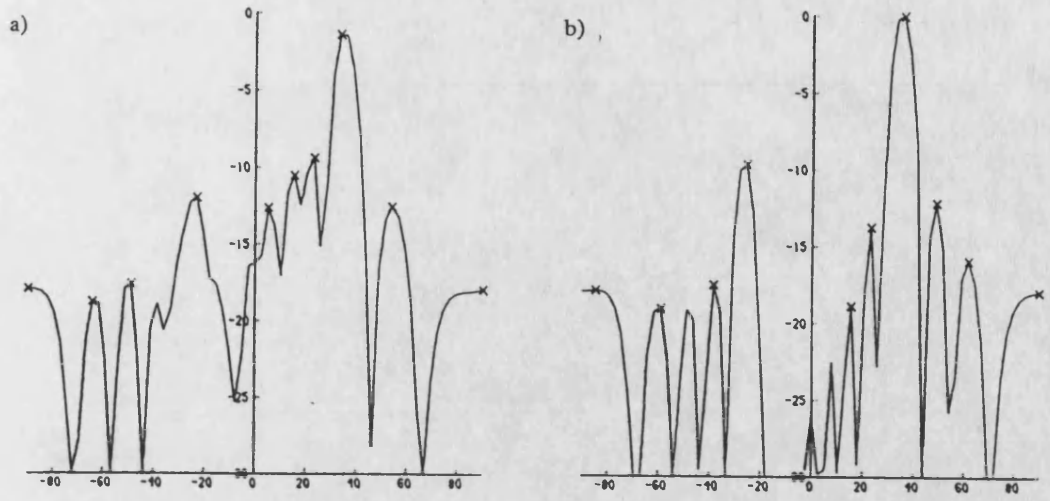

Fig 30.2 : Two beam patterns to show the improvement occurring for removal of element errors of 1m or so, with special reference to the observability of the second source at -25°, whose power is 10dB less than that of the primary, and noise is at -10dB too. Errors for a) are $(a_1, a_2, a_3^*, a_4^*) = (1.2, 1.0, 0.9, -0.4)$m b) is the pattern for the correct shape.

Observations of bias for the 192m array using only 2° sampling, led to different results to those presented in the table — the value then being sensitive to the source direction. Likewise, the results achieved for 8 element arrays using [-50°, 50°] were dubious (possibly due to aliasing), hence the reduction in angular search sector.

A few trials showed that the adjustment numbers depended upon the choice of shading function — uniform weighting causing the minimum value. Hann and Hamming produced results 3-4 times that for uniform, whilst Half-Cosine and Bartlett were intermediate. However, the magnitude of the compensatory term is not important, rather the range of usefulness i.e. linearity should be emphasised. It is found that linearity breaks down for Hamming weighting at about the same offset values as for uniform.

Although the requirement for different basis functions for different arrays may be a little cumbersome, it is not hard to implement. Appropriate values for various sections of the array could be stored in a look-up table, or else determined by preliminary simulation work as here.

No. of elements	Constant length, $L = 48$m			Constant separation, $d = 3$m		
n	d	α_{31}	α_{42}	L	α_{31}	α_{42}
8	6.00	0.73	0.27	24.	0.70	0.26
16	3.00	1.12	0.56	48.	1.12	0.56
32	1.50	1.40	0.71	96.	1.33	0.71
64	0.75	1.52	0.79	192.	1.57	0.80

Table 30.2 : Values of the basis adjustments, α_{31} and α_{42} for differently designed arrays. For most cases, beamforming was over $[-50^o, 50^o]$ in steps of 2^o, however, 1^o samples were used for 96m array and 0.75^o for 192m one, whilst the range $[-27^o, 27^o]$ was used for 8 elements. Results are accurate to about 3%.

31. APPLICATION OF GRADIENT SEARCH METHODS

31.1 Introduction

This project has concentrated more on determining the probability and limits of many power functions for array shape retrieval and source detection, than on actually implementing an efficient (i.e. fast) implementation of such. A technique common to many problems involving maximization of a function of many values is to use a gradient search routine. This examines the effect on a function, $f(u_1, u_2, \cdots)$ of slight changes in the variables u_i, in order to produce a vector description of the gradient:-

$$f' = \left(\frac{df}{du_1}, \frac{df}{du_2}, \cdots \right)^T \qquad [31.1]$$

Locally, this will represent the steepest change of gradient. This may not necessarily be straight towards the peak though, as this depends upon the structure of the surface around the peak. More advanced routines exist which utilize other information to infer the direction of the peak relative to the gradient vector.

The implementation used here simply calculates the gradient as above and then applies a linear search in that direction. When the maximum in that direction is found, its position is located more accurately by fitting a quadratic curve to the highest pf values (as detailed in appendix 9) — this achieves reasonable accuracy without requiring many shapes to be tested. The procedure is then repeated from this new position, and continued either a set number of times or until a local maximum achieved.

31.2 Application to Real Surfaces

Although the gradient method can be applied to a problem of many unknowns, discussion here is confined to only 2 parameters, so that contour plots may be used to illustrate the points. Firstly, Fig 31.1 shows a situation for which convergence is straightforward, as the surface has only one peak, and all parts of the surface slope in approximately the right direction.

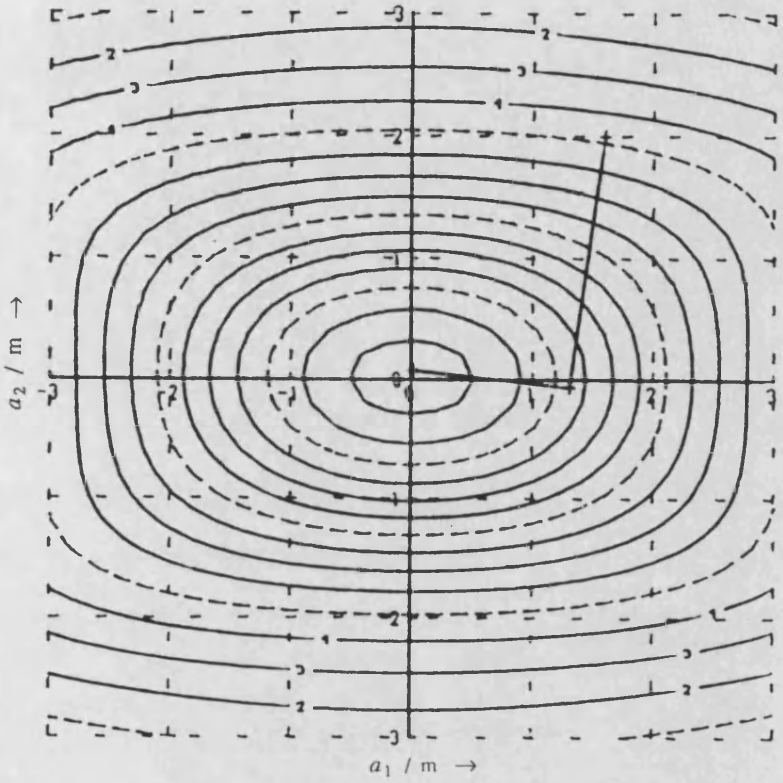

Fig 31.1 : Contour plot showing a situation for which a simple gradient routine can quickly locate the peak. [Line represents convergence route adopted for one initial estimate.]

The second diagram, [Fig 31.2] shows a slightly more complex situation — from the particular starting point chosen, the route pursued is rather circuitous, as the orientation of the local gradient vector is not close to the direction of the pf maximum. However, convergence is still achieved.

More complicated pf variations, corresponding to interaction of several sources and/or high noise levels, have several subsidiaries which may divert the algorithm from the global peak. Note, all that is required is a local maximum; these subsidiaries do not have to be very prominent, as

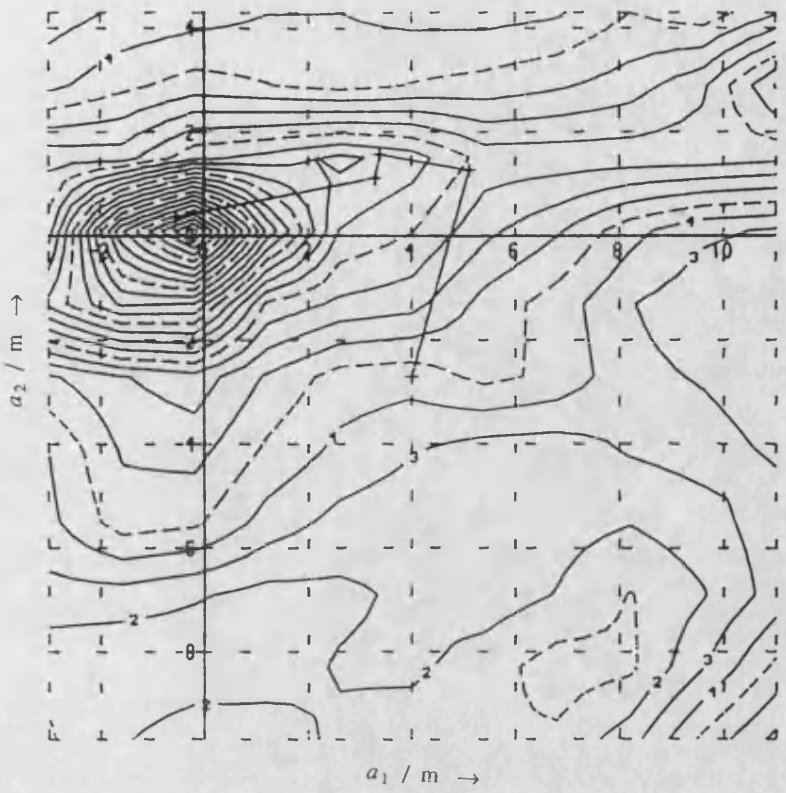

Fig 31.2 : Contour plot showing a situation for which the simple gradient routine is slow.

evidenced by the pf surfaces in Fig 31.3. [Those maxima caused by the interaction of 2 sources lie at fairly well defined locations, hence the suggestion of a 'jump' stage to the algorithm [chapter 28.3], followed by quick convergence up the correct slope.]

Fig 31.4 illustrates one situation for which the gradient routine successfully and quickly proceeds from an estimate whose beam pattern shows no source to one enabling two to be found.

The simulation was for a 32 element array, insonified by two sources (one 3.7dB weaker than the other) with uncorrelated additive noise at -1.9dB relative to the stronger one. The multiplicative noise field was characterized by $\sigma_m = 0.7$, $\alpha = 0.95$ [see chapter 26.1 for explanation of values]. The various parts of Fig 31.4 show the beam patterns associated with the initial shape estimate, the final shape estimate and the true array shape. A summary of the parameters derived from the beam patterns is given in Table 31.1.

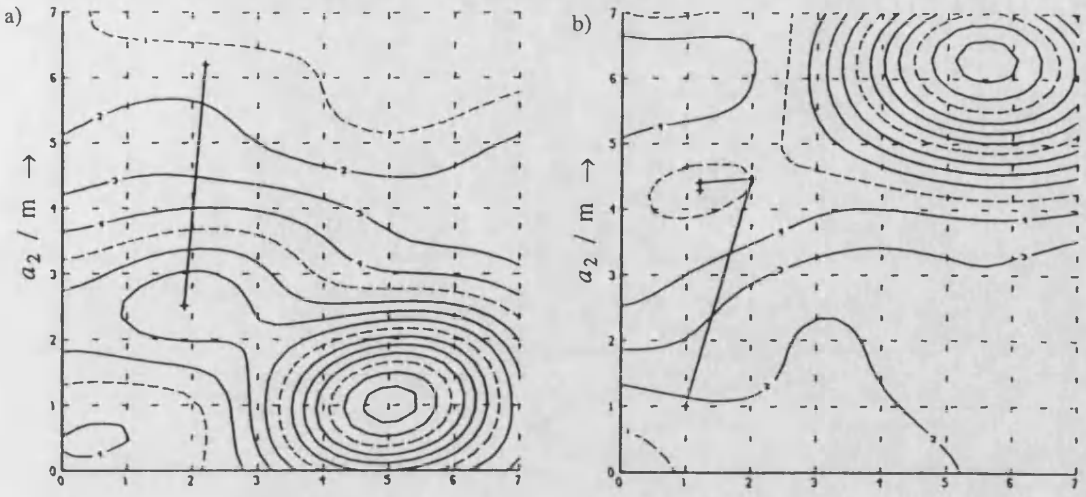

Fig 31.3 : Diagrams to show that even weak local maxima may be sufficient to prevent correct convergence.

Description of array shape used for beamforming	Shape Coefficients		Source Estimates		
	a_1 / m	a_2 / m	θ_1 / degs	θ_2 / degs	P_2 / P_1
Initial estimate	8.50	5.20	14.0	(40.0)*	—
After 2 gradient searches	-1.35	-0.36	24.7	-33.3	- 11.4 dB
Final convergence point	-0.72	0.32	24.7	-34.0	- 10.5 dB
True shape	0.00	0.00	24.7	-33.3	- 10.0 dB
Simulation values	0.00	0.00	24.7	-34.4	- 3.7 dB

Table 31.1 : Comparison of the source parameters determined from the beam patterns of Fig 31.4.

* For initial shape, many peaks exist exceeding that near to the direction of second source.

[Note, bearing accuracy limited by beam separation, which was 0.67^o.]

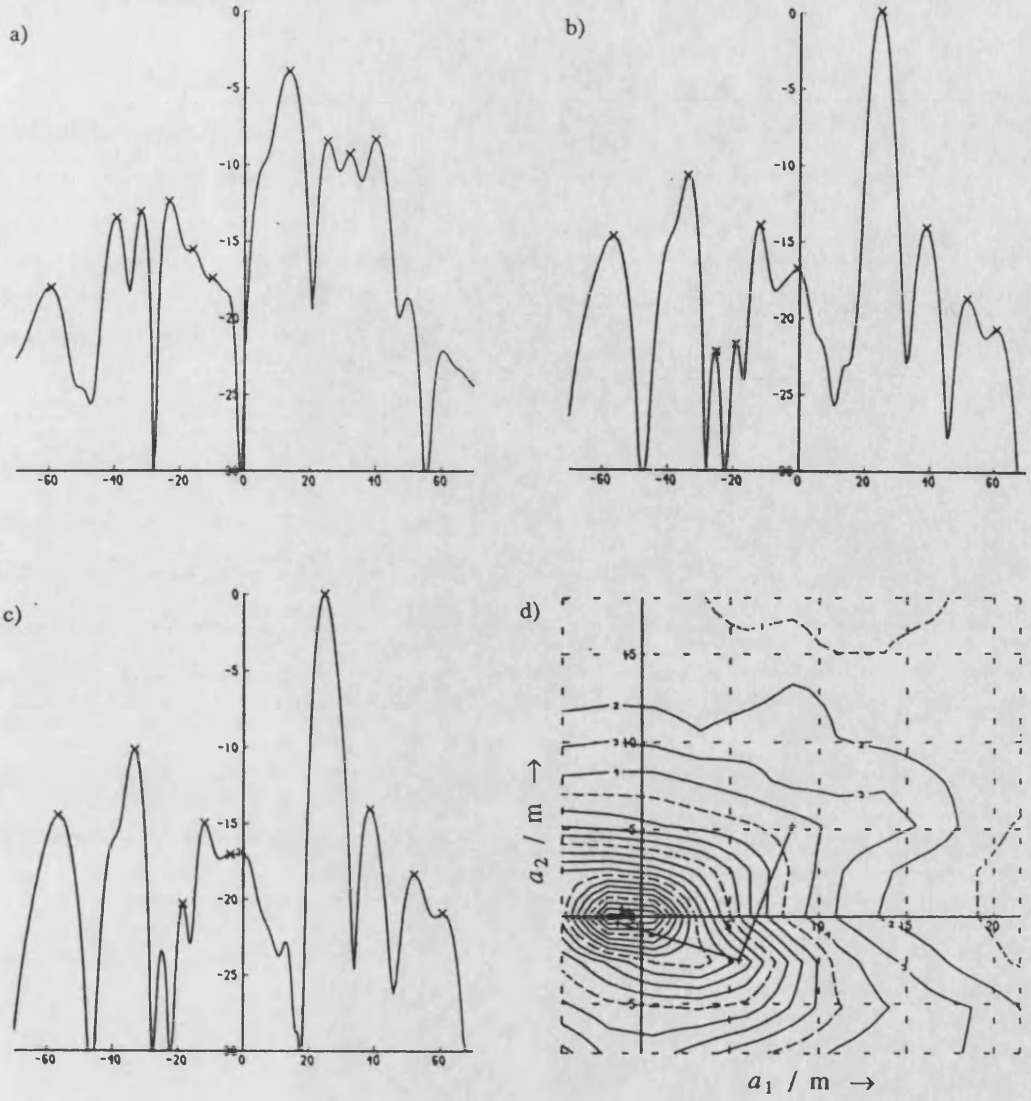

Fig 31.4 : Diagram to show how application of gradient methods to a pf surface may lead to quick convergence to true shape. a) Beam pattern using initial shape estimate ; b) Beam pattern using final shape estimate ; c) Beam pattern using correct array shape ; d) Contour plot of the power function used (pf4) showing convergence route.

Note, power in the direction of the primary source is greater by 0.3dB for the final shape estimate than for the true shape. Several realizations, using the same descriptors for the noise field, indicate that the observed P_2 / P_1 ratio for the true shape is not typically less than that allocated in the simulation routine.

31.3 Comparison to Linear Search

The first two contour plots in Fig 31.5 show the convergence route adopted for a given situation by a) repeated linear searches over a_1 and a_3, b) linear searches along directions of local gradient. Although the latter requires extra beamforming operations in order to determine the gradient, this is clearly made up for by the more rapid arrival at the peak. This overall reduction in the number of shapes to be tested (and hence in computation time) is commonly observed, although for cases such as Fig 31.2 the repeated linear search may be quicker.

Fig 31.5c shows the effect of applying the repeated linear search method with the modified basis functions introduced in chapter 30. [In this particular case, f_3' is being used, which corresponds to a change in a_1 of 1.12 for each increment in a_3 of 1.] In many situations involving gradient climbing routines to locate maxima, a 'slow' convergence is used, wherein small steps are taken and the the gradient redetermined after each one. This is particularly appropriate for tracking problems, where the routine is required to ascend and follow the summit of a gradually varying pattern, using the latest data set at each stage of the journey. The route pursued by such a means is illustrated in Fig 31.5d for completeness, but is of little use in this work due to the greater time involved in the extra gradient calculations.

[Note, for the case shown, repeated linear searches using a_1 first do not lead to convergence to the correct value, rather the routine tends to some subsidiary off the region covered in the plots. The importance of selecting the correct variable for the first search, is another shortcoming of the non-gradient method.]

With the gradient routine applied to the pf4 measure, it is not clear whether there is any benefit to be gained from changing to the modified basis of chapter 30.

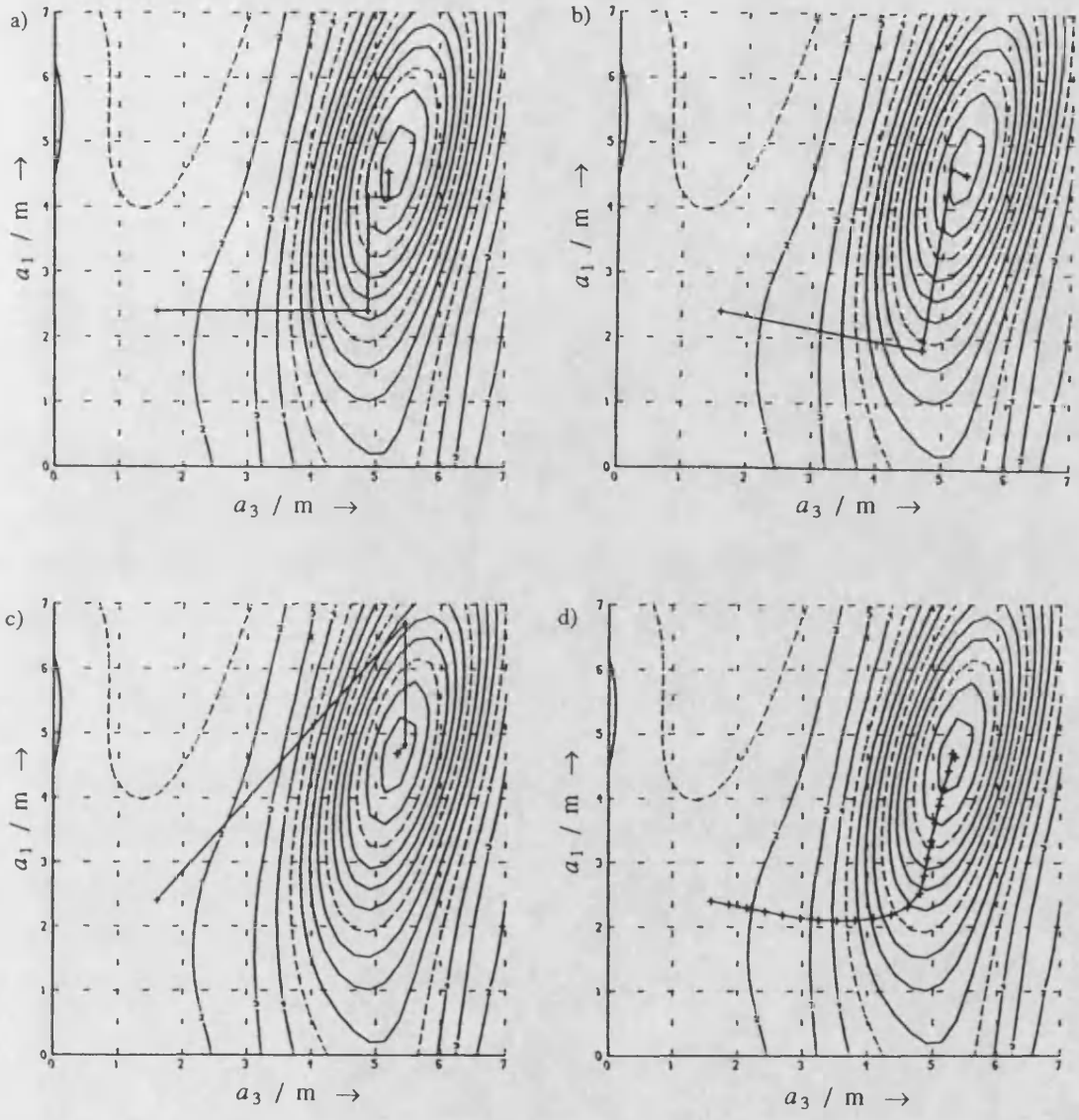

Fig 31.5 : Four contour plots for same situation illustrating different routes followed to the peak.

a) Repeated linear searches over a_1 and a_3 ; b) Use of gradient routine as advocated in chapter 31.1 ;

c) Repeated linear searches over a_1 and a_3^* ; d) Use of 'slow' gradient routine.

32. COMPARISON OF THE PERFORMANCE OF DIFFERENT POWER FUNCTIONS

32.1 Introduction

The power functions that were examined are defined in chapter 12. Some of these were not really intended as estimators themselves, but rather as part of other definitions, for example pf1 and pf2 are measures of the total power in the chosen sector. As power is roughly constant, these themselves are of no use for shape estimation, however, their values are required for normalization of others.

The integral $\int_{\theta=-1/2\pi}^{1/2\pi} p\cos\theta\, d\theta$ for a straight array represents the total power received from all directions, which equals the sum of the powers at the individual hydrophones. Significantly misshapen arrays would result in different values for the integrated power, as then $\cos\theta$ is not the appropriate angular shading; however for shapes approximating to a straight line, $\cos\theta$ will suffice. In most situations beamforming is only performed over a reduced sector — [-90°, 90°] or smaller. In which case increased error in estimate of array shape will lead to greater overspill of power from the sector containing the source, and consequently the estimate of power will decrease. The other important point to note is that the equivalence to total power is strictly only for the integral formulation, whereas in evaluation as a power function this is approximated by a summation.

All this explains why the 'total power' cannot be expected to be completely constant over all trial shapes. When evaluated over a wide range of trial shapes, pf1 and pf2 vary by only a small fraction of their values, with the peak not necessarily near the true parameter value [see Fig 16.2]. When used for normalizing others, they can only cause a minor modification to the original. In cases where the accuracy of an estimator is being assessed, pf1 and pf2 change so little over the range of parameter values as to have minimal effect. In cases of convergence range, the variation in parameter value is much greater, such that pf1 may fluctuate enough to have a minor effect.

32.2 Accuracy

In work concerned with how precisely shape parameters could be determined, it was found that uniform weighting and a fairly frequent sampling rate (several beams per lobe) gave the best results. Under these conditions, most of the simple integral pfs (principally nos. 3-6) give almost identical results, although at very high SNR pf5, pf6, pf19 and pf20 (all of which involve a p^3 term) are better than pf4. The estimator based on peak height, pf8, has more difficulty still with such low noise signals, although use of a much finer angular resolution does enable it to produce performance figures of the order of the others. For sources far from broadside, no real difference was found between estimators containing the cosθ term and those without.

At low sampling rates (just over one beam per beamwidth) most estimators show similar performance values as before for estimation of the a_1 term, but have greater variance in their estimates of a_2. An exception is pf18, which was designed to overcome the problem of low sampling rate.

32.3 Convergence

In work concerned with determining the convergence region, use of Hamming weights at the beamforming stage was shown to render the pf surfaces more amenable to gradient climbing routines. Of the simple integral pfs, pf4 proves to be generally better than those involving a p^3 term. The peak height measure, pf8, has smaller convergence intervals, although these tend to be much larger than the range of shapes for which the source is visible.

Some of the correlation and interpolation pfs [see chapter 12], which had been designed with precision shape determination in mind, give superior convergence performance to pf4. However, care must be taken over selection of the correct correlation interval (numeral k in $p_i p_{i+k}$). This is dependent on the angular sampling rate — the best estimators use a convergence interval corresponding to a shift of about a beamwidth.

33. RECOMMENDATIONS FOR FURTHER WORK

This project attempted to cover a great many facets of a large problem, but limits of time imply that there are many parts that could benefit from further investigation. Some of the more important ones are listed below:-

- Further determination of the locations of 'fixed' subsidiary maxima in more than 2 dimensions, and of how they depend upon array characterization and scenario used.
- Determine a more representative way of measuring convergence region in 2 or more dimensions, rather than just looking independently at two terms of the basis i.e. determine location of nearest saddle points.
- Investigate the effect of signal clipping i.e. reducing the precision of the data used, either just the digitization of input, or else reduced numerical accuracy throughout the processing — more complicated functions may be more sensitive.
- Perform simulations with signal at 2 or more frequencies; determine what emphasis should be placed on each if the SNR at each frequency is different.
- Use multiplicative noise that is different at different frequencies, but shows correlation between close values.
- Investigate whether some measure may be devised, such that comparison of its value at a frequency containing possible source emissions with that at one not expected to contain any, will yield an estimate of the likely SNR of any sources present, and thus whether the pf algorithm can be usefully applied, or whether it will end up focusing random noise.
- Produce a faster algorithm, to work in real time, possibly using a transputer or dedicated processor.
- High resolution non-linear methods are generally much more susceptible to errors than Conventional Beamforming techniques. At high SNRs, the pf method can lead to very

accurate determinations of the sensor positions, such that ML or MUSIC might be beneficially applied. Such high signal strengths occur in fields other than underwater acoustics. When the noise and signal are of comparable power, and thus the residual errors larger, it is unlikely that high resolution methods can yield better quality information on source positions and relative powers; however, no work has been done on such.

- Obtain useful data on likely array configurations (not necessarily as a series of Fourier terms) so that realistic contortions can be simulated, rather than ones just believed to be likely. [The present work has been able to encompass all gently undulating shapes, but there was little information on the period of ripples in the array, radius of ship's turning circle or magnitude of oscillations.]

- Adapt work to perform on consecutive array shapes, using a hydrodynamical model to produce a good initial estimate of new array shape, from the shape found from the previous data set. At high noise levels there is a compromise to be found between independent inaccurate shape determination for each set of signals, and summing the time records prior to application of algorithm, which will cause difficulties if the shape changes much in that time span.

- Comparison of different shape estimation algorithms i.e. power function method versus mini array approach of Hinich & Rule [see chapter 10.3]. It is expected that the pf method will be the slower, but more able to cope with high levels of noise.

- Application to real data — the real proof of the pudding!

34. CONCLUSIONS

This work has been concerned with use of Conventional Beamforming techniques applied to a series of sensors lying along a curved line. An investigation was made into the deterioration in quality of the beam pattern for various erroneous estimates of the positions of the sources.

From such images, a series of measures was proposed, each of which in some way characterizing the degree of focusing in an image. These measures, here termed 'power functions', were generally expressed as weighted summations of functions of the power distribution in the beam pattern. In the absence of noise these were all shown to be at their maximum for processing using the true array shape. Presence of any noise terms — additive, multiplicative or other sources — tends to disturb the position of the pf (power function) maximum away from that of the true array shape; the deviation increasing with the magnitude of the noise terms.

To simplify the problem of so many poorly determined sensor locations, the array shape was characterized by a modified Fourier Series of low order. For most of the work, no more than 4 terms were considered, although it was shown that the work could be extended to higher orders if further terms were deemed necessary. The modification to the Fourier Series is that those elements of the basis containing an even number of half periods have a linear term subtracted out, such that the best-fit line (in a least squares sense) has a constant orientation. This was shown to stabilise the direction of the main lobe against errors in the even terms, and also to aid the estimation of their values.

Many of the results quoted herein are for processing at a frequency of 250 Hz (λ=6m), however it is shown that values generally scale with wavelength.

Considerable work was done on the accuracy with which power functions could determine the various coefficients and hence the array shape. Under moderate conditions, most of the estimators showed similar behaviour, with little dependence on search sector or angular sampling rate. If the source lay outside the search sector or the beam separation was of the order of a beamwidth then all the estimates were affected, indicating the importance to be placed on sufficient

sampling from bearings close to the source(s). However, use of very fine sampling such that the summations are close to their appropriate integral limits gave negligible improvement over sampling at a rate of 2-4 times per beamwidth. Thus there is an optimum sampling rate, such that less frequently reduces estimation accuracy, whilst more frequently increases the computation time for no overall gain. The accuracy was also shown to depend on the system of sensor shading used. The error increases with the spread of the weighting values — uniform weighting being the optimum choice for precision shape estimation.

For a given level of additive uncorrelated noise, it was predicted that the attainable accuracy in a Fourier coefficient should depend upon the bearing and frequency of the source according to:-

$$\Delta a_i = (\Delta a_i)_0 \cdot (f_0/f) \cdot \sec\theta$$

where Δa_i is the rms error in the estimate of the ith term, and $(\Delta a_i)_0$ is the error at frequency, f_0, for a source at broadside ($\theta=0$). Simulation experiments matched the above expression well, apart from for sources at angles of 65° or greater, in which case the precision was less than predicted.

Uncorrelated additive noise and uncorrelated multiplicative noise were shown to be exactly equivalent at low levels. [Multiplicative noise was used to imitate the uncertainties in refractive index along a particular ray path, which cause the variations in the phase and amplitude along that route.] Denoting the optimum estimator to be that which exactly matches the phase disturbances by using sufficient Fourier terms, it was shown that the performance accuracy of such, when applied to signals containing uncorrelated noise, was governed by:-

$$[\Delta a_i]_0 = \frac{\sigma_n}{\sqrt{2n}\, k\, \zeta_i}$$

where k is the wavenumber ($=2\pi/\lambda$), n is the number of elements, σ_n is the amplitude ratio of the noise and signal terms and ζ_i is a factor relating rms displacement errors to the errors in the amplitudes of the various Fourier coefficients. Investigation using the pf4 estimator yielded rms errors for the coefficients inversely proportional to ζ_i as predicted. Their magnitudes increased approximately linearly with noise level, being between 0.9 and 1.2 times that for the optimum estimator. Very low noise levels (< -50dB on input) gave greater difficulties for the estimator in that it retained a bias rather than continuing to decrease with amplitude. For a 16 element array, input noise levels greater than 3dB also led to errors of a size greater than proportionality predicts;

however, by then the combination of considerable noise and significant shape errors is too great for any source to be really visible.

Significantly correlated additive noise was shown to resemble the signal from a single source passing through a partially decorrelating medium. A measure was introduced which was representative of the correlation across the array as a whole. Comparison of arrays of different length insonified by noise of different correlations indicated that shape estimation accuracy is principally dependent on the aforementioned measure.

When another source is present, insonifying the array at precisely the same frequency, then the interaction of the two leads to greater errors in shape estimation than if just the one was there. The interaction causes a bias in the estimation of shape coefficients and source bearings. These biases are observed to be sinusoidally dependent on the phase difference of the two signals; due to the varying nature of the sea, two sources cannot maintain a constant phase difference, hence averaging will remove the bias entirely. Note, the error in shape estimates is small, but the bearing of the weaker source wanders by a few degrees.

The other main focus of this work concerned the likelihood that the true element locations (and hence source bearings) could be retrieved from highly erroneous initial estimates. Provided that noise conditions are not too severe, a power function will peak at shape parameters close to the true values. However, as evaluating a power function for each shape involves beamforming — for large arrays, a process that takes several seconds on the mainframe — it is impractical to try all possible combinations of values for 4 or more coefficients. A gradient search method is preferable, but that places certain constraints on the pf variations. For the gradient method to cause convergence from an initial shape estimate to the pf peak close to the true shape requires that a continuous uphill route exists between the two.

The work contained herein concentrated primarily on cases of just one or two unknowns, as it was possible to illustrate the problems for such cases. However, extension of the concepts to a question of more unknowns is relatively straightforward. In one dimension (i.e. with just one parameter to be determined), a convergence interval may be defined, corresponding to all values of the unknown for which a slight increment in the estimate causes the pf to change in a manner that infers the direction of the correct value. Viewed as a graph of pf value against parameter, it can be seen that all points on the same lobe of the graph as the maximum are ones for which convergence is

certain. Therefore the local minima ($\frac{d}{da_i}$ pf=0, where a_i is the ith Fourier coefficient) define the limits of the interval. For 2 unknowns the situation is more complicated — subsidiary maxima and saddle points occurring at various points not necessarily on either of the axes.

It was found that use of Hamming weights at the beamforming stage greatly enhanced the convergence properties, although they did increase the inaccuracy of the location of the power function maximum. With this weighting system employed, a single source with little or no added noise had convergence intervals over all coefficients that exceeded any values that might occur in reality. When significant levels of additive noise are simulated, the convergence intervals are curtailed somewhat. Using combinations of different length arrays and different levels of noise, it was found that the convergence intervals for a_1 and a_2 seemed to be dependent on their product i.e. the possible output SNR. For a value of 12dB, the convergence intervals for a_1 and a_2 are approximately 9m and 6m. Weaker signals than that give insufficient guide to the shape estimator, such that the selected shapes are so far from true that the source cannot be located; thus convergence intervals are meaningless for an output SNR much below 12dB.

The addition of a second source to the scenario has a great effect on the situation. As mentioned earlier the location of the peak experiences a small bias dependent on the phase difference of the signals. A more pronounced effect of the interaction is shown when considering a contour plot covering errors in the first two coefficients a_1 and a_2. For sources of comparable strength (power ratio in the range 0-6dB) and separated by about 30°, a circle of subsidiary maxima occur about the true pf peak. These are approximately located at $(\Delta a_1, \Delta a_2) = (0., \pm 3.)$m and $(\pm 4., \pm 1.5)$m. Not all are always present — those on the Δa_2 axis occurring for less than half of the possible phase differences. The other 4 maxima vary in prominence too, depending on the phase relationship of the sources, but there are always some present. These subsidiary maxima prove a distraction for gradient routines approaching from highly erroneous shapes.

To overcome this problem of an incorrect maximum being achieved, it was proposed that when a peak is reached, a 'jump' routine be invoked. This compares the value of the power function at the current peak with those at the 6 locations corresponding to changes in shape of $(\Delta a_1, \Delta a_2) = (0., \pm 3.)$m and $(\pm 4., \pm 1.5)$m; the largest being selected as nearest to true, and the gradient method applied again to achieve that peak. This method is based on the approximate constancy in locations of the maxima. The above values for the jump size are correct for a 16 element array with the sources about 25-50° apart. If the sources are more widely separated, the interaction is less and consequently the maxima lie further out, albeit along the same vector direction.

The distance that the maxima lie from the true peak is also roughly proportional to the number of elements.

Correlated multiplicative noise is shown to have only minor effects on the contour plots such that the convergence region remains large. The combination of two sources and multiplicative terms does cause subsidiary maxima to exist, though they tend to be less frequent than for scenarios involving just 2 sources i.e. the multiplicative terms have reduced the interaction of the 2 signals.

Thus it can be seen that measures calculated from the beam patterns for particular shape estimates can be very useful guides in determining the positions of the hydrophones, and hence the bearings of distant sources. It has been shown that by a suitable choice of weighting function, rapid convergence from highly erroneous estimates can be achieved, despite the presence of many noise effects.

REFERENCES

1) Aitken G.J.M. & Johnson R. 'High-Resolution Reconstruction of Photon-Limited Stellar Images using Phase Gradients' Can J. Phys **66,** 847-853 (1988)

2) Akulicheva V.P. & Frolov V.M. 'Fluctuations of the Levels, Angles, and Time Differences of the Arrivals of Sound Signals received over Separate Paths in the Ocean' Sov.P-Ac **32,** 465-468 (1986)

3) Ali H.B., Ferla M.C. & Akal T. 'Temporal and Spatial Variabilities in Shallow Water Acoustics: Measurements and Predictions' Proc.IoA **7.3,** 143-150 (1985)

4) Aredov A.A., Okhrimenko N.N. & Furduev A.V. 'Anisotropy of the Noise Field in the Ocean (Experiment and Calculations)' Sov.P-Ac. **34,** 128-131 (1988)

5) Artel'nyi V.V., Didenkulov I.N. & Raevskii M.A. 'Low-Frequency Dynamic Noise in a Randomly Inhomogeneous Ocean' Sov.P-Ac **34,** 7-10 (1988)

6) Ayers G.R., Northcott M.J. & Dainty J.C. 'Knox-Thompson and Triple-Correlation Imaging Through Atmospheric Turbulence' JOSA-A **5,** 963-985 (1988)

7) Barrett R.F. & McMahon D.R.A. 'Comparison of Frequency Estimators for Underwater Acoustic Data' JASA **79,** 1461-1471 (1986)

8) Bedendender J.W. 'Three-Dimensional Boundary Value Problems for Flexible Cables' 2nd Offshore Technology Conference (Houston, Texas) **OTC-1281,** 541-556 (1970)

9) Beran M.J. & Whitman A.M. 'Effect of Random Velocity Fluctuations on Underwater Scattering' JASA **81,** 647-649 (1987)

10) Bouvet M. 'Beamforming of a Distorted Line Array in the Presence of Uncertainties on the Sensor Positions' JASA **81,** 1833-1840 (1987)

11) Bouvet M. & Schwartz S.C. 'Underwater Noises : Statistical Modeling, Detection, and Normalization' JASA **83,** 1023-1033 (1988)

12) Brandenburg W. 'A Point Mechanical Model for the Dynamics of Towed Arrays' ICASSP **84,** 40.3.1-4 (1984)

13) Brown W.D. & Ghiglia D.C. 'Some Methods for Reducing Propagation-Induced Phase Errors in Coherent Imaging Systems. I. Formalism' JOSA-A **5,** 924-941 (1988)

14) Bucker H.P. 'Cross-Sensor Beamforming with a Sparse Line Array'
JASA **61,** 494-498 (1977)

15) Bucker H.P. 'Comparison of FFT and Prony Algorithms for Bearing Estimation of Narrow-Band Signals in a Realistic Ocean Environment' JASA **61** 756-763 (1977)

16) Bucker H.P. 'Beamforming a Towed Line Array of Unknown Shape'
JASA **63,** 1451-1454 (1978)

17) Buckley R. 'Diffraction by a Random Phase-Changing Screen: A Numerical Experiment'
J-ATP **37,** 1431-1446 (1975)

18) Burg J.P. 'Maximum Entropy Spectral Analysis' Proc. 37th Mtg Society of Exploration Geophysicists (Oklahoma City, OK) Oct 31 (1967)

19) Burlakova I.B., Saichev A.I. & Slavinski M.M. 'Spectrum of a Signal with the Elimination of Frequency Wandering' Sov.P-Ac. **33,** 236-241 (1987)

20) Butler D. 'Beamforming with a Distorted Towed Array' from 'Adaptive Methods in Underwater Acoustics' edited by Urban H.G. pp 469-475 Reidel : ISBN 90-277-1982-9

21) Byrne C.L. & Steele A.K. 'Stable Nonlinear Methods for Sensor Array Processing'
J-OE **10,** 255-259 (1985)

22) Capon J. 'High-Resolution Frequency-Wavenumber Spectrum Analysis'
Proc IEEE **57,** 1408-1418 (1969)

23) Cartwright R. & Mayers D.F. 'The Motion of a Towed Array of Hydrophones'
chap 11 of "Industrial Numerical Analysis" edited by Elliott C.M. & McKee S.
OUP : ISBN 0-19-853190-7

24) Chotiros N.P. & Culbertson C.R. 'A Method for Predicting Acoustic Signal Fluctuations using a Distribution of Gaussian Correlation Functions' JASA **82,** 257-264 (1987)

25) Compton-Hall R. 'The Incredible Shrinking Submarine' New Scientist **1658,** 34-37 (1989)

26) Cowie L.L & Songaila A. 'Atmospheric Isoplanatism and Astronomical Image Reconstruction on Mauna Kea' JOSA-A **5,** 1015-1022 (1988)

27) Cox H., Zeskind R.M. & Kooij T. 'Practical Supergain' ASSP **34,** 393-398 (1986)

28) Cox H., Zeskind R.M. & Owen M.M. 'Effects of Amplitude and Phase Errors on Linear Predictive Array Processors' ASSP **36,** 10-19 (1988)

29) Desaubies Y.J.F. 'On the Scattering of Sound by Internal Waves in the Ocean'
JASA **64,** 1460-1469 (1978)

30) Dolph C.L. 'A Current Distribution for Broadside Arrays which Optimizes the Relationship between Beam Width and Side-Lobe Level' Proc. IRE **34,** 335-347 (1946)

31) Ewart T.E. 'Acoustic Fluctuations in the Open Ocean — A Measurement using a Fixed Refracted Path' JASA **60,** 46-59 (1976)

32) Ewart T.E. 'A Numerical Simulation of the Effects of Oceanic Finestructure on Acoustic Transmission' JASA **67,** 496-503 (1980)

33) Ewart T.E., Ehrenberg J.E. & Reynolds S.A. 'Observations of the Phase and Amplitude of Individual Fermat Paths in a Multipath Environment' JASA **63,** 1801-1808 (1978)

34) Farrier D.R. & Jeffries D.J. 'Robust High Resolution Array Beamforming' Proc. IoA **7.4,** 17-24 (1985)

35) Ferguson B.G. & Wylie D.V. 'Comparison of Observed and Theoretical Responses of a Horizontal Line Array to Wind-Induced Noise in the Deep Ocean' JASA **82,** 601-605 (1987)

36) Fertner A. & Sjölund A. 'Comparison of Various Time Delay Estimation Methods by Computer Simulation' ASSP **34,** 1329-1340 (1986)

37) Fizell R.G. 'Application of High-Resolution Processing to Range and Depth Estimation using Ambiguity Function Methods' JASA **82,** 606-613 (1987)

38) Flatté S.M. & Stoughton R.B. 'Predictions of Internal-Wave Effects on Ocean Acoustic Coherence, Travel-Time Variance, and Intensity Moments for Very Long-range Propagation' JASA **84,** 1414-1424 (1988)

39) Galkin O.P. & Frolov V.M. 'Fluctuations of the Arrival Angle of a Sound Signal Reflected from the Ocean Surface' Sov.P-Ac. **31,** 98-99 (1985)

40) Ginzkey L. 'Influence of Hydrophone Position Errors on Spatial Signal Processing Algorithms' from 'Adaptive Methods in Underwater Acoustics' edited by Urban H.G. pp 477-482 Reidel : ISBN 90-277-1982-9

41) Gitel'son V.S., Glebova G.M. & Kuznetsov G.N. 'Determination of the Parameters of Correlated Signals by the Prony Method' Sov.P-Ac. **34,** 94-95 (1988)

42) Godara L.C. 'The Effect of Phase-Shifter Errors on the Performance of an Antenna-Array Beamformer' J-OE **10,** 278-283 (1985)

43) Gray D.A. 'Effect of Time-Delay Errors on the Beam Pattern of a Linear Array' J-OE **10,** 269-277 (1985)

44) Gregg M.C. 'Variations in the intensity of small scale mixing in the main thermocline' J. Phys. Ocean. **7,** 436-454 (1977)

45) Harris F.J. 'On the Use of Windows for Harmonic Analysis with the Discrete Fourier Transform' Proc. IEEE **66,** 51-83 (1978)

46) Hamson R.M. 'The Theoretical Responses of Vertical and Horizontal Line Arrays to Wind-Induced Noise in Shallow Water' JASA **78,** 1702-1712 (1985)

47) Hebbert R.S. & Barkakati L.T. 'High-Resolution Beamforming by Fitting a Plane-Wave Model to Acoustic Data' JASA **79,** 1844-1849 (1986)

48) Hinich M.J. 'Bearing Estimation using a Perturbed Linear Array' JASA **61,** 1540-1544 (1977)

49) Hinich M.J. & Rule W. 'Bearing Estimation using a Large Towed Array' JASA **58,** 1023-1029 (1975)

50) Hodgkiss W.S. 'The Effects of Array Shape Perturbation on Beamforming and Passive Ranging' J-OE **8,** 120-130 (1983)

51) Högbom J.A. 'Aperture Synthesis with a Non-Regular Distribution of Interferometer Baselines' Ast. Ast. Supp. **15,** 417-426 (1974)

52) Jensen F.B. 'Wave Theory Modeling : A Convenient Approach to CW and Pulse Propagation Modeling in Low-Frequency Acoustics' J-OE **13,** 186-197 (1988)

53) Kay S.M. & Marple S.L. 'Spectrum Analysis — A Modern Perspective' Proc. IEEE **69,** 1380-1419 (1981)

54) Kazmirtsak V.Yu. & Tyutekin Yu.V. 'Variability of the Characteristics of an Algorithm for the Space-Time Processing of a Sound Field with Level Quantization' Sov.P-Ac. **31,** 318-319 (1985)

55) Kesler S.B., Boodaghians S. & Kesler J. 'Resolving Uncorrelated and Correlated Sources by Linear Prediction' AP **33,** 1221-1226 (1985)

56) Ketchman J. 'Vibration Induced in Towed Linear Underwater Array Cables' J-OE **6,** 77-87 (1981)

57) Kirlin R.L. & Dewey L.A. 'Optimum Delay Estimation in a Multiple Sensor Array having Spatially Correlated Noise' ASSP **33,** 1387-1396 (1985)

58) Kleinberg L.I. 'Array Gain for Signals and Noise having Amplitude and Phase Fluctuations' JASA **67,** 572-577 (1980)

59) Knapp C.H. 'Signal Detectors for Deformable Hydrophone Arrays' ASSP **37,** 1-7 (1989)

60) Knox K.T. 'Image Retrieval from Astronomical Speckle Patterns' JOSA **66,** 1236-1239 (1976)

61) Knox K.T. & Johnson B.J. 'Recovery of Images from Atmospherically Degraded Short-Exposure Photographs' Astrophys. J. **193,** L45-L48 (1974)

62) Komissarov V.M. 'Amplitude and Phase Fluctuations and Their Correlation in The Propagation of Waves in a Medium with Random, Statistically Anisotropic Inhomogeneities' Sov.P-Ac. **10,** 143-152 (1964)

63) Labeyie A. 'Attainment of Diffraction Limited Resolution in Large Telescopes by Fourier Analyzing Speckle Patterns in Star Images' Ast. Ast. **6,** 85-87 (1970)

64) Lee E.A. & Dorny C.N. 'A Generalized Self-Survey Technique for Self-Cohering of Large Arrays' AP **35,** 496-503 (1987)

65) Ling H., Lo Y.T. & Rahmat-Samii Y. 'Reflector Sidelobe Degradation due to Random Surface Errors' AP **34,** 164-172 (1986)

66) Luthra A.K. & Steinberg B.D. 'Analysis of Maximum Entropy Processing in the Space-Angle Domain : Two Target Case' AP **33,** 594-599 (1985)

67) Marple S.L. 'Digital Spectral Analysis with Applications' Prentice-Hall Inc. : ISBN 0-13-214149-3

68) Medwin H. 'Sound Phase and Amplitude Fluctuations due to Temperature Microstructure in the Upper Ocean' JASA **56,** 1105-1110 (1974)

69) Mendus V.I. & Postnov G.A. 'Optimization of the Parameters of a Multielement Underwater Acoustic Array with Allowance for the Possibility of Element Failures' Sov.P-Ac. **33,** 554-555 (1987)

70) Meredith R.W. & Ramsdale D.J. 'Performance Comparison of the Wagstaff-Berrou and Maximum Entropy Method Beamformers' JASA **81,** 1014-1024 (1987)

71) Muller R.A. & Buffington A. 'Real-Time Correction of Atmospherically Degraded Telescope Images through Image Sharpening' JOSA **64,** 1200-1210 (1974)

72) Mumford P.J. & Lawton A.D. 'Transducer Tolerance Effects on Conventional and Maximum-Likelihood Beamformers' Proc. IoA **7.4,** 127-135 (1985)

73) Nakatsuka K. 'Beam Deviations of Large Linear Arrays due to Wavy Phase Errors' AP **36,** 1014-1018 (1988)

74) Nikias C.L. & Pan R. 'Time Delay Estimation in Unknown Gaussian Spatially Correlated Noise' ASSP **36,** 1706-1714 (1988)

75) Nystuen J.A. & Farmer D.M. 'The Influence of Wind on the Underwater Sound Generated by Light Rain' JASA **82,** 270-274 (1987)

76) Owsley N.L. & Fay J.F. 'Optimum Turbulent Boundary Layer Induced Noise Suppression with Suboptimum Realizations' JASA **66,** 1404-1411 (1979)

77) Paulraj A. & Kailath T. 'Eigenstructure Methods for Direction of Arrival Estimation in the Presence of Unknown Noise Fields' ASSP **34,** 13-20 (1986)

78) Paulraj A. & Kailath T. 'Direction of Arrival Estimation by Eigenstructure Methods with Imperfect Spatial Coherence of Wave Fronts' JASA **83,** 1034-1040 (1988)

79) Pisarenko V.F. 'The Retrieval of Harmonics from a Covariance Function' Geophys J. Roy. Astro. Soc. **33,** 347-366 (1973)

80) Porter M.B., Dicus R.L. & Fizell R.G. 'Simulations of Matched-Field Processing in a Deep-Water Pacific Environment' J-OE **12,** 173-181 (1987)

81) Quazi A.H. 'Array Beam Response in the Presence of Amplitude and Phase Fluctuations' JASA **72,** 171-180 (1982)

82) Ramsdale D.J. & Howerton R.A. 'Effect of Element Failure and Random Errors in Amplitude and Phase on the Sidelobe Level Attainable with a Linear Array' JASA **68,** 901-906 (1980)

83) Reed F.A. 'The Behavior of Absolutely Optimal Array Filters for Sensor Arrays in the Presence of Noise' ASSP **35,** 1489-1491 (1987)

84) Riblet H.J. & Dolph C.L. 'Discussion on "A Current Distribution for Broadside Arrays which Optimizes the Relationship between Beam Width and Side-Lobe Level"' Proc. IRE **35,** 489-492 (1947)

85) Rockah Y. & Schultheiss P.M. 'Array Shape Calibration using Sources in Unknown Locations — Part I : Far-Field Sources' ASSP **35,** 286-299 (1987)

86) Rosenfeld A. & Kak A.C. 'Digital Picture Processing' pp.153-255 Academic Press Inc. : ISBN 0-12-597360-8

87) Roy R., Paulraj A. & Kailath T. 'ESPRIT — A Subspace Rotation Approach to Estimation of Parameters of Cisoids in Noise' ASSP **34,** 1340-1342 (1986)

88) Schmidt R.O. 'Multiple Emitter Location and Signal Parameter Estimation' AP **34,** 276-280 (1986)

89) Scholz B. & Kroll W. 'Application of High Resolution Spatial Processing Methods to Real Data of a Fixed Array in Shallow Water' from 'Adaptive Methods in Underwater Acoustics' edited by Urban H.G. pp 309-315 Reidel : ISBN 90-277-1982-9

90) Schultheiss P.M. & Ianniello J.P. 'Optimum Range and Bearing Estimation with Randomly Perturbed Arrays' JASA **68,** 167-173 (1980)

91) Schwarz U.J. 'Mathematical-Statistical Description of the Iterative Beam Removing Technique (Method CLEAN)' Ast. Ast. **65,** 345-356 (1978)

92) Schwarz U.J. 'The Method "CLEAN" — Use, Misuse and Variations'
from 'Image Formation from Coherence Functions in Astronomy' edited by van Schoonveld C. pp 261-275 (Reidel,1979)

93) Scrimger J.A., Evans D.J., McBean G.A., Farmer D.M. & Kerman B.R. 'Underwater Noise due to Rain, Hail and Snow' JASA **81,** 79-86 (1987)

94) Sica L. 'Image-Sharpness Criterion for Space-Variant Imaging' JOSA **71,** 1172-1175 (1981)

95) Sica L. 'Use of a Sharpness Criterion in Correcting Images degraded by Random Distortion' JOSA-A **5,** 1492-1501 (1988)

96) Steinberg B.D. 'Tolerance Theory' chap 13 of "Principles of Array and Aperture System Design" Wiley : ISBN 0-471-82102-0

97) Steinberg B.D. & Yadin E. 'Effect of Multipath and Scattering on Array Gain of a Large Adaptive Beam Forming Phased Array' AP **33,** 481-487 (1985)

98) Tough R.J.A. 'The Description and Simulation of Correlated Non-Gaussian Noise' Proc. IoA **8.5,** 36-42 (1986)

99) Tsao J. & Steinberg B.D. 'Reduction of Sidelobe and Speckle Artifacts in Microwave Imaging : The CLEAN Technique' AP **36,** 543-556 (1988)

100) Urick R.J. 'Models for the Amplitude Fluctuations of Narrow-Band Signals and Noise in the Sea' JASA **62,** 878-887 (1977)

101) Urick R.J. 'Spatial Coherence (Correlation)' chap 13 of "Sound Propagation in the Sea" Peninsula Publishing : ISBN 0-932146-08-2

102) Urick R.J. 'Fluctuations of Signals and Noise in the Sea and their Effect On Sonar Target Detection' Proc. IoA **8.5,** 53-69 (1986)

103) Wang H.S.C. 'Amplitude Shading of Sonar Transducer Arrays' JASA **57,** 1076-1084 (1975)

104) Ward R.K. & Saleh B.E.A. 'Deblurring Random Blur' ASSP **35,** 1494-1498 (1987)

105) Whitmarsh D.C., Skudrzyk E. & Urick R.J. 'Forward Scattering of Sound in the Sea and its Correlation with the Temperature Microstructure' JASA **29,** 1124-1143 (1957)

106) Wilson H.L. & Tappert F.D. 'Acoustic Propagation in Random Oceans Using the Radiation Transport Equation' JASA **66,** 256-274 (1979)

107) Yang C.C. & McDaniel S.T. 'Decorrelation of Acoustic Energy Propagated over Disjoint Paths in a Turbulent Ocean' JASA **81,** 295-300 (1987)

AP	-	IEEE Antennas and Propagation
ASSP	-	IEEE Acoustics, Speech & Signal Processing
Ast.Ast.	-	Astronomy & Astrophysics
Astrophys. J	-	Astrophysical Journal
ICASSP	-	International Conference on Acoustics, Speech & Signal Processing
JASA	-	Journal of the Acoustical Society of America
J-ATP	-	Journal of Atmospheric and Terrestrial Physics
J-OE	-	Journal of Oceanic Engineering
JOSA	-	Journal of the Optical Society of America
J. Phys. Ocean	-	Journal of Physics of the Ocean
Proc. IoA	-	Proceedings of the Institute of Acoustics
Sov.P-Ac	-	Soviet Physics (Acoustics)

App 1. THE RELATIONSHIP BETWEEN BEAM PATTERN AND DIRECTIVITY PATTERN

i) A **beam pattern** may be defined as the distribution of the power perceived from a direction, θ, when only a source at θ_0 is present.

ii) A **directivity pattern** is the sensitivity of a processor looking in direction θ_0, to a source at variable angle, θ.

Let there be N sensors, arbitrarily distributed with respect to a set of co-ordinate axes. Their position vectors are $\{r_i\}, i=1,N$, and the wavevector for a far-field source at θ' is k'.

i) Ignoring an arbitrary phase term, the signal at the sensors due to a unit magnitude source is given by the complex voltage, v_i, where $v_i = \exp(jk_0 \cdot r_i)$. The voltage perceived in the look direction, θ, is thus:-

$$V(\theta) = \sum_{i=1}^{N} \exp(jk_0 \cdot r_i) \exp(-jk \cdot r_i) = \sum_{i=1}^{N} \exp[j(k_0 - k) \cdot r_i] \qquad [A1.1]$$

and the power distribution, $P(\theta)$, is given by the square of that.

ii) However, if the source was at θ, the signal becomes $v_i = \exp(jk \cdot r_i)$, and the overspill into the look direction, θ_0 is then given by:-

$$V'(\theta) = \sum_{i=1}^{N} \exp(jk \cdot r_i) \exp(-jk_0 \cdot r_i) = \sum_{i=1}^{N} \exp[j(k - k_0) \cdot r_i] \qquad [A1.2]$$

and the directivity function, $D(\theta)$, by its square.

It is easily seen that $V(\theta)=-V'(\theta)$ and hence that $D(\theta)=P(\theta)$ for any distribution of sensors. Thus although the terms beam pattern and directivity pattern have very different definitions, they have the same mathematical form and may be used interchangeably in this context.

Note, however, that 'beam pattern' is more generally used to refer to the perceived image pattern for a certain signal record, which may contain several sources and additive noise, whereas a 'directivity pattern' is always the response to a single source under ideal conditions.

App 2. BEAM PATTERN FOR A STRAIGHT ARRAY

If a perfectly straight array of n elements, at equal spacing, d, is insonified by a unit source at angle θ_0 to its normal, the complex voltage at each sensor is given by:-

$$v_i = e^{-jkdi\sin\theta_0} \qquad , i=1,n \qquad \text{[A2.1]}$$

Beamforming yields the power perceived from direction, θ as:-

$$p(\theta) = V(\theta).V^*(\theta) \qquad \text{[A2.2]}$$

where:-

$$V(\theta) = \sum_{i=1}^{n} v_i e^{jkdi\sin\theta} \qquad \text{[A2.3]}$$

[Note a normalization factor of $1/n$ is commonly used.]

$$\rightarrow V(\theta) = \sum_{i=1}^{n} e^{jkdi(\sin\theta-\sin\theta_0)} \qquad \text{[A2.4]}$$

$$= \sum_{i=1}^{n} z^i \qquad \text{, where } z = e^{jkd(\sin\theta - \sin\theta_0)}$$

$$= z\,\frac{z^n - 1}{z - 1} = \frac{z^{n/2} - z^{-n/2}}{z^{1/2} - z^{-1/2}} \cdot \frac{z.z^{n/2}}{z^{1/2}}$$

$$= \frac{\sin(1/2 kdn.\Delta s)}{\sin(1/2 kd.\Delta s)} \cdot e^{j(n+1)kd.\Delta s/2} \qquad \text{[A2.5]}$$

where $\Delta s = (\sin\theta - \sin\theta_0)$. Thus:-

$$p(\theta) = \frac{\sin^2(1/2 kdn.\Delta s)}{\sin^2(1/2 kd.\Delta s)} = \frac{\sin^2(\pi dn.\Delta s/\lambda)}{\sin^2(\pi d.\Delta s/\lambda)} \qquad \text{[A2.6]}$$

Note the pattern is dependent only on the difference of the *sines* of the angles rather than the absolute values themselves. The beamwidth at broadside is given by:-

$$\Delta\theta \approx \Delta s = \lambda / D \qquad \text{[A2.7]}$$

where $D = n\,d$ is the length of the array. The beamwidth corresponds to the necessary change in angle for the argument of the numerator of [A2.6] to alter by π radians.

App 3. PROOF OF LINEARITY

FOR CONVENTIONAL BEAMFORMING

Consider an array of n sensors, with cartesian co-ordinates x_i, y_i, insonified by a source at θ_1. Then the signal at each of the sensors would be:-

$$v_i = A_1 e^{jk_1 \cdot r_i} \qquad \text{[A3.1]}$$

where $k_1 = \frac{2\pi}{\lambda}\ (\sin\theta_1 , \cos\theta_1)$, $r_i = (x_i, y_i)$ and A_1 is a complex number containing both amplitude and initial phase of signal.

Conventional beamforming produces a beam pattern given by:-

$$V_1(\theta) = V'(k) = \sum_{i=1}^{n} w_i v_i e^{-jk\hat{r}_i} \qquad , k = \left[\frac{-2\pi}{\lambda}, \frac{2\pi}{\lambda} \right] \qquad \text{[A3.2]}$$

where w_i are the values of the weights, $\hat{r}_i = (\hat{x}_i, \hat{y}_i)$ are the estimated element locations, and k is the wavenumber vector corresponding to angle θ.

$$\rightarrow V_1(\theta) = \sum_{i=1}^{n} A_1 w_i e^{j(k_1 \cdot r_i - k\hat{r}_i)} \qquad \text{[A3.3a]}$$

Similarly, the pattern due to a source at θ_2 to the array is:-

$$V_2(\theta) = \sum_{i=1}^{n} A_2 w_i e^{j(k_2 \cdot r_i - k\hat{r}_i)} \qquad \text{[A3.3b]}$$

If the array receives the signals from both sensors simultaneously, the sensor voltages are given by:-

$$v_i = A_1 e^{jk_1 \cdot r_i} + A_2 e^{jk_2 \cdot r_i} \qquad \text{[A3.4]}$$

Application of the beamforming algorithm then yields:-

$$V_{12}(\theta) = \sum_{i=1}^{n} w_i v_i e^{-jk\hat{r}_i}$$

$$= \sum_{i=1}^{n} w_i A_1 e^{j(k_1 r_i - k\hat{r}_i)} + \sum_{i=1}^{n} w_i A_2 e^{j(k_2 r_i - k\hat{r}_i)}$$

$$\rightarrow V_{12}(\theta) = V_1(\theta) + V_2(\theta) \qquad \text{[A3.5]}$$

Now, $P = VV^*$, and expressing the values A_i explicitly in terms of amplitude and phase i.e. $A_i = a_i e^{j\phi_i}$, it follows that:-

$$P_{12}(\theta) = [V_1(\theta) + V_2(\theta)][V_1^*(\theta) + V_2^*(\theta)]$$

$$= V_1 V_1^* + V_2 V_2^* + P' \qquad \text{[A3.6]}$$

where:-

$$P' = \sum_{i=1}^{n}\sum_{j=1}^{n} a_1 a_2 w_i w_j \left[e^{j(k_1 r_i - k\hat{r}_i + \phi_1 - k_2 r_j + k\hat{r}_j - \phi_2)} + e^{j(k_2 r_j - k\hat{r}_j + \phi_2 - k_1 r_i + k\hat{r}_i - \phi_1)} \right]$$

$$= \sum_{i=1}^{n}\sum_{j=1}^{n} a_1 a_2 w_i w_j \cdot 2\cos[(k_1 r_i - k_2 r_j) + k(\hat{r}_i - \hat{r}_j) + (\phi_1 - \phi_2)] \qquad \text{[A3.7]}$$

Use of the trigonometric relation $\cos(\psi + \Delta\phi) = \cos\psi \cos\Delta\phi - \sin\psi \sin\Delta\phi$, enables the dependence on phase difference, $\Delta\phi$, to be brought through the summation to give:-

$$P_{12}(\theta) = P_1(\theta) + P_2(\theta) + \tilde{P}(\theta)\cos(\Delta\phi) + \hat{P}(\theta)\sin(\Delta\phi) \qquad \text{[A3.8]}$$

The last terms (the cross-product terms) depend on the initial phases of the two signals. Thus any single realization of a simulation of the two source scenario will not immediately lead to a beam pattern that is the sum of the two individual ones. However, in the real world, even the slightest motion of sources will lead to the difference in their initial phases changing completely. Accepting that $\Delta\phi$ is highly variable, the expectation operator may be applied to [A3.8] to give:-

$$E[P_{12}(\theta)] = P_1(\theta) + P_2(\theta) \qquad \text{[A3.9]}$$

Note, in simple modelling of situations the sources are phase locked to one another. To remove any such effect, several realizations must be done with different relative phases of the sources. Actually, for the 2-source case, it would be sufficient to perform two realizations, changing the phase of one source by π radians between them — the average of the two patterns so formed should have no cross-product terms.

Thus, it can be seen that the expected response due to two sources is simply the sum of those due to each separately, for *any* array shape, 'guessed' shape and elemental weighting.

App 4. SYMMETRY OF THE BEAM PATTERN AND ITS DEPENDENCE ON ERRORS

Part I

Consider the beamformer output expressed in terms of $s=\sin\theta$, noting that $s_0=\sin\theta_0$, where θ_0 is the bearing of the only source (angle is relative to array normal). Letting w_i be the values of the amplitude shading of the elements, and assuming that there are no noise effects present, the beamformer output an amount s' either side of the source direction (i.e. for $s=s_0\pm s'$) is given by:-

$$V(s_0+s') = \sum_{i=1}^{n} w_i e^{jkdi\,(s_0-s)} = \sum_{i=1}^{n} w_i e^{-jkdis'} \qquad \text{[A4.1]}$$

$$V(s_0-s') = \sum_{i=1}^{n} w_i e^{jkdi\,(s_0-s)} = \sum_{i=1}^{n} w_i e^{jkdis'} \qquad \text{[A4.2]}$$

$$= \left[\sum_{i=1}^{n} w_i^* e^{-jkdis'} \right]^* = V^*(s_0+s') \qquad \text{[A4.3]}$$

Noting that $P(s)=V(s)\,V^*(s)$, it can be seen that the power perceived at equal angles from the source direction are the same, independent of the elemental weighting used. This means that the beam pattern is symmetrical about the true direction. Note, the weights need not even be symmetrically arranged about the centre of the array for this to be so. Therefore weighting errors cannot cause an asymmetric beam pattern, nor it is possible to adjust the weights so as to lower the side lobes on one side of the main beam at the expense of the other.

Such an effect is achieved by phase mis-match errors; this is equivalent to using complex weights, in which case $w_i=w_i^*$ no longer holds, and thus the above analysis fails.

Part II

An error in phase compensation is *exactly* the same as the presence of phase components in the weighting values. Re-examining equations A4.1, A4.2 in this light leads to:-

$$V(s_0+s') = \sum_{i=1}^{n} w_i e^{-jkdis'} \qquad \text{[A4.1]}$$

$$V(s_0-s') = \sum_{i=1}^{n} w_i e^{jkdis'} = \sum_{m=1}^{n} w_{n+1-m}\, e^{jkd(n+1)s'-jkdms'} \qquad , m=n+1-i$$

$$= e^{jkd(n+1)s'} \sum_{m=1}^{n} w_{n+1-m} e^{-jkdms'} \qquad \text{[A4.4]}$$

Thus, $P(s_0+s') = P(s_0-s')$ if $w_{n+1-i} = w_i$ for all i, i.e. the beam pattern due to the source will be symmetrical if both the true weightings ($\mathrm{Re}\{w_i\}$) and the errors in phase are symmetrical.

Coupled with the earlier result, one may conclude that asymmetric beam patterns can only occur if:-

a) phase compensation errors exist when asymmetric weighting is used (e.g. when element failure has occurred).

b) errors in phase are not symmetrically arranged.

Note, another implication of this result is that a weak source nearby to a strong one may be rendered more clearly visible by incorrect focusing, such that the side lobes of the stronger source are away from the weak source's main lobe. However, it might be more convenient to adopt a system of weights, such as Dolph-Chebyshev, which when correctly focused give low side lobes on both sides.

Part III

Continuing with the representation of phase mis-match as the phase component of the weighting values, one may compare the beam patterns for two erroneous estimates of the true shape corresponding to equal and opposite errors on each element. Let V_+, V_- correspond to the perceived voltage displays for the two beamforming attempts; the change in phase error between the two cases is simply represented by the transformation $w_i \rightarrow w_i^*$. The perceived voltage in a given direction for the first shape estimate (remembering that the errors are contained in the weighting terms) is given by:-

$$V_+(s_0+s') = \sum w_i e^{-jkdis'} \qquad \text{[A4.1]}$$

That for the second estimate is given by:-

$$V_-(s_0+s') = \sum w_i^* e^{-jkdis'} = \left[\sum w_i e^{jkdis'} \right]^*$$

$$= V_+^*(s_0-s') \qquad \text{[A4.5]}$$

Thus a reversal of the signs of all the phase errors causes an inversion of the single source beam pattern about the true bearing of the source. Assuming that the source is not too near to end-fire, the full beam pattern will contain almost exactly the same power levels as the first*. Thus power function formulae acting over the full range of sinθ will give the same values for each. Therefore the power functions will be symmetrical about the value for the true shape. [* For $d=\lambda/2$, the aliasing that occurs is such that, any part of the pattern reflected out of the allowable domain of sinθ will be translated back in.]

Part IV

Now consider a general array shape given by x_i , y_i and an estimate of this shape which errs by Δx_i , Δy_i in those values. The resultant errors in phase compensation for a direction θ are given by:-

$$\Delta\phi_i = (\Delta y_i \cos\theta + \Delta x_i \sin\theta) / \lambda \qquad \text{[A4.6]}$$

The distribution of $\Delta\phi_i$ across the array may be viewed as the sum of two distributions — one even, one odd. When expressed as simple complex numbers (as used above) the relationship is given by:-

$$\mu_i \nu_i = e^{-j\Delta\phi_i} \qquad \text{[A4.7]}$$

where μ_i and ν_i are the even and odd distributions respectively. Using m as an index for counting from the other end, i.e. $m = n+1-i$, the symmetry properties of the various weightings, including w_i (now used simply as the amplitude component), may be summarised as below:-

$$w_m = w_i = w_m^* = w_i^* \qquad \mu_m = \mu_i \qquad \nu_m = \nu_i^* \qquad \text{[A4.8]}$$

It is also helpful to define a constant, Φ, as follows:-

$$\Phi = e^{jkd(n+1)s'} \qquad \text{[A4.9]}$$

Now take V_+ as the array response for one set of phase errors, i.e.:-

$$V_+(s_0+s') = \sum_{i=1}^{n} w_i \mu_i \nu_i e^{-jkdis'} \qquad [A4.1']$$

Then one may easily compare it with the response achieved for another set of phase errors corresponding to the inversion of only the even term:-

$$V_-(s_0-s') = \sum_{i=1}^{n} w_i \mu_i^* \nu_i e^{-jkdis'} = \sum_{m=1}^{n} w_m^* \mu_m^* \nu_m^* e^{-jkd(n+1-m)s'}$$

$$= \Phi^* V_+^*(s_0+s') \qquad [A4.10a]$$

Alternatively, V_- can be defined to be the array response for an inversion of the odd component of the phase errors; in which case, it becomes:-

$$V_-(s_0-s') = \sum_{i=1}^{n} w_i \mu_i \nu_i^* e^{jkdis'} = \sum_{m=1}^{n} w_m \mu_m \nu_m e^{jkd(n+1-m)s'}$$

$$= \Phi V_+(s_0+s') \qquad [A4.10b]$$

The importance of these last two results is that if beamforming is attempted for many possible array shapes, then the beam patterns (power responses) for a set of shapes differing only in their choice of the odd terms in the phase, will be symmetrical about the zero error term, for any choice of even errors. Therefore a power function should mimic this symmetry, and hence possibly lead to the discovery of the odd error terms even when significant errors in the even are present. The reverse is also true i.e. that the true even terms can be found independently of the odd terms.

Therefore, it makes extremely good sense to model the array shape with a set of functions which are either even or odd, as an error in the estimation of one symmetry set will not affect the other.

NOTE: The above only proves that any power function of the beam pattern will be symmetrical about the true shape; it does not show that anything other than a local extremum occurs there. Also, observe that all the above analysis was carried out in zero noise conditions; such is not realistic, the true conditions having noise levels commensurate with that of the signal, as well as other sources being present. No proof has yet been obtained for power function performance with even the simplest noise; hence the need for repeated simulations. However, the above analysis indicates aspects of the behaviour to be looked for.

App 5. SIMULATION OF SIGNAL

FOR NEAR AND FAR-FIELD SOURCES

Consider an array positioned such that its centre is at the origin of the co-ordinate system, and it lies roughly along the x-axis. The position of the sensors are given by $\{x_i, y_i\}$, and that of one of the sources by (x_j, y_j). Defining $\{r_i\}$ and r_j to be the distances of these points from the origin, the time lead, τ_{ij}, of the signal from the jth source reaching the ith sensor before the origin is given by:-

$$\tau_{ij} = (r_j - r_{ij})/c$$

$$= \frac{1}{c}\left[r_j - \sqrt{(x_j-x_i)^2 + (y_j-y_i)^2} \right]$$

$$= \frac{1}{c}\left[r_j - \sqrt{x_j^2+y_j^2-2x_ix_j-2y_iy_j+x_i^2+y_i^2} \right]$$

$$= \frac{r_j}{c}\left[1 - \sqrt{1-(2x_ix_j+2y_iy_j-x_i^2-y_i^2)/r_j^2} \right] \qquad \text{[A5.1]}$$

Using $\sqrt{1-x} = 1 - x/2 - x^2/8 - \cdots$, we obtain:-

$$\tau_{ij} \approx \frac{r_j}{c}\left[\frac{1}{2}(2x_ix_j+2y_iy_j-x_i^2-y_i^2)/r_j^2 + \frac{1}{8}(2x_ix_j+2y_iy_j-x_i^2-y_i^2)^2/r_j^4 \right] \qquad \text{[A5.2]}$$

Noting that $x_j/r_j = \sin\theta$ and $y_j/r_j = \cos\theta$, and also that $x_i^2 + y_i^2 \ll | x_ix_j + y_iy_j |$, this simplifies to:-

$$\tau_{ij} \approx \frac{1}{c}\left[x_i\sin\theta + y_i\cos\theta - (x_i^2+y_i^2)/2r_j + (x_i\sin\theta + y_i\cos\theta)^2/2r_j \right] \qquad \text{[A5.3a]}$$

$$= \frac{1}{c}\left[x_i\sin\theta + y_i\cos\theta \right] - \frac{1}{2r_jc}\left[x_i^2(1-\sin^2\theta) - 2x_iy_i\sin\theta\cos\theta + y_i^2(1-\cos^2\theta) \right]$$

$$= \frac{1}{c}\left[x_i\sin\theta + y_i\cos\theta \right] - \frac{1}{2r_jc}\left[x_i\cos\theta - y_i\sin\theta \right]^2 \qquad \text{[A5.3b]}$$

Note, for a far-field source, $r_j \gg r_i$, this reduces to the familiar

$$\tau_{ij} \approx \frac{1}{c}\left[x_i\sin\theta + y_i\cos\theta \right] \qquad \text{[A5.4]}$$

App 6. RELATIONSHIP BETWEEN SOURCE RANGE AND PERCEIVED ARRAY SHAPE

Consider an array of some shape specified by its parameters, a_i, $i=1,n$, which is insonified by a near-field source at range, r, and bearing, θ. From appendix 5, the relevant time delays are:-

$$\tau_i = \frac{1}{c}\left[x_i\sin\theta + y_i\cos\theta\right] - \frac{1}{2rc}\left[x_i\cos\theta - y_i\sin\theta\right]^2 \qquad \text{[A6.1]}$$

In the special case of an approximately straight line (and provided that $|\theta|$ is not close to 90°), $|x_i\cos\theta| \gg |y_i\sin\theta|$, and consequently the second order term may be simplified to give:-

$$\tau_i = \frac{1}{c}\left[x_i\sin\theta + y_i\cos\theta\right] - \frac{1}{2rc}x_i^2\cos^2\theta \qquad \text{[A6.2]}$$

Now, consider a sample quadratic given by $y = 1-(2x/\pi - 1)^2$. This is chosen, as over the interval $[0, \pi]$ it has zero value at the ends, and unity magnitude at the peak (in the centre). Fourier analysis of this shows that:-

$$y \approx \frac{32}{\pi^3}\left[\frac{\sin x}{1} + \frac{\sin 3x}{3^3} + \frac{\sin 5x}{5^3} + \cdots\right] \qquad \text{[A6.3]}$$

In the derivation of [A6.2], time delays were calculated relative to the centre of the array, hence the maximum value of x_i^2 is $L^2/4$. Thus the magnitude of the quadratic term in [A6.2] is $[L^2\cos^2\theta/4]\,/\,2r_jc$, and consequently the expression for the delays may be approximated by:-

$$\tau_i = \frac{1}{c}\left[x_i\sin\theta + y_i'\cos\theta\right] \qquad \text{[A6.4a]}$$

where

$$y_i' = y_i + \frac{L^2\cos\theta}{8r_j}\cdot\frac{32}{\pi^3}\left[\frac{\sin(\pi x/L)}{1} + \frac{\sin(3\pi x/L)}{3^3} + \cdots\right] \qquad \text{[A6.4b]}$$

As all the terms other than the first are small, the effect of these modified time delays will be to cause the shape estimation algorithm to overestimate a_1 by $L^2\cos\theta\,/\,8r_j$ — $32/\pi^3$ being very close to 1.

App 7. THE LINE OF THE ARRAY

There is a problem inherent in the use of components of a Fourier Series, and that is that those basis functions which have odd symmetry about the array centre cause the 'line of the array' to be no longer parallel to the x-axis, as is illustrated in Fig A7.1. Quite clearly, this effect is greater for the lower order terms.

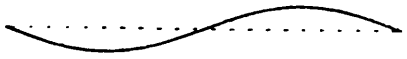

Fig A7.1a : Basis function for n=2

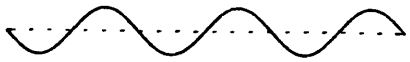

Fig A7.1b : Basis function for n=6

Note, an array as shown in Fig A7.1a will not shift the main beam of the array by θ if the correct element positions are used; the shift of θ corresponds to the effect of processing assuming that all the elements lie along the x-axis. However, it is useful to investigate the effect of pointing bias due to errors in the estimation of such a component, and of how this effect may be removed by altering the characterization of the array shape. Clearly the locational bias is not the only problem associated with incorrect estimation of the Fourier components — the quality of the beam pattern is also degraded such that when errors start being of the order of a third of a wavelength, one of the sidelobes may become dominant; for those conditions, the analysis given here is irrelevant.

For ease of analysis, the array is positioned such that the origin lies at the centre of the array. Thus a basis function of the array shape is given by:-

$$y = a_n \sin(n\pi x/L) \qquad , x = [-L/2 , L/2] \qquad \text{[A7.1]}$$

where L is the length of the array, and the order n corresponds to the number of sinusoidal half-periods in the whole array, and thus is always even, for the cases of interest here. The best fit straight line is given by:-

$$y = m\,x \qquad \text{[A7.2]}$$

where gradient m is to be determined. S is defined as the sum of the squares of the error of the fit. For simplicity an integral representation is used here:-

$$S = \int_{-L/2}^{L/2} [\,a_n \sin(n\pi x/L) - mx\,]^2\,dx$$

$$= \int_{-L/2}^{L/2} a_n^2 \sin^2(n\pi x/L)\,dx \;-\; \int_{-L/2}^{L/2} 2ma_n x \sin(n\pi x/L)\,dx \;+\; \int_{-L/2}^{L/2} m^2 x^2\,dx$$

$$= a_n^2 \cdot \tfrac{1}{2} \cdot L \;+\; 2ma_nL^2/n\pi \cdot s_n \;+\; m^2 \cdot 2 \cdot \frac{(L/2)^3}{3} \qquad \text{[A7.3]}$$

where $s_n = (-1)^{n/2} = -1, 1, -1, \ldots$ for $n=2, 4, 6, \ldots$

The best fit corresponds to setting the derivative with respect to m to zero, leading to:-

$$2a_nL^2/n\pi \cdot s_n \;+\; m \cdot L^3/6 \;=\; 0$$

$$\rightarrow\; m = -(12/n\pi L)\,s_n \cdot a_n \qquad \text{[A7.4]}$$

This implies that the resultant pointing bias, $\Delta\theta$ due to an error Δa_n in the estimation of an even Fourier coefficient is given by:-

$$\Delta\theta = (12/n\pi L)\;s_n \cdot \Delta a_n \qquad \text{[A7.5]}$$

Alternatively, the basis functions may be redefined with the necessary linear term removed viz:-

$$f_n(x) = \sin(n\pi x/L) \;+\; (12\,s_n / n\,\pi L)\,x \qquad \text{[A7.6]}$$

[Note, the actual implementation used in this work defines bases over the range [0, L] — the change of interval automatically causes all the s_n to be of the same sign.]

App 8. FITTING A PLANE TO A 2-D ARRAY OF POINTS

Formulae have been produced that enable a straight line to be fitted to a set of points, with the optimizing constraint that it should be chosen to minimize the sum of the squares of the deviations of the points from that line. Similarly, a plane, $z = a\,x + b\,y + c$, can be fitted to a set of points $z_{i,j} = f\,(x_i, y_j)$, such that S is minimized, where the sum of the squares, S, is defined by:-

$$S = \sum_{i,j} \left[z_{i,j} - a\,x_i - b\,y_j - c \right]^2 \qquad \text{[A8.1a]}$$

$$= S_1 - a\,S_2 - b\,S_3 - c\,S_4 + a^2\,S_5 + ab\,S_6 + ac\,S_7 + b^2\,S_8 + bc\,S_9 + c^2\,S_{10} \qquad \text{[A8.1b]}$$

where:-

$$S_1 = \sum_{i,j} z_{i,j}^2 \qquad S_2 = \sum_{i,j} 2x_i z_{i,j} \qquad S_3 = \sum_{i,j} 2y_j z_{i,j} \qquad S_4 = \sum_{i,j} 2z_{i,j} \qquad S_5 = \sum_{i,j} x_i^2$$

$$S_6 = \sum_{i,j} 2x_i y_j \qquad S_7 = \sum_{i,j} 2x_i \qquad S_8 = \sum_{i,j} y_i^2 \qquad S_9 = \sum_{i,j} 2y_j \qquad S_{10} = \sum_{i,j} 1$$

$$= \text{number of points} \qquad \text{[A8.2]}$$

The derivatives of S with respect to the 3 unknowns may be found, and equated to zero to locate the extremum, thus:-

$$dS/da \quad = \quad dS/db \quad = \quad dS/dc \quad = \quad 0 \qquad \text{[A8.3]}$$

Application of [A8.3] to [A8.1b] gives 3 simulataneous equations in 3 unknowns. Lengthy algebraic manipulation yields the final result:-

$$a = a'/d \qquad b = b'/d \qquad c = c'/d \qquad \text{[A8.4a]}$$

where:-

$$a' = 8S_2S_8S_{10} - 4S_4S_7S_8 - 2S_2S_9S_9 - 4S_3S_6S_{10} + 2S_3S_7S_9 + 2S_4S_6S_9 \qquad \text{[A8.4b]}$$

$$b' = 8S_3S_5S_{10} - 4S_4S_5S_9 - 2S_3S_7S_7 - 4S_2S_6S_{10} + 2S_2S_7S_9 + 2S_4S_6S_7 \qquad \text{[A8.4c]}$$

$$c' = 8S_4S_5S_8 - 4S_2S_7S_8 - 2S_4S_6S_6 - 4S_3S_5S_9 + 2S_2S_6S_9 + 2S_3S_6S_7 \qquad \text{[A8.4d]}$$

$$d = 16S_5S_8S_{10} - 4S_7S_7S_8 - 4S_5S_9S_9 - 4S_6S_6S_{10} + 4S_6S_7S_9 \qquad \text{[A8.4e]}$$

App 9. FITTING A QUADRATIC CURVE

Given three points (x_1,y_1), (x_2,y_2), (x_3,y_3), where the x_i are different, it is always possible to fit a quadratic curve through all the points. If the three points used are *near* the maximum of a smooth unknown curve, then the peak of the fitted quadratic will be a good estimate of the location of the peak of the unknown curve. Let the quadratic be represented by $y=ax^2+bx+c$, where a, b and c are yet to be determined. Then:-

$$y_i = ax_i^2 + bx_i + c \qquad , i=1,3 \qquad \text{[A9.1]}$$

Writing out in full for i=1,3, and then treating as simultaneous equations yields the values for parameters a and b as:-

$$a = -\frac{x_1(y_2-y_3) + x_2(y_3-y_1) + x_3(y_1-y_2)}{x_1^2(x_2-x_3) + x_2^2(x_3-x_1) + x_3^2(x_1-x_2)} \qquad \text{[A9.2a]}$$

$$b = \frac{x_1^2(y_2-y_3) + x_2^2(y_3-y_1) + x_3^2(y_1-y_2)}{x_1^2(x_2-x_3) + x_2^2(x_3-x_1) + x_3^2(x_1-x_2)} \qquad \text{[A9.2b]}$$

The extremum of such a quadratic occurs at:-

$$x' = -b / 2a$$

$$= \frac{1}{2} \cdot \frac{x_1^2(y_2-y_3) + x_2^2(y_3-y_1) + x_3^2(y_1-y_2)}{x_1(y_2-y_3) + x_2(y_3-y_1) + x_3(y_1-y_2)} \qquad [A9.3]$$

If the x_i are equally spaced, the x-axis may be rescaled to render $x_i=-1,0,1$, and thus the form for x' reduces to:-

$$x' = \frac{{}^1/_2 (y_1-y_3)}{y_1+y_3-2y_2} \qquad [A9.4]$$

Therefore, for equally spaced values of x :-

$$x' = x_2 + \frac{{}^1/_2 (y_1-y_3)}{y_1+y_3-2y_2} \Delta x \qquad [A9.5]$$

This is the form generally used in the program. Simulations with various curves have confirmed that this is fairly good at estimating x'.

App 10. JUSTIFICATION OF POWER FUNCTIONS

(And A Brief Discussion of Their Merits)

As has been stated earlier, the power distributed over a beam pattern is fixed, independent of the choice of array shape used for processing i.e. $\int p \, d\theta$ = a constant. [Note, this and other expressions should more correctly be written in terms of $\sin\theta$ i.e. $\int p \, d(\sin\theta)$, but the difference is

unimportant here.] However, different estimates of array configuration lead to markedly different beam patterns, those closer to the true array shape leading to patterns which are better *focused*. The idea of a focused pattern is intuitively clear, however it is necessary to reflect briefly upon it, as such a concept has to be coded for a computer. Comparing beam patterns due to shape estimates both near and far from true (e.g. Figs 15.1-4), it is seen that the pattern of the true shape is characterized by the following points:-

1) The highest main lobe

2) The greatest variation in power with respect to θ

3) The deepest nulls

4) The sharpest pattern (i.e. steepest gradient, $dp/d\theta$)

5) The narrowest main lobe

6) The greatest concentration of power around the peak of the beam pattern

7) The closest resemblance to an 'ideal' beam pattern.

Note — the above are merely observations of what occurs when no noise is present — no proof is included, and indeed several might be of little use in the presence of additive noise or other effects. Many of these may be implemented in the form of a 'power function' by calculating $\sum f(p_i,\theta_i)$, using different choices for $f(p(\theta_i),\theta_i)$. [N.B. In all cases where a summation is given, it is derived from an $\int$ representation of the above properties. The behaviour of the sums will be close to those of the corresponding integrals, provided that the beam sampling is often enough i.e. $\Delta\theta$ is small.]

1) $f(p,\theta)=p(\theta).\delta(\theta-\theta_0)$ where θ_0 is the angle corresponding to the peak of the pattern (i.e. the summation just contains the peak value). It is easily seen that for a single source with no additive noise, this will always be maximized for the true array shape. However, this measure uses only one figure from the many values of $p(\theta)$ available, and it certainly seems likely that some information is wasted when several sources of similar power are present.

2a) $f(p,\theta)=[p(\theta)-\bar{p}]^2=p^2(\theta)-2\bar{p}p(\theta)+\bar{p}^2$. This represents the variance in the power levels; summation over θ leads to:-

$$\sum f(p,\theta) = \sum p^2(\theta) - \sum \bar{p}^2$$

As the total power level, and hence $\bar{p}$, is believed to be independent of the shape chosen for processing, this power function reduces to $\sum p^2$.

2b) Higher order moments of the distribution can also be calculated e.g. skewness corresponds to $f(p,\theta) = [p(\theta) - \bar{p}]^3$, which upon summation and removal of constants reduces to a form containing $\sum p^2$ and $\sum p^3$ only.

3) $f(p,\theta) = -\ln(p)$ or $1/p$ would give great emphasis to the depth of the nulls in a beam pattern. In the absence of any noise, this will provide a good measure of how focused the pattern is; however, in taking note of the depth of the nulls, it is using the parts *most* sensitive to noise.

4) $f(p,\theta) = \left[\frac{dp}{d\theta}\right]$ or $\left[\frac{dp}{d\theta}\right]^2$. When applied to just the main lobe, the summation for the first expression will simply yield twice the peak height. When applied to the whole angular range, it is a measure of the 'spikiness' of the pattern. The expression $\left[\frac{dp}{d\theta}\right]^2$ will take greater note of the sharp declines. Alternatively, one could form $\left[\frac{d(p^2)}{d\theta}\right] = p\left[\frac{dp}{d\theta}\right]$.

5) As complete nulls will not exist in the presence of noise, the width of the main lobe must, of necessity, be defined in terms of the breadth at a certain power level relative to the peak (e.g. 10dB). Such is not easily determined accurately as power levels are only known at discrete angles.

6) $f(p,\theta) = -p \cdot (\theta - \theta_0)^2$. This provides the second moment of the power distribution about the perceived source direction. Note, this method and that for number 5 are difficult to generalise for several sources.

7) Comparison of experimental beam patterns with that for an ideal will show how much of the power in the former can be accounted for by the main source. This is similar to using a matched filter to detect a known form of signal.

App 11. INCREASING THE EFFECTIVE SAMPLING FOR POWER FUNCTIONS

A beam pattern is a smooth curve, values existing for all angles, θ. However computational limits require that the values only be calculated for N different angles (usually equally spaced), and thus power functions are formed from this set of N figures. However, if N is sufficiently large, values for the power between selected angles, θ_i, may be given closely by a linear approximation:-

$$p(\theta_i+\frac{m}{M}\Delta\theta) \approx \frac{M-m}{M}.p(\theta_i) + \frac{m}{M}.p(\theta_{i+1})$$

$$= \frac{1}{M}\Big((M-m)p_i + mp_{i+1} \Big) \qquad \text{[A11.1]}$$

From the original N data points, two of the power functions that may be formed are given below:-

$$P_2 = \sum_{i=1}^{N} p_i^2 \qquad \text{[A11.2a]}$$

$$\tilde{P} = \sum_{i=1}^{N-1} p_i p_{i+1} \qquad \text{[A11.2b]}$$

Note that the second one purely gives a measure of the correlation between neighbouring angles. It is a simple extension to define a power function of the form of P_2, but also acting on the M-1 interpolation points between each angle used for beamforming:-

$$Q_2 = \sum_{k=1}^{K} p^2(\theta_k) \qquad \text{, where } K = M(N-1)+1 \qquad \text{[A11.3]}$$

$$= p_1^2 + \sum_{i=1}^{N-1}\sum_{m=1}^{M} \left\{ \frac{1}{M}\Big((M-m)p_i + mp_{i+1} \Big) \right\}^2$$

$$\approx \frac{1}{M^2}\Sigma\Sigma \left\{ (M-m)^2 p_i^2 + m^2 p_{i+1}^2 + 2m(M-m)p_i p_{i+1} \right\}$$

$$= \frac{1}{M^2}\sum \left\{ \tfrac{1}{6}(M-1)M(2M-1)p_i^2 + \tfrac{1}{6}M(M+1)(2M+1)p_{i+1}^2 \right.$$

$$\left. + \left[M^2(M+1) - \tfrac{1}{3}M(M+1)(2M+1) \right] p_i p_{i+1} \right\}$$

$$\approx \frac{(2M^3-3M^2+M)+(2M^3+3M^2+M)}{6M^2}\sum p_i^2 + \frac{(3M^3+3M)-(2M^3+3M^2+M)}{3M^2}\sum p_i p_{i+1}$$

$$= \frac{2}{3}\left(M + \frac{1}{2M} \right) P_2 + \frac{1}{3}\left(M - \frac{1}{M} \right) \tilde{P} \qquad \text{[A11.4]}$$

Now, if interpolation is only calculated for midpoints (i.e. M=2), then the factors become $\frac{3}{2}, \frac{1}{2}$. The results of such interpolation can be easily compared against results for original beamforming with $2N$-1 beams, to test the validity of the interpolation. The natural continuation is then to implement it for infinite M i.e. for all points along interpolation line. This is easily done, as the actual interpolation values are not required; it is sufficient to use the correct multiples of P_2 and $\tilde{P}$. In this case:-

$$\lim_{M\to\infty} Q_2 = \tfrac{2}{3}P_2 + \tfrac{1}{3}\tilde{P} \qquad \text{[A11.5]}$$

[Note dropping a factor of 'M' throughout makes no difference to the performance of the power function.] A similar extension of $\sum p^3$ leads to:-

$$Q_3 = \tfrac{1}{2}\sum p_i^3 + \tfrac{1}{2}\sum p_i^2 p_{i+1} \qquad \text{[A11.6]}$$

Equivalent forms for $\sum p^2\cos\theta$ are easily produced: the cross-correlation part may simply use $p_i p_{i+1}\cos\theta_i$ rather than $p_i p_{i+1}\sqrt{\cos\theta_i \cos\theta_{i+1}}$ as $p(\theta)$ varies much more quickly than the cosine term.

Also, note that performing the linear interpolation in p_i^2 would not lead to an improved power function. It might be more accurate if the linear interpolation was applied to V(θ); however, this would lead to much more complicated arithmetic, so such has not been considered worthy of implementation as yet. Another possible improvement is to use a quadratic interpolation — this will lead to an overall power function containing summations of the form $\sum p_i^2$, $\sum p_i p_{i+1}$ and $\sum p_i p_{i+2}$.

App 12. ESTIMATION OF THE PARAMETERS OF A SINUSOID

If a sinusoid of known period is sampled, an estimate can be made of its mean value and the amplitude of its oscillations. Let the sinusoid have period, T, amplitude, a, phase lead, ϕ and bias, b, i.e.

$$y = b + a\cos(2\pi t/T + \phi) \qquad \text{[A12.1]}$$

As the period is known *a priori*, samples can be taken at regular intervals throughout one cycle i.e. for $t_i = iT/n$, $i = 0, n-1$. Then the value of the ith sample is given by:-

$$y_i = b + a\cos(2\pi i/n + \phi) = b + \mathrm{R}\left\{Ae^{j\omega i}\right\} \qquad \text{[A12.2]}$$

where $A = ae^{j\phi}$, $\omega = 2\pi/n$ and $\mathrm{R}\{\cdots\}$ is the operation taking the real part of a number. The sum of the samples is given by:-

$$S_1 = bn + \mathrm{R}\left\{\sum_{i=1}^{n} Ae^{j\omega i}\right\} = bn + A\,\mathrm{R}\left\{\frac{e^{j\omega n}-1}{e^{j\omega}-1}\right\} \qquad \text{[A12.3]}$$

As $n\omega = 2\pi$, the mean of the samples, $m = S_1/n$ will simply yield b, provided that $e^{j\omega} \neq 1$; the equality only occurs for $n = 1$.

Similarly, designating the sum of the squared deviations from the mean by S_2, yields (for $n \neq 1$):-

$$S_2 = \sum_{i=1}^{n} a^2\cos^2(\omega i + \phi) = \sum_{i=1}^{n} a^2\left[\tfrac{1}{2} + \tfrac{1}{2}\cos(2\omega i + 2\phi)\right]$$

$$= \frac{a^2 n}{2} + A_2\,\mathrm{R}\left\{\frac{e^{2j\omega n}-1}{e^{2j\omega}-1}\right\} \qquad \text{[A12.4]}$$

Thus, the variance, $\sigma^2 = S_2/n$ will yield the correct rms value, $a^2/2$, as long as n is neither 1 nor 2. It may be concluded that 3 *correctly* spaced samples are all that is required to make an unbiased estimate of the mean and standard deviation of a sinusoid.

App 13. STATISTICS OF SAMPLES FROM A GAUSSIAN DISTRIBUTION

A commonly used pdf (probability distribution function) is that referred to as a Gaussian or normal distribution. In such a model, the probability of a variable having a certain value, x, is given by:-

$$p_r(x) = \frac{1}{\sqrt{2\pi}\,\alpha} e^{-(x-x_0)^2/2\alpha^2} \qquad \text{[A13.1]}$$

where the mean value is x_0, and the standard deviation, α. For many uses, x is measured from the mean, so in the analysis below $x_0 = 0$ and is hence omitted. Some simple mathematical manipulations show the following:-

$$\int_{-\infty}^{\infty} \frac{1}{\sqrt{2\pi}\,\alpha} e^{-x^2/2\alpha^2}\, dx = 1 \qquad \text{[A13.2]}$$

$$\int_{-\infty}^{\infty} x \frac{1}{\sqrt{2\pi}\,\alpha} e^{-x^2/2\alpha^2}\, dx = 0 \qquad \text{[A13.3]}$$

$$\int_{-\infty}^{\infty} x^2 \frac{1}{\sqrt{2\pi}\,\alpha} e^{-x^2/2\alpha^2}\, dx = \alpha^2 \qquad \text{[A13.4]}$$

The first equation shows the distribution is correctly normalized i.e. probability that x is between minus and plus infinity is unity; the second that the mean is zero; and the third that the variance is α^2. Simple integration by parts yields the expectation of x^4, and thus the kurtosis, κ :-

$$\int_{-\infty}^{\infty} x^4 \frac{1}{\sqrt{2\pi}\,\alpha} e^{-x^2/2\alpha^2}\, dx = 3\alpha^4 \qquad \text{[A13.5]}$$

$$\kappa = E[x^4] - E^2[x^2] = 2\alpha^4 \qquad \text{[A13.6]}$$

Another figure of occasional interest is the expected absolute deviation from zero, as opposed to rms deviation i.e. the standard deviation; the form for the former is given below:-

$$\int_{-\infty}^{\infty} |x| \frac{1}{\sqrt{2\pi}\,\alpha} e^{-x^2/2\alpha^2}\, dx = \int_0^{\infty} \frac{2x}{\sqrt{2\pi}\,\alpha} e^{-x^2/2\alpha^2}\, dx = \sqrt{2/\pi}\,\alpha \qquad \text{[A13.7]}$$

This project has entailed statistical analysis of many simulation results, which generally approximate to a Gaussian distribution [see chapter 17]. In any case, the Central Limit Theorem states that the average of many simulations will follow such a distribution. In order to compare different conditions or different methods of processing, it is desirable to *know* the mean and s.d. of the estimate for any given situation. However, such can only be measured approximately, and that by averaging independent realizations. The ensemble mean and variance are defined as follows:-

$$\bar{x} = \frac{1}{n}\sum_{i=1}^{n} x_i \qquad \text{[A13.8]}$$

$$\text{var}(x) = \frac{1}{n}\sum_{i=1}^{n} x_i^2 \qquad \text{[A13.9]}$$

Note, in the second case, it is tacitly assumed that the mean is zero. Using [A13.2-5], the expected statistics of $\bar{x}$ and var(x) can be deduced as follows:-

$$\mathrm{E}[\bar{x}] = \frac{1}{n}\sum_{i=1}^{n} \mathrm{E}[x_i] = 0 \qquad \text{[A13.10]}$$

$$\text{var}(\bar{x}) = \mathrm{E}[\bar{x}^2] - \mathrm{E}^2[\bar{x}] = \frac{1}{n^2}\sum_{i=1}^{n}\sum_{j=1}^{n} \mathrm{E}[x_i x_j] - 0 = \frac{1}{n}\mathrm{E}[x^2] = \alpha^2/n \qquad \text{[A13.11]}$$

$$\mathrm{E}[\text{var}(x)] = \frac{1}{n}\sum_{i=1}^{n} \mathrm{E}[x_i^2] = \mathrm{E}[x^2] = \alpha^2 \qquad \text{[A13.12]}$$

$$\text{var}(\text{var}(x)) = \mathrm{E}\left[(\text{var}(x)-\alpha^2)^2\right] = \mathrm{E}\left[\left(\frac{1}{n}\sum_i x_i^2 - \alpha^2\right)\left(\frac{1}{n}\sum_j x_j^2 - \alpha^2\right)\right]$$

$$= \frac{1}{n^2}\sum_i\sum_j \mathrm{E}\left[(x_i^2-\alpha^2)(x_j^2-\alpha^2)\right] = \frac{1}{n}\left\{\mathrm{E}[x_i^4] - \alpha^4\right\} = 2\alpha^4/n \qquad \text{[A13.13]}$$

It follows, therefore, that the estimate of the mean will be unbiased, but subject to variation with s.d. equal to α^2/n. The estimated mean is thus unlikely ($< 5\%$) to differ by more than 2 s.d. from that correctly associated with the estimator. [Its value may differ significantly from the expected mean; this discrepancy can then be attributed to a slightly biased estimator, rather than a statistical fluctuation.]

Similarly, ensemble averaging will yield an unbiased estimate of the variance, α^2; its variation from this value will have a s.d. of $\sqrt{2/n}\,\alpha^2$, so that if 200 realizations are averaged, the variance measured will be correct to within 10%, and, consequently, the measured s.d. of the estimates will be within 5% of true. This is quite a large value for the variation, implying that rms

estimates for 2 situations of identical error may be expected to differ by 7%. Such, a problem has been observed several times e.g. when a source at 15° led to less errors than one at 0° [Table 23.2]. Note that if only 50 simulations were used instead of 200, in order to save computer time, the associated errors in the rms values would be doubled.

This is the reason that several of the simulations for comparing processing parameters and element failure operate on stored databases. It being expected that slight differences which would be hidden by the random statistics of different realizations, may be more clearly seen when all the processing is performed on identical signal records.